

# Gold Nanoparticles: Plasmonic Aspects And Applications

Dr. Abhitosh Kedia  
Dr. Pandian Senthil Kumar

Gold Nanoparticles:  
Plasmonic Aspects and Applications



**EMPYREAL PUBLISHING HOUSE**

Guwahati

# Gold Nanoparticles: Plasmonic Aspects and Applications

By:

Dr. Abhitosh Kedia

Dr. Pandian Senthil Kumar

First Impression: 2018

## Gold Nanoparticles: Plasmonic Aspects and Applications

ISBN : 978-81-939070-0-9

Rs. 550/-

No part of the book may be printed, copied, stored, retrieved, duplicated and reproduced in any form without the written permission of the author/publisher.

### **DISCLAIMER**

Information contained in this book has been published by Empyreal Publishing House and has been obtained by the author from sources believed to be reliable and are correct to the best of his knowledge. The author is solely responsible for the contents of the articles compiled in this book. Responsibility of authenticity of the work or the concepts / views presented by the author through this book shall lie with the author and the publisher has no role or claim or any responsibility in this regards. Errors, if any, are purely unintentional and readers are requested to communicate such error to the author to avoid discrepancies in future.

Published by:  
Empyreal Publishing House  
Guwahati, Assam  
Mobile No: 9999817591  
Email: info@editedbook.in

Dedicated to

**Almighty, Lord Krishna**

**Dr. Abhitosh Kedia**

## Preface

The preparation of nanometer-scale metal particles with controlled geometries (such as spheres, faceted polyhedras, nanorice, nanokites and nanostars) in solution is a major subject in the field of nanochemistry because of their unusual optical properties (typical colors coming from gold and silver nanoparticles). The size/shape tunable optical properties of these metallic nanoparticles have exciting practical applications in the field of nanoelectronics, catalysis, optical filters, photonics and surface-enhanced Raman scattering (SERS) and their vast potential applications in many other areas. It has been shown that the oscillation of electrons at the metal dielectric interface is strongly dependent on the size and shape of metal NPs.

The physical/chemical methods utilized for producing such low-dimensional metal nanostructures require precise tuning of nucleation and growth steps to achieve better crystallographic control. Currently available experimental capabilities to create/design versatile metal nanoparticles on demand have validated the bottom-up wet chemical/colloidal synthesis procedures (the atom-by-atom building block approach) for engineering the morphology right from the nucleation stage itself, followed by their stabilized growth into thermodynamically unfavorable size/shapes, the exciting results of which has already been suitably explained in terms of respective synthesis protocols.

One of the main ingredients in the chemical synthesis of nanoparticles is the capping agents (either polymers or surfactants), which in general, can act both as stabilizers and shape directing agents. Additionally, separation between nucleation and growth processes were enthused by the presence of capping agents, wherein smaller seed particles nucleate first and are grown into larger nanoparticles through the reaction assisted ripening process derived from the well-known LaMer mechanism.

The major theme of this book extensively correlates the mild reducing ability of such polymer poly(Vinyl Pyrrolidone) PVP that invariably advocates the formation of size/shape controlled anisotropic metal (gold) nanostructures exemplified by the observed molecular ligand exchange growth mechanism, by simultaneously considering their nucleation and kinetic growth mechanism through combined data analysis of spectroscopic/microscopic techniques in a rather significant manner.

In chapter 1, we examined the some facts related to gold/gold complexes. We focus majorly on the fundamentals of plasmonics and optical properties of noble metals. A discussion on the various synthesis methods of nanomaterials and role of ligands/capping agent is provided. The introduction ended with the discussion on physical/chemical/spectroscopic of PVP which was found suitable not only for stable surface stabilization but also for rendering mild reducing power towards the formation of various metal nanoparticles.

Chapter 2 give brief description about characterizations techniques such as UV-Vis spectroscopy, Transmission electron microscopy, Raman Spectroscopy, Fourier transform Infra Red spectroscopy, scanning electron microscopy etc. for characterizing nanomaterials.

In chapter 3, PVP in different (in)organic solvents along with gold ion at the given specific monomer to metal ratio is well utilized in achieving morphology driven localized surface plasmon suitable for wide range of plasmonic as well as photonic applications by simultaneously considering their nucleation and kinetic growth mechanism through various spectroscopic/microscopic techniques.

Chapter 4 demonstrate on single step seedless/templateless organic synthesis procedure for the complex 3-D gold nanostars with a high degree of size/shape control. On the basis of the kinetic optical absorption and FTIR spectroscopy measurements, a convenient ligand exchange mechanism has been proposed. Also CL spectroscopy was effectively illustrate locally/selectively excite plasmonic aspects of multi-branched gold nanostars.

Further controlled tuning of the plasmonics eigenmodes of gold nanostars in a sequential manner from visible to the near IR region with morphology correlation were accomplished with exceptional level of wavelength agility by independently introducing the NaOH or co-solvent in the precursor reaction mixture in chapter 5 and by halide ions in chapter 6.

Finally last chapter examines the surface roughness/sharpness of as prepared gold nanoparticles for their SERS efficiency; so as to expedite them as promising SERS substrates with ease.

Each chapter ends with a summary of all the important points discussed therein. Sincere efforts have been made to discuss all the important aspects of plasmonics nanostructures.

**Dr. Abhitosh Kedia**  
**Dr. Pandian Senthil Kumar**

## **Acknowledgements**

I would like to express my gratitude to many people who saw me through this book; to all those who provided support, talked things over, read, wrote, offered comments, allowed me to quote their remarks and assisted in the editing, proofreading and designing.

I would like to tribute my sincere thanks to Dr. P. Senthil Kumar who selflessly encourage and help in a friendly way through his deep-rooted knowledge, masterly approach, meticulous guidance, critical suggestions. He is greatly acknowledged for influencing my personnel and professional life in positive way. I take this opportunity to place on record my heart-felt and sincere gratitude and deep indebtedness to him.

I would like to thanks all my friends with whom I constantly enjoyed the savor of interaction. They are greatly acknowledged for making my stay comfortable and helping me in every sense.

I specially thank to University of Delhi, Delhi for financial support, M.Tech. (NSNT) and IR chemistry for Material characterizations and CSIR for fellowship.

I owe this book to my family for their support and love from the very first day of my journey of life.

Lastly, I thank to all who are with me or not but their constant blessing always bestowed me a helping hand to accomplishing this work.

**Dr. Abhitosh Kedia**

**Dr. Pandian Senthil Kumar**

## Abbreviations

<b>CL</b>	Cathodoluminescence
<b>CTAB</b>	Cetyl Trimethylammonium Bromide
<b>CTTS</b>	Charge-Transfer-to-Solvent
<b>CV</b>	Crystal Violet
<b>DLS</b>	Dynamic Light Scattering
<b>DMF</b>	Dimethylformamide
<b>EF</b>	Enhancement Factor
<b>EM</b>	Electromagnetic
<b>FDTD</b>	Finite-Difference Time-Domain
<b>FTIR</b>	Fourier Transform-Infra Red
<b>HMTEM</b>	High Magnification Transmission Electron Microscopy
<b>HRTEM</b>	High-Resolution Transmission Electron Microscopy
<b>IR</b>	Infrared
<b>ITO</b>	Indium Tin Oxide
<b>LDOS</b>	Local Density of Optical States
<b>LSPR</b>	Localized Surface Plasmon Resonance
<b>NMR</b>	Nuclear Magnetic Resonance
<b>NPs</b>	Nanoparticles
<b>PVP</b>	Poly(Vinyl Pyrrolidone)
<b>SAED</b>	Selected Area Electron Diffraction
<b>SEM</b>	Scanning Electron Microscope
<b>SERS</b>	Surface Enhancement Raman Scattering
<b>SPR</b>	Surface Plasmon Resonance
<b>TEM</b>	Transmission Electron Microscopy
<b>UV-Vis</b>	Ultraviolet Visible
<b>XPS</b>	X-ray Photoelectron Spectroscopy

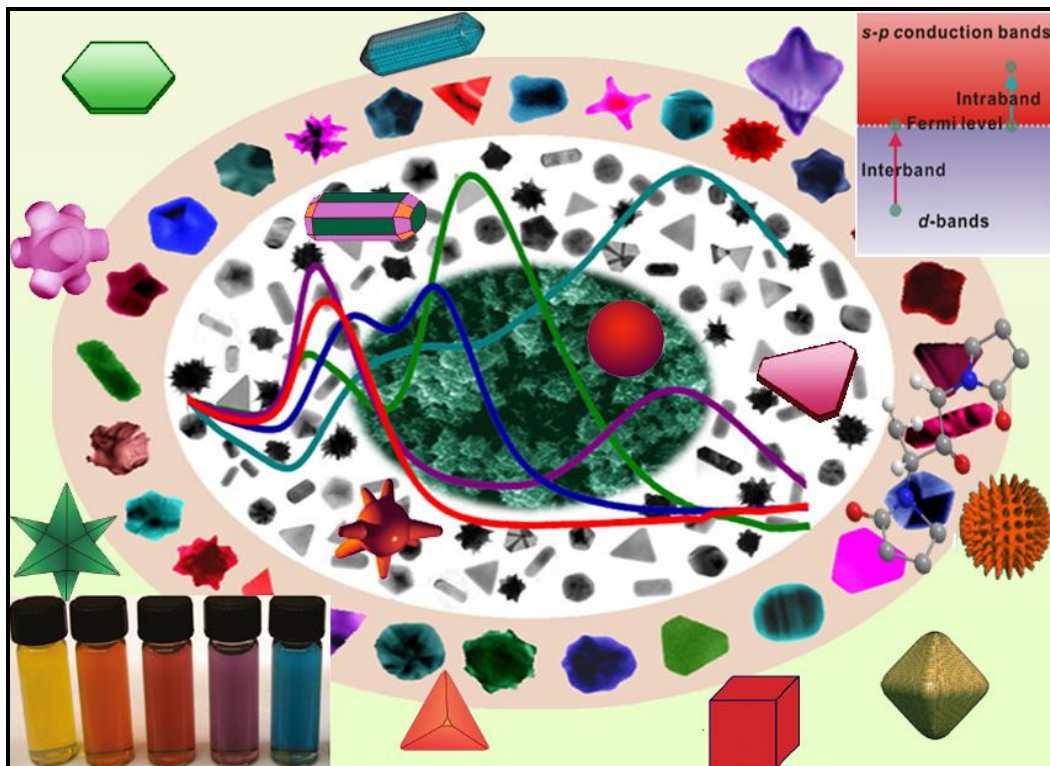
## Table of Contents

<b>Preface</b>	<b>V – VI</b>
<b>Acknowledgement</b>	<b>VII</b>
<b>Abbreviations</b>	<b>VIII</b>
<b>Table of Contents</b>	<b>IX - X</b>
<b>Chapter 1: Introduction</b>	<b>1 – 16</b>
1.1 Gold - A Historical Background	2 – 3
1.2 Optical properties of Metal Nanoparticles	3 – 8
1.3 Physical / Chemical Properties of Gold Complexes	9 – 11
1.4 Synthesis Methodologies for Plasmonic Resonant Nanoparticles	11 – 12
1.5 Role of Surfactant in Synthesis of Metal Nanoparticles	12 – 14
1.6 Poly (Vinyl Pyrrolidone)	14 – 15
1.7 Objective of the thesis	15 - 16
<b>Chapter 2: Materials And Methods</b>	<b>17 – 28</b>
2.1 Synthesis Protocol	18
2.2 Spectroscopies	18 – 25
2.3 Microscopies	25 – 28
<b>Chapter 3: Poly (Vinyl Pyrrolidone) Induced Anisotropic Gold Nanostructures</b>	<b>29 – 40</b>
3.1 Theme of the Chapter	30
3.2 Synthesis Protocol	30
3.3 Structure Correlated Plasmonic Signatures	31 – 32
3.4 Spectroscopic Study of Molecular Interaction	32 – 40
<b>Chapter 4: One Step Synthesis of Gold Nanostars: Combined Optical and Cathodoluminescence Study</b>	<b>41 – 54</b>
4.1 Theme of the Chapter	42
4.2 Synthesis Protocol	42
4.3 Structural and Morphological Investigations	43 – 44
4.4 Optical Aspects	44 – 48
4.5 Effective Role of HCl	49 – 50
4.6 Nucleation and Growth Mechanism	50 - 54
<b>Chapter 5: Structural-Correlated Plasmon Tuning Mechanism of Gold Nanostars</b>	<b>55 – 72</b>
5.1 Theme of the Chapter	56
<b>Section A</b>	
5.2 Synthesis Protocol	56
5.3 Results and Discussion	57 – 65
<b>Section B</b>	
5.4 Synthesis Protocol	65
5.5 Results and Discussion	66 – 72

<b>Chapter 6: Self-Organization/Reshaping of Gold Nanostars</b>	<b>73 – 84</b>
6.1 Theme of the Chapter	74
6.2 Synthesis Protocol	74
6.3 In-Situ Addition of Halide Ions	75 – 82
6.4 Ex-Situ Addition of Halide Ion	83 – 84
<b>Chapter 7: Shape Selective Surface Enhanced Raman Measurements</b>	<b>85 – 89</b>
7.1 Shape Selective SERS Enhancement	86 – 89
<b>Summary of Book</b>	<b>90 – 91</b>
<b>References</b>	<b>92 – 109</b>
<b>Appendix</b>	<b>110 - 118</b>

# Chapter - 1

## Introduction



## 1.1 GOLD – A HISTORICAL BACKGROUND

Humans, almost intuitively, attribute a high value to gold, associating it with power, beauty and the cultural elite - long before it became one of the standard medium for exchange. Historical evidences suggest the presence of gold under the name of *Swarna Bhasma* and *Makaradhwaja* in traditional medicine system of India called Ayurveda, which dates back to 1<sup>st</sup> millennium BC [1]. The use of gold in modern medicine began in 1890, when the German bacteriologist *Robert Koch* discovered that gold cyanide was bacteriostatic to the tubercle bacillus *in vitro* [2].

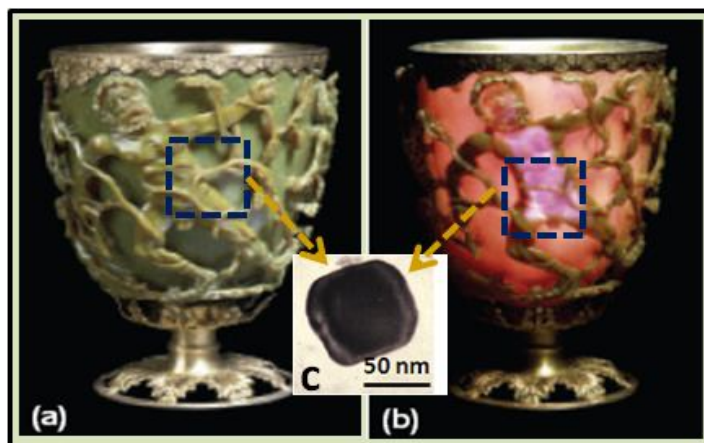


Figure-1.1: The Lycurgus Cup (reprint from ref [4]) in (a) reflected and (b) transmitted light. (c) Transmission electron microscopy (TEM) image from the selected regions show the presence of silver-gold alloy nanoparticles, which impart bright color to it.

Important aspects of gold compounds were to impart bright colors, which had been known for many centuries. The Egyptians, Greeks and Romans were exceptional in making colored pigments for the decoration of their buildings, ceramics and glass-ware. The *state of the art* work involving the embodiment of tiny gold particles in glasses could be seen as early as the 4<sup>th</sup> century AD in the famous *Lycurgus Cup* (figure 1.1), currently exhibited in the British Museum [3].

This Roman cut glass vessel is extraordinary in several respects: firstly, in its intriguing method of fabrication and the exceptional workmanship involved; secondly, in terms of its unusual optical effects. The glass cup is dichroic in nature - resembling a jade with an opaque greenish-yellow tone in direct light, but turns to a translucent ruby color (figure 1.1a and b), when light shines through the glass (transmitted light), the sophisticated chemical analysis of which suggest the presence of a mixture of both gold and silver nanoparticles contributing to its essential color; the gold component being mainly responsible for the reddish transmission and the silver for the greenish reflection [4]. Experts attributed this dichroic coloring to the *surface plasmon resonance (SPR)* of metal nanocrystals (typically 50-100 nm in diameter, which is responsible for this anomalous behavior, see figure 1.1c) [4, 5]. The specific optical properties of these small metal nanoparticles attracted many scientists working in both the theoretical and experimental field and instrumental in the evolving of modern colloid chemistry.

### 1.1.1 Scientific Approach towards Colloidal Gold

In the middle of nineteenth century, systematic scientific interests in colloidal systems began. Dr. Michael Faraday in the year 1857, in his renowned Bakerian Lecture entitled, “*Experimental Relations of Gold (and other metals) to Light*” [6] (first documented scientific investigation for the chemical synthesis of colloidal gold), described his optical investigations of very thin gold films and of ruby-red colored suspensions of ultramicroscopic gold particles in various liquids (figure 1.2). He observed that *...gold is reduced in exceedingly fine particles, which becoming diffused, to produce a beautiful ruby fluid* and further adds that *the fluids have all the appearance of solutions, only diffused gold*. Faraday’s discovery that metals could form colloids was a major breakthrough, although the importance of his observations on the concept of colloid chemistry could not be fully realized at that point of time. The word “*colloid*” however, was first introduced by his London colleague, Thomas Graham (1805-1869), then known as the father of colloid chemistry.



Figure-1.2: Colloidal gold solutions (inset) alias the “ruby fluid” as synthesized by Michael Faraday in his laboratory in 1857.

*Gustav Mie* [7] calculated the absorbance of colloidal gold particles as a function of the particle size using classical electromagnetic theory by utilizing the bulk parameters of metallic gold and scientifically explained the Faraday results. In 1917, *Richard Zsigmondy* found that monodispersed gold colloids were readily produced by using faraday gold sols as seed crystals with high reproducibility, further improved by *Turkevich* in 1951 [8] and *Frens* in 1973 [9]. In 1925, *Richard Zsigmondy* received the Nobel Prize in Chemistry for his work in the field of modern colloid chemistry by studying the properties of gold sols and inventing an ultra microscope, through which he noticed not only a color change of the individual particles, but also considerable change in the number of particles.

From then onwards, synthesis of metal nanoparticles has received considerable attention collectively by physicists, chemists, biologists and most importantly engineers for exclusively studying the fascinating effects on the respective properties due to their increase in surface to volume ratio [10]. At nanoscale, the electronic structure of materials also gets modified resulting in the development of discrete energy levels in contrast to the continuum in bulk materials [11, 12], which leads to dramatic modification of many [10] fundamental properties such as electrical and thermal conductivity, band gap, density of states, electron affinity, mechanical, magnetic and optical properties etc [10]. We mainly focus our discussion on the optical properties of metal nanoparticles in the following section.

## **1.2 OPTICAL PROPERTIES OF METAL NANOPARTICLES**

Classical electromagnetic (EM) theory provided the first rigorous explanation of the optical properties of noble metal nanoparticles (whose dimensions are much less than that of the wavelength of light used), attributing their unusually vibrant colors to the EM resonances due to collective oscillations of the conduction electrons [13-15], termed aptly as ‘*plasmons*’ or to be precise ‘*surface plasmons*’, that exist most importantly in the visible/optical wavelength region for noble metals such as gold, silver and copper. The term ‘*plasmon*’ was first coined in 1956 to describe collective electronic oscillations in solids, which were very similar to electronic oscillations/surface waves called free electron plasma or solid state plasma.

Surface waves originating in a plasma were initially considered to be just a tool for basic research, until they were successfully used for the generation of plasma aided nanoscale synthesis, processing and fabrication of metal-based nanostructures into plasmonic devices - the missing link needed to bridge not only surface waves from traditional plasma physics and surface plasmons from optics, but also, more topically, macroscopic gaseous and nanoscale metal plasmas [16].

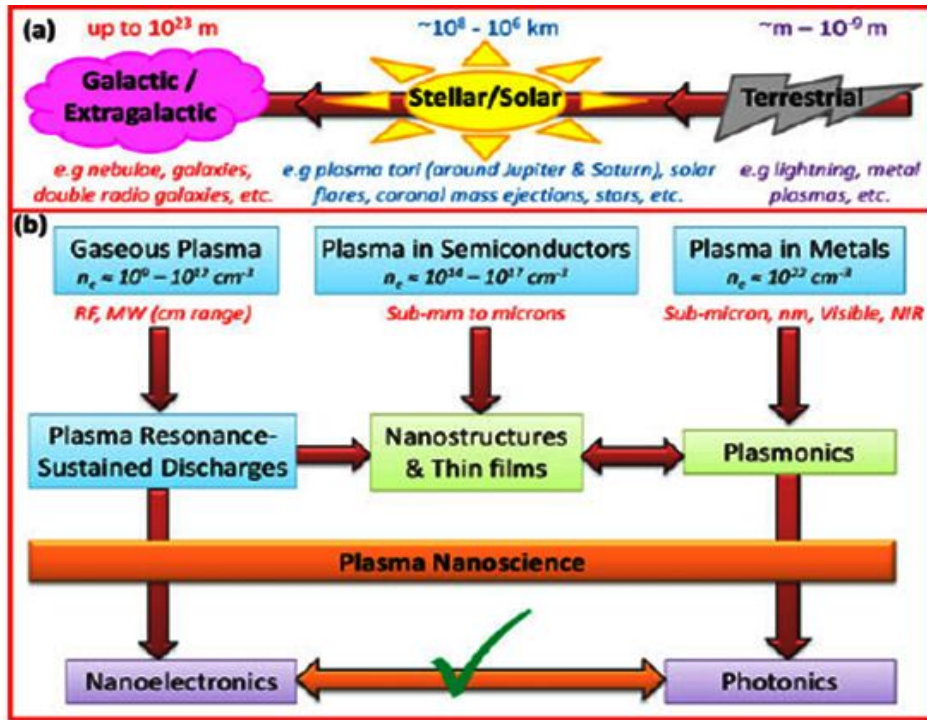


Figure-1.3: (a) Typical sizes of plasmas – from extragalactic plasmas to the metal plasmas of our interest. (b) Logic flowchart – from gaseous plasmas to nanoelectronics and photonics having relationship through plasma nanoscience, where  $n_e$  is the number density of electron (reprinted from [16] with permission from Springer).

Figure 1.3 describe how related areas of research may be linked through plasma nanoscience showing, by closely looking at the essential physics as well as current/future applications, how everything old, is new, once again [16].

Since the plasmons are characteristics of the interaction of light with metals and most of the physics behind it is hidden in the frequency dependent complex dielectric function, which proficiently explains the overall optical properties of bulk metals (in particular, the noble metals such as Ag, Au and Cu) utilizing the Drude-Sommerfeld model, taking into account the effect of (i) the freely moving conduction electrons and (ii) inter-band transitions [17-20].

### 1.2.1 Drude-Sommerfeld Model

The equation of motion for electrons of the plasma sea subjected to an external field  $E$  can be written using Drude-Sommerfeld model as follows:

$$m_e \frac{\partial^2 r}{\partial t^2} + m_e \gamma_d \frac{\partial r}{\partial t} = e E_0 e^{-i\omega t} \quad (1.1)$$

where  $e$  and  $m_e$  are the charge and the effective mass of the free electrons, and  $E_0$  and  $\omega$  are the amplitude and the frequency of the applied electric field. These electrons move freely with unspecified collision centers (lattice ions, other electrons, defects, phonons, etc.), which occur with an average rate of  $\gamma_d = \tau^{-1}$  with  $\tau$  being the so-called electron relaxation time. In the presence of an electric field, all free electrons results in a macroscopic polarization per unit volume  $P = n\mu$ , where  $n$  is the number of electrons per unit of volume. The material specific dielectric function directly connects the external field with the electric displacement field  $D$ , which accounts for the effects of free charge in the medium and the polarization density  $P$ .

Also, the electric displacement  $D$  is related to this macroscopic polarization by

$$D(r,t) = \epsilon_0 E(r,t) + P(r,t) \quad (1.2)$$

Using the time dependent plane wave solution,  $r(t) = r_0 e^{-i\omega t}$ ,  $P = n\mu$ ,  $D = \epsilon\epsilon_0 E$  and substituting equation 2 in 1 yields

$$\epsilon_{Drude}(\omega) = 1 - \frac{\omega_p^2}{\omega^2 + i\tau\omega} \quad (1.3)$$

Here  $\omega_p^2 = ne^2 / m\epsilon\epsilon_0$  is the volume plasma frequency. Expression (1.3) can be divided into real and imaginary parts as follows.

$$\epsilon_{Drude}(\omega) = 1 - \frac{\omega_p^2}{\omega(\omega^2 + \tau^2)} + i \frac{\tau\omega_p^2}{\omega(\omega^2 + \tau^2)} \quad (1.4)$$

Neglecting  $\tau$ , we get  $\epsilon_{Drude}(re(\omega)) = 1 - \omega_p^2 / \omega^2$ .

In the low frequency region ( $\omega_p^2 \gg \omega^2$ ),  $\epsilon_{drude}$  becomes negative and  $n$  is imaginary. An imaginary refractive index implies that an EM wave cannot propagate inside the medium. The specific value of  $\omega_p$  for most metals lies in the ultraviolet region, which is the reason why they are shiny and glittering in the visible spectrum. A light wave with  $\omega < \omega_p$  is reflected, on the other hand, if  $\omega > \omega_p$ , the light wave gets transmitted (the metal becomes transparent).

### 1.2.2 Noble Metals and Inter-band Transitions

Optical measurements on noble metals (having filled d shell like Au and Ag) show a somewhat ambiguous behavior at high energy: whereas the low energy values are well described by the Drude-Sommerfeld model, implying the presence of additional contributions at higher energies ie, the excitation of electrons from deeper bands into the conduction band, the so-called inter-band excitations or classically the excited state oscillation of bound electrons, which invariably affect the  $\epsilon(\omega)$  (figure 1.4) [18-22].

In noble metals, the d electrons are very close to Fermi level as shown in figure 1.4 (d electrons are shown in red color lying near to Fermi surface) and inter band transition from these occupied bands to the conduction band can be excited with energy corresponding to visible and UV frequencies (at higher energy). At these frequencies, both the free electrons and inter-band transitions would contribute effectively to the metal dielectric function [23].

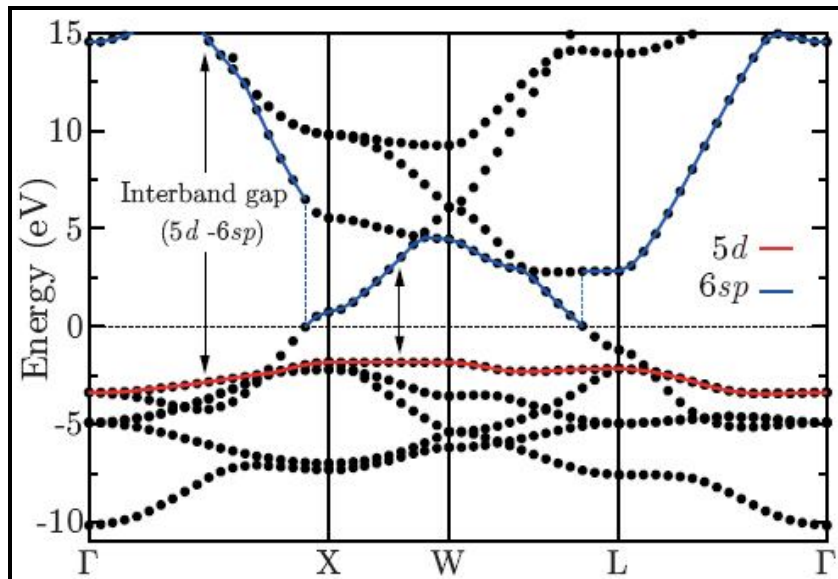


Figure-1.4: The Au band structure, calculated by density functional theory (reprint with permission from ref [21]). The Fermi level is set to 0 (dashed-black line). Red (grey) lines disentangle 5d-character topmost occupied bands, while blue (black) lines indicate 6sp- like lower most empty bands. The arrows show the inter-band gap between the highest occupied 5d band and the lowest unoccupied 6sp bands.

Applying the same free electron procedure to the bound electrons, their equation of motion reads as follows:

$$m \frac{\partial^2 r}{\partial t^2} + m\gamma_d \frac{\partial r}{\partial t} + \alpha r = eE_0 e^{-i\omega t} \quad (1.5)$$

where  $\alpha$  is the spring constant of the potential that keeps the electron in place. Using similar plane wave solutions as before, we find the contribution of bound electrons to the dielectric function in term of real and imaginary parts as

$$\varepsilon_{Interband}(\omega) = 1 + \frac{\omega_p^2(\omega_0^2 - \omega^2)}{(\omega_0^2 - \omega^2)^2 + \gamma_d^2 \omega^2} + i \frac{\tau \omega_p^2 \omega}{(\omega_0^2 - \omega^2)^2 + \gamma_d^2 \omega^2} \quad (1.6)$$

Here  $\omega_p = \sqrt{n_1 e^2 / m \varepsilon_0}$  with  $n_1$  being the density of the bound electrons.  $\omega_p$  is introduced in analogy to the plasma frequency in the Drude-Sommerfeld model, however, obviously here with a different physical meaning  $\omega_0 = \sqrt{\alpha / m}$ .

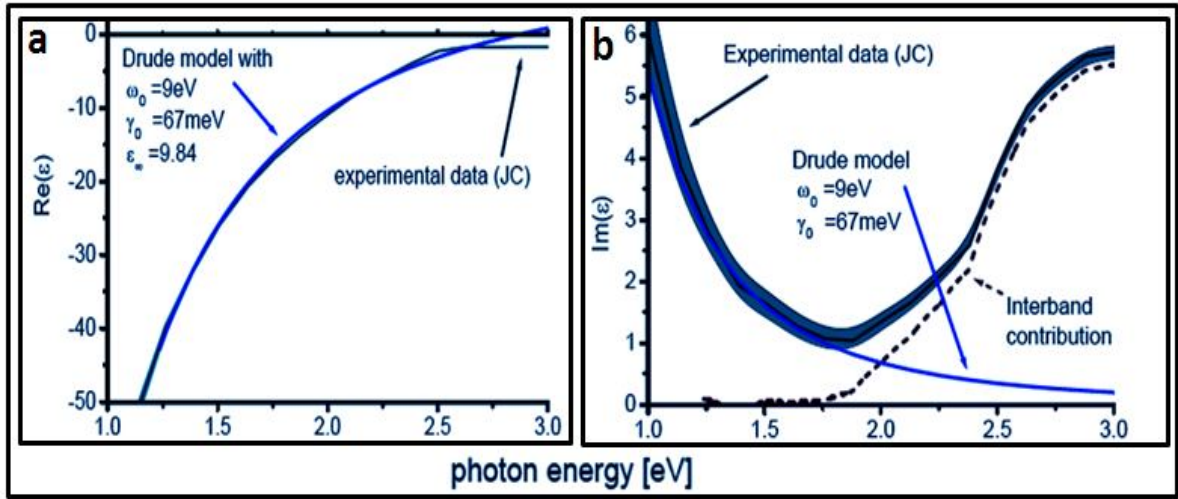


Figure-1.5: Experimental (a) Real and (b) imaginary parts of the dielectric function for gold together with the measuring uncertainty (shaded area around the experimental data). Experimental data (JC) from Johnson and Christy (1972, [18]) compared to calculated values using Drude model with the parameters indicated in the graph. The inter-band contribution (broken line) is calculated from the difference of the experimental data to the Drude model.

The plot of real and imaginary parts of dielectric constant as a function of light frequency for gold is shown in figure 1.5 along with the data taken from the reference of Johnson & Christy [18]. The real part is well described by the model but the strong deviation is observed above 1.8 eV, for the imaginary part which are due to the inter-band transitions. Clearly, this model is not adequate for describing either real or imaginary part of  $\varepsilon$  at high energy, and in the case of Au, its validity breaks down already at the boundary between the near-infrared and the visible. Physically, this means that the natural oscillations of the free-electron plasma are affected by the presence of inter-band transitions.

Here, we are interested in small NPs mostly stable at room temperature; hence, we have to consider that electrons can be also dispersed by the NP surface, because the free electron's mean free path (is characteristic of collision time  $\tau$ ) is now comparable or larger than the dimension of the particle. Therefore, it is necessary to include an extra damping term  $\tau(a)$  to  $\varepsilon_{drude}(\omega)$  due to the surface scattering of the free electrons and hence shifted optical transition to visible region [24]. The surface dispersion not only depends on the particle size, but also on its shape [25]. The surface dispersion of a sphere of radius 'a' given by,  $1/\tau(a) = v_f/a$ , where  $v_f$  is the Fermi velocity of the electron cloud. The smaller the particle, the more important is the surface dispersion effect.

### 1.2.3 Surface Plasmon Resonance and its Origin

The expression of the dielectric constant found for the bulk would essentially qualify the conditions for which the valence electron cloud resonates in case of NPs. Besides, as the NP size is very small with regard to the incident wavelength, one can consider that all the electrons confined in a NP see the same field at a given time  $t$  or spatially constant field with a time dependent phase: the electric field is considered as independent of position [24, 26, 27]. This hypothesis, called as the quasi-static approximation, results in the polarization of charges at the surface of metal NPs and the arising restoring force again (see figure 1.6) forms a collective plasmonic oscillation (called surface plasmon resonance (SPR)) [28-32]. This aspect of the problem justifies the use of the term “surface” in the designation of the global phenomenon. Thus, plasmons are quantum of quasi-particles representing the elementary excitations, similar to that of the charge density oscillations in plasma; just like photon - the quantization of EM field. However, one has to keep in mind that all the electrons are moving collectively while under the effect of the field. Such collective oscillation leads to plasmon polaritons or surface plasmons, in contrast to the free plasmons occurring in the case of a bulk metal.

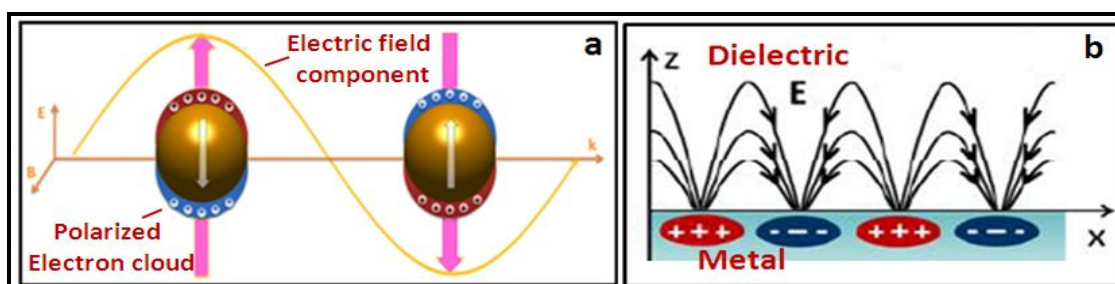


Figure-1.6: (a) Schematics for localized plasmon oscillations (surface plasmons) for a sphere; showing displacement of conduction electrons charge cloud relative to nuclei. (b) Schematic representation of the EM field associated with a surface-plasmon polariton propagating along a metal–dielectric interface.

The resonance condition is determined from optical absorption/scattering spectroscopy and is found to depend on the shape, size and dielectric constants of both the metal and the surrounding dielectric medium [17, 33-37]. The SPR can be of two types: localized or propagating (see figure 1.6) [29-31, 38]. Propagating surface plasmons, also called surface plasmon polaritons (SPP), are oscillations of electric charges travelling at a metal–dielectric (thin film like silicon, glass, ITO) interface. But in colloidal solution, oscillations are localized on individual particle surfaces and are thus called localized surface plasmon resonance or LSPR. This particle-confined oscillation occurs over the entire particle surface, howsoever the strongest electric fields are found at the metal–dielectric interface (hence the name “surface”).

Three wavelength-dependent phenomena arise from SPR: enhancement of the electric field on the surface of the particle, strong surface plasmon absorption bands (photon absorption), and strong light scattering. The former gives rise to the EM contribution in surface-enhanced spectroscopies [39]. The latter two are directly responsible for color and highly dependent on the size/shape of the respective materials (Au, Ag, Pd and Cu) [39]. These precise properties prompted not only the fundamental interests in SPR for better understanding the optical components of metallic nanoparticles, but also encourages ongoing research in SPR based superfast computer chips [40], new possibilities to treat cancer [41], ultrasensitive molecular detectors [42, 43], nanoantennas for light emitting diode [44, 45], the ability of making things invisible with negative-refraction materials [46-48] or plasmonic waveguiding (confining or guiding the EM fields over dimensions smaller than the sub-wavelength scale) etc [49-52].

One of the interesting features of reduced size NPs is that the optical transition is shifted to visible region (dielectric function become more negative) as compared to transitions at near infra-red region in case of bulk materials [53]. This distinctive behavior of smaller particles originates from the high surface atoms density relative to the interior atoms. The main consequence of this concerning surface plasmon is an increased damping and competition between the two excitations (intra/inter band transition) at visible frequencies along with surface dispersion and as a result, retardation effects of the EM field across the metal particle can cause huge shifts and broadening of plasmon resonances depending upon their size/shape, thus making them most important for plasmonic studies. One can consider that a metal is good for plasmonics or will give

sharp resonance only if  $\text{Re}(\epsilon)$  is negative in the wavelength range of interest (typically the visible and near infrared and also  $\text{Im}(\epsilon)$  should be very much small enough ( $\ll 1$ )).

### 1.2.4 Comparison between Au and Ag

For many optical phenomena, silver is *gold* and gold is *silver*. The optical conductivity  $\text{Im}[\epsilon(\omega)]/\lambda$  (which is measure of frequency dependent dielectric function and absorption coefficient) of Au and Ag are of crucial importance for many plasmonic aspects. The difference between the optical conductivity of silver and gold is highlighted in the figure 1.7 [17].

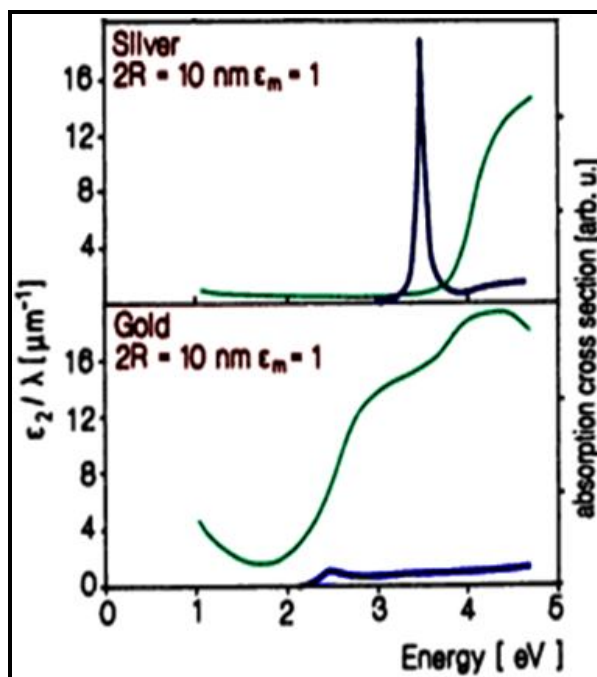


Figure-1.7:  $\text{Im}[\epsilon(\omega)]/\lambda$  (green line) of gold and silver and absorption cross section (blue line) as a function of photon energy clearly signifying the inter band transition effect on plasmon resonances due to which it become weak in case of gold.

The dipolar surface plasmon resonance is pronounced in case of silver since damping ( $\text{Im}[\epsilon(\omega)]$ , green line) is small in the visible part of spectrum whereas it is weak in case of gold due to large  $\text{Im}[\epsilon(\omega)]$ . The presence of more pronounced inter-band transitions in gold is the main reason for this behavior, which clearly differentiates gold and silver, as far as the optical response is concerned, by way of increasing the  $\text{Re}[\epsilon(\omega)]$  in the region, where the gold plasmon resonances should have occurred, thereby shifting them towards longer wavelength in comparison with silver. More importantly, it increases dramatically the optical absorption ( $\alpha$  or  $\text{Im}[\epsilon(\omega)]$ ), so as to make it much larger for Au than for Ag in the region, where  $\text{Re}[\epsilon(\omega)] < 0$ . This conveys completely different properties to both metals as far as plasmons are concerned. We re-emphasize the fact that the higher absorption for Au at  $\lambda < 600$  nm produces more *lossy* plasmon resonances that result in less enhancement in general. It is equally important to remark that this is no longer true at longer wavelengths, typically  $\lambda > 600$ -650 nm [53]. Gold should therefore exhibit comparable plasmonic properties as silver (in particular in terms of local field enhancements) in this longer wavelength range.

As in the case of silver, surface oxidation is prominent, thus making their stabilization at smaller dimensions highly critical. Hence, our major research interest lies in the colloidal synthesis of different anisotropic gold nanostructures and carefully analyzing their intrinsic plasmonic response. The different oxidation state as well as ligand exchange ability of gold complexes along with their structural geometry provides vital control over the nanoparticle morphology. Aqueous solutions containing gold complexes like  $[\text{AuCl}_4]^-$  or  $[\text{AuBr}_4]^-$  were easily reduced under controlled reaction conditions and stable colloidal gold can be easily obtained. In this regard, we would first like to discuss the chemistry and colloidal aspects of gold-complexes, which have profound implications in the formation of various size/shape controlled anisotropic gold nanostructures as we have shown in the later part of this book.

### 1.3 PHYSICAL/CHEMICAL PROPERTIES OF GOLD COMPLEXES

Some of physical properties of gold are given in appendix in table A1.1. The electronic configuration of gold(0) is  $5d^{10}6s^1$ . Ratio of relativistic radius of the valence electrons to their non-relativistic radius as a function of atomic number shows local minimum for gold [54]. This theoretical approach leads to the conclusion that gold actually occupies a unique position among the elements and result in several consequences in gold chemistry:

1. Color of gold. Gold absorbs light at around 2.4 eV (516 nm), attributed to the transition from filled 5d band to the Fermi level (essentially the 6s band). It therefore reflects red and yellow light and strongly absorbs blue and violet.
2. In gold, more than in silver, both states are now available for bonding. The closed shell  $5d^{10}$  in gold(I) is no longer chemically inert and can interact with other gold atoms. It also becomes possible to rationalize bonding between different gold(I) centers, confirming the great affinity between gold atoms. They try to be as close as possible to each other and Au–Au distances are normally even shorter than those found in metallic gold. This effect is known as aurophilic attraction or aurophilicity.
3. The destabilization of 5d orbitals allows the easy formation of the oxidation state III in gold to be explained; this is almost absent in silver; and the stabilization of the 6s orbitals explains the formation of the gold(I), oxidation state, which is unknown in silver.
4. The small difference in energy between the s, p and d states lead to the efficient formation of sd or sp hybridizations, which are important for explaining the pronounced tendency of gold(I) to form linear two-coordinate complexes.
5. Electrochemical potential of Au is the lowest of any other metal means that Au in any cationic form will accept  $e^-$  from virtually any reducing agent to form metallic Au.

#### 1.3.1 Chemical Stability of Gold Complexes

The gold metal and its natural complexes enjoy special characteristics that make them suitable for multi-purpose applications. Gold is found to be stable mainly in two oxidation states; the aurous ion ( $Au^+$ ) having a transitory existence, readily converts into the stable auric ion ( $Au^{3+}$ ) containing compounds/complexes, which are far more common in practice. No authentic examples of bivalent gold are known till now. The stability of gold complexes directly correlate with the ligand atom that is bound to the core central gold atom, the strength of which tends to decrease with increasing electro-negativity of the ligand donor atom [55, 56].

##### Gold (I) Complexes

$Au^+$  has a closed shell electronic configuration  $[Xe] 4f^{14}5d^{10}$ . Therefore, gold(I) complexes are diamagnetic and the stereochemistry is linear with a coordination number of two. The stability of the  $[AuX_2]^+$  ions (X=halide) increases with heavier halide ions.

##### Gold (II) Complexes

The oxidation state two is the dominant oxidation state for copper, but is very rare for a gold atom. In gold(II) complexes, the metal atom has a  $5d^9$  configuration and such complexes are expected to be paramagnetic. This oxidation state can be established as transient intermediates in redox reactions between the stable oxidation states I and III.

##### Gold (III) Complexes

The oxidation state III is very important for gold. All known gold(III) complexes are diamagnetic with a low-spin  $5d^8$  electron configuration, and the vast majority of these compounds have the four coordinate square-planar stereochemistry.

Gold is probably the most noble of the metals, being the only one which is not attacked in water by either oxygen or sulphur at any temperature. Even in the absence of coordinating ligands, gold cannot be easily oxidized by dissolved oxygen in the presence of either strong acids or strong alkalis [56]. However, gold can dissolve in aqueous solutions containing good ligands and an oxidizing agent, but neither condition alone is sufficient. Pourbaix diagram shown in figure 1.8 summarizes the effect of the addition of chloride

ion to the gold-water system and it can be seen clearly the complex  $[\text{AuCl}_4]^-$  is the most stable and used mostly all over world in chemical reactions.

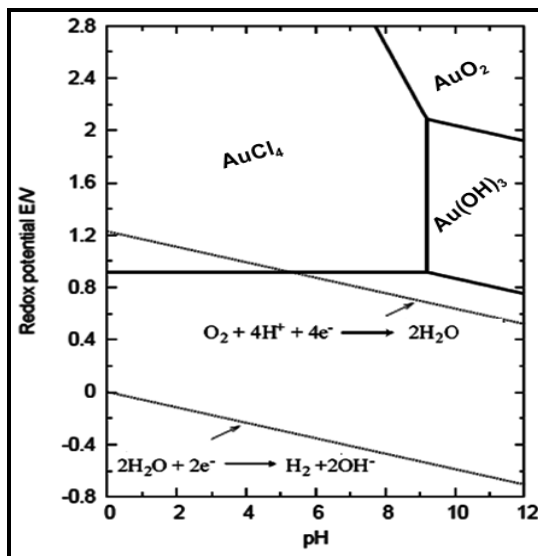


Figure-1.8: Simplified Pourbaix diagram for the gold water-Cl at 25<sup>0</sup>C showing the stability of AuCl<sub>4</sub> complex over a wide range of pH (reproduced from ref 56).

Thus, our research interests focus mainly on the extensive study of electronic/molecular spectra of the square planar gold(III) complexes and their kinetic dissociation characteristics under different chemical reaction conditions. Figure 1.9 shows a qualitative molecular orbital energy level diagram for the square-planar gold(III) complex, in which the ligand-field transitions usually occur as weak bands at low energy. Further, high extinction coefficients observed in the optical absorption spectra of HAuCl<sub>4</sub> in different solvents identify that these electron transfer bands were not actually the ligand-field transitions occurring within the metal d shell, but essentially the ligand-to-metal charge transfer transitions [55, 56].

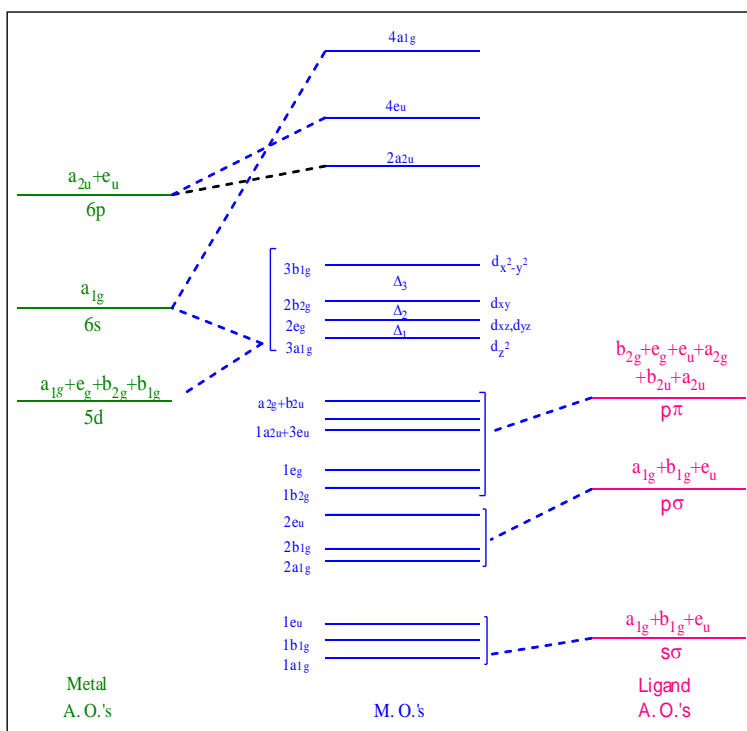


Figure-1.9: Qualitative Molecular orbital energy levels for a square-planar gold (III) complex.

From last decade, rigorous research activities related to the colloidal synthesis of various size/shaped metal nanostructures with controlled geometries such as spheres, faceted polyhedras, nanorice, nanokites and nanostars have been routinely carried out [57-60]. Such small nanoparticles become especially catalytic active at certain sizes along with their potential application in photonics, information storage, plasmonics, optoelectronics etc [61-71]. Due to such wide diversity of applications, nanoparticles have gained importance and various protocols for synthesis of nanoparticles have been reported.

#### 1.4 SYNTHESIS METHODOLOGIES FOR PLASMONIC RESONANT NANOPARTICLES

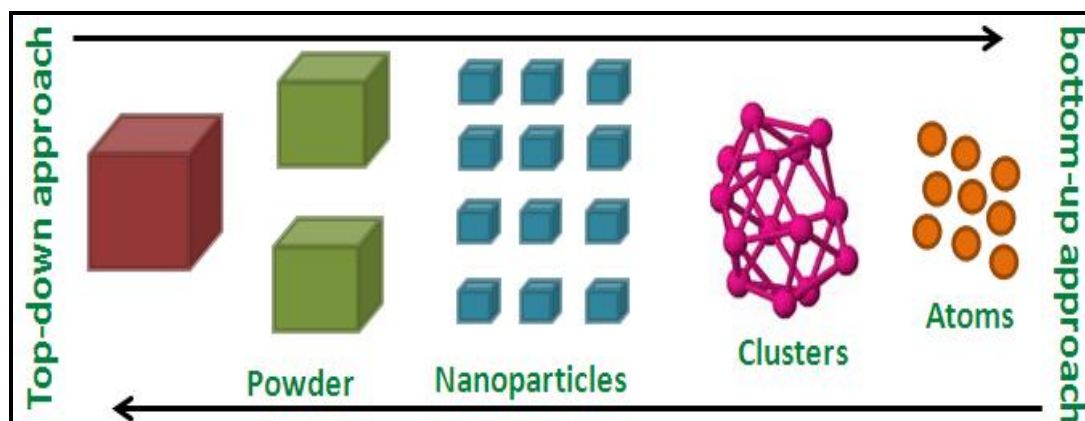


Figure-1.10: Top down and bottom up approaches for the synthesis of nanoparticles.

Two classifications that are generally used to distinguish the synthesis of NPs are i) top down approach which involves slicing or successive cutting of bulk material to obtain nanosize [10, 72] and ii) bottom up that involves building up the material atom by atom, molecule by molecule or cluster by cluster [72] which can be considered as physical and chemical methods respectively (figure 1.10). Nowadays, researchers also focus their attention towards the bio-inspired/biomimetic processes for the NPs synthesis.

In general, top-down approaches are highly physical in nature and thus have less control over the size distribution and also could be destructive. Among others, the biggest problem with top-down approach is the imperfection of the surface structure. It is well known that the conventional top-down techniques such as lithography causes significant crystallographic damage to the processed patterns and additional defects may be introduced even during the etching steps [72].

Bottom-up methods are chemically controllable and generally non-destructive. All the living things in nature observe growth by this approach only. An advantage of the bottom-up approach is the better possibilities to obtain nanostructures with less defects and more homogeneous chemical compositions by way of reducing the overall Gibbs free energy, so that the produced nanostructures are in a state closer to the thermodynamic equilibrium. Table 1.1 shows detailed classification of various methods for synthesizing metal nanoparticles.

Table-1.1: Shows detailed classification for synthesis of nanoparticles.

<i>Physical Methods</i>	<i>Chemical Methods</i>	<i>Biological methods</i>	
		<i>Biosynthesis</i>	<i>Bio- mimetic</i>
<b>Evaporation method Pulse/chemical vapour deposition [10, 60, 73]</b>	<b>Sol-gel method [10, 73]</b>	<b>Bacteria, Fungi [74-76]</b>	<b>DNA/RNA [74, 77]</b>
<b>Solvated Metal Atom Dispersion [78]</b>	<b>Chemical Precipitation [10, 72, 73]</b>	<b>Plants and Plant extracts [75, 79]</b>	<b>Viruses [80]</b>
<b>Laser ablation [68]</b>	<b>Hydrothermal synthesis [73]</b>	<b>Amino acids [81]</b>	<b>Proteins [74]</b>
<b>Sonochemical Methods [60, 79]</b>	<b>Micelles or micro-emulsion synthesis [10, 60]</b>	<b>Peptides [82]</b>	
<b>Photolytic and Radiolytic methods [60, 79]</b>	<b>Galvanic replacement Reaction [60]</b>		

### 1.4.1 Wet Chemical Synthesis

The bottom-up approach usually employs solution-phase colloid chemistry for the synthesis. The colloidal chemical synthesis of metal nanoparticles in aqueous/organic solution (often referred as wet chemistry in which reaction takes place on liquid phase) is most widely practiced method [57, 58, 63]. In a typical synthesis of metal nanoparticles using wet chemistry; metal salts precursor is reduced in solution in the presence of capping/surfactants, which prevents aggregation. Generally, these process of nanoparticles synthesis involve three steps; nucleation (seed particles formation), particle growth and stabilization in presence of capping agents. Due to the flexibility in selecting different reducing agents, particle capping agents, solvent systems as well as synthesis conditions, colloidal synthesis offers a great variety of options for composition, shape, size and surface chemistry control in easy and efficient way. The bottom-up approach is also suitable for controlling monodispersity of the nanoparticles as well for large scale synthesis. With all these advantages, the colloidal synthesis approach has become the main route to nanomaterials production and well utilized in present case in obtaining different nanostructures [57-59, 63, 83].

### 1.5 ROLE OF SURFACTANT IN SYNTHESIS OF METAL NANOPARTICLES

It is well known that the main ingredient in the chemical synthesis of nanoparticles is the ligands that are used as capping and/or shape directing agents. In many cases, the surface-modifying agents used, can act both as stabilizers and shape directing agents. And in some of cases, surfactants can also be employed as reducing agent (e.g. Poly(vinyl pyrrolidone) commonly known as PVP [84]). Use of ligands which can perform multiple tasks reduces the number of steps involved in the synthesis, thus making the task easy and manageable. Moreover, usage of molecules with multiple functional groups enables the preparation of functional nanoparticles that can be used for targeted drug delivery and multi-valent expositions that can be used for specific applications [85]. In the following section, we briefly summarize the different roles played by the ligands in the synthesis of nanomaterials.

#### 1.5.1 Stabilization of Nanoparticles

Stability is one of the important factors that determine the application potentials of the nanoparticles. Stability of nanoparticles especially as dispersion can be achieved by electrostatic or steric stabilization (using ligand/surfactants) as shown in figure 1.11.

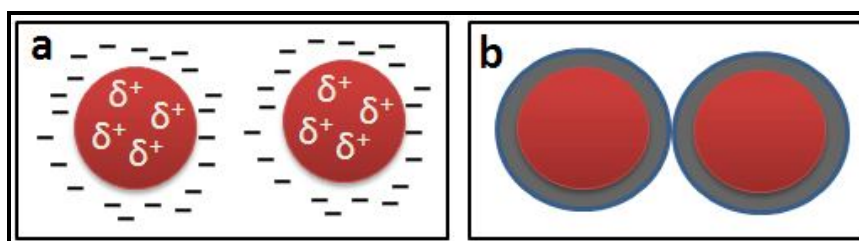


Figure-1.11: Illustrated stabilization of nanoparticles via (a) electrostatic (b) steric stabilization.

In electrostatic stabilization, the particles are surrounded by an electric double layer arising due to adsorption of reactant ions on the surface of NPs resulting into two forces acting on nanoparticles: 1) Van der Waals force of attraction between metal cores and 2) electrostatic force of repulsion (potential energy) due to charged ions on the surface. Stability of NPs is dependent on the combination of these two forces as explained by DLVO theory [10, 72]. Further the electrostatic stabilization of metal nanoparticles is rather weak and it is very sensitive to ionic strength of the dispersion medium.

**Table-1.2: Illustrating different ligand used in synthesis of different nanoparticles.**

<i>Thiols</i>	used to capped Gold (Au) [86-88], Silver (Ag) [88-90], Platinum (Pt) [91], Palladium (Pd) [92] and semiconductor nanoparticles [93].
<i>Amines</i>	Au [94-96], Ag [97], Pt [98] and Pd [99].
<i>Carboxylic acid</i>	Ag [100, 101] and magnetic nanoparticles (Co, Ni,Fe) [102, 103].
<i>Phosphines</i>	Au [104], and magnetic nanoparticles [105, 106].
<i>Silanes</i>	Metals [107, 108] and Metal oxide [109].
<i>PVP</i>	Au [110-112], Ag [111-113], Rh, Pt [114, 115] and Pd [116].
<i>CTAB</i>	Au, Ag and Pt [117-120].

Steric stabilization of nanoparticles can be achieved by co-ordination of organic molecules on the surface of nanoparticles, which act as capping ligands. In this way nanoparticle cores are separated from each other and agglomeration is prevented. In case of metal nanoparticles system, ligands that are commonly used as stabilizing agent include thiols, amines, silane, phosphines, Cetyl trimethylammonium bromide (CTAB), PVP, carboxylic acid (especially for transition metals) etc as shown in table 1.2. One of the major reasons why these ligands are preferred for capping is due to their binding ability with the surface of nanoparticles.

### 1.5.2 Influence of Ligand on Shape and Size of Nanoparticles

Major factor that plays an important role in governing the shape and size of nanoparticles is the ligands/surfactants that are responsible for the stable formation of different thermodynamically unfavorable anisotropic nanoparticles (figure 1.12).

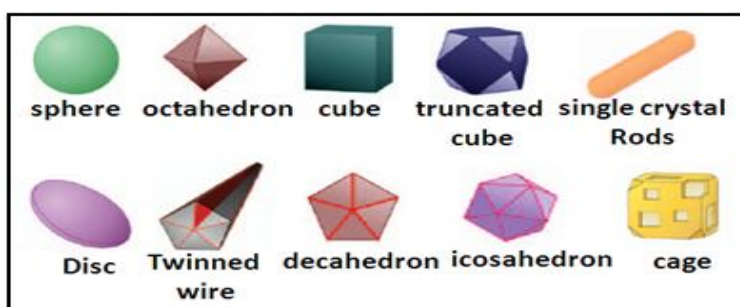


Figure-1.12: Illustration of different nanostructure shapes stabilized using the different ligands.

Concentration of surfactants like sodium dodecyl sulphate (SDS) and CTAB were varied and their effects on the size/shape of resulting nanoparticles were investigated in detail [121]. Change in concentration of these surfactants resulted in formation of different micelle structures or different interaction of ligands with metal precursor which are responsible for control of shape and size of nanoparticles. Detailed investigation of formation of different shapes on nanoparticles with different ligands has been carried out by various groups worldwide using methods like preformed-seed-mediated growth method [122-124], high-temperature reduction method [125, 126], spatially confined medium/template approach [127, 128], electrochemical synthesis [129, 130]; photochemical method [131] and biosynthesis [132] which result in different anisotropic nanoparticles. They have concluded that among the many factors that govern the shape of nanoparticles additives like surfactants and ligands play a major role [110-112, 116, 119, 133-138].

### 1.5.3 Role of Ligands in Assembly Formation

One of the key steps towards the application of nanoparticles in various fields is their assembly into desired nanoarchitectures [139]. There are various techniques like i) self-assembly of nanoparticles by colloidal synthesis [140, 141] ii) template directed self-assembly [142, 143] iii) assembly by lithography or patterning [144, 145], that could lead to the assemblies of nanoparticles. Application of these small clusters in devices requires them to be arranged in one, two or three dimensions (1D, 2D and 3D) where again, the ligands play an important role [146-148]. Nanoparticles stabilized by ligands (steric force) are more preferred to obtain reliable assemblies. The factors that govern the assembly formation include size, ligands used, chain length of the ligand, substrate used for formation of assemblies etc. Shiffrin and co-workers, used thiol based ligands for capping and obtaining the assembly of Au nanoparticles [149], thereby opening up endless assembling capabilities utilizing different ligands like dodecanthiol, dodecylamine, octadecylsilane, trioctyl phosphine, dodecyl bromide, dodecyl iodide, dodecanol and decane [150]. Extra careful efforts have already been taken to assemble anisotropic nanoparticles like rods. Thomas and his group have been successful in achieving chains of gold nanorods using different ligands [151]. Using  $\alpha$ ,  $\omega$ -alkane dithiols nanorods were organized in end to end fashion where the alkane dithiols acts as linkers. Mirkin's group used biological entities like DNA to achieve assembly of nanoparticles [152].

Thus, from above discussion, we observe that ligands/surfactants play a vital role in synthesis, shape control and assemblies of nanoparticles. We will focus our discussion on ligand - PVP; used for synthesis of various shaped metal nanostructures which in particular, has received special attention because of its unique properties (figure 1.13). The outstanding compatibility of PVP with a huge number of compounds like organic and inorganic salts, dyes, active compounds, plasticizers, bacteria, blood opens up a wide field of

opportunity and applications in different industries. Now we will discuss some physical and chemical properties of PVP and its use in synthesis of various nanoparticles.

### 1.6 POLY (VINYL PYRROLIDONE)

It was in late 1930 that Professor Walter Reppe of BASF first invented soluble PVP; the first polymerization product of *N*-vinylpyrrolidone, which was patented in 1939 [153] (figure 1.13, center). PVP is a typical homogeneous amphiphilic polymer containing a strong hydrophilic component (the amide group) and a significant hydrophobic moiety (six carbons per monomer unit). The mechanism for terminating the polymerization reaction makes it possible to produce soluble PVP of almost any molecular weight (available from many manufacturers). Some of important properties/applications of PVP are summarized in figure 1.13. One of salient features of povidone (PVP) is its universal solubility, which extends from extremely hydrophilic solvents, such as water, to hydrophobic liquids, such as butanol (see also appendix table A1.2). The viscosity of alcoholic solutions of povidone is significantly higher than that of aqueous solutions and is independent of their pH over a wide range [153].

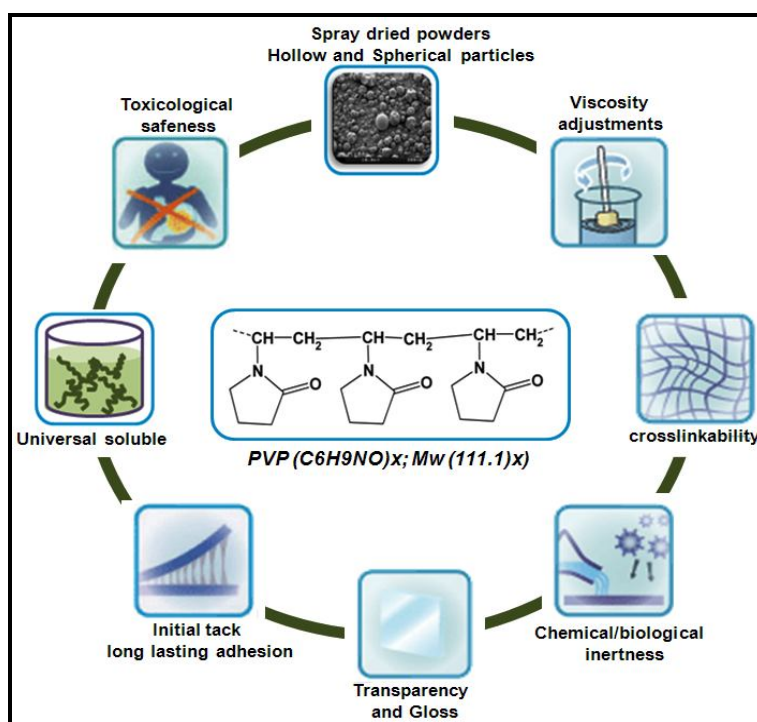


Figure-1.13: shows summarized major properties as well as applications of PVP among which universal solubility, remarkable capacity to interact with a wide variety of organic and inorganic compounds, good biocompatibility, non-toxicity to living tissues are the few.

#### 1.6.1 Spectroscopic Properties of PVP

PVP shows a group of ultraviolet maxima in water around 215  $\mu\text{m}$  which may be attributed to the presence of pyrrolidone rings, with weak shoulder at 240  $\mu\text{m}$  in some cases attributed to unreacted vinyl groups [155]. The spectrum is considerably independent of pH except at extreme values of pH. Below pH 1-2 and above pH 11-12, the spectra are shifted to shorter wave lengths [156]. PVP is positively charged in the acid region and negatively charged in the basic region, while at neutral pH the polymer is only very feebly charged negatively [155, 156]. Complex formation between PVP and molecular iodine was examined by following alterations in spectra of the iodine. Dyes bound to PVP show altered spectral and photochemical properties from that of the free dye [156, 157]. Hence Interaction of PVP with various substances can be revealed by the altered UV and visible spectra of the interacting system.

There are only few reports related to the thermal decomposition behavior of this polymer. Peniche et. al. pointed out that the formation of pyrrolidone is the main product of the thermal degradation of PVP [158]. Bianco et. al. suggested that the main volatile products of the thermal degradation of PVP are compounds with ester groups, ammonia ( $\text{NH}_3$ ) and hydrocarbons (unsaturated structures)[159]. Bogatyrev et. al.

suggested that thermal decomposition of the PVP is accompanied by breakdown of both main chain and side groups [160]. Avila- Ortega et. al. found that the vinyl pyrrolidone is the main volatile products of the thermal degradation of PVP using thermogravimetric–FTIR and NMR in details [161]. Most of the authors reported that the thermal degradation of PVP exhibits only one mass loss around 750 K.

### **1.6.2 PVP - Capping vs Mild Reducing Agent**

There is wealth of reports in the literature, where PVP has been extensively used in the solution-phase synthesis of many types of colloidal particles, mainly as a steric stabilizer or capping agent [110-112, 162-166]. PVP was widely used as protecting agent against agglomeration of metal colloids in well known polyol process [167-171], although some authors mentioned the potential of PVP to act as a reducing or nucleating agent [84, 172]. Degradation studies carried out on PVP aqueous solutions have shown that this polymer can be oxidized at mild conditions and that this reaction is accelerated by metal salts which can be reduced during the process [158-161]. Most recently in aqueous solutions synthesis (from last 7 years), it had been discovered that such a polymer could serve as a new class of reductant, whose mild reducing power is instrumental in the kinetically controlled synthesis of metal nanoparticles. Hoppe et al [84] and Jiliang Wu et. al. [173] proposed that the reduction of the metal salts to form nanoparticles is attributed to the presence of the polymer by considering two main possible reactions: (1) direct abstraction of hydrogen atoms from the polymer by the metal ion and (2) reduction of the metal precursor by organic macro-radicals formed by degradation of PVP.

Younan Xia et al. [172] found that in commercially available PVP, the end groups are terminated with the hydroxyl (–OH) group, that could serve as mild reductant. He had extensively studied the initiative role of PVP in obtaining various size/shaped metal nanoparticles [113, 169-171]. Although Kan et. al. [174] mentioned the reduction power of PVP, they could not identify the exact role of its end groups. Min Zhou et. al. [175] also proposed that in presence of PVP, the addition of NaOH could probably accelerate the polymer degradation and further active the sites for the reduction of Au ions. The mechanism of the formation of metal nanoparticles using the reducing power of PVP still remains a subject of controversy with the fact that slow reduction rate associated with the mild reducing power of PVP plays a critical role in forming nanoplate like structures during nucleation as well as their stable growth into highly anisotropic nanostructures.

## **1.7 OBJECTIVE OF THE BOOK**

Based on this extensive available information, in this present book, PVP has been extensively and exclusively utilized in the size/shape controlled synthesis of gold nanostructures is investigated by considering kinetics and growth mechanism with combined spectroscopic/microscopic techniques and their morphology correlated plasmonic signatures are studied which further utilized for specific applications such as the surface enhancement Raman scattering (SERS).

### **1.7.1 Book Overview**

The major contents of this book are divided into seven chapters. *Chapter 1* focuses on the fundamentals of plasmonics and optical properties of noble metals, which helps the reader to follow the objectives of this book. Also, a general introduction to the physical/chemical properties of gold/gold complexes has been extensively discussed. This chapter, in the context of literature, deals with various methods available for synthesis of nanoparticles. The prominent roles of surfactants used in the colloidal synthesis approach are also highlighted in detail, with particular reference to the physicochemical properties of the polymer PVP.

**Chapter 2** describes the general materials synthesis protocols utilized for synthesis of nanoparticles and briefly introduces the basic aspects of the utilized characterization tools and techniques.

The major theme of **Chapter 3** effectively utilizes the solvent interaction with PVP which has been reiterated as a crucial factor in differentiating not only the kinetic/thermodynamics of metal nanoparticle synthesis, but also vital in delineating the exclusive dependence of the individual reaction parameters in manipulating the as-grown nanoparticle aesthetics. This connotation is employed in achieving the stable formation of different size/shape controlled anisotropic Au nanostructures exemplified by the observed molecular ligand exchange growth mechanism through combined data analysis of spectroscopic/microscopic techniques in a rather significant manner, which has not been properly understood in its true sense till now and summarizing them as promising candidates for SERS. Wide range of Au nanostructure morphologies

obtained under the same PVP to metal ratio in different solvents depict clearly the complexity of not only the polymer-solvent, but also the polymer-solvent-metal ion interaction even under normal conditions.

In **Chapter 4**, we describe our facile/versatile single step seedless/templateless room temperature colloidal synthesis protocol for high degree of size/shape control of the 3D complex shaped gold nanostars with perfection, by employing hydrochloric acid (HCl) as an effective mediator. The abundant acetone quenched reaction mixture (containing DMF, PVP and H<sub>2</sub>AuCl<sub>4</sub>) at various time intervals sequentially identifies the growth of anisotropic branched nanostructures as a result of selective attachment and simultaneous ripening of dynamically nucleated gold seed particles rigorously mediated by the excess crystal habit modifier, PVP. The methodical molecular kinetic study clearly identifies the sequential ligand exchange as well as the desolvation process responsible for scheming such intriguing metal nanoarchitectures, which iteratively illustrates the combined kinetic effects of the solvent, polymer as well as the metal ion in designing the intricate morphology of the gold nanostars through systematic atomic/molecular spectroscopic measurements. Additionally, our recent work on the cathodoluminescence (CL) spectra and imaging of multi-branched gold nanostars demonstrate evidently the strong intra-particle plasmonic coupling between different non-planar oriented tips, causing asymmetric distribution of local density of states (LDOS) within the single Au nanostar, further illustrating beautifully the direct visualization of their intriguing plasmon hybridization mechanism, providing useful insights in understanding the local density of plasmonic eigenstates both in spatial as well as spectral domain with high clarity.

The tuning/reshaping of these gold nanostars (changes in the core size, the number, length and broadening of the branches) would be highly advantageous owing to the change in their overall nanostructure defined properties with reference to different specific applications, as the size of the core plays a critical role in focalization of electric field at the tips/edges. **Chapter 5** demonstrates our tweaked single step room temperature colloidal synthesis procedure by simple external addition of a standard base like NaOH to the precursor reaction mixture or utilizing 2-propanol as a co-solvent along with DMF, which has not been plausible with conventional nanocrystal growth methods or realized using existing patterning/lithographic techniques. Spectroscopic studies extensively reveal that the presence of NaOH have a large impact on the reaction kinetics of nanoparticle formation due to the reliable oxidation of chemically inserted OH species; whereas in the case of 2-propanol co-solvent, foreseeable conformational changes in the polymer PVP evolve as the major factor for controlled tuning of gold nanostars and can be directly utilized for exciting plasmonic applications.

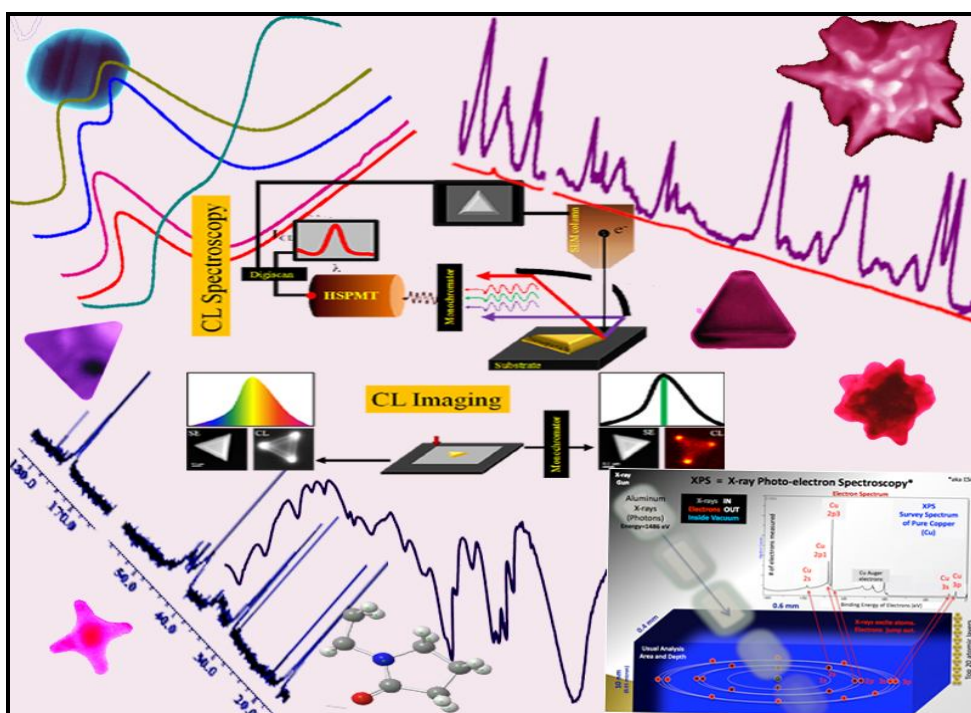
Encouraged by the idea that introduction of foreign agents in the precursor reaction medium substantially affecting the size/shape of gold nanostars, we have carefully analyzed the effective role of the individual inorganic halide (chloride, bromide and iodide) ions upon addition into the DMF–PVP system in **Chapter 6**, which systematically reveals the synthesis of sequentially reshaped gold nanostars with drastically changed optical properties owing to the blue/red shifting of the longitudinal surface plasmon resonance (LSPR) bands as well as the emerging of new plasmon bands, aesthetically illustrating the synchronized size/shape tuning enhanced with intriguing self-organization, as confirmed from TEM measurements. Such co-ordinated morphology tuning have been very well understood in terms of the distinct reaction kinetics imparted by the different adsorption affinity of inorganic halide ions towards metal ions/surfaces with the irresistible PVP-X-Au (X = halide) interaction at the early stages of the colloidal synthesis; the systematic results of which are being discussed rigorously in conjunction with the uncommon/unusual assemblies of anisotropic/elongated gold nanostructures, the first of its kind to the best of our knowledge.

**Chapter 7** investigates the shape effects of gold nanoparticles in terms of their respective surface roughness/sharpness for their SERS efficiency; so as to expedite them as promising SERS substrates with ease. The stronger SERS enhancement obtained for gold nanostars in DMF (the multi-branched nanostructures) were compared with other nanoparticle size/shapes and is ascribed to their aesthetics that possesses very efficient SERS-active sites (such as the sharp edges/tips).

The vast potential of gold nanoparticles including their nucleation and growth mechanism has been examined accordingly for its perspective scope and appropriate future plans.

## Chapter-2

### Materials and Methods



This Chapter embraces various analytical tools and their principles employed for the characterizations of the as prepared samples synthesized. Basic principles involve and data analysis in UV-Visible spectroscopy, Raman spectroscopy, Fourier transform infrared spectroscopy, Dynamic light scattering, Transmission electron microscopy, Cathodoluminescence-Scanning electron microscopy and X-ray photoelectron spectroscopy is explained in the present chapter.

This chapter deals with a brief description of materials, method and characterization techniques used for the synthesizing gold nanoparticles. The description and the principle of operation along with the way of data analysis of these techniques are discussed briefly in this chapter.

## 2.1 SYNTHESIS PROTOCOL

➤ Hydrochloroauric acid ( $\text{HAuCl}_4 \cdot 3\text{H}_2\text{O}$ ), CTAB, Silver Nitrate ( $\text{AgNO}_3$ ), PVP and salt NaCl, NaBr, KI were purchased from Aldrich and Merck respectively. Solvent/reagents like HCl, HBr,  $\text{Br}_2$  Methanol, Ethanol (EtOH), Chloroform ( $\text{CHCl}_3$ ), 1-Propanol, 2-Propanol and Dimethylformamide (DMF) from Merck were used in synthesis of metal nanoparticles. All experiments and the various sample preparation procedures were carried out at room temperature under continuous stirring. In all our present synthesis procedures, we used PVP average Mw 10000 and the molar ratio of PVP to metal gold ions is calculated in terms of polymer repeating unit or monomer chain length and kept as  $\sim 3250$  in our solution mixture unless otherwise mentioned. The color of the solution starts changing from pale yellow to colorless and then finally to brilliant colors, indicating the formation of gold nanostructures. For all the synthesis and characterization purpose milli pore water was used. All the glasswares were washed with aqua regia (1 part  $\text{HNO}_3$  + 3 part  $\text{H}_2\text{SO}_4$ ) and then by milli pore water prior to use.

## 2.2 SPECTROSCOPES

Spectroscopy or molecular spectroscopy deals with the interaction of electromagnetic radiation with matter (absorption or emission) and a spectrum thus represents the variation of interaction with the frequency of radiation.

### 2.2.1 UV-Vis/Optical Absorption Spectroscopy

Optical absorption spectroscopy is very useful technique to study metals, semiconductors and insulators in bulk, colloidal, thin films nanostructures etc. Semiconductors show absorption by involving electronic transitions as they have optical band gap while metal NPs exhibit absorption bands or broad regions of absorption in the ultraviolet-visible range due to the excitation of plasma resonances (detailed in chapter 1). The working principle of this technique is the Beer-Lambert law ( $A = \log(I_0/I) = \epsilon cl$ ) which relates the molecular absorption to its concentration [176, 177]. Generally, the SPR includes both of absorption and scattering components which are termed as extinction. In plasmonics UV-Vis spectroscopy has become a popular tool for far-field optical characterization of plasmonic materials. Absorption spectra of the colloids can vary because of polydispersity, partial aggregation, or departures from sphericity [178, 179]. In present study, the UV-Vis spectroscopy is used to investigate the SPR of Au NPs in solution, thus useful in the screening of the synthetic formula of controlling morphology.

In general, a spectrophotometer consists of a light source, sample holder, a diffraction grating or monochromator to separate the different wavelength of light, and a detector. The radiation source is often a tungsten filament, a deuterium arc lamp and more recently light emitting diodes and xenon arc lamps. Hydrogen gas discharge lamp below 350 nm; whereas above 350 nm tungsten filament lamp is a preferred source. The detector is typically a photodiode or a charged coupled device (CCD). A spectrophotometer can either be single beam or double beam. In either type, the instrument is calibrated with a reference cell containing only solvent necessary for an absorbance instrument. The dual beam design greatly simplifies this process by concurrently measuring intensity of the sample and reference cell respectively (figure 2.1a.)

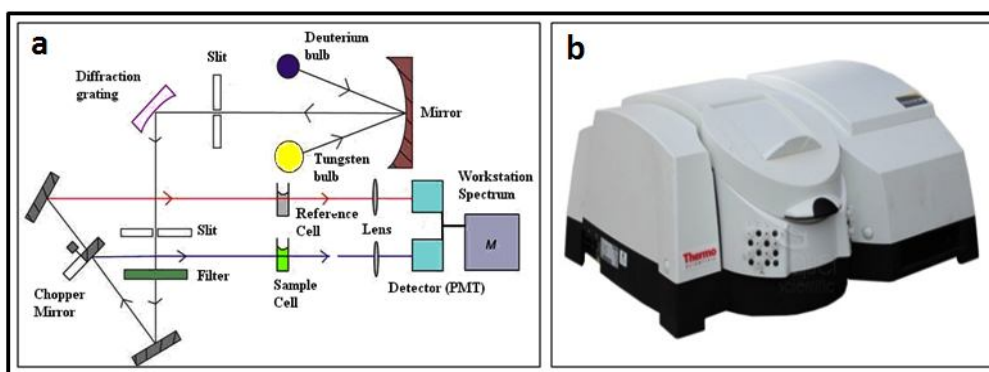


Figure-2.1: (a) Schematic diagram of dual beam UV-Vis spectrophotometer. (b) Thermo Scientific absorption spectrophotometer

### Experimental details

Optical absorption measurements were carried out in all our as-prepared nanoparticles solution samples in the wavelength range of 200–1100 nm using Thermo Scientific absorption spectrophotometer (figure 2.1b). The data were collected with scan rate of 240 nm per min with a data interval of 1 nm.

### Normalization of Absorption Data

Metallic gold exhibits an optical response that is relatively independent of size/shape in the wavelength range 350-450 nm, which lies within the region of inter-band transitions [180, 181]. Hence, the measured kinetic absorption spectra were plotted upon normalization at 400 nm and the spectra are manually stacked one above the other for better clarity, where the absorbance is mainly due to inter-band transitions, hence independent of size/shape, facilitating direct comparison.

### Calibration/Calculation of Amount of Metallic Gold (Au<sup>0</sup>) in Suspension to Optical Extinction at 400 nm

The absorbance at 400 nm depends predominantly on the number and volume of Au<sup>0</sup> nanoparticles present; therefore, this has been used in the past to provide an estimate of Au<sup>0</sup> concentration. The amount of metallic gold in suspension was found by regression to be approximately [181-184].

$$\text{Au}^0(\text{mM})=0.416 \times \text{abs}@400 \text{ nm.} \quad (2.1)$$

### 2.2.2 Dynamic Light Scattering (DLS)

Particle size can be determined by measuring the random changes in the intensity of light scattered from a suspension or solution. This technique is commonly known as DLS. DLS is most commonly used to analyze nanoparticles examples include determining nanoparticles size, protein size, latex size, and colloid size. It can also be used to probe the behavior of complex fluids such as concentrated polymer solutions. In general, the technique is best used for submicron particles and can be used to measure particle with sizes less than few nm.

When light hits small particles, the light scatters in all directions (Rayleigh scattering) as long as the particles are small compared to the wavelength (below 250 nm). If the light source is a laser, then one observes a time-dependent fluctuation in the scattering intensity due to the undergoing Brownian motion by small molecules in solutions, and so the distance between the scatterers in the solution is constantly changing with time. This scattered light then undergoes either constructive or destructive interference by the surrounding particles, and within this intensity fluctuation, information is contained about the time scale of movement of the scatterers. This random motion is modeled by the Stokes-Einstein equation.

Below the equation is given in the form most often used for particle size analysis.

$$D_h = \frac{k_B T}{3\pi\eta D_t} \quad (2.2)$$

where  $k$ ,  $T$ , and  $\eta$  are the Boltzmann-constant, temperature and the viscosity respectively. However, the particle size determined by DLS is the hydrodynamic size which means the determined particle size is the size of a sphere that diffuses the way through the medium. The calculations are handled by instrument software. Generally in DLS light from the laser light source illuminates the sample in the cell. The scattered light signal is collected with one of two detectors, either at a 90 degree (right angle) or 173 degree (back angle) scattering angle. The provision of both detectors allows more flexibility in choosing measurement conditions (figure 2.2a). The obtained optical signal shows random changes due to the randomly changing relative position of the particles.

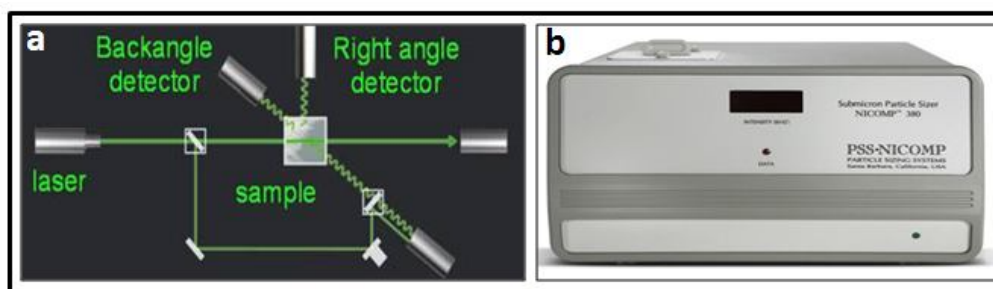


Figure-2.2: (a) Optical setup for dynamic light scattering (DLS) nanoparticle size analyzer. (b) Digital photograph of Nicomp 380 submicron particle sizer.

### Experimental Details

DLS was performed using a Nicomp 380 submicron particle sizer (PSS, Santa Barbara, CA) at a measurement angle of 90° (Internal He-Ne laser, wavelength 633 nm) (figure 2.2b).

#### 2.2.3 Fourier Transformed-Infra Red (FTIR) Spectroscopy

FTIR spectroscopy is one of the important tools employed for the identification of various functional groups and analyzing the chemical bonding information [185-188]. In FTIR spectra are collected based on measurements of the temporal coherence of a radiative source, using time domain measurements of the electromagnetic radiation or other type radiation.

Chemical bonds have specific frequencies at which they vibrate corresponding to energy levels. Atoms in a molecule do not remain in a fixed relative position and vibrate about some mean position and when there is a periodic alternation in the dipole moment during vibration (molecule vibrates with increased amplitude by the absorption of energy from the incident radiation) then such mode vibration is infrared (IR) active. When the molecule reverts from the excited state to the ground state, the absorbed energy is released and distinct peaks are observed in the spectrum. The IR region of the electromagnetic spectrum is 100 μm – 1 μm wavelengths.

In FTIR spectra each functional group has specific range of vibrational frequencies and is very sensitive to the chemical environment and thus provides valuable information regarding the presence of certain functional groups in the specific sample for their further characterization [185]. The frequency of vibration is given below:

$$v = \frac{1}{2\pi} \sqrt{\frac{k}{\mu}} \quad (2.3)$$

where, k is force constant, μ is reduced mass.

A typical FTIR instrument is based on the principle of Michelson Interferometer which works as follows (figure 2.3a): It consists of three active components: a moving mirror, a fixed mirror, and a beam splitter. The two mirrors are perpendicular to each other. The beam splitter is a semi reflecting device and is often made by depositing a thin film of germanium onto a flat potassium bromide (KBr) substrate. Radiation from the broadband IR source is collimated and directed into the interferometer, and impinges on the beam splitter. At the beam splitter, one beam transmitted/alternately reflected through the sample while other beam is employed as reference beam. This transmitted/reflected beam recombines with the reference beam after a path difference has been introduced. The interference pattern so produced is Fourier transformed to produce the spectrum of material as a function of wavelength or wave number of incident radiation (figure 2.3a).

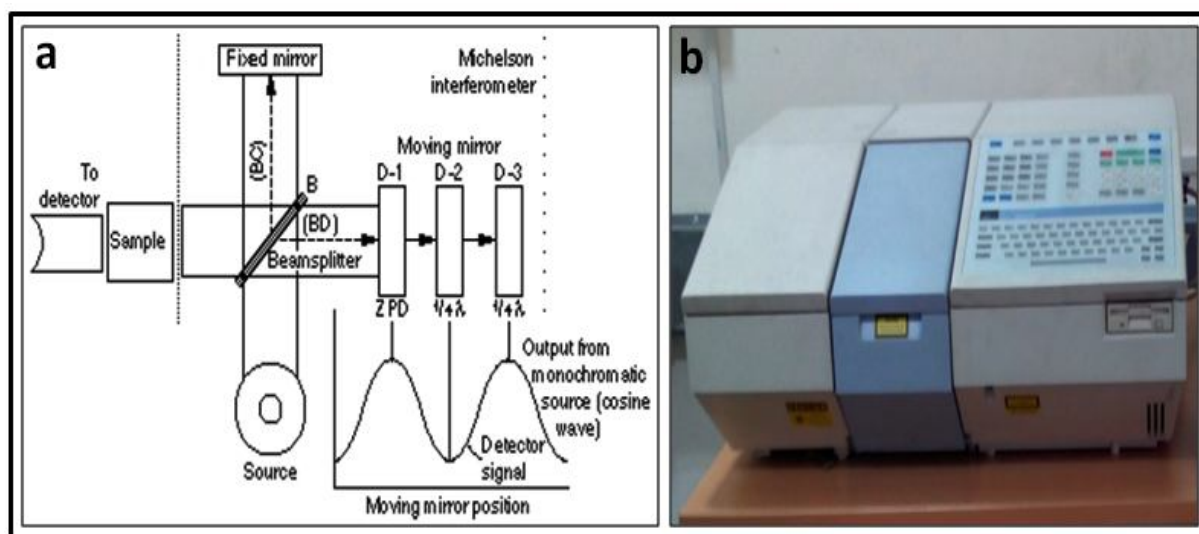


Figure-2.3: (a) Schematic representation of FTIR Instrument with Michelson Interferometer. (b) FTIR-spectrum RX I, Perkin-Elmer, Fourier Transformation Infrared Spectrometer.

### Experimental details

FTIR spectra were recorded at FTIR-spectrum RX I by Perkin-Elmer spectrometer (figure 2.3b). It has better than  $0.8\text{ cm}^{-1}$  spectral resolution to isolate sharp absorbance bands along with frequency range of  $4400\text{--}400\text{ cm}^{-1}$  using a Ge-coated KBr beam splitter. Measurements were made at  $4\text{ cm}^{-1}$  resolution.

In ATR mode aliquots of solution samples were dropped on a zinc selenide (ZnSe) plate and their IR spectra were carried out over the wavenumber range of  $650\text{--}4000\text{ cm}^{-1}$  (chapter 3). While to measure FTIR using KBr mode (chapters 4/5), aliquots of solution samples were drop coated on the well-dried KBr pellets, and immediately their IR spectra were carried out (to avoid the influence of moisture) over the wavenumber range of  $400\text{--}4000\text{ cm}^{-1}$ .

### Baseline Correction

IR spectrum of solute in different solvent has been widely obtained. Solvents usually have absorptions in the IR region, and their bands may overlap with the areas of the solute molecules and therefore, its influence has to be compensated for in a suitable way. One solution to this problem is a suitable choice of the solvent; for example carbon tetrachloride and carbon disulfide which often used as a solvent pair, having their bands in the fingerprint region of the spectrum [188]. Another widely used data manipulation technique in contemporary IR spectrometry is spectral subtraction [188, 189] where one subtracts the spectrum of the solvent suitably scaled to obtain the best compensation of the solvent bands from the spectrum of solution. Upward/downward peaks appear if solvent molecules are more or less than the background spectrum respectively. Therefore solvent peaks were multiplied by appropriate factor before subtracting it from all of our FTIR spectra by way of baseline correction with free solvents which greatly simplifies our problem in analysis of FTIR spectra.

### 2.2.4 Raman Spectroscopy

Raman spectroscopy is a spectroscopic technique used to study vibrational, rotational, and other low-frequency modes in a system [186, 190-192]. Raman scattering is the inelastic scattering of a photon, first time discovered by Sir C.V. Raman in liquids and later by Grigory Landsberg and Leonid Mandelstam in crystals. It is a non-destructive technique and most elegant analytical tool which gives the structural information required for both basic and applied research like SERS (detailed in next section) etc. In scattering, the molecule is excited to an unstable energy level which is called virtual state.

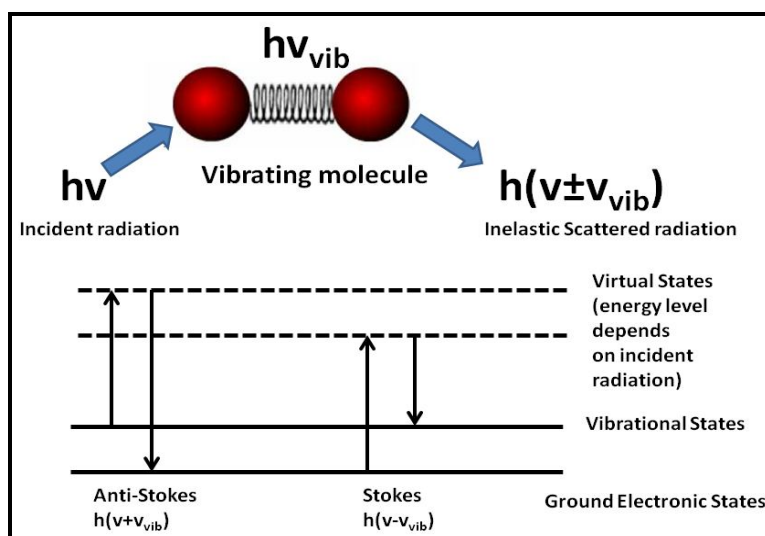


Figure-2.4: Demonstration for Raman scattering between different vibrational levels.

In Raman scattering, an incident optical photon of energy  $h\nu$  interacts with the lattice and excites the molecule from the ground state to a virtual energy state. When photons interact with a molecule, some of their energy can be converted into various modes of vibrations of the molecules. In Stokes effect, the incident light loses energy to cause molecular vibration and the scattered light has lower frequency than the incident light. On the contrary, anti-Stokes effect involves transfer of energy from the molecules, already in excited vibrational state, to the incident light and therefore the scattered light possesses higher frequency than the incident light (see figure 2.4).

However, with usage and tuning the frequency of the laser light with respect to the electronic transition characteristics of the molecule under investigation can greatly increase the Raman scattering. The effect is called resonance Raman scattering and is due to a coupling of electronic and vibrational transitions [191].

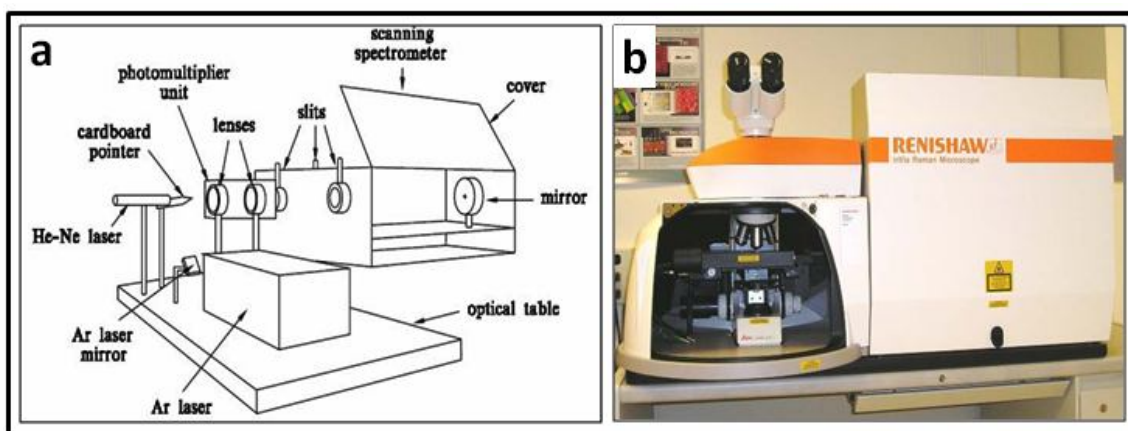


Figure-2.5: (a) Schematic diagram of Raman spectrometer. (b) Digital photograph of the Renishaw in via Raman spectrophotometer.

The laser beam from the Argon-ion laser is filtered for monochromaticity and directed by a system of mirrors to a focusing/collecting lens (figure 2.5a). The beam is focused onto the sample; the scattered light which passes back through the same lens is then passed through a second lens into the first stage of the spectrometer. The spectrometer itself is a commercial "triple-grating" system and physically, it is separated into two stages.

The first stage is called a monochromator, but is really used as a filter. Its structure is basically two diffraction gratings, separated by a slit, with input and output focusing mirrors, the incoming signal from the collecting lenses is focused on the first grating, which separates the different wavelengths. This spread-out light is then passed through a slit. Because light of different wavelengths is now travelling in different directions, the slit width can be tuned to reject wavelengths outside of a user-defined range. The light which makes it through the slit is then refocused on the second grating, whose purpose is only to compensate for any wavelength dependence in the dispersion of the first grating. This grating is oriented such that its dispersion pattern is the mirror image of that from the first grating. Finally the light is refocused and sent out to the second stage. The second stage focuses the filtered light on the final grating. The dispersed light is now analyzed as a function of position, which corresponds to wavelength. The signal as a function of position is read by the system detector. In the present case the detector is a multichannel charge coupled device array in which the different positions (wavelengths) are read simultaneously. The wavelength/intensity information is then read to a computer and converted in software to frequency/intensity. This is the Raman spectrum which appears as the raw data.

#### 2.2.4.1 Surface Enhance Raman Scattering (SERS)

Researchers recognized the enormous potential inherent in Raman scattering, but their efforts in applying Raman spectroscopy were hampered by the extremely small scattering cross sections ( $\sim 10^{-30}$  cm<sup>2</sup> per molecule). Researchers have implemented several methods to increase the Raman scattering efficiency, including using stimulated Raman processes and electronic resonance enhancement; however, the most significant amplification of the Raman signal comes from SERS as they are capable of significantly enhancing these small cross sections.

SERS is a surface-sensitive technique that enhances Raman scattering by molecules adsorbed on rough metal surfaces or in the vicinity of metal nanostructures [53, 193-198]. SERS gives the possibility to acquire information specifically from the surface of materials with advantage that the spatial resolution is determined not by the diffraction limit. In 1974, Fleischmann et al. [199] obtained first SERS spectrum from pyridine adsorbed to a roughened silver electrode but they incorrectly attributed the increase in Raman intensities to the increase in the electrode surface area. In 1977 Jeanmaire with Van Duyne [200] and Albrecht with Creighton [201] independently proposed that the Raman scattering cross section of the adsorbed molecule is enhanced by either a chemical or electromagnetic mechanism. These papers sparked a debate that continues to the present day over the fundamental mechanisms of SERS.

Enhancement of the Raman signal can take place by either increasing the electric field (E) experienced by the molecule (electromagnetic (EM) enhancement) or by changing the molecular polarizability of the adsorbate (chemical enhancement) [194]. The most significant mechanism involved in chemical enhancement is believed to involve a charge transfer between the metal and the adsorbate molecule. The main concept is that chemical adsorption to the metal surface induces intermediate electronic states that are available for quasi-resonance Raman enhancement.

Another EM enhancement mechanism is explained by a phenomenon known as SPR in which the conduction electrons of a metal are polarized by an external light field that produces intense electromagnetic fields near the metal surface. The magnitude of such fields depends on surface morphology (size and shape of particles), the dielectric properties of the metal, and the wavelength of the incident light [53, 193, 194, 202, 203].

Furthermore if any target molecule gets trapped at the interstices between two nanostructures, often termed “hot-spots or sandwich structures” the scattering cross-section of the trapped molecule can increase up further to a large extent [53, 193, 194]. Hence, a variety of electrochemically roughened metal substrates, nanolithographically fabricated metal substrates, differently shape NPs and their aggregates have been utilized to efficiently trap the molecule of interest between nanostructured metals in order to obtain the maximum EM enhancement [53, 193, 194, 204, 205]. However EM enhancement is thought to be the dominant mechanism over chemical enhancement.

### Experimental details

The Raman and surface enhanced Raman scattering (SERS) spectra were obtained using a Renishaw inVia Raman Spectrometer (figure 2.5b) equipped with a charged coupled device system with 785 nm He-Ne laser source, objective 50X, spot size of 1 $\mu$ m, expose time 10 second with laser power 30 mV.

### SERS Substrate Preparation

We present a simple method for the formation of stable reproducible plasmonic substrates, by making a monolayer of fivefold centrifuged PVP coated gold nanostructures dispersed in chloroform further spreading them to the air-water interface at considerably reduced pressures and was lifted onto silicon/ITO substrate followed by the drop-cast deposition of the 10<sup>-6</sup> M of the dye molecule, crystal violet/methylene blue.

### 2.2.5 Nuclear Magnetic Resonance Spectroscopy (NMR)

NMR was for the first time observed in 1946 by two independent groups [Bloch et. al., 1946 [206]; Purcell et al., 1946 [207]], and for this work they shared the Nobel Prize of physics in 1952. In 1950 it was discovered that the resonance frequency of a nucleus is influenced by its chemical environment (chemical shift) and that a nucleus could further influence the resonance of another through the phenomenon of chemical bonds. Later it was discovered that the chemical shift and spin-spin couplings could be directly related to chemical structure [185].

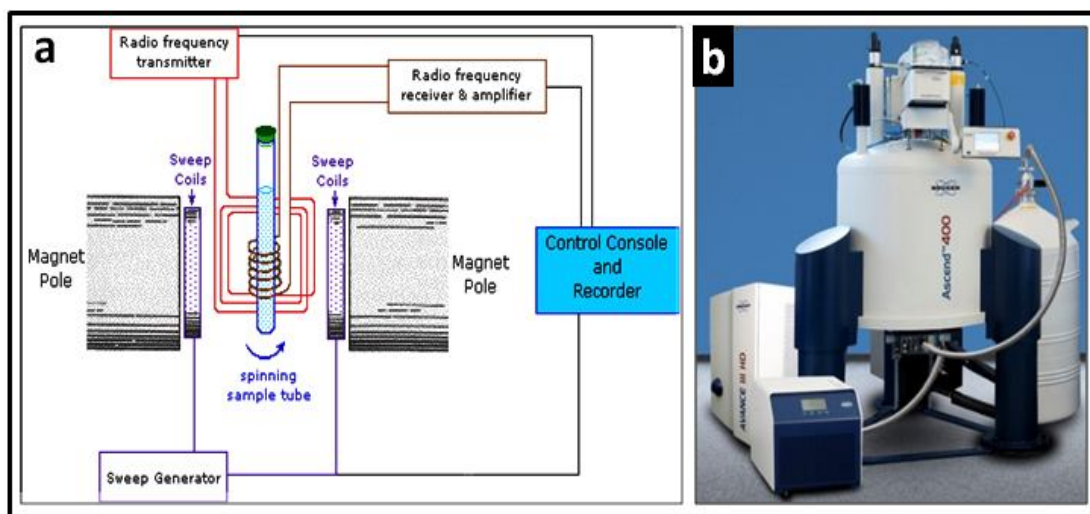


Figure-2.6: (a) The basic schematic showing various elements of the NMR. (b) Digital photograph of Bruker Avance-400 spectrometer.

The basis of NMR is that nuclei exhibit magnetic properties such as nuclear spin ( $I$ ) and magnetic moment ( $\mu$ ). NMR spectroscopy functions by the application of strong magnetic fields and radio frequency (RF) pulses to the nuclei of atoms. Magnetic resonance arises from a nucleus with  $I \neq 0$  placed in a magnetic field ( $B_0$ ) if RF is applied to the nucleus which induces transitions between different energy states. The excited nucleus undergoes relaxation by emission of radiation and this time dependent decay is acquired and Fourier transformed into a frequency-domain in order to give an NMR spectrum for the nucleus concerned. The schematic diagram of an NMR spectrometer is shown in figure 2.6a. The precise resonant frequency of the energy transition is dependent on the effective magnetic field at the nucleus, and this field is affected of shielding by electrons orbiting the nucleus. Consequently, nuclei in different chemical environments absorb energy at slightly different RF and this effect is referred to as the chemical shift. This also means that sample conditions, such as pH and ion strength, will affect the observed spectrum. Several parameters can be read from the spectra which provide information about the structure of the molecule. The sensitivity of NMR varies considerably depending on the nucleus observed, its abundance and its chemical environment. NMR spectrum can be broadened owing to the paramagnetic components in the sample which do not affect the resolution of IR or Raman spectra. Generally 1-D proton and carbon NMR experiments are more common in practice.

### Experimental details

The  $^{13}\text{C}$  NMR spectra were recorded on Bruker Avance-400 spectrometer operating with magnetic field 9.4 Tesla and RF frequency 100 MHz using TMS as internal standard and  $\text{CdCl}_3$  as a NMR solvent (figure 2.6b) and chemical shift is in ppm.

### 2.2.6 X-Ray Photoelectron Spectroscopy (XPS)

XPS is a non-destructive technique that uses X-rays in an ultra high vacuum environment which gives both quantitative and qualitative information about the elemental composition, empirical formula, chemical state and electronic state of the elements that exist within a material [208]. XPS, uses either monochromatic Aluminum  $K\alpha$  (1486.6 eV) or non-monochromatic Magnesium  $K\alpha$  (1253.6 eV) X-rays at the sample's surface to eject a photoelectron from the inner electronic shell of atom (Compton scattering). An electrons from a higher energy level then falls to fill the hole left behind and its emitted radiation energy is used to eject an Auger electron (figure 2.7).

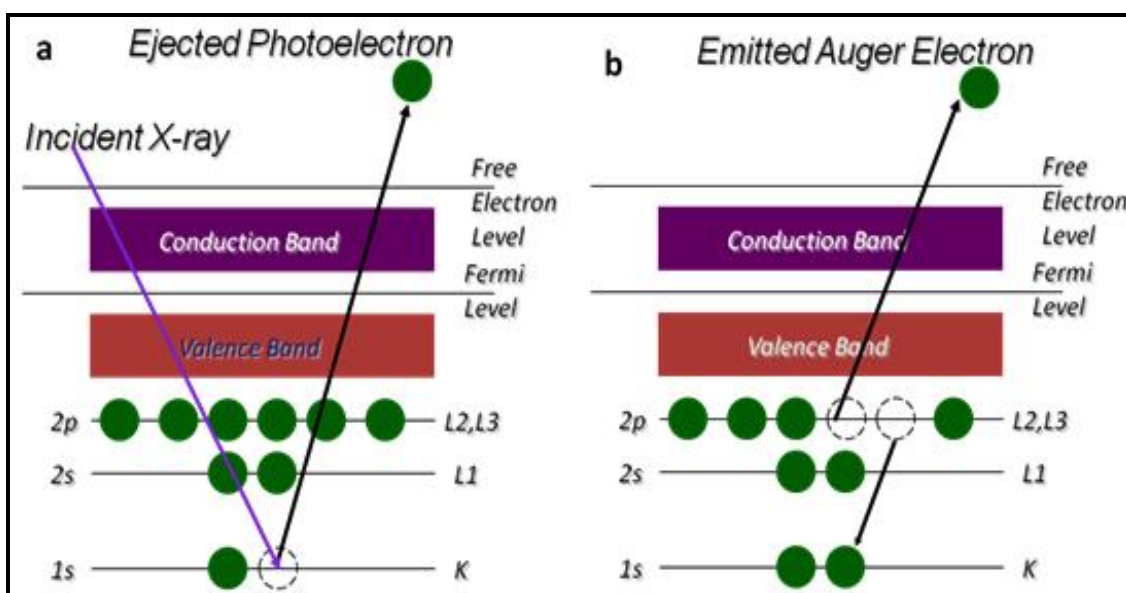


Figure-2.7: Schematic illustration for the emission of an electron from inner shell of an atom.

Thus, XPS emits both photoelectrons and Auger electrons which can be seen in the spectrum. Those photoelectrons are collected by a detector and their energies are measured. This process is expressed with the following Einstein's relation;

$$E_B = h\nu - E_K - \Phi \quad (2.4)$$

$E_B$  is binding energy of the ejected  $e^-$ ,  $h\nu$  is the energy of the incident photon,  $E_K$  is the measured kinetic energy of the ejected electron and  $\Phi$  is the work function which relates to the minimum energy required to eject an electrons from the solid matrix to the vacuum level. A schematic representation of a XPS measurement is shown in figure (2.8a).

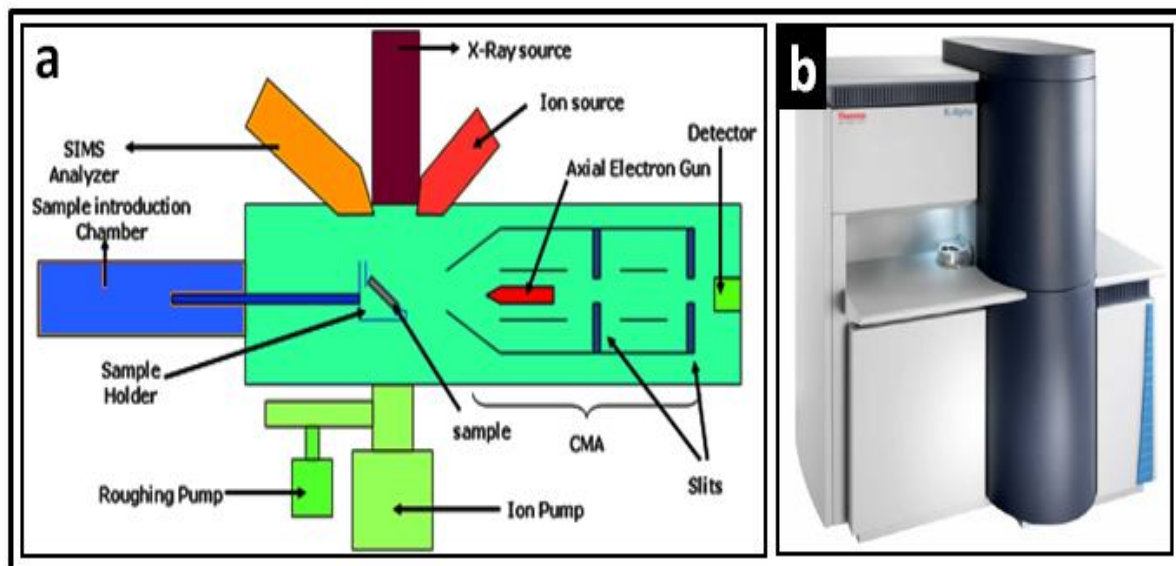


Figure-2.8: (a) Schematic showing components and working of XPS. (b) Thermo  $K\alpha$  XPS instrument

Subtracting the measured kinetic energies of the photoelectrons from the energy of X-rays gives us the binding energies of the electrons. Since binding energies are specific to each atom for its specific energy level, and elements besides hydrogen can be detected and their relative amounts can be easily determined with this technique. Chemical specificity is a big advantage of XPS. Besides determination of the types of atoms on the surface, XPS can even give information about the oxidation states of those atoms. The chemical state of the atoms strongly influences the binding energy of the ejected electrons. The binding energy would be large for tightly bound electrons; hence, for positively charged species a larger binding energy than the neutral state is measured.

### Experimental details

XPS measurements were carried out using Thermo  $K\alpha$  XPS instrument (figure 2.8b) at a pressure better than  $10^{-9}$  Torr and different element (C 1s, O 1s, N 1s, and Au 4f) core-level spectra were recorded using Mg  $K\alpha$  radiation (photon energy = 1253.6 eV) at a pass energy of 50 eV, an electrons take off angle of  $90^\circ$  with resolution of 0.1 eV. Samples for XPS were prepared by drop casting the 5-fold centrifuged samples on silicon substrates, the core-level spectra were background corrected using Shirley algorithm, and chemically distinct species were resolved using a nonlinear least-squares fitting procedure. The C 1s core-level spectra at 285 eV were taken as reference for the charge correction in other core-level spectra.

## 2.3 MICROSCOPIES

### 2.3.1 Transmission Electron Microscopy (TEM)

This technique in the morphological and structural aspect of materials science is of great importance. It also helps in understanding the micro-structural examination through high-resolution imaging. It also provides the information on structural transformation, its preferred orientations and contaminants or defect through diffraction pattern [209, 210]. Optical and electron microscopes are very similar in producing the image of a specimen, but, the resolving power of the electron microscope is very large as compared to optical microscope due to the use of electron beam of about  $10^6$  times shorter wavelength in electron microscope than that of light photon in optical microscope [37]. TEM measurements use the thermionically excited tungsten or LaB6 filament as a source of electron beam, which is accelerated towards anode and focused with the help of condenser lens. The imaging system in the TEM consists of an objective lens, projector lens, electromagnetic lenses, and fluorescence screen (figure 2.9a).

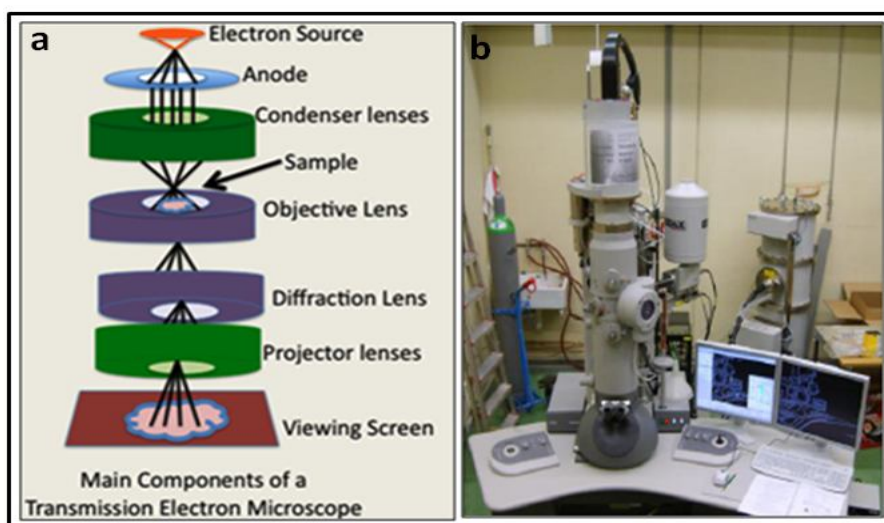


Figure-2.9: (a) Schematic diagram of Transmission Electron Microscope. (b) Transmission Electron Microscope, Tecnai (300 kV), FEI.

The electromagnetic lenses of TEM instruments consist of ferromagnets and copper coils, whose focal length can be changed by changing the current passing through the coil. The schematic diagram for TEM is given in figure 2.9a. The electron gun used as a source of electron, producing a stream of monochromatic electrons. This monochromatic beam of electrons is focused to a small coherent beam by condenser lenses. The first condenser lens determines the size of the beam spot, whereas, the second one is responsible for the convergence of the beam on the sample so that a specified area of the sample gets illuminated. Further, the beam is obstructed by the condenser aperture blocking the diverge electrons from the optic axis. The coherent beam falls on the specimen and parts of its intensity is transmitted. The transmitted beam is focused by the objective lens and forming the first image. The formed image is passed through the intermediate part, known as column and magnified all the way by using the projector lens. The magnified image is projected on the phosphor screen and a black and white image is appeared on the screen for user. Depending on the intensity of electron beam, darker the area on the screen lesser the electron transmitted or visa versa.

### 2.3.1.1 Imaging Modes

The imaging modes used for the operation for TEM are (1) Bright field (BF), (2) Dark field (DF) and (3) High-resolution (HR) as shown in figure 2.10

Bright field TEM image shows the intensity distribution in the transmitted beam whereas dark field TEM image shows the intensity distribution of the diffracted beam. In order to reduce the spherical aberration, deflection coil is used to tilt the incident beam and bring the diffracted beam parallel to optic axis in the dark field mode. HRTEM imaging mode can provide atomic resolution of microstructures by using a larger aperture in the bright field mode to include both transmitted and diffracted beam. HRTEM image is formed by the interference between the transmitted beam and diffracted beam.

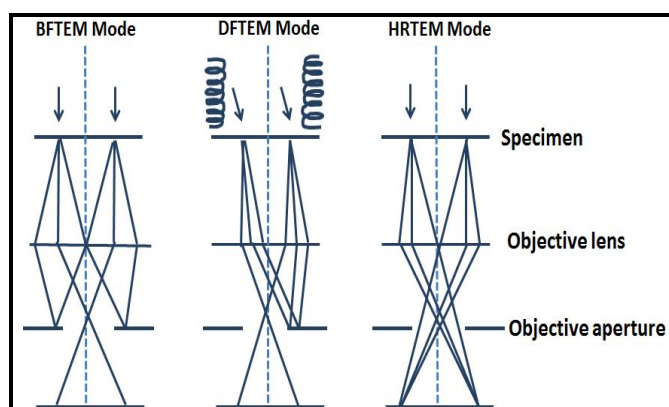


Figure-2.10: Schematic ray diagram of electron beam for BF, DF and HRTEM.

### Experimental details

TEM images along with the selected area electron diffraction (SAED) patterns of gold nanostructures had been obtained on Tecnai (300 kV), FEI, Holland (figure 2.9b). It has a tungsten electron gun, operated at 300 kV. The as prepared nanoparticles were five-fold centrifuged in water/ethanol medium and dropped on carbon 100 mesh copper grids.

*In order to avoid aggregation, dilution must be appropriate. Parafilm (hydrophobic) beneath the grid give better drop casting of water dispersed nanoparticles. SAED pattern was taken on well dispersed nanoparticles images so as to acquire better information.*

### 2.3.2 Scanning Electron Microscopy (SEM)

SEM can provide information for the surface morphology, topography and chemical states of the samples. This technique is capable in producing three dimension images with high resolution and high depth of field images of conducting and non-conducting materials and provides extra advantage regarding the surface structure. The working principal of SEM is based on the reflection of secondary electron from the surface the samples (analogy to the reflecting light microscope). Backscattered electrons which are coming out from the specimen due to interaction of incident electron beam (figure 2.11a) are used to map the surface topology or detect the contrast between areas of different chemical compositions [211]. The contrast of the backscattered electrons image tends to increase with the higher atomic numbers.

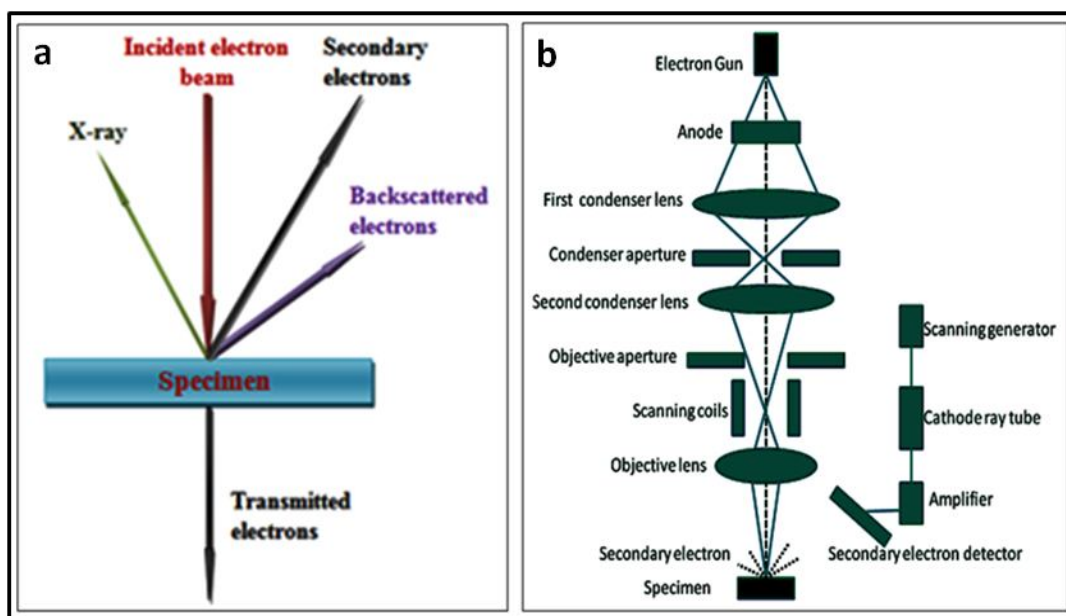


Figure-2.11: (a) Schematic representations of various electron beams coming out from the specimen due to interaction of incident electron beam. (b) Schematic presentation of working principle of SEM.

The schematic diagram of an SEM is shown in figure 2.11b. In SEM, electrons are thermionically emitted from cathode made up of tungsten, lanthanum hexaboride (LaB6) or by using field emission gun (FEG). The emitted electrons are accelerated by a voltage of 0.5 – 30 kV towards an anode which forms a fine beam of diameter 10– 50  $\mu\text{m}$  near the anode. The electron beam is focused by one or two condenser lenses into a beam with a very fine focal spot size. Today, most SEMs are able to produce an electron beam of spot size  $\sim$  5 – 10 nm. The beam passes through pairs of scanning coils in the objective lens, which deflect the beam in a raster fashion over a rectangular area of the sample surface. The raster scanning of the sample is achieved by changing the current in the coil. The objective lens has a variable, relatively long focal length which allows a large working distance of about 5 – 30 mm between the specimen and the lower pole piece. At each scanning point, secondary and back-scattered electrons are generated and these electrons are detected by the detector. The counted electron in the detector is used for determining the relative intensity of the pixel point in the final processed image.

The intensity of the image also depends on the atomic number of the specimen, higher atomic number specimen has larger backscattered electrons and hence, brighter image. SEM measurement also provides

analytic information of the samples due to generation of X-rays as a result of the interaction of electron beam and sample material with the transition of electron from higher energy level to lower energy levels. Thus, SEM measurements are useful not only for image processing but also for qualitative and quantitative elemental analysis.

Cathodoluminescence (CL) imaging spectroscopy is a powerful tool to investigate the optical properties of materials, with a resolution below the diffraction limit of light [212]. Present used scanning electron microscopes (SEMs), with beam diameters of several nanometers give the opportunity to excite surface plasmons at a well defined position with dimensions far below the diffraction limit of light, in combination with a CL setup to image the surface plasmons.

Figure 2.12 schematically shows the excitation and collection of light. A CL system is an extension to either a TEM or SEM. An aluminium parabolic mirror is placed between the sample stage and the pole pieces. Through a hole in the mirror, the sample is irradiated with electrons and the luminescence is collected. For the most efficient collection, the sample must be in the focal point of the mirror, which is 1 mm below the mirror itself. Because of the parabolic shape, the mirror reflects the light as a parallel beam into a waveguide. The detection of the light by the MonoCL system can occur in two modes. In the panchromatic mode all the emitted light is collected by the detector, while in the monochromatic mode the light is led through a monochromator, which allows one to take a spectrum, or make an image at one particular wavelength. Two mirrors are used for switching between these modes.

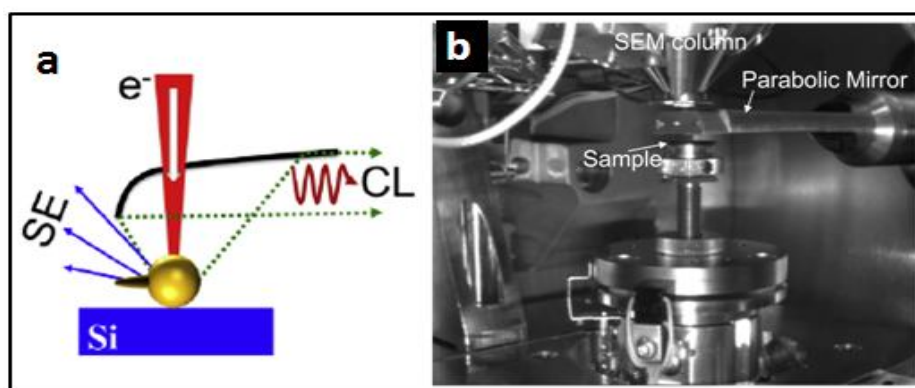


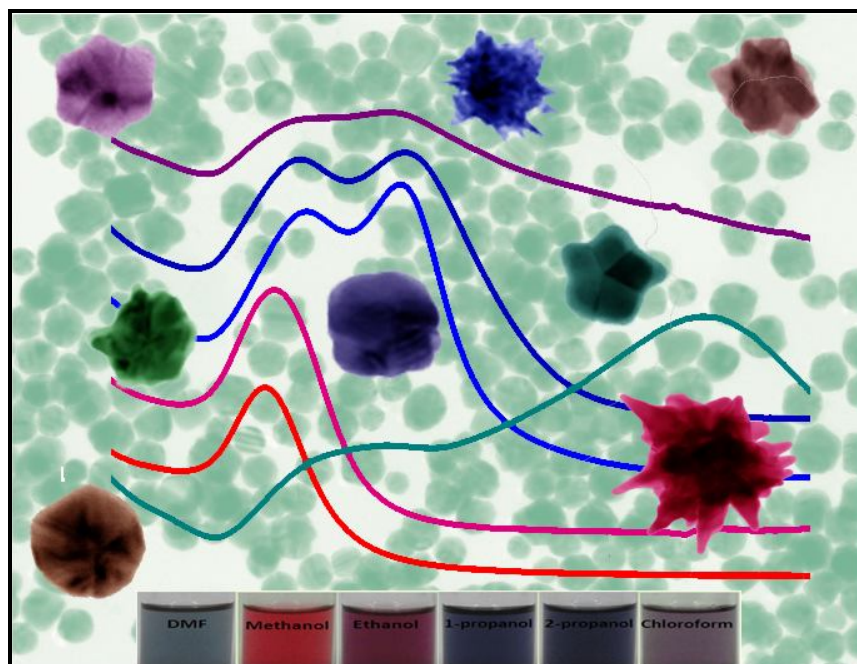
Figure-2.12: (a) Schematic illustration.(b) camera image of CL experimental setup.

### Experimental Details

CL or electron beam induced radiation emission imaging/mapping on an isolated single multi-branched Au nanoparticle (Au nanostar) on Silicon substrate was performed in a ZEISS SUPRA40 SEM equipped with the Gatan MonoCL3 CL system operated in two modes monoCL and panCL. The ZEISS SUPRA40 SEM has a hot Schottky field emission gun (FEG) and the attached MonoCL3 system uses a retractable paraboloidal light collection mirror. The parabolic mirror collects light that is emitted from the sample covering  $1.42\pi$  sr of the full  $2\pi$  of the upper half sphere and collimates it through a hollow aluminium tube to a 300 mm Czerny-Turner type optical monochromator and finally the signal is fed to a high-sensitivity photomultiplier tube (HSPMT). In the present study, data were recorded with an electron acceleration voltage of 30 kV and beam current of about 15 nA with a beam diameter of  $\sim 5$  nm. To minimize sample drift during acquisition, we have acquired the experimental spectra in two wavelength ranges separately: 500–700 nm and 700–900 nm. The total exposure time of one spectrum was approximately 12.5 s. Spectra have been averaged for each e-beam position and corrected for the substrate background. The monochromatic photon map is then built up at a selected peak wavelength of the EIRE spectrum by scanning the e-beam over the sample. For each e-beam position, the luminescence is collected over the entire sample. The bright pixels then correspond to the areas where the strongly excited plasmon mode emits the photons. When adding all the position-dependent partial maps, obtained for each e-beam position, we obtain a full CL map of the plasmon mode associated with a particular wavelength. This CL image is proportional to the radiative local density of optical states (LDOS) of the plasmonic structure.

## Chapter-3

# Poly (Vinyl Pyrrolidone) Induced Anisotropic Gold Nanostructures



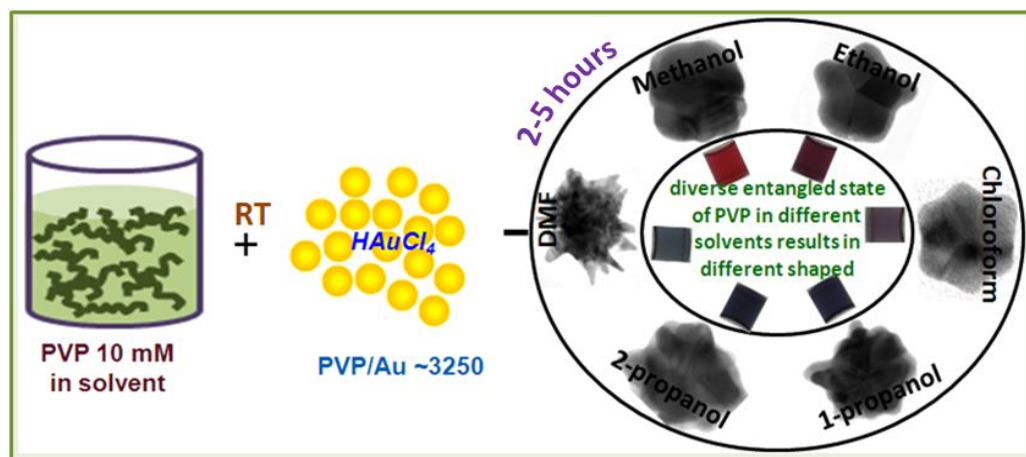
Distinct conformational behavior of PVP in respective solvent dictates its reducing ability for a particular PVP to metal ion ratio, which in turn advocates the stabilization of different anisotropic size/shape controlled metal nanoparticles suitable for wide range of plasmonic as well as sensing applications.

### 3.1 THEME OF THE CHAPTER

- PVP interaction with metal nanoparticles for size/shape selective synthesis have been well studied in detail [162-165, 170, 174, 213-215], but very few reports really assimilated the solvent interaction with PVP [216-218] in the presence of metal ions, that has been reiterated as a crucial factor in the present chapter not only in differentiating the kinetics/thermodynamics of metal nanoparticle synthesis, but also the exclusive dependence of the external energy sources in manipulating the morphology of the nanocrystals.
- PVP is remarkably a stable polymer with its inert physicochemical properties over a wide range of pH/salt content but strongly depends upon the surrounding fluid environment. Hydrogen bonding/dipolar interaction/Van der Waal forces; all have considerable effect on the microscopic/macrosopic properties of PVP, when mixed with various protic/aprotic polar solvents such as water/alcohols/DMF and depending upon their extent of interaction, changes the dynamics of neat components [189, 217, 219-222].
- Based on this premise, we demonstrate that under normal conditions, this dynamic solvent-solute interaction dominates the nucleation regime of metal nanoparticles in precise and further plays a significant role in polymer chemisorptions onto the various facets of the tiny metal seed particles, directing them to grow into different size/shapes, the essence of which has been lacking in the literature reports [110, 162-164, 166, 213, 215, 223, 224]. Current chapter deals with the combined spectroscopic measurements like NMR, FTIR and XPS on the real time interaction between PVP and the dispersed solvent in the presence of metal ions, thereby revealing the characteristic binding of the carbonyl/amide/amine groups adsorbed onto the specific metal ion/nanocrystal surfaces, that further signifies a fine paradigm for the microscopic characterization of the nucleation/growth/stabilization of complex size/shaped metal gold nanostructures with excellent application potentials like SERS response, which has not been properly understood in its true sense till now.

### 3.2 SYNTHESIS PROTOCOL

- In a typical synthesis, 0.27 mM aqueous solution of Hydrochloroauric acid ( $\text{HAuCl}_4 \cdot 3\text{H}_2\text{O}$ ) was mixed with 15 ml of 10 mM PVP solution in Methanol, Ethanol (EtOH), Chloroform( $\text{CHCl}_3$ ), 1-Propanol, 2-Propanol (Prop) and DMF respectively. The general experimental section can be represented as shown in scheme 3.1.
- **Scheme 3.1:** Single step colloidal synthesis procedure for obtaining different anisotropic shaped gold nanostructures. Molar ratio of PVP to metal gold ions is kept at 3250. The chemical reaction is visually monitored through the change in initial solution color from yellowish to colorless and finally to different charming colors indicating the formation of gold nanostructures.



### 3.3 STRUCTURE CORRELATED PLASMONIC SIGNATURES

As illustrated in scheme 3.1, the only variant in the reaction protocol is the individual solvents used; resulting in the structure correlated plasmonic signatures as clearly shown in figures 3.1 and 3.2.

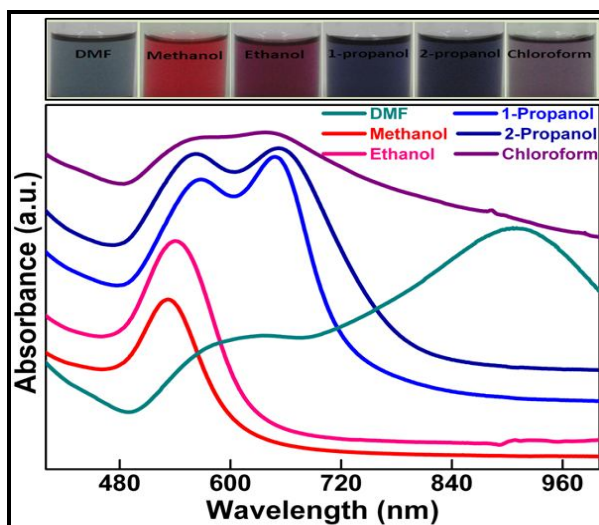


Figure-3.1: UV-Visible absorption spectra of the as-formed gold nanoparticles in their respective solvents for the same monomer to metal ratio (~ 3250) clearly differentiating the size/shape effect on the SPR.

Single surface plasmon band centered around 530-540 nm, clearly visible in the low chain alcohol medium, such as methanol and ethanol, is the foremost essential character of the geometrical nanostructures less deviated from sphericity; whereas in chloroform, propanol and DMF solvents, the presence of two surface plasmon bands (one at around 540 nm and other in the range 700-900 nm) indicates the general formation of anisotropic/elongated nanoparticle shapes, further in confirmation with the TEM images as shown in figure 3.2.

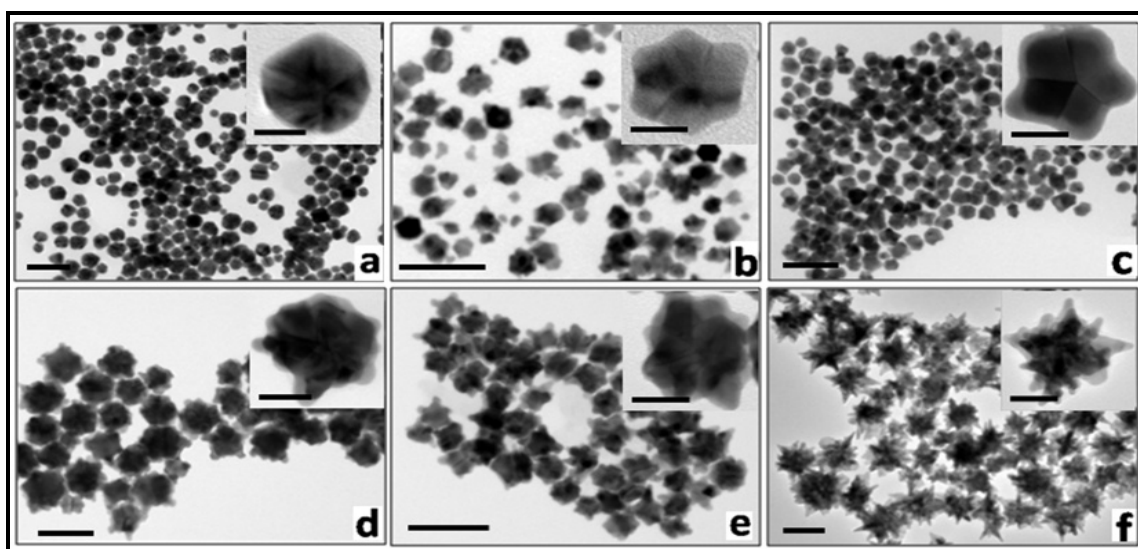


Figure-3.2: Low (Scale bar = 100 nm) and high magnification (scale bar = 20 nm, image in inset) TEM images of as-prepared anisotropic gold nanoparticles in (a) Methanol (b) Chloroform (c) Ethanol (d) 1-Propanol (e) 2-Propanol and (f) DMF solvents. The anisotropy in the structure increases with increase in alcohol chain length and in DMF solvent.

It would be valid to mention that, with increase in chain length (in between or at the end) of alcohol as reaction medium, anisotropy in shape increases. In general, the plasmon band at lower wavelength (higher energy) arises due to the transverse oscillation of the valence electrons with respect to the incident light; whereas the plasmon band at higher wavelength (lower energy) occurs due to the longitudinal oscillations in

relevance with the surface roughness/tips/edges [167] of the respective metal nanostructures. As the particle becomes more complex (decrease in symmetry with reference to both size/shape), many more non-degenerate multi-polar modes arise (essentially due to the higher degrees of freedom easily available for free electron oscillations) and thus their optical absorption reveals asymmetrical bands over a broad spectral region, as for example seen clearly in case of DMF solvent, where two plasmon bands are simultaneously present corroborating the one around 580 nm (due to the core) and 900 nm (due to the tips), which is in overall agreement with the size/shape of the gold nanostars.

The charming characteristic color of the colloidal solutions (red in methanol, pink in ethanol, purple in chloroform, violet in propanol and blue in DMF; see top of figure 3.1) distinguishes the representative polycrystalline quasi-spherical and five-fold asymmetrical decahedral gold nanostructures from other polyhedral, anisotropic multi-/hyper-branched gold nanostructures respectively, as seen from their individual TEM images (figure 3.2). Moreover, the number, sharpness and length of the tip like structures are far more in DMF solvent in comparison with other already known anisotropic branched/multipod gold nanostructures [26, 225-227], which by itself extends the longitudinal plasmon band towards the near IR region (figure 3.1), visually signifying their integral micro-engineered floral core design, an intriguing topology drastically different from the routinely faceted nanostructures, which are of current research interest worldwide due to their vast variety of potential applications, ranging from plasmonic nanoantennas to sensing [49, 228-230].

Interestingly, such a wide range of gold nanostructure morphologies under the same PVP to metal ratio, depicts clearly the deviation from sphericity in the following order; *methanol* < *chloroform* < *ethanol* < *propanol* < *DMF*, as shown by the high magnification TEM images (figure 3.2), strongly implying the complexity of the polymer-solvent-metal ion interaction even under normal conditions.

### **3.4 SPECTROSCOPIC STUDY OF MOLECULAR INTERACTION**

Besides the already known reducing ability of PVP in aqueous medium [84, 172, 173, 175], its stimulating solvent adaptable feature in conjunction with simultaneous active metal coordination, the efficacy of which has not been entirely looked upon till now, outlines the major key point of focus in our present synthesis protocol. Although, the inherent mild reducing ability of PVP commences the nucleation of gold seed particles, its active metal ion/particle coordination interaction not only instantly/strictly prohibits their random aggregation (quite common in case of aqueous synthesis procedures) [57, 231, 232] but also effectively dictates their shape evolution process (the kinetics of adsorption/desorption of PVP in various solvents is different for the different crystallographic planes of metal) [83, 113, 163, 164, 167, 215, 223], summarizing the precise formation of various complex size/shape controlled metal nanostructures.

For the basic understanding of this intriguing nucleation/growth mechanism, one has to ostensibly include the polymer/solvent interaction, probed systematically through <sup>13</sup>C NMR and FTIR measurements, for the first time, the overwhelming results of which are essential in elucidating the final nanoparticle XPS measurements for the determination of surface functionalization of metal nanoparticles with PVP, as discussed methodically in great detail in the following sections.

#### **3.4.1 PVP-Solvent Interaction**

##### **3.4.1.1 NMR Spectroscopy**

From chemical thermodynamics viewpoint, generally for PVP in solution, the carbonyl group of the lactam as well as the monomer chain forms co-operative hydrophilic (hydrogen bonding)/hydrophobic interaction [189, 217, 219-222], the varied strength of which emphasizes coherently the fact that PVP interacts both intra/inter-molecularly with the respective surrounding fluid environment, enumerated by the sheer presence of NMR peaks (see appendix A3.1) further extended in the range of 180-170 ppm and 40-60 ppm (figure 3.3), being related to the C resonance of carbonyl group and C-H group of PVP [172, 233, 234].

In polar aprotic DMF solvent, carbonyl peaks shift up-field by 2.220 ppm, indicative of partial double bond characteristics due to resonance effect, asserting the fact that along with PVP-DMF hydrogen bonding, dipole-dipole interaction is also predominant [217, 235]; while in case of protic solvents like alcohols (propanol and ethanol) and chloroform, they shift downfield with little chemical shifts of 0.428, 0.410 and 0.110 ppm respectively (figure 3.3 and table 3.1).

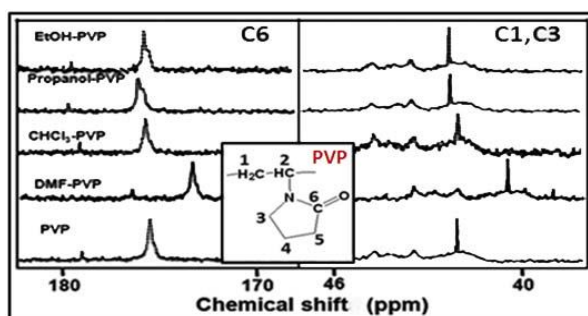


Figure-3.3: Extended C6, C3 and C1 peaks in  $^{13}\text{C}$  NMR spectra of PVP (related peaks are marked in structure (see inset)), PVP-solvent complex formed in respective solvents. Chemical shift in NMR spectra, sensitive to changes in the local chemical structure of polymers, is being well employed for investigating the interaction between PVP and surrounding dielectric environments as relevantly discussed in text.

Such changes in NMR spectra clearly represent the dominant hydrogen bonded configuration, the further contrasting evidence of which arises from the minimal chemical shift in the case of C-H bond (at 42.07 ppm; see figure 3.3 and table 3.1) for propanol, ethanol and chloroform; while a strong up-field chemical shift for DMF signify the mainly strong dipolar/hydrophilic interaction in the polar aprotic solvents.

**Table-3.1: Chemical shift (in ppm) observed for the different carbon environments in PVP. ( $\Delta \delta 1$  is the change in chemical shift of the respective PVP-solvent complex with respect to PVP.**

System	Chemical shift (ppm)		Chemical shift (ppm)	
	$\delta C6$	$\Delta \delta 1$	$\delta C1,C3$	$\Delta \delta 1$
PVP	175.410	-----	42.084	-----
DMF-PVP	173.190	2.220	40.425	1.659
$\text{CHCl}_3$ -PVP	175.520	0.110	42.084	0.000
Propanol-PVP	175.838	0.428	42.190	0.106
Ethanol-PVP	175.820	0.410	42.240	0.156

Further to verify this point, we have taken the  $^{13}\text{C}$  NMR spectra of PVP in DMSO and as expected a strong up-field shift in the PVP carbonyl peak is observed like that in DMF (see figure A3.2), suggesting the existence of strong dipolar/hydrophilic interaction in the polar aprotic solvents, which plays a prominent role in the formation of highly anisotropic gold nanoparticles under the present experimental conditions.

#### 3.4.1.2 FTIR Spectroscopy

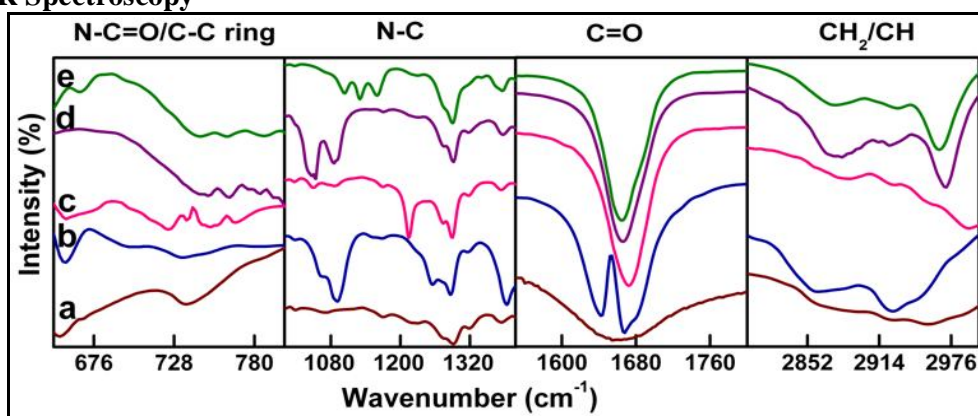


Figure-3.4: Vibrational peaks in the selected wavenumber range for (a) PVP, (b) DMF-PVP, (c) chloroform-PVP, (d) ethanol-PVP, (e) 2-propanol-PVP, are as shown. Substantial contributions from the carbonyl C=O and nitrogen coupled with other chemical bonds can be clearly seen.

The possibility of hydrogen bonding and associated complex of PVP with various protic and aprotic solvents acting as cross-linking points or bridges among the entangled PVP results together in their diverse complex network, duly expressed through irreducible changes in the vibrational aspects of the combined PVP-solvent system as shown by FTIR spectroscopy (see figure 3.4 and table 3.2).

The selective FTIR peaks of PVP dissolved in different solvents in comparison with the pure PVP powder are presented in figure 3.4 (their full range FTIR spectra are shown in appendix figure A3.3) and their individual peak positions are listed in comparison with literature as in table 3.2 [163, 165, 189, 224].

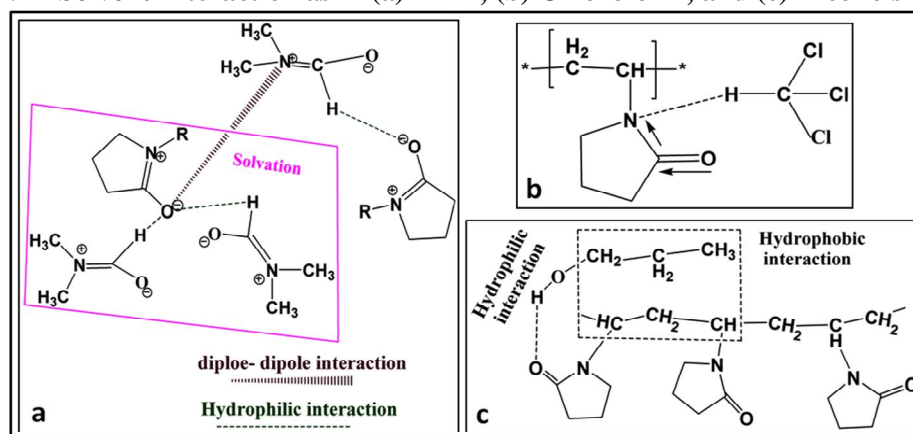
**Table-3.2: Observed baseline corrected vibrational peaks for PVP in different solvents**

*Peak Assignment	PVP Powder	CHCl <sub>3</sub> -PVP	EtOH-PVP	Prop-PVP	DMF-PVP
Asym. ring (CH <sub>2</sub> ) stretch	2985, 2955	2990	2971	2965	2948
Sym. (CH <sub>2</sub> ) chain	2924	2925	2922	2928	2928
C-H stretch	2874	2884	2877	2875	2859
Sym. (C=O) stretch	1663	1672	1666	1665	1642, 1667
Ring (C-N) stretch	1495	1493	1495	1495	1495
Ring (CH <sub>2</sub> ) scissor + Ring (C-N) stretch + (CH) bending	1463, 1439 1423	1461, 1437 1423	1463, 1443 1426	1461, 1441 1424	1459, 1429 1406
Ring (CH <sub>2</sub> ) +(NC) stretch	1374, 1319	1373, 1317	1379, 1316	1375	1383, 1316
Ring (CH <sub>2</sub> ) wag+ (CN) Stretch	1292	1289	1294	1289	1285
CH <sub>2</sub> twist + NC Stretch	1229	1215	1226	----	1256
Weak Ring CH <sub>2</sub> twist	1170	1170	1173	1162, 1130	1166, 1150
(CN) stretch	1071	1049	1087, 1047	1103, 1016	1091, 1062, 1018
(C-C) ring breathing	934	930	933	951	932
C-C ring	846	893, 881, 846	880, 847, 806	895, 846, 816	893, 864, 843
(C-C) chain	736	767, 751, 736, 726	763, 747	785, 762, 746	783, 733, 700
(N-C=O) bend	651	657	-----	668	657

All wave numbers are given in cm<sup>-1</sup>. The illustrated peaks in figure 3.4 are in brown color for easy reference purpose. Peaks in green color are shown in full range FTIR spectra in appendix figure A3.3. \* (peak value is assigned from literatures reports [163, 165, 189]).

For PVP in DMF, two intense bands are seen at 1642 and 1666 cm<sup>-1</sup>, attributed to the carbonyl stretch bonded DMF-PVP complex and unbounded PVP respectively. The strong decrease in C=O absorption frequency (see table 3.2) is being attributed to hydrophilic interaction (H-bonding) between carbonyl oxygen of PVP and formyl proton of DMF along with the dipole-dipole interaction between the carbonyl groups of DMF and the lactam of PVP molecules further quantified from the gradual increase in C-N stretching related frequencies such as 1374 to 1383 cm<sup>-1</sup>, 1229 to 1256 cm<sup>-1</sup> and 1071 to 1091 cm<sup>-1</sup> (see figure 3.4 and table 3.2, weakening of carbonyl group of PVP molecule results in conjugation hence making the C-N bond stronger) as represented in scheme 3.2a.

**Scheme-3.2: PVP–Solvent Interaction as in (a) DMF, (b) Chloroform, and (c) Alcohols like Propanol**



The C=O stretching vibration absorption band of PVP is found to be strongly sensitive to formation of H-bonds and undergoes an apparent red shift (moving to lower wavenumber) with hydrogen donors [217]. Hence, a large red shift for PVP in DMF signifies the strong solvation of PVP molecules (see scheme 3.2a).

For PVP in chloroform, the major vibrational peak position changes corresponding to CH<sub>2</sub>/CH (vinyl group), C=O and C-N coupled bands (as illustrated in table 3.2) clearly indicates that the PVP molecule interacts with CHCl<sub>3</sub> solvent effectively through N-C stretch vibrational bands of N-C=O and N-C-C in the pyrrolidone ring further weakening its conjugation, thereby strengthening the carbonyl group as shown in scheme 3.2b. Although segmental motion of PVP was studied in CHCl<sub>3</sub> but lacking the modes of interaction present in solution [236].

For PVP in alcohol, the alcohol chain molecules are in dynamic equilibrium due to the continuous breakage and re-formation of H-bond [221]. Moreover, for PVP-alcohol medium, the highly dynamic correlated hydrophilic (hydrogen bonding between C=O in the pyrrolidone ring and hydroxyl group of alcohols) vs hydrophobic (bonding between methyl/methylene groups and polymer monomer chain) interaction (shown in scheme 3.2c) essentially nullifies the overall observed changes in the PVP carbonyl peak. Comparing this micellar like hydrophilic-hydrophobic interaction of PVP with various alcohols, one can easily accredit their strength of interaction in the following order: *propanol* > *ethanol* > *methanol*. Nevertheless, at fixed 10 mM of PVP concentration in all our synthesis procedures, the hydrophobic interaction seems to dominate, as vindicated by the visible changes in the CH<sub>2</sub>/CH as well as C-N peaks (table 3.2).

### 3.4.1.3 XPS Studies

For the first time to the best of our knowledge, the PVP-solvent interaction is explicitly exemplified through XPS measurements, as shown in figure 3.5 and table 3.3. It can be inferred that visible conformational changes emerging in the intrinsic chemical structure of polymer PVP upon complexation with different solvents were in direct corroboration with our present NMR and FTIR measurements. The obtained XPS spectra are deconvoluted by rigorous peak fitting exercise shown by the dotted lines in figure 3.5.

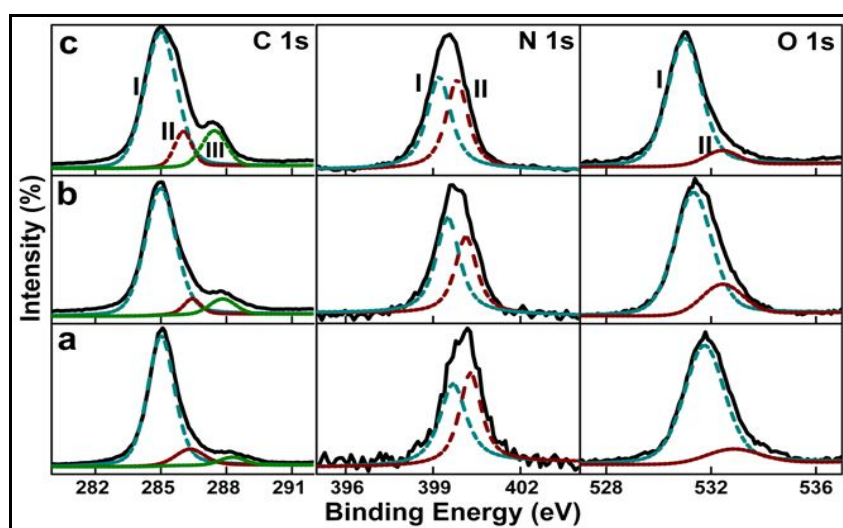


Figure-3.5: XPS spectra of PVP in (a) DMF (b) propanol (c) EtOH (drop casted on silicon) illustrating the corresponding carbon (C 1s), Nitrogen (N 1s) and Oxygen (O 1s) regions (solid black peaks), that are deconvoluted further into three (C 1s I, C 1s II and C 1s III), two (N 1s I and N 1s II) and two (O1s I and O1s II) peaks (dashed color lines) respectively as mentioned in table 3.3.

The deconvoluted carbon, oxygen and nitrogen binding energy (BE) peak positions of PVP (10 mM) in different solvents respectively, are illustrated in table 3.3. The BE peak (marked as I) in both N 1s and O 1s were conveniently attributed to the intra-chain and free carboxyl (C=O) oxygen of PVP; whereas the BE peak (marked as II) represents the contribution arising due to inter-molecular interaction between different solvents and PVP. The higher BE of N 1s (400.28 eV) and O 1s (532.83 eV) along with N-C=O (C 1s III, 288.28 eV) component in PVP-DMF complex (see table 3.3), in comparison with ethanol/propanol signifies the essential participation from both carbonyl oxygen as well as nitrogen as a result of hydrophilic as well as dipole-dipole interaction (when the number of bonds to electronegative atoms increases, the XPS chemical shift also increases) [237, 238]. The deconvoluted C 1s spectra illustrating more C-C peak percentage contribution as well as shift in C-N/C-N=O peaks for propanol in comparison to ethanol further in sharp agreement with NMR and FTIR results in the previous section.

**Table-3.3: XPS binding energy peak positions obtained from the different component core levels of PVP (MW=10 k; 10 mM in different solvents).**

Peak	PVP-DMF	PVP-propanol	PVP-EtOH
<i>C 1s I (C-C)</i>	285.01 (68)*	284.98 (66)*	284.99 (60)*
<i>C 1s II (C-N)</i>	286.34	286.44	286.03
<i>C 1s III (N-C=O)</i>	288.28	287.83	287.45
<i>N 1s I</i>	399.68	399.50	399.22
<i>N 1s II</i>	400.28	400.13	399.85
<i>O 1s I</i>	531.74	531.32	531.00
<i>O 1s II</i>	532.83	532.43	532.42

\*(Percentage contribution as extracted from the area of the C-C peak)

The subtle changes in the peak positions with varied strength of their peak intensities directly correlate the surrounding chemical environment around the polymer in different solvent. Hence, our combined spectroscopic measurements illustrate the co-operative strength of a complex solvophobic interacting network of PVP in respective solvents varies as: *DMF* > *Propanol* > *Ethanol* > *Chloroform*.

### 3.4.2 PVP-Solvent-Metal Ion Interaction

We have already shown that polymer-solvent complex is formed which result in entanglement of PVP molecules as seen by considerably changes in NMR and FTIR peaks (figures 3.3/3.4). When  $\text{HAuCl}_4$  is added to this PVP-solvent mixture with a high monomer to metal ratio ( $\sim 3250$ ), donation of lone pair of electrons both from the intra-/inter-chain of the entangled PVP network to the as-formed dynamically unstable PVP-solvent- $\text{AuCl}_4^-$  complex takes place, thereby sequential ligand substitution occurs in the square planar metal centered complex, disproportionating itself to yield  $\text{Au}^0$  species (discussed in detail in next chapter for DMF-PVP system, pp: 103-104).

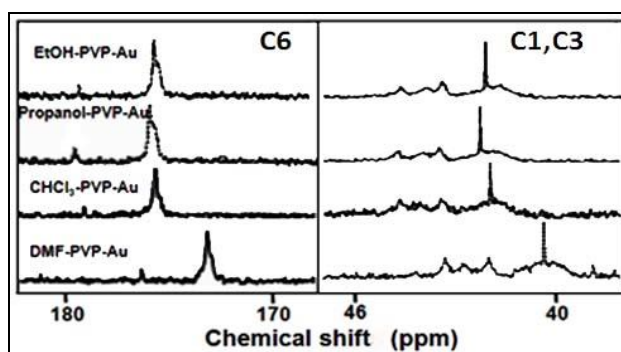


Figure-3.6: Shows extended  $^{13}\text{C}$  NMR spectra (C6, C3 and C1 peaks) for different Au nanostructures formed in respective solvents.

Few reports indicate the strong interaction between PVP segments and the metal ions in solid state [217, 235, 239, 240], suggesting significant changes in the conformation of polymers in the final nanoparticle spectra from their respective complexes with solvents.

**Table-3.4: Chemical shift (in ppm) observed for the different carbon environments in Au nanoparticles ( $\Delta \delta 1$  and  $\Delta \delta 2$  are the changes in chemical shift with respect to PVP and their respective PVP-solvent complex respectively).**

System	Chemical shift (ppm)			Chemical shift (ppm)		
	$\delta C6$	$\Delta \delta$		$\delta C1, C3$	$\Delta \delta$	
		$\Delta \delta 1$	$\Delta \delta 2$		$\Delta \delta 1$	$\Delta \delta 2$
DMF-PVP-Au	173.061	2.349	0.129	40.301	1.783	0.124
$\text{CHCl}_3$ -PVP-Au	175.560	0.150	0.040	42.090	0.006	0.006
Propanol-PVP-Au	175.857	0.447	0.019	42.210	0.126	0.020
Ethanol-PVP-Au	175.780	0.370	0.040	42.110	0.026	0.130

To our pleasant surprise, we observed no such appreciable changes in the FTIR/NMR spectra (figures 3.3/3.4/3.6/3.7 and tables 3.1/3.2/3.4/3.5), signaling the fact that formation of nanoparticles were accomplished not only by the reduction of Au<sup>3+</sup> to Au<sup>0</sup> species, but also involves other ensemble processes which had been overlooked upon in most of the literature reports, where either only final Au NPs spectrum is considered or PVP-metal ions in solid state [83, 163, 164, 213, 215, 239] alone, leaving ample lacunae for our meticulous molecular spectroscopic data to stand tall in the crowd.

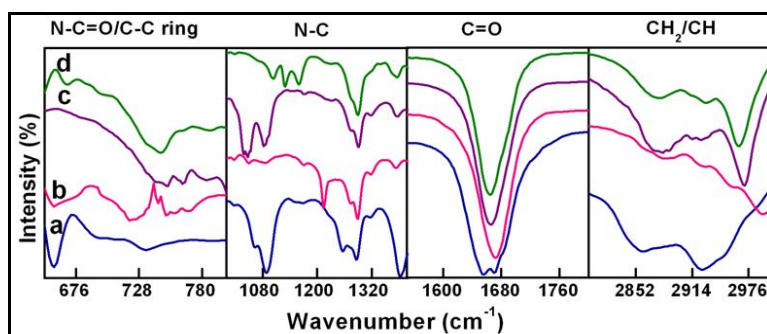


Figure-3.7: selected vibrational peaks for Au NPs formed in respective solvents (a) DMF, (b) chloroform, (c) ethanol, (d) 2-propanol are essentially found to be similar to that of the corresponding PVP-solvent spectra as shown in figure 3.4, suggesting collective reaction regime as discussed in the text.

Our detailed analytical observations suggest that these *in situ* formed small gold seed particles then compete with PVP over the respective fluid surroundings strongly inducing desolvation effects, thus allowing the stabilizer polymer be chemisorbed on to the seed surface in an intricate manner right from its immediate nucleation, thereby preventing random agglomeration by steric stabilization.

These two synergetic effects, desolvation (highly dependent on solvent character) and polymer coordination interaction with the metal ion (see scheme 3.3) [217], predominates the kinetic reaction mechanism under normal conditions, resulting in equilibration of the PVP-solvent (figures 3.4/3.5 and tables 3.1/3.2) and PVP-solvent-Au spectroscopic data (figures 3.6/3.7 and tables 3.4/3.5), effectively illustrating the cohesiveness of the well-known ligand exchange mechanism of metal square planar complexes [240], even in the case of non-aqueous solvents.

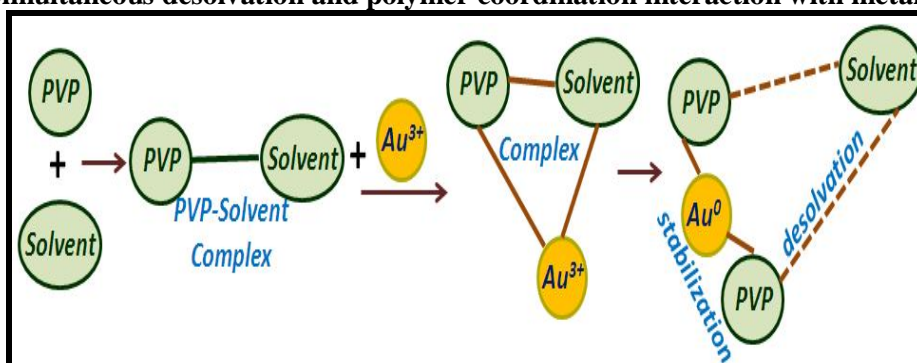
**Table-3.5: Observed baseline corrected vibrational peaks for PVP in pristine Au nanoparticles.**

Peak Assignment	PVP-CHCl <sub>3</sub> -Au	PVP-EtOH - Au	PVP-Prop- Au	PVP-DMF-Au
Asym ring (CH <sub>2</sub> ) stretch	2990	2971	2965	2948
Sym (CH <sub>2</sub> ) chain	2925	2922	2928	2926
C-H stretch	2884	2877	2875	2861
Sym (C=O) stretch	1672	1666	1665	1669,1655
Ring (C-N) stretch	1493,	1495	1495	1497
Ring (CH <sub>2</sub> ) scissor + Ring (C-N) stretch + (CH) bending	1461, 1437 1423	1463, 1443 1426	1461, 1441 1424	1459, 1430 1404
Ring (CH <sub>2</sub> ) +(NC) stretch	1373,1317	1379,1316	1375	1383,1316
Ring (CH <sub>2</sub> ) wag+ (CN) Stretch	1289	1294	1289	1286
CH <sub>2</sub> twist + NC Stretch	1215	1226	----	1255
Weak Ring CH <sub>2</sub> twist	1170	1173	1162,1130	1170,1151
(CN) stretch	1049	1084,1041	1103,1016	1088,1063,1017
(C-C) ring breathing	930	933	952	933
C-C ring	893,881,846	883,846,806	895,846,816	894,864,845
(C-C) chain	769, 752, 744, 736, 723	763,747	785,762, 748	733, 700
(N-C=O) bend	657	-----	669	657

(All wave numbers are given in cm<sup>-1</sup>. The illustrated peaks in figure 3.7 are brown in color. Peaks in green color are shown in full range FTIR spectra in appendix figure A3.3.

Thus, our combined NMR and FTIR results unmistakably exemplifies the significance of highly dynamic sensitivity of PVP-solvent interaction, further elucidating the fact that pyrrolidone monomer units radically adheres to the Au metal surface, both in ionic as well as particulate nature, which has been largely misunderstood for the formation of various unstable oxidation byproducts [84, 240], for the lack of methodical kinetic molecular studies, as meticulously pointed in the case of formation of gold nanostars in next chapter, aesthetically interpreting the importance of solvent-solute interactions in determining the final morphology of the metal nanoparticles.

**Scheme-3.3: Simultaneous desolvation and polymer coordination interaction with metal ions**



Further, careful surface chemical composition analysis of the as-prepared anisotropic gold nanostructures (drop cast five-fold centrifuge samples in ethanol on silicon) using XPS studies visualize the chemisorption of PVP ligand with different size/shaped Au nanocrystals and their corresponding effective interaction, thereby providing novel insights into the quantitative role played by the individual components of PVP in seedless surface mediation under normal experimental conditions.

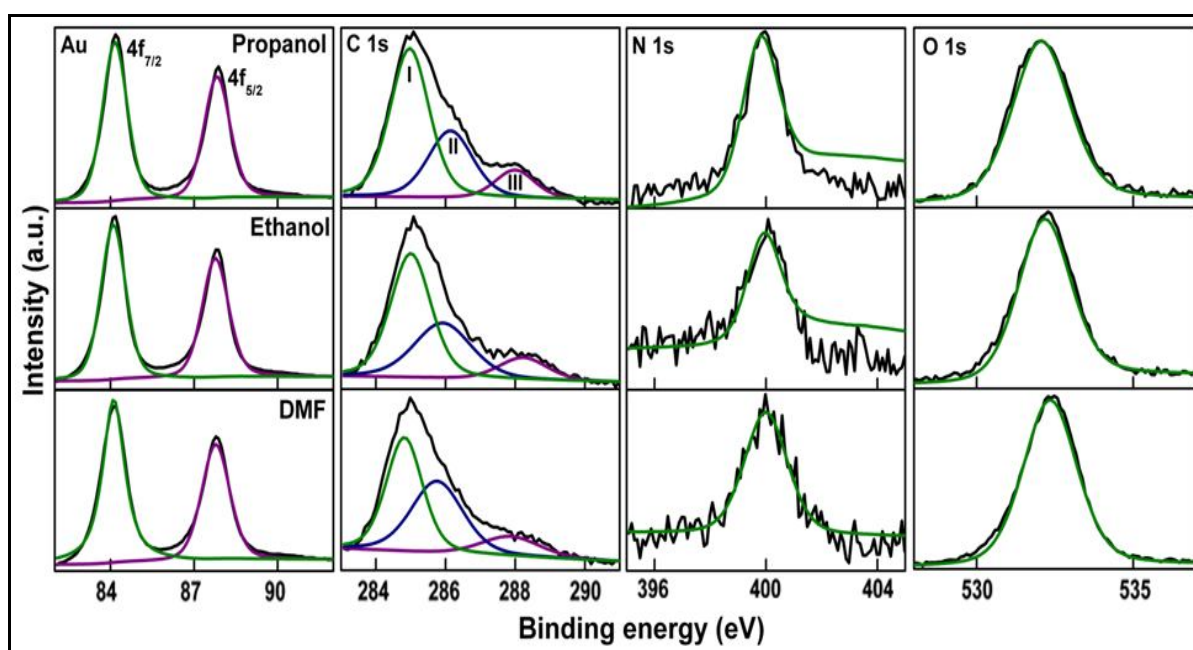


Figure-3.8: XPS spectra of PVP-capped Au nanoparticles (synthesized in different solvents as shown) illustrating the corresponding C 1s, N 1s, O 1s, and Au 4f regions (solid black lines), further deconvoluted into respective peaks (colored lines) as represented in table 3.6.

Figure 3.8 shows a typical C 1s, O 1s and N 1s and Au 4f core level spectrum of the purified Au nanoparticle samples, which strongly corroborate the presence of PVP molecules on the metal surface, further in tune with the diverse interaction between PVP and various gold crystalline facets as being reported [175, 241]. It is generally believed that PVP interacts with metal nanoparticles through its O atom in the pyrrolidone ring by ligand-to-metal charge transfer interaction; while the direct participation of N atoms is less favored due to steric hindrance effects [175, 242].

**Table-3.6: XPS Binding Energy Peak Positions Obtained from figure 3.8.**

Peak	DMF	Ethanol	2-Propanol	PVP
Au4f7/2	84.11	84.10	84.16	-----
Au4f5/2	87.76	87.77	87.83	-----
C1s (C-C)	284.82 (45)*	285.01 (52)*	285.01 (63)*	285.12
C1s (C-N)	285.80	286.00	286.27	286.00
C1s (N-C=O)	287.81	288.31	287.93	287.80
N1s	400.07	400.16	399.89	399.7
O1s	532.48	532.22	532.06	531.35

\*(Percentage contribution as extracted from the area of the C–C peak)

The oxygen and nitrogen peaks in final Au NPs XPS spectra are fitted into single peak assuming there is no free PVP due to repetitive centrifuge cycles. In the O 1s region, the peak arising from the carbonyl (C=O) oxygen for pure PVP (531.3 eV) [241] cohesively red shifts to 532.35, 532.17 and 532.06 eV for the Au nanoparticles synthesized in DMF, ethanol and propanol respectively (figure 3.8 and table 3.6), illustrating the fact that the electron density consistently decreases around the carbonyl (C=O) oxygen due to significant interaction between the PVP molecule and the Au particle core. Likewise, the N 1s core level peak of pure PVP (399.6 eV) [241] shifts asymmetrically to slightly higher binding energies (400.07, 400.16 and 399.89 eV) for the Au nanostructures in DMF, ethanol and propanol respectively (figure 3.8 and table 3.6), directly depicting the selective participation of nitrogen in assimilating nucleation and growth of anisotropic gold nanostructures as evidenced from the TEM images (figure 3.2).

In terms of better quantifying specific charge-transfer interaction of the polymeric stabilizer with the Au nanoparticles with high clarity, the observed C 1s core level spectra were deconvoluted into three peaks by standard non-linear curve fitting procedures, representing the C-C, C-N, N-C=O bonds of the PVP molecule (see figure 3.8) respectively, the varied strength of their peak intensities directly affiliates the surrounding chemical environment around the polymer. These relative changes in individual C 1s components delineate the following interesting facts:

For the Au nanostructure in DMF solvent, practically no BE shift occurs for C-N and N-C=O peaks, but the C-C peak shifts to lower binding energy in comparison with pure PVP, clearly distinguishing the subtle changes observed in their respective N 1s and O 1s core level spectra (figure 3.8 and table 3.6), preferably asserting the fact that the combined dipolar/hydrophilic interaction of PVP molecules in the polar aprotic reaction medium primarily exercise a strong electron density distribution around both nitrogen and oxygen components in the pyrrolidone ring, but sensitizes the C-C component due to the implicit change in overall chemical environment.

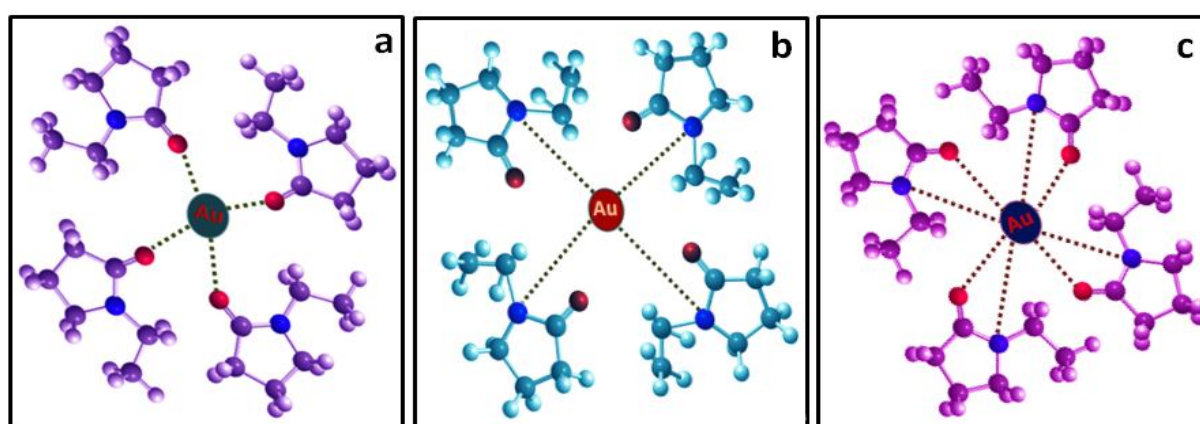
Similarly in ethanol solvent, the major contribution from the N-C=O component in comparison with pure PVP (table 3.6) indicates partial bond weakening upon chemisorptions with Au, implying stronger interaction between the polymer-gold interface, which practically controls the aggregation/arrangement of reduced Au atoms, essentially dictating the defect induced formation of decahedral gold nanostructures.

In case of propanol, minimal red shift in C-N and N-C=O peaks along with a slight blue-shift in C-C peak (with increasing C-C percentage contribution as we go from DMF to ethanol to propanol) with respect to pure PVP (figure 3.8 and table 3.6) signifies the fact that hydrophobic interaction dominates (scheme 3.2c) which is in narrow coincidence with our FTIR results (figure 3.4 and table 3.2), intuitively suggesting the indirect but significant contribution from the monomeric chain of PVP in the design and controlled formation of complex multi/hyper-branched gold nanostructures.

Hence, the present comprehensive XPS analysis shows that the electron cloud density unequivocally hovers around the N-C=O region of the pyrrolidone ring of PVP through the so-called conjugation effect, confirming the impartial charge transfer from both the oxygen and nitrogen atom in the pyrrolidone ring when dispersed in DMF solvent, the dynamic equilibrium of which sequentially gets drifted through solvent specific intra/inter-molecular redistribution aptly supported by the monomer chain component, particularly when PVP is dispersed in alcohol environments.

Moreover, in comparison with bulk Au atoms (84.0 eV for Au 4f<sub>7/2</sub>, 87.7 eV for Au 4f<sub>5/2</sub>) [175, 241], the BE of Au 4f<sub>7/2</sub> core level peak arises at 84.11, 84.10 and 84.16 eV and that of Au 4f<sub>5/2</sub> core level peak arises at 87.76 eV, 87.77 eV and 87.83 eV respectively, in DMF, ethanol and propanol solvent medium (figure 3.8 and table 3.6), the concurrent changes of which drastically differs from the XPS data on other molecular/surfactant/polymer capped Au clusters/nanoparticles [57, 83, 103, 113, 173, 175, 231-236, 240, 241]. This retrospectively implying a complex charge transfer process enabled by the convoluted electron-donating ability of PVP to metal ions, leading to ample nucleation followed by selective aggregation/interfacial alignment of reduced Au<sup>0</sup> species, in the absence of external reducing agent under normal conditions or energy sources like temperature, microwave/ultrasonication, seed mediation etc.

**Scheme-3.4: Adsorption of PVP on the surface of gold colloids through chemisorptions via three possible modes (a) Oxygen (b) Nitrogen and (c) Both Nitrogen and Oxygen occurring simultaneously which bridge adjacent metal atoms on the nanoparticle surface, the strength of interaction depends upon the solvents used.**

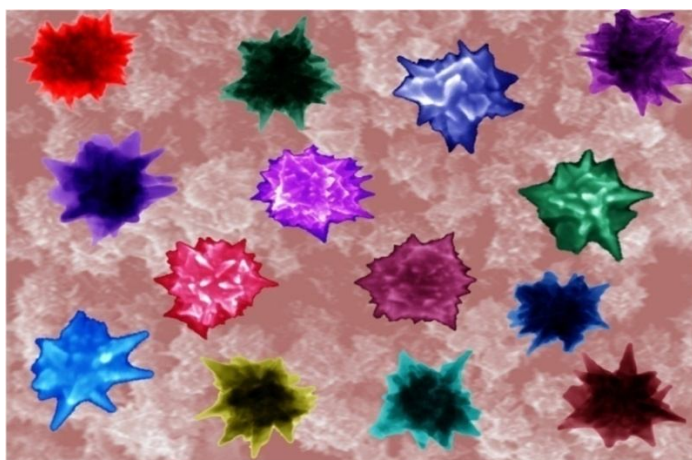


This duly reaffirming the quantitative role of PVP in intuitively evaluating the bridging ligands (scheme 3.4) with reference to the surrounding dielectric environment, to indeed evolve on its own, as vividly supported by the classical coordination chemistry model for metallic nanocrystals [221, 235, 243, 244].

In summary, our present work quantitatively illustrates different coordination bonds formed by PVP in their respective solvent medium along with the redox potential of metal precursor ions initiate the reduction process themselves in the absence of external reducing agent under normal conditions for the first time to best of our knowledge, thereby constantly rejuvenating its chemical interaction with Au, proceeding from ionic to particulate form, simultaneously entrusting the bridging ligands mechanism which indeed evolve on its own. Combined molecular/spectroscopic studies invariably facilitate the deep insight in understanding kinetic nucleation and growth of stable and reproducible anisotropic size/shaped metal nanostructures. Various results obtained for present case essentially highlighting the urgent need to critically understand the physico-chemical aspects of PVP as natural reductant/stabilizer system in the absence of external energy resources, so as to systematically tune/design the complex structure-property relationship between the polymer PVP and the metal nanoparticles, thereby enhancing their plasmonic and photonic application potentials, as never seen before.

## Chapter - 4

# One Step Synthesis of Gold Nanostars: Combined Optical And Cathodoluminescence Study



Single step seedless/templateless colloidal synthesis of complex 3D gold nanostars involves complexation of PVP in polar aprotic solvent, DMF and their reduction of  $\text{AuCl}_4^-$  ions along with HCl as an effective mediator. The meticulously proposed ligand exchange mechanism iteratively illustrates the combined kinetic effects of the solvent, polymer as well as the metal ion in designing the intricate nanoarchitecture of the gold nanostars through various atomic/molecular spectroscopic measurements. Further, CL spectroscopy highlights the significance of anti-bonding plasmon modes (by virtue of its aesthetics) for nanoantenna as well as sensing applications.

#### 4.1 THEME OF THE CHAPTER

High yield seed mediated colloidal synthesis procedure were widely utilized for the monodisperse synthesis of gold nanostars (by reduction of  $\text{HAuCl}_4$  in PVP complexed with polar aprotic solvent DMF [245, 246], which effectively act as nanoantennas for receiving/transmitting light at nanometer scale and an excellent candidate for SERS applications [229, 245, 247, 248]. Notably, similar branched nanostructures were also obtained in the above mentioned synthesis protocol even in the absence of external seeds as discussed in the previous chapter also, but with significantly higher polydispersity and larger particle sizes [246].

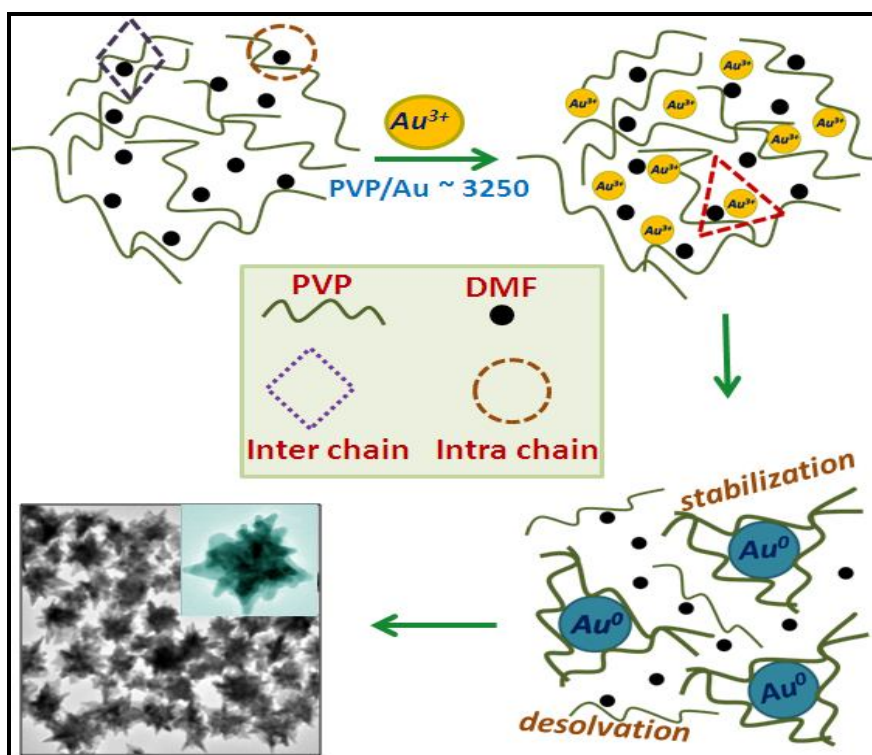
Encouraged by this idea of seedless reduction, we efficiently demonstrate a modified single step chemical solution synthesis procedure for the formation of complex 3-D gold nanostars with perfection, high degree of size/shape control. CL spectroscopy in conjunction with optical absorption studies were effectively utilized for the analysis of the plasmonic eigenstates/modes of these gold nanostars and the corresponding intensity maps of the respective plasmonic modes in the gold nanostars were found to be in excellent agreement with the finite difference time domain (FDTD) simulations [249].

A methodical molecular kinetic study involving the complexation of universally soluble homogeneous polymer, PVP in DMF and their simultaneous reduction of pH sensitive  $\text{AuCl}_4^-$  ions along with HCl as an effective mediator [250] has been studied in great detail for the first time in terms of identifying/understanding the sequential ligand exchange mechanism responsible for designing such intriguing nanoarchitectures. The knowledge on this basic interactive ligand exchange not only benefits the researchers on the preparation/stability of the polymer stabilized metal colloids, but also stimulates the development of next-generation materials with substantially enhanced performances [229, 247, 248, 251-253].

#### 4.2 SYNTHESIS PROTOCOL

In a typical synthesis for the formation of gold nanostars, a freshly prepared solution of 10 mM PVP in DMF is homogeneously mixed with adequate amount of tetrachloroauric acid ( $\text{HAuCl}_4 \cdot 3\text{H}_2\text{O}$ ). In order to get one step monodisperse gold nanostars, HCl is added in aliquots to DMF (concentration mentioned in text) and mixed well just before the addition of PVP and the rest of the reaction conditions are the same as mentioned above.

**Scheme-4.1:** Single step seedless/templateless colloidal synthesis procedure for obtaining 3-D complex gold nanostars.



### 4.3 STRUCTURAL AND MORPHOLOGICAL INVESTIGATIONS

With due reference to the discussion in chapter 3 (pp: 62-72), the strength of polymer PVP dispersion in the given solvent not only have a significant influence on its conformational behavior, but also dictates their mild reducing ability and the corresponding stabilizing action, essentially leading to the integral size/shape tuning of the metal nanostructures in the absence of any other external energy resources.

This key factor, as highlighted throughout in the present chapter, is being observed through the intricate complexation of the polar aprotic solvent DMF, in conjunction with the structurally similar homogenous polymer, PVP, which additionally supervises the interfacial/intermediate formation of anisotropic metal nanostructures in the reaction medium, thereby facilitating a kinetically controlled growth, resulting in the mesostructural organization of spike/tip like nanoarchitectures, finally resembling stable 3-D flower/star like gold nanostructures under ambient conditions.

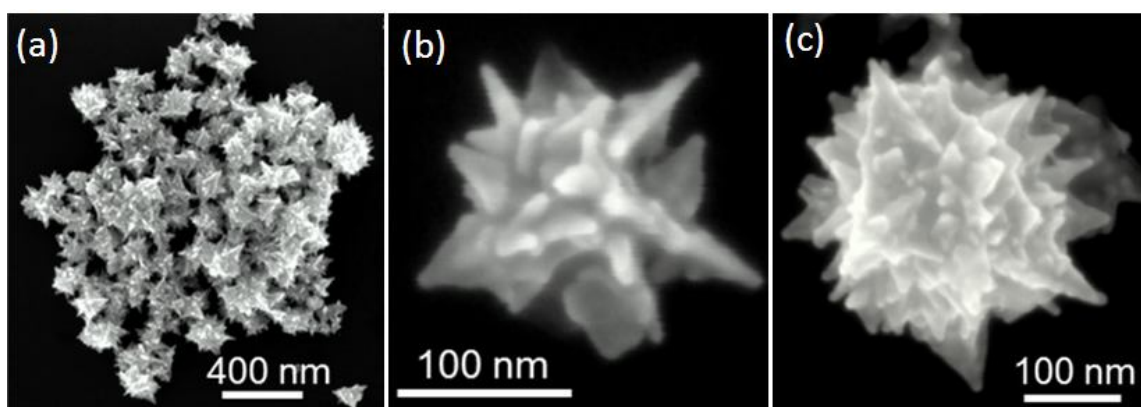


Figure-4.1: (a) Low and (b), (c) High resolution FE-SEM images of multi-branched gold nanostars, illustrating the highly anisotropic complex branching in comparison with other reported planar nanostars.

Interestingly, the SEM and TEM images of the as-prepared, exceedingly reproducible and extremely stable gold nanostars (figures 4.1 and 4.2a) reveal a complex multi-layered core with a number of (non)planar single crystalline spikes, radially projecting outward from the centre, quite akin to predominantly a flower like structure. The number of tips/spikes and their respective aspect ratio vary from particle to particle. Remarkably, similar monodisperse star-like morphologies with high degree of size/shape control were also obtained utilizing the seed mediated growth as previously reported [245, 254], which has been normalized in the present case with controlled addition of 0.6 mM HCl, as significantly evidenced from the Gaussian nature of the virtual core diameter distribution plots (figure 4.2c).

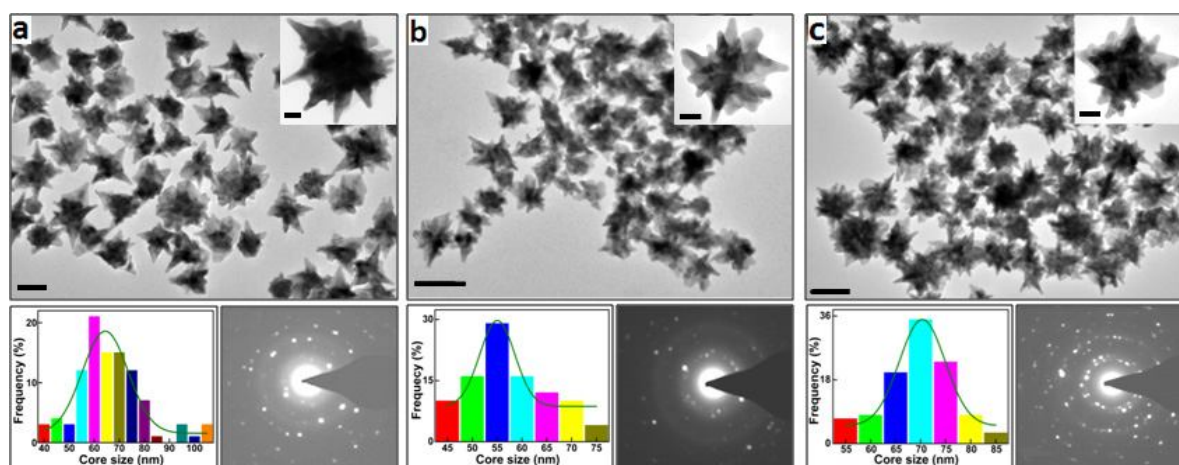


Figure-4.2: Low magnification TEM images (scale bar = 100 nm) along with magnified image (inset, scale bar = 20 nm) for the as-prepared gold nanostars (a) without HCl (b) with 0.3 mM HCl (c) with 0.6 mM HCl addition. The corresponding irregular selected area electron diffraction pattern (SAED) patterns show strong crystallinity as well as interlaced, non-planar, 3-D complex gold nanostars and Gaussian fit to the assumed core diameter depicts the monodisperse nature for the addition of 0.6 mM HCl to the reaction mixture.

The irregular, clustered bright spots obtained in (SAED) pattern (figure 4.2) is in good agreement with that obtained for the seed mediated gold nanostars [246], except for the increase in the number density of bright spots with increasing HCl addition, depicting the presence of dynamic fluctuating 3-D nature of the core, with extensive interlacing among the composed spike/tip like nanostructures, further confirming their individual strong  $\langle 011 \rangle$  direction oriented crystallinity, even observed from different particles, as similarly reported for Pt nanothorn assemblies [255], thereby ruling out the intrusion of twinning or any such defects, right from the nucleation stage itself. This uncommon growth of the higher surface energy facets, as compared with the lower surface energy and facets of an fcc lattice, stems from the rational reducing/stabilizing ability of the universally soluble polymer PVP along with the suitable polymer/metal ratio, which manifests the creation/collective organization of metal seed particles in their respective manner, as evidenced through detailed spectroscopic characterization discussed in the following sections. Surprisingly, none of the other reported star/multipod/branched nano gold morphologies show such strong/long term stable crystalline nature [225, 256-260], evincing great interest in our present size/shape tunable gold nanostars for their promising plasmonic/sensing applications [228, 229, 247, 248, 254, 256, 258, 260-263].

#### 4.4 OPTICAL ASPECTS

##### 4.4.1 UV-Vis Spectroscopy

Room temperature kinetic disproportionation of  $\text{Au}^{3+}$  into  $\text{Au}^+$  and subsequently to  $\text{Au}^0$  nanoparticles was followed by UV-visible spectroscopy in order to understand the formation mechanism of these complex shaped gold nanostars.

With the molar ratio of PVP to metal ions fixed at  $\sim 3250$  in DMF solvent, the  $\text{Au}^{3+}$  CTTS (charge-transfer-to-solvent) absorption band (strongly dependent on the solvent character) at 325 nm disappears in the first minute itself, clearly revealing that the absorbance value at any instant of time cannot be directly correlated with the metal ion/nanoparticle concentration. Hence, the measured kinetic absorption spectra were plotted (figure 4.3) upon normalization at 400 nm (see chapter 2 pp: 37).

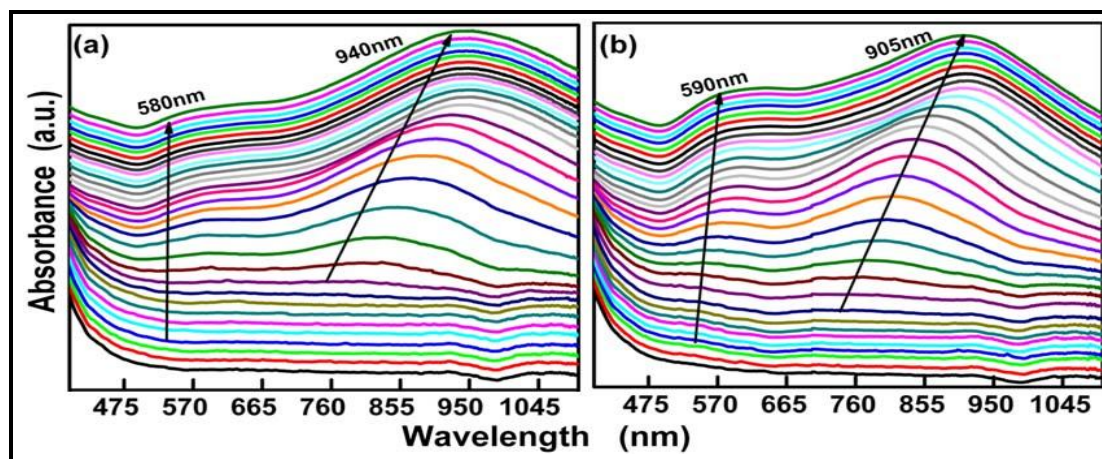


Figure-4.3: Kinetic optical absorption spectra (normalized at 400 nm) recorded for every 4 minutes interval for the growth of Au nanostars (a) without HCl and (b) with 0.6 mM HCl. The spectra are manually stacked one above the other so as to clearly depict the formation and growth of transverse as well as longitudinal SPR peaks as indicated by the arrows.

A broad hump like feature, centered around 500 nm, starts emerging right from the first minute of the reaction (figure 4.3a), that become clearly visible after 30 minutes, indicating the dynamic/instantaneous nucleation of anisotropic/elongated gold seed particles, due to the mild reduction ability of DMF-PVP complex as well as the presence of relatively high monomer to metal ratio, as visibly observed from the kinetic TEM images obtained from quenching the reaction (mixture containing DMF, PVP and  $\text{HAuCl}_4$ ) by abundant acetone at specific time intervals shown in figure 4.4.

The more relevant issue is to understand the growth of each tip in the direction of the  $\langle 110 \rangle$ , which is indicative of a weak interaction of Au atom with the PVP molecules for  $\{110\}$  facets, as compared with

{111} and {100}. At nucleation stage, PVP acts as an anisotropic confiner to gold seeds to induce and maintain anisotropic crystallography by selective passivation of certain facets. These primary gold seed particles selectively agglomerate themselves to compensate the overall surface energy of the reaction mixture (figure 4.4), which superficially changes the color of the solution from colorless to a purple tint during the first 40/45 minutes of the reaction, thereby gradually enhancing the absorption hump into two visibly prominent peaks, a small one centered around 560 nm and a broader one at around 800 nm.

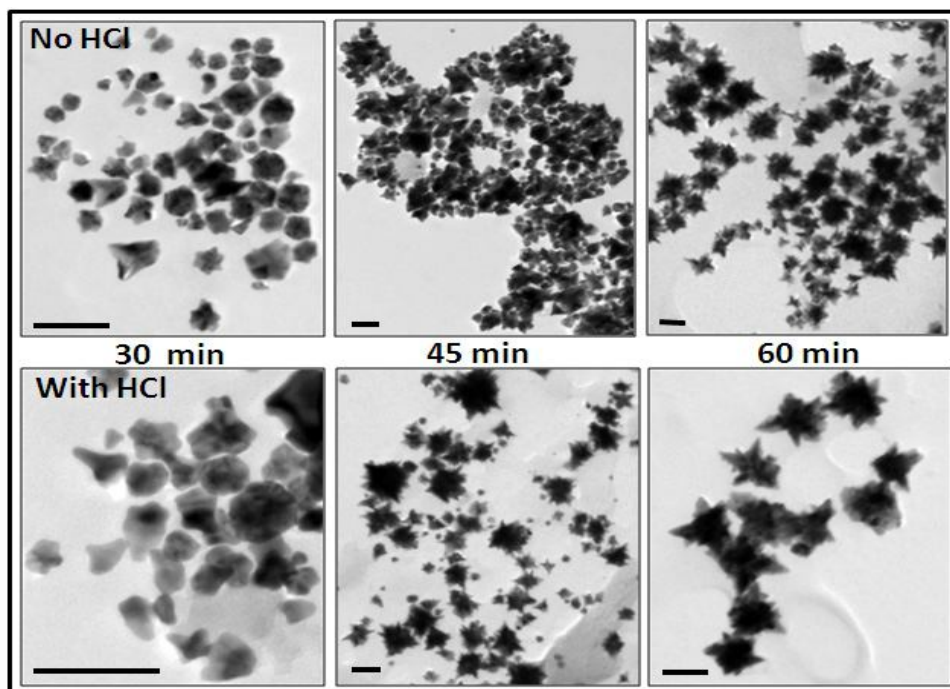
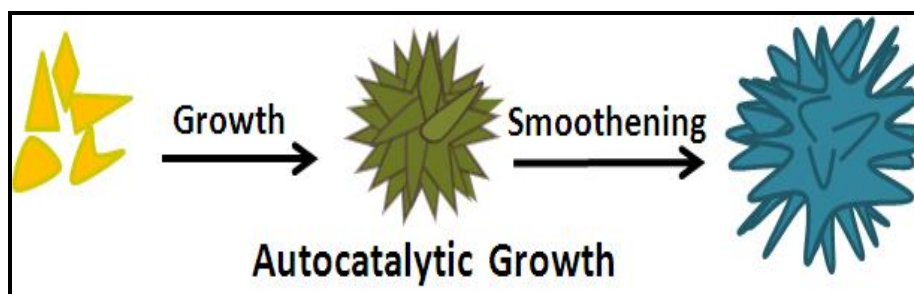


Figure-4.4: Low magnification TEM images (scale bar = 100 nm) of the Au nanostructures formed in the reaction mixture (DMF/HCl+PVP+HAuCl<sub>4</sub>) quenched in presence of excess acetone at different intervals of time, clearly illustrating the sequential growth of 3-D branched nanostructures.

Due to high concentration of PVP; at the growth stage selective ripening of these elongated structures bounded by {111} and {100} take place maintaining size/shape monodispersity which is possible only if growth (tips) occurs along [011] growth direction. Thereafter, suppressed smoothening of the agglomerates takes place (see scheme 4.2) by inter-particle ripening arbitrated by the surrounding interactively networked DMF-PVP complex, signaling the stabilization of the absorption peaks at 580 nm and 940 nm after 70 minutes of the reaction time (figure 4.3).

**Scheme-4.2:** Autocatalytic growth of Au nanostars from selective attachment and simultaneous smoothening of dynamically nucleated anisotropic gold seed particles



With optimal addition of HCl (up to 0.6 mM), the reaction essentially proceeds in a similar fashion, except for the delayed induction time (50 minutes), with absorption peaks around 590 and 905 nm (see figure 4.3b), not only standardize the kinetics, but also intuitively blue shifts the longitudinal SPR peak to 905 nm (previous seed mediated approach [245, 254] could only extend the longitudinal SPR to a maximum of 800 nm).

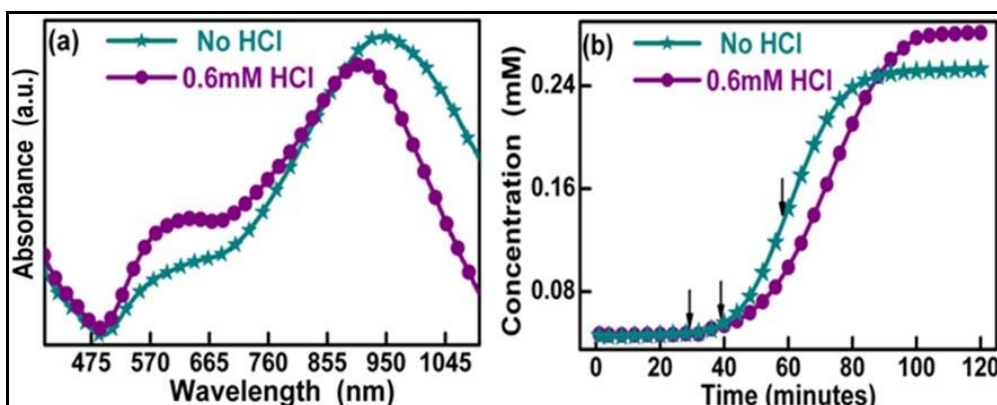


Figure-4.5: (a) Comparison of UV-Visible absorbance spectra of as prepared gold nanostars with (0.6 mM) and without HCl, illustrating monodispersity from the Gaussian nature of longitudinal SPR peaks: (b) Nucleation and growth curve for the formation of Au nanostars as derived from the size/shape independent  $Au^0$  concentration at 400 nm, with the arrow marks showing the time scale for quenching the reaction as shown in figure 4.4.

Figure 4.5a shows the UV-Vis spectra of as-prepared gold nanostars with(out) 0.6 mM HCl, indicating monodispersity in size/shape from the Gaussian nature of high wavelength SPR (as depicted from the TEM images (figure 4.2c) also). But with the presence of high polymer to metal ratio, *in situ* kinetic microscopic measurements would be extremely difficult under the present experimental conditions so as to understand the nucleation and growth of the mesostructural organization necessary for the formation of these complex 3-D oriented gold nanostars. Hence the temporal evolution curve (figure 4.5b) plotted for the isosbestic point at 400 nm (chapter 2, pp: 37) show that the reaction duly follows an autocatalytic course.

Further these formed gold nanostars remain stable for more than a year as well as pH and refractive index resistant as appropriately shown in figure 4.6.

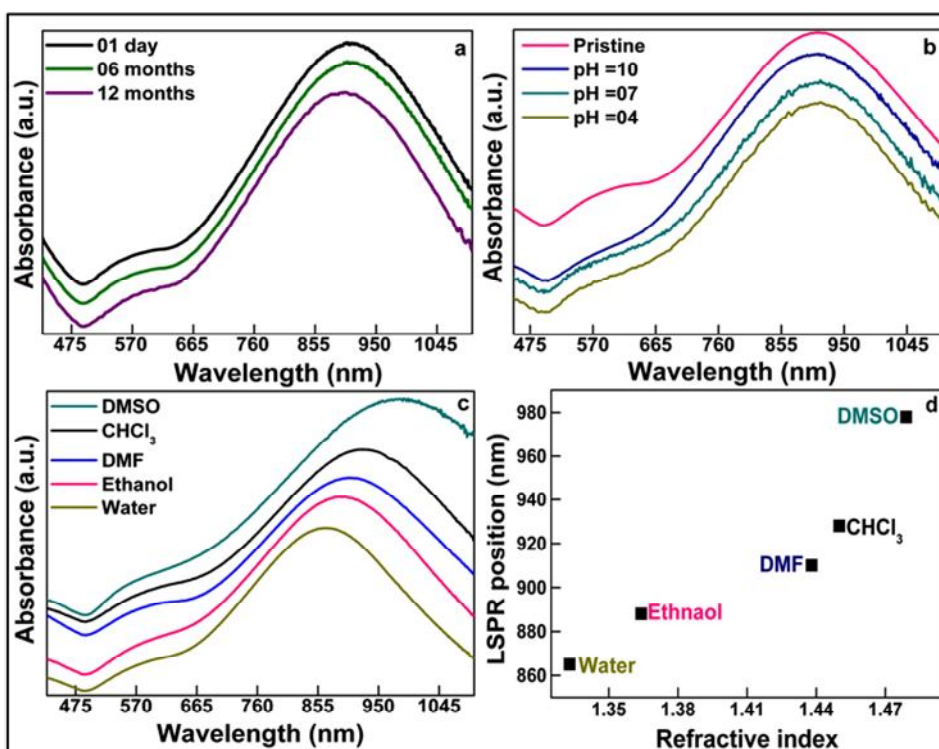


Figure-4.6: Optical absorption spectra showing the stability of as-formed gold nanostars (a) for more than one year under normal conditions, (b) under different pH values, (c) in different solvents and (d) the shifts in LSPR peak position with respect to refractive index of different solvents, the linear response of which demonstrates the robustness of Au nanostars visually showing the incremental dielectric effect.

#### 4.4.2 CL Spectroscopy and Imaging

The conventional optical methods such as UV–Vis spectroscopy have some limitations in determining the spatial distribution of LSPs in individual NPs and are consequently limited by large inhomogeneous broadening induced by the size and shape distribution of the ensemble giving an average signal of large LSP modes, even the sophisticated spectroscopic techniques, such as the dark field microscopy (DFM) probe the single metal nanoparticle as a whole entity and therefore cannot distinguish the rich individual/coupled features arising from the different parts of highly asymmetric nanostructures such as the nanostars. Although, our literature survey finds enough evidence for the plasmon hybridization picture in Archimedian type nanostructures [229, 264, 265]; the only direct local measurement of the plasmon modes of complex gold nanostars has been reported through STEM-EELS by Kociak et. al. [266], albeit with a severe constraint that the thicker core of the gold nanostars imposes serious hurdle in the continual mapping of point-to-point local density of optical states, thereby losing out significant plasmonic information.

Therefore, CL spectroscopy (based on scanning electron microscopy) offer the opportunity to perform such measurements (local density of optical states) with nanometric spatial resolution and excellent alternative to determine local density of states of plasmonic nanostructures over optical microscopy. Hence, for the first time CL spectroscopy in conjunction with optical absorption studies are effectively utilized for the analysis of the plasmonic eigenstates/modes of complex shaped gold nanostars drop-coated on a silicon substrate. Experimental details of the same are given in chapter 2.

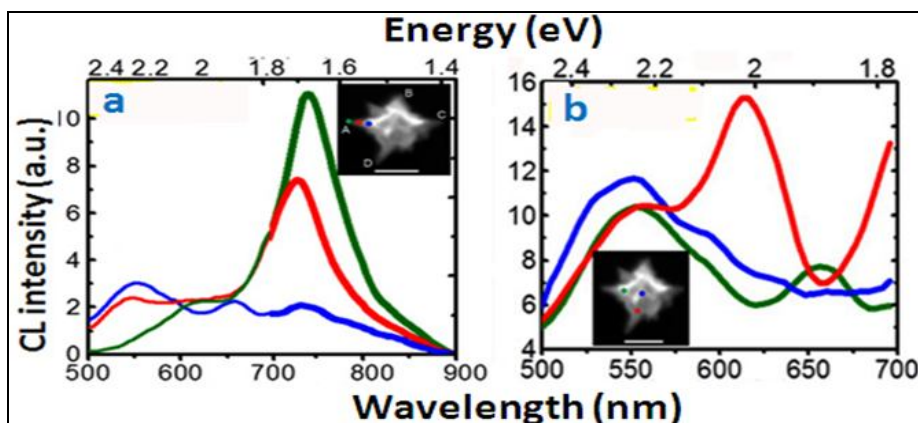


Figure-4.7: Experimental CL spectra of the Au nanostars for different e beam position (a) on a single spike (b) on a core region as marked by colored circles. The spectra were acquired in two wavelength ranges separately as 500–700 nm (thin line) and 700–900 nm (bold line) and then merged with proper normalization. Associated SEM image is shown as inset (scale bar=100 nm).

Figure 4.7(a, b) presents the experimental CL spectra obtained in the wavelength range from 500 nm to 900 nm by the perpendicular incident electron beam focused on different locations of a single spike and the core region of the gold nanostars respectively (marked as colored circles in the inset of figure 4.7(a, b)). The CL spectra clearly depict the strong dependence of peak intensity upon the point of impact of the electron beam even over a single spike.

One of the observed peaks from CL measurements is the low energy peak at around 750 nm (corresponding to the apex of tips), while the other high energy peak is located between 550 and 600 nm (figure 4.7a). Additionally, another noteworthy resonance peak appears around 660 nm when the gold nanostar was excited at the base of the tip (blue curve in figure 4.7a). Interestingly, as we go from the apex region of the tip towards the core region, the low energy peak (750 nm) intensity decreases and concurrently the high energy peak (550 nm) intensity increase. To get a better understanding of the effect of the core of the nanostar on the CL response, we also acquired CL spectra from different e-beam positions in the core region (figure 4.7b). The CL spectra, corresponding to all the three impact points of the core (inset), exhibit a peak at 550 nm (representative of the central portion of the core region) along with two more resonance peaks, each at 620 and 660 nm, for the e-beam incident near the periphery of the core region, i.e. at the base of the tip, intuitively in agreement with our earlier notion of criss-crossed tips ensuring a non-uniform dynamic core structure. To clearly understand this intriguing spatial/spectral distribution of the photon emission, we

acquired monochromatic CL maps at different peak wavelengths along with panchromatic CL image, while raster scanning the e-beam over the entire multi-branched Au nanostar particle (figure 4.8).

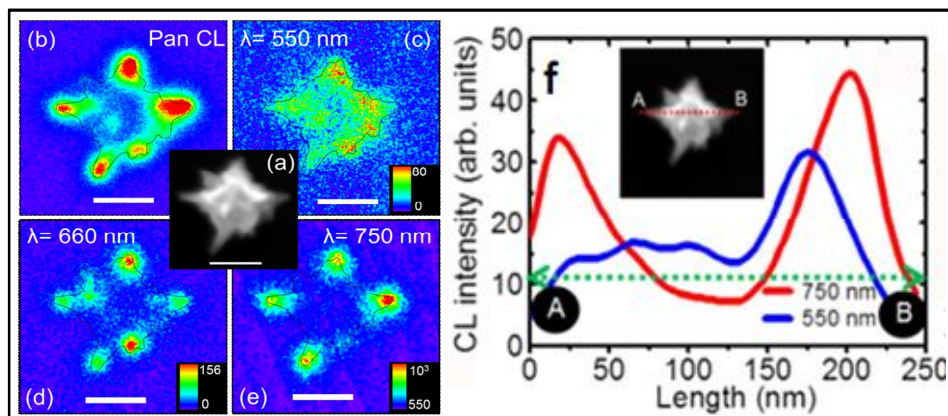


Figure-4.8: Experimental CL imaging on the isolated Au nanostar recorded at different wavelength with (a) SEM image (b) Pan CL image (c), (d), (e) monochromatic CL emission maps recorded at wavelengths 550 nm, 660 nm and 750 nm. Scale bars correspond to 100 nm. (f) Monochromatic CL profile along the AC path with a 2.5 nm step at 550 nm and 750 nm.

The monochromatic CL images at their respective specified wavelengths show brighter pixels, only when the evanescent field associated with the electron beam for a particular impact position on the nanoparticle surface strongly excites either of its resonant plasmonic eigenmodes, such as that at wavelengths 550 nm, 660 nm and 750 nm shown separately, which are the designated localized surface plasmon (LSP) modes for our gold nanostars.

The monochromatic CL image obtained at 550 nm wavelength shows luminescent intensity when the electron beam scans over the core region (figure 4.8c); whereas the strong light emission occurs at 660 nm (figure 4.8d) and 750 nm (figure 4.8e) when the e-beam scans over the peripheral region of spherical core and tip apex. The 550 nm resonant peak is well reported in earlier studies as well [246, 264, 266], universally agreed as the transverse mode of the sphere like core region. When going towards higher wavelengths (750 nm), the luminescence enhancement is shifted gradually towards the tip region and is strongly confined to the far ends of the longer tips (figure 4.8e). The LSPR at ~660 nm gives rise to photon emission coming from the region where the tip meets the periphery of core or at shank (below the apex) of the longer tip (figures 4.7 and 4.8).

We will henceforth designate the resonant peak at 550 nm as the core LSP mode and the 750 nm peaks as the tip LSP mode. The tip LSPR position and intensities depend on the e-beam excitation position on the tip region as well as on the tip dimensions. To determine the spatial extent of the tip and core modes, we acquired monochromatic CL line profile at 750 nm and at 550 nm by placing the 30 keV electron beam at 100 points along the AC path (2.5 nm step, as shown in figure 4.8f). Strong luminescence occurs near the two tip ends at 750 nm, implying strong photon confinement of the tip mode to the apex region of the tips (points A and B). Moreover, the CL spectroscopic and imaging data of figures 4.7 and 4.8 reveal that the intensity level of the tip mode is more than five times higher than that of the core mode with the associated LSPR being narrower than that of the core mode. The line scan at 550 nm gives a non-uniform variation of CL intensity pattern/asymmetric distribution of LDOS within the single Au nanostar induced by the strong intra-particle plasmonic coupling; directly related to the irregular shape of the core region, due to the presence of the numerous asymmetrical non-planar tips oriented in random direction.

And this is the foremost reason for the tilted transverse SPR peaks at around 580/590 nm in comparison with that of gold nanorods [267] or any other branched/multipod nanostructures [254, 258-260, 268] visually signifying its micro-engineered floral core design drastically different from that of routinely faceted nanostructures, vastly relating to the dual role of PVP, both as a reductant [84, 172-175] and crystal-habit modifier [110-112, 162-169], simultaneously promoting reduction as well as stabilization onto specific crystal faces while preventing other facets, leading to a plethora of exotic nanostructures robustly depending on the respective reaction conditions.

#### 4.5 EFFECTIVE ROLE OF HCl

Results obtained here employ that HCl plays a significant role in obtaining monodisperse Au nanostars, where proton ( $H^+$ ) is preferentially solvated by DMF [269, 270] and the chloride ions ( $Cl^-$ ) maintain the equilibrium concentration of  $AuCl_4^-$  ions, thus decreasing the net nucleation rate. In terms of separating the roles played by  $H^+$  and  $Cl^-$ , we replace HCl with equimolar amount of  $HNO_3$  and KCl (figure 4.9). However, with  $HNO_3$ , owing to the absence of  $Cl^-$  ions, uneven nucleation of seed particles dominates; while with KCl, only weak solvation by DMF takes place due to the electronegative character of  $K^+$  ions, thereby leading to polydispersity.

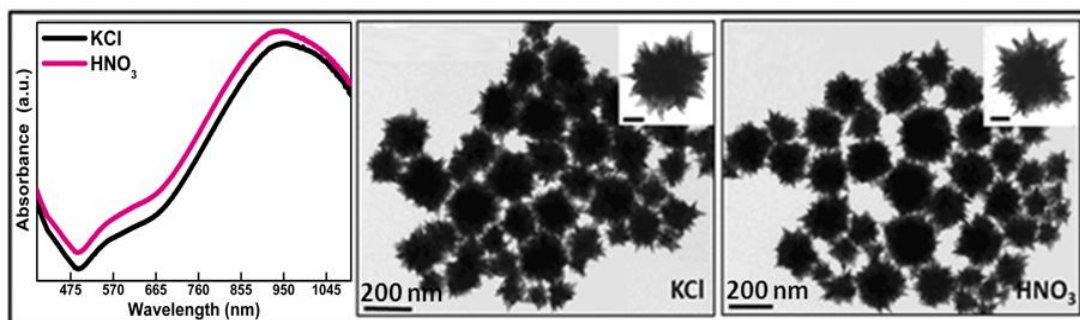


Figure-4.9: UV-Vis spectra and TEM images of Au nanostars with same equimolar amounts of KCl and  $HNO_3$ . HMTEM image of single Au nanostars are shown in insets (at 50 nm scale bar).

These empirical observations suggest that HCl is an excellent mediator candidate for the synthesis of monodisperse Au nanostars where DMF solvent molecules with its characteristic large dipole moment and the excess vinyl pyrrolidone monomers with its strong crystal habit modifying ability [83, 163, 164, 167, 215, 223], both are coordinating reagents to the sequentially formed Au nanocrystals, thereby maintaining the necessary balance between nucleation and growth, which is the key towards the formation of nanocrystals with a high degree size/shape control. In summary, homogeneous nucleation leading to monodisperse size/shaped nanocrystals is often characterized by sufficiently high nucleation but reduced/controlled growth rate.

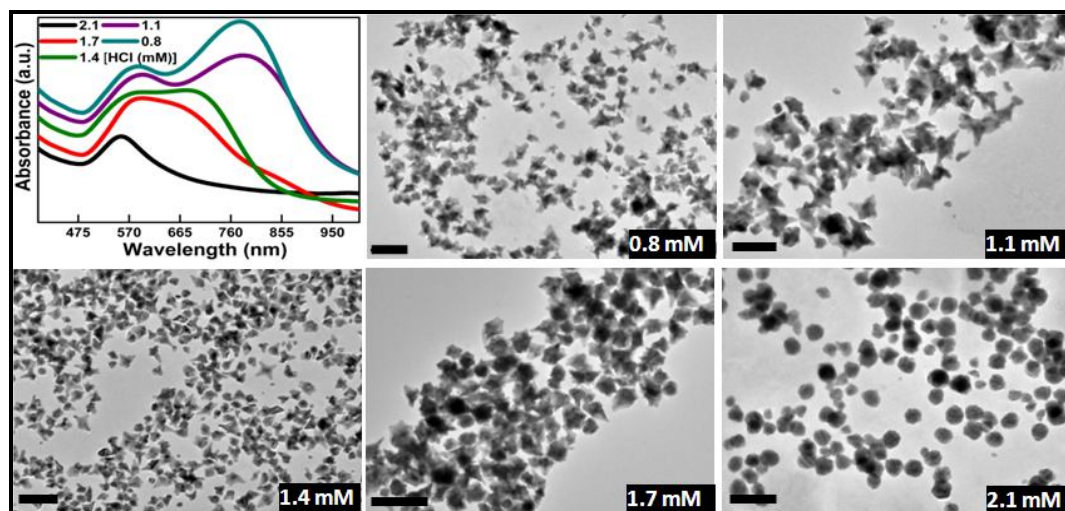


Figure-4.10: TEM images of gold nanostructures (scale bar=100 nm) and their corresponding optical spectra obtained with increasing HCl concentration as mentioned

On the basis of present experimental results, it is essentially concluded that 0.6 mM HCl represents an ideal concentration for the synthesis of monodisperse gold nanostars. With increasing addition of HCl, protonated DMF along with conformational changes in PVP as well as the conproportionation of  $AuCl_4^-$  ions fundamentally dictates the reaction mixture thereby delaying the nucleation to a large extent, further leading to step-by-step dissociation of star like Au NPs (figure 4.10), condensing towards the formation of quasi-spherical gold nanoparticles, strongly suggesting that excess HCl dramatically modifies the course of the reaction steering towards a more conventional thermodynamic regime.

It is plausible that the rapid dynamic nucleation of anisotropic Au seed particles, followed by controlled growth and stabilization (see figure 4.4), which sequentially identifies the growth of branched NPs as a result of selective attachment and simultaneous ripening strongly mediated by the excess crystal habit modifier PVP [83, 164, 215], which could further be quantified from the kinetic FTIR studies as discussed below.

#### 4.6 NUCLEATION AND GROWTH MECHANISM

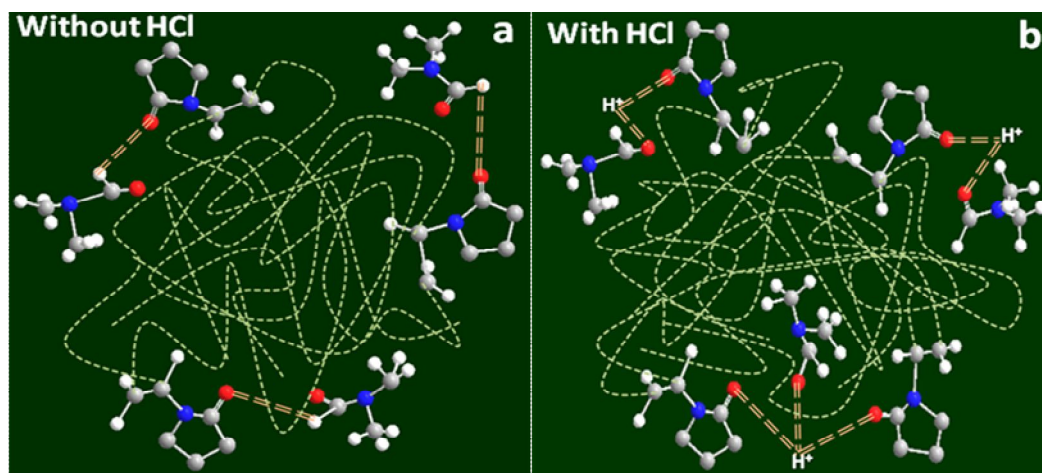
After clearly identifying the macroscopic kinetic/thermodynamic regimes (figure 4.6), we now focus our attention exclusively on the molecular interactions responsible for addressing the morphology evolution of the as-formed nanostructures with or without HCl addition. To better understand and elucidate a plausible reaction mechanism, the following aspects have been taken into careful consideration:

- Polymer (PVP) and solvent (DMF/HCl) interaction
- Interaction of PVP-DMF/HCl complex with  $\text{AuCl}_4^-$  ions
- Kinetic study on the size/shape evolution of Au nanostars

##### 4.5.1 FTIR Spectroscopy

With reference to discussion in chapter 3 (pp: 65-69) and in collusion with the earlier reports [217, 235], hydrophilic as well as dipole-dipole interaction between DMF and PVP molecules instantaneously enables the polar solvent DMF molecules as ‘cross-linking points’ between the entangled inter/intra-molecular PVP chains (higher the PVP concentration, higher is the entanglement) [235, 271], leading to the formation of a complex solvophobic interacting network (see scheme 4.3a). Moreover, controlled addition of HCl (0.6 mM) weakens the hydrogen bonding between PVP and DMF, thus slightly modifying their dipole-dipole interaction, thereby promoting higher entangled state (see scheme 4.3b).

**Scheme-4.3:** Entangled state of PVP as a result of H-bonding as well as dipole-dipole interaction in (a) DMF, (b) DMF-HCl



Convinced with their subtle nature, we tried to explain the effective role of solvent DMF (with(out) HCl) in binding/complexing with PVP, thereby dictating the reaction kinetics with different metal ions, transforming them into size/shape controlled metal nanostructures, through the scholarly data analysis of traditional room temperature kinetic FTIR spectra.

From the literature survey, it has been clearly understood that DMF acts as a reactive solvent medium only under extreme conditions such as temperature, microwave/ultrasonic irradiation etc [111, 271-275]. Under the present room temperature reaction conditions, DMF thus largely remains as a solvent, but cohesive with PVP (higher the PVP concentration, stronger the cohesiveness), impulsively quantifying the PVP-DMF complexes, as the major driving factor in influencing the effective formation of ensemble of different size/shaped gold nanostructures. In this regard, to quantify exclusively the individual/combined effects of PVP and DMF, the predominant solvent DMF background in all our FTIR spectra has been removed by way of baseline correction with free DMF (see the detailed discussion in chapter 2, pp: 42), which greatly simplifies our problem deemed with excellent agreement from the individual deconvoluted spectra as well (see appendix figures A4.1/4.2 in appendix), thereby validating the novelty of our approach. This free DMF

baseline corrected PVP-DMF complex not only reveals meticulously the fractionation of bound ( $1624\text{ cm}^{-1}$ ) and unbound ( $1690\text{ cm}^{-1}$ ) carbonyl(C=O) groups (figure 4.11), but also enumerates substantial changes in the C-N ( $1094$  and  $1068\text{ cm}^{-1}$ ) as well as O=C-N ( $661\text{ cm}^{-1}$ ) stretching as detailed in figure 4.11 and table 4.1.

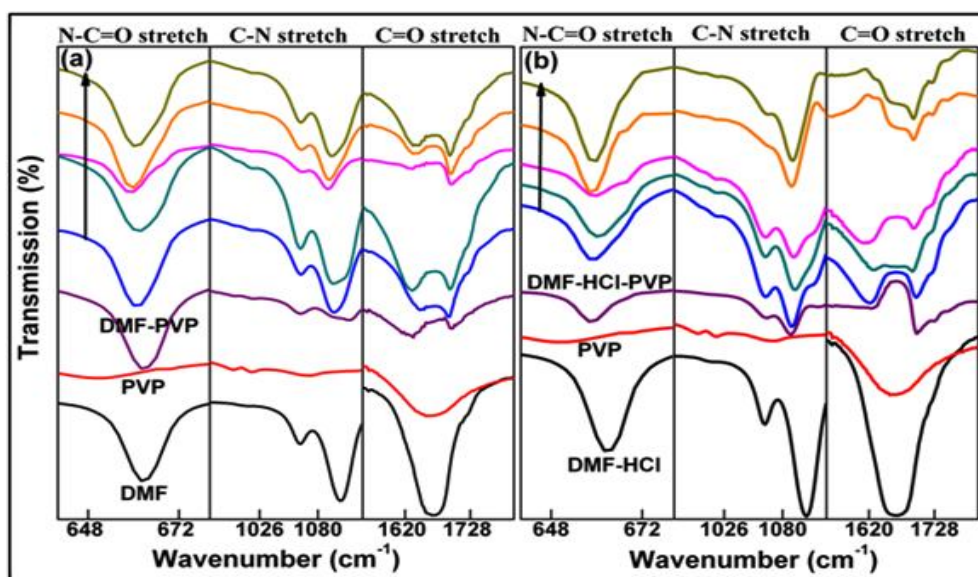


Figure-4.11: Vibrational peak evolution with time (as indicated by the arrow mark) in the selected wavenumber range for the nucleation/growth of Au nanostars with (a) DMF-PVP-HAuCl<sub>4</sub> and (b) DMF/HCl-PVP-HAuCl<sub>4</sub> system, demonstrating substantial contributions from carbonyl C=O ( $1664\text{ cm}^{-1}$ ) and nitrogen coupled bonds at  $1071$  and  $661\text{ cm}^{-1}$ , respectively. For comparison, individual spectra for DMF/HCl, PVP, and DMF/HCl-PVP are also given.

Figure 4.11 shows the kinetic FTIR spectra (sliced from the full range spectra as shown in figure A4.1) right from nucleation to growth/stabilization stage in comparison with DMF and PVP spectra, demonstrating the kinetic changes in its three major constituents C=O, C-N and N-C=O stretch, so as to discuss with clarity the chronological molecular evolution of the gold nanostructures.

**Table-4.1: PVP, DMF, PVP-DMF complex and Baseline corrected PVP-DMF complex IR ( $\text{cm}^{-1}$ ) and their corresponding peak assignments.**

PVP IR	DMF IR	*Assignments	DMF-PVP IR observed	DMF-PVP IR after Baseline correction
3432	3447	OH stretch	3498	3234, 3580
2955	-----	Asymmetric ring (CH <sub>2</sub> ) stretch	-----	-----
-----	2956	Asymmetric (CH <sub>3</sub> ) stretch	2932	2925
2875	2857	Symmetric (CH) stretch	2877	2872
1663	1664	Symmetric (C=O) stretch	1664	1695,1628
1495	1495	Symmetric (CN) stretch	1495	1495
1463,1423, 1439	-----	Ring (CH <sub>2</sub> ) scissor + Ring (C-N) stretch + (CH) bending	1463	1445
-----	1439	Asymmetric (CH <sub>3</sub> ) bending	1440	1435
-----	1411	Bending (N-CH <sub>3</sub> )	1413	1425
1374	-----	CH bend + Ring (CH <sub>2</sub> ) wag + (NC) stretch	-----	-----
-----	1388	Symmetric (CH <sub>3</sub> ) bending	1388	1383
1290	-----	Ring (CH <sub>2</sub> ) wag + (CN) Stretch	-----	-----
-----	1255	Asymmetric (C <sub>2</sub> N) stretch	1257	1280
1229	-----	CH <sub>2</sub> twist + NC Stretch	-----	-----
1170	-----	Weak Ring CH <sub>2</sub> twist	-----	-----

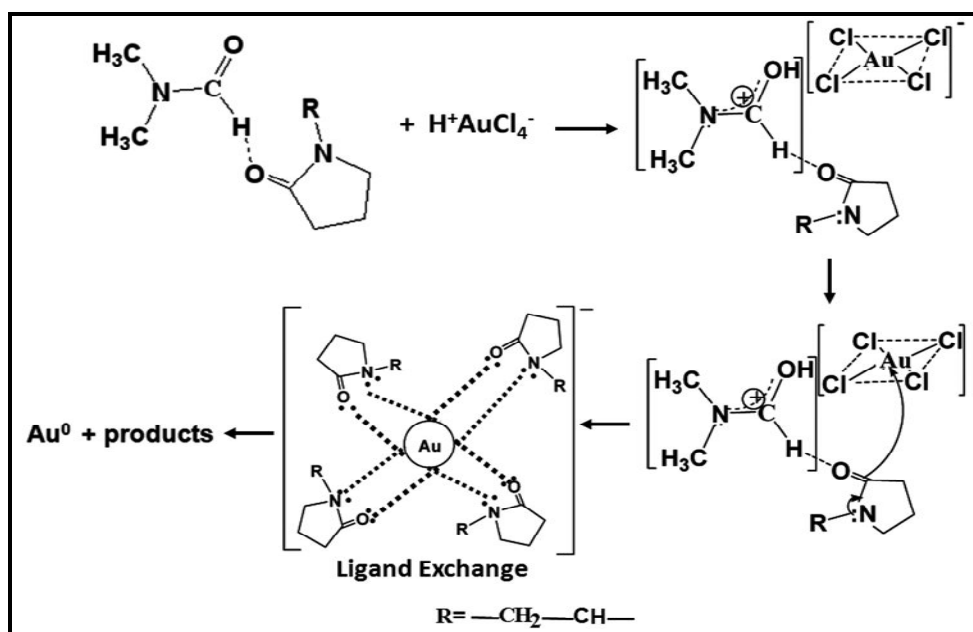
1071	-----	(CN) stretch	-----	-----
-----	1096,1064	Rocking (CH <sub>3</sub> )	1098,1064	1086,1063
934	-----	(C-C) ring breathing	-----	-----
846	-----	C-C ring	-----	-----
736	-----	(C-C) chain	-----	-----
651	-----	(N-C=O) bend	-----	-----
-----	661	Bending (CO) + asymmetric (NC) stretch	662	659

\* (Peak assignments are taken from the references [163, 165, 189, 276] for PVP and [277, 278] for DMF)

This is supported with the general fact that, in PVP, the carbonyl interaction dominates (as steric hindrance weakens the amine group interaction) [215]; while in DMF (a small molecule), the amide group interaction predominates [273], thereby distinctly identifying the significance of local PVP-DMF molecular structure in governing the overall physico-chemical aspects of this complex fluid. Essentially, similar arguments are valid for the 0.6 mM HCl modified PVP-DMF complex, except that the nucleophilicity of PVP decreases.

When trace amount of aqueous HAuCl<sub>4</sub> is added to this concentrated PVP in DMF solution, an unstable metal complex, such as PVP-DMF<sup>+</sup>-AuCl<sub>4</sub><sup>-</sup> forms through coordination interaction (see scheme 4.4).

**Scheme-4.4:** Reaction between DMF-PVP and HAuCl<sub>4</sub> leading to the formation of Au Nanostars through Ligand Exchange Mechanism



This is the foremost reason for the diverse reaction mechanism of other cationic metal salts with PVP [166, 174, 279], as compared to gold or platinum, mostly existing as anions in their salts, which in turn is responsible for the formation of uncommon NPs in a straightforward manner [251, 253, 255, 280]. Due to the dynamic instability of this coordinated metal complex in solution, both the (un)bound (C=O) as well as polar (C-N) groups in the pyrrolidone ring of intra/inter-chain PVP initiates the complexation of their lone pair of electrons to the metal centered square planar AuCl<sub>4</sub><sup>-</sup> ion [243, 281]; thereby ligand substitution readily occurs (see scheme 4.4), forming intermediate [AuCl<sub>3</sub>(PVP)] complexes, which sequentially disproportionates to yield Au<sup>0</sup> species, as depicted by the corresponding correlated changes in the bound C=O peak (starting from 1624 cm<sup>-1</sup> for the PVP-DMF complex, shifts to 1645 cm<sup>-1</sup> with HAuCl<sub>4</sub> addition and then stabilizes at 1636 cm<sup>-1</sup> following successive ligand replacement), completely in agreement with the nucleation/growth time derived from optical absorption measurements (figures 4.3 and 4.5). While the O=C-N and C-N stretching peaks, sensitive to the formation of metal complexes [114, 217]; also shifts slightly but definitely owing to the entangled state, overpowering the steric hindrance effect of the monomer chains

confining the amine group of the PVP polymer (figure 4.11). Besides, this is attributed to the fact that at very high molar polymer to metal ratios, not only the carbonyl groups, but also inter/intra chain amine groups predominantly participates in the charge transfer interaction illustrated through visible changes in the kinetic shape/intensity of carbonyl and amide groups as shown in figure 4.11, which is being reported for the first time to the best of our knowledge. In the same manner, for 0.6 mM HCl addition to DMF, the above arguments holds true, except for the increase in induction time, as vindicated by the action of both proton and chloride ions. This simple but effective ligand exchange mechanism is schematically represented as shown in scheme 4.4.

The *in situ* formed small Au seeds compete with PVP molecules for DMF, inducing a slight desolvation by destroying the partial network of PVP molecules. These two synergetic effects, desolvation and coordination interaction, simultaneously influence the state of aggregation of the PVP molecules in DMF [217, 235], thus allowing the stabilizer polymer chemisorbed on the surface of the Au nuclei/seeds in an intricate manner, reducing their growth rate (figure 4.11) and preventing the flocculation of the Au organosols by steric stabilization. By virtue, this very idea of desolvation (common to HCl addition as well) necessitates the compactness of metal-polymer complexes and in turn refutes unwarranted claims of any generalized oxidation products (as shown by the absence of any new vibrational bands in figure 4.11), which should otherwise be reaction centric.

Specifically, this strong chemisorption owing to high monomer to metal ratio ensures that the pyrrolidone rings of PVP binds in a side-on bridging fashion rather than a single coordination with the metal ion/nanoparticle surface, as envisaged from the classical coordination chemistry model for metal nanocrystals capped by surface ligands [166, 215, 243], further analyzed with XPS which details the differentiation in chemisorptions of PVP ligand to gold nanostars resulting in monodispersity with HCl.

#### 4.5.2 XPS Studies

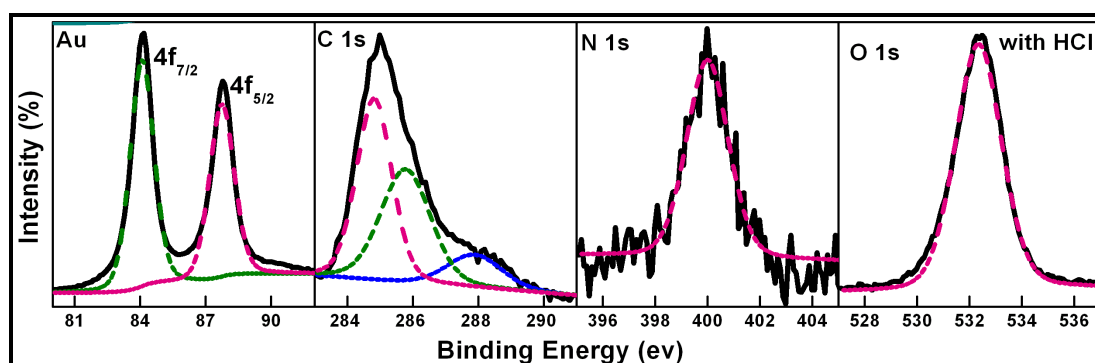


Figure-4.12: XPS spectra of PVP-capped Au nanostars synthesized with HCl; illustrating the corresponding C 1s, N 1s and O 1s region (solid black lines) along with their deconvoluted peaks (colored dashed lines).

The detailed XPS discussion of on PVP coated Au nanostars without HCl is given in chapter 3 (pp: 76-79), which shows that the electron density unequivocally hovers around the N-C=O region of the pyrrolidone ring of PVP through the so-called conjugation effect, confirming the impartial charge transfer from both the oxygen and nitrogen atom in the pyrrolidone ring to the Au nanostars surface. The Au-polymer surface seems to be one of the sensitive chemical parameter responsible for the size/shape control.

**Table-4.2: XPS binding energy peak positions obtained from figure 4.12**

Peak	Without HCl	With HCl
<i>Au4f<sub>7/2</sub></i>	<b>84.06</b>	<b>84.08</b>
<i>Au4f<sub>5/2</sub></i>	<b>87.75</b>	<b>87.76</b>
<i>CI<sub>s</sub> (C-C)</i>	<b>284.93(43)</b>	<b>284.82(47)</b>
<i>CI<sub>s</sub> (C-N)</i>	<b>285.94 (42)</b>	<b>285.78(40)</b>
<i>CI<sub>s</sub> (N-C=O)</i>	<b>287.98 (15)</b>	<b>287.89(13)</b>
<i>NI<sub>s</sub></i>	<b>399.98</b>	<b>399.99</b>
<i>OI<sub>s</sub></i>	<b>532.52</b>	<b>532.35</b>

Comparing the XPS data of gold nanostars formed with and without HCl (figure 4.12), it is observed that there are no appreciable BE changes, except for the minimal shift in O=C and C-N peaks (see table 4.2). The smaller chemical shift in the O=C BE peak attributes to the in comprehensive nucleation and selective aggregation of reduced Au<sup>0</sup> species to form monodisperse Au nanostars. The relative strength of carbonyl interaction in both cases changes subtly along with contribution from their carbon counterparts, as vividly supported by the slight decrease in C-N binding energy.

Moreover, in comparison with bulk Au atoms (84.0 eV for Au 4f<sub>7/2</sub> and 87.7 eV for Au 4f<sub>5/2</sub>), the BE of Au 4f<sub>7/2</sub> core level peak lies around 84.05 eV and that of Au 4f<sub>5/2</sub> core level peak arises at 87.75 eV in both the cases (see figure 4.12 and table 4.2), implying that only appropriate balanced charge transfer process by the convoluted electron-donating ability of N and O counterpart of PVP to metal ions would lead to the synthesis of monodisperse gold nanostars with reference to the addition of ample amount of HCl to DMF, thereby initiating a whole new perspective in the synthesis of gold nanostars.

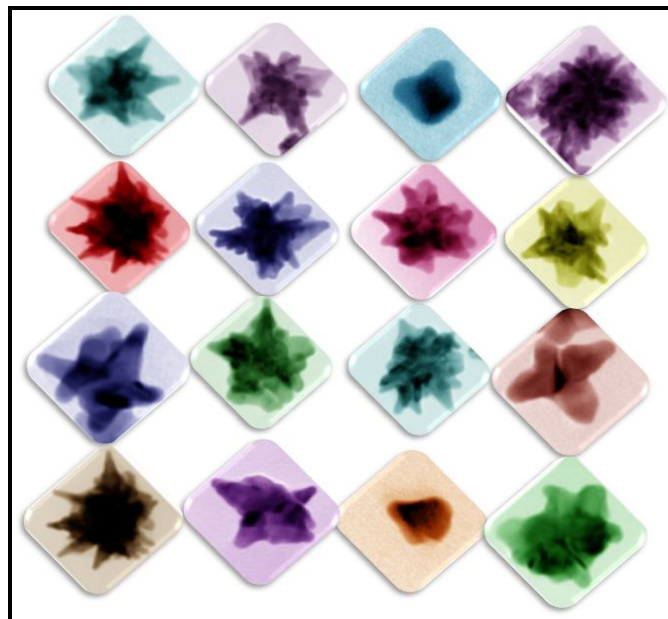
Specifically, the regularly irregular morphology of these real gold nanostar systems defy the conventional dimensionality and the inherent coupling of the finer plasmon rich structure with the far-field radiation as seen in CL illustrates beautifully the direct visualization of the nature of plasmons as well as their intriguing hybridization mechanism, further providing useful insights in understanding the local density of plasmonic eigenstates both in spatial as well as spectral domain with high clarity particularly in nanoparticles with higher symmetry. CL spectra efficiently evaluates the individual signature of both bonding and anti-bonding hybridized plasmons in association with substrate polarization, resulting in anti-nodal enhancements in the electric field intensity; the peak at 660 nm signifies the same, which is in sync with the present experimental as well as theoretical observation, further corroborating the intrinsic nanoantenna mechanism associated with such kind of sharp edged, multi-branched noble metal nanostructures and imposing a challenging task for modelling/simulating their integral optical features, which is explained beautifully using cumulative FDTD simulations by Pabitra das et al. [249] incorporating the significant contribution from the substrate as well.

Summarily, the FDTD results reiterate the fact that the theoretically simulated spectra were dominated by a LSPR at ~750 nm in accordance with the experimental results, further illustrating the at most insensitiveness of the position of the tip modes to the presence of the substrate with only a three-fold decrease in their respective intensity. Drastic spectral changes, if any, induced by the position of the tips with respect to the substrate were critical for surface enhanced spectroscopies and sensing applications. Also, the FDTD simulation results demonstrate that the long tips in multi-branched nanostars can serve as efficient emitters at optical frequencies that can be precisely tuned by engineering the tip-substrate separation. However, to the best of our knowledge, this aspect had not been discussed so far in literature for nanoparticles exhibiting spikes/tips.

In a nutshell, the basic knowledge of the PVP-DMF-HCl complexation mechanism in which DMF molecules acting as cross-linking points or bridges among the entangled PVP invariably facilitates the deep insight in understanding kinetic nucleation and growth to obtain monodisperse gold nanostars. TEM/SEM images reveal the prominent flower-like morphology with crisscrossed (non)planar single crystalline spike/tips branching out from the complex core. The kinetic optical absorption and TEM study illustrate an autocatalytic type reaction, where selective attachment and simultaneous smoothing of dynamically nucleated anisotropic gold seed particles occur. Based on our FTIR measurements, a general ligand exchange mechanism has been proposed for the first time to the best of our knowledge. The XPS studies on metal nanoparticles reveal PVP forms strong coordinating bonds via intra/inter-chain amine-N and carbonyl-O donors, which bridge adjacent metal atoms on the nanoparticle surface. Au nanostars formed with HCl experiences ideal balanced electron density distribution exercised via both nitrogen and oxygen in the N-C=O component of the pyrrolidone ring of PVP, resulting not only the intricate changes in the N 1s and O 1s core level spectra, but also leads to size/shape monodisperse Au nanostars.

# Chapter-5

## Structure-Correlated Plasmon Tuning Mechanism Of Gold Nanostars



Controlled tuning of the plasmonic eigenmodes of gold nanostars in a sequential manner from visible to the near IR region with morphology correlation were accomplished with exceptional level of wavelength agility by independently introducing the NaOH or co-solvent in the precursor reaction mixture and are utilized for specific applications such as the SERS.

### 5.1 THEME OF THE CHAPTER

The fascinating 3-D complex morphology of Au nanostars, exhibit intense localized EM fields at their tips/edges, hence have attracted significant attention and utilization in SERS/bio-sensing applications [247, 252, 260, 263, 280, 282-285] and responsible for high reactivity [283, 285-288]. The tuning/reshaping of these Au nanostars would be highly advantageous owing to the change in their overall characteristic physico-chemical properties with respect to specific applications such as SERS, high density data storage, light up-conversion phenomena or in nanoantennas, as the size of core plays critical role in focalization of electric field at the tips/edges [68, 247, 263, 280, 249, 284, 288-290].

Tuning the LSPR (from 800 to 650 nm) of PVP capped gold nanostars obtained via seed mediated synthesis were already achieved in controlled fashion by varying the size/concentration of the seed particles with respect to the precursor metal salt concentration in the DMF growth solution, which induces changes in the core size, the number, length and broadening of the branches [245, 254]. These processes require extra optimization of desired PVP concentration or complication of synthesizing several seed batches and recalculating the reagent concentration to yield desired star size [245, 254].

Hence to simplify this two step tuning process of Au nanostars, we tweaked our novel single step, seedless/templateless synthesis procedure for the preparation of Au nanostars by simple external addition of a standard base like NaOH to the DMF-PVP mixture (detailed in section A) or using 2-propanol as a co-solvent with DMF (see section B), so as to gradually tune/reshape the formation of Au NPs, which can be directly utilized for exciting plasmonic applications.

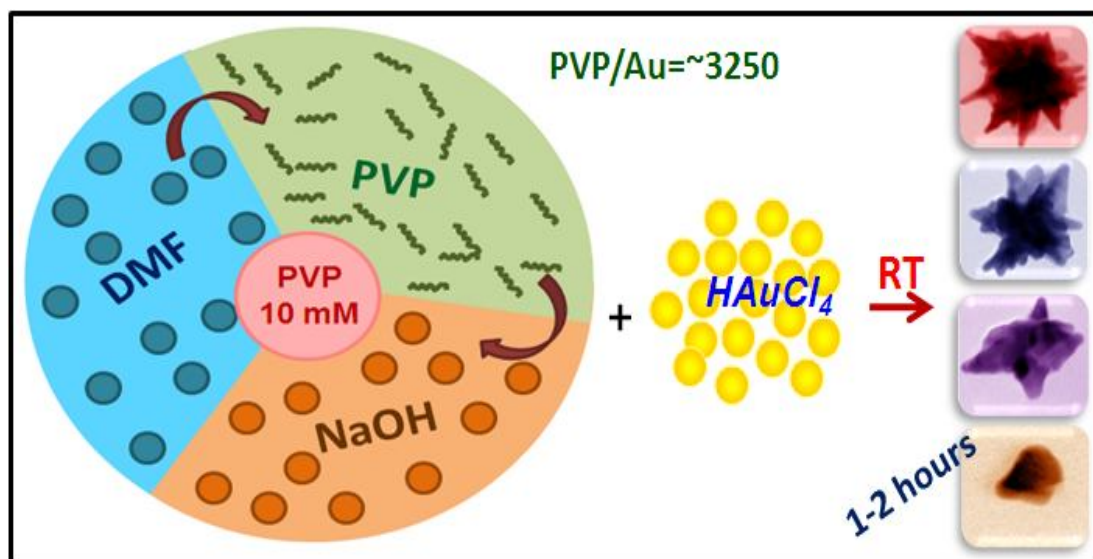
### SECTION – A

This section of present chapter deals with the effect of NaOH on the precursor mixture in order to get wide range of plasmonic bands. Through various characterization techniques, gradual tuning in size/shape and number of sharp tips/edges of the gold nanostars is demonstrated in detail.

### 5.2 SYNTHESIS PROTOCOL

In a typical synthesis,  $0.27 \text{ mol/m}^3$  aqueous solution of gold(III) chloride trihydrate ( $\text{HAuCl}_4 \cdot 3\text{H}_2\text{O}$ ) was mixed with  $10 \text{ mol/m}^3$  PVP solution in DMF respectively in order to obtain gold nanostars. The influence of NaOH is studied by adding it into DMF-PVP complex in different concentration (as mentioned in text) before the addition of metal precursor (see scheme 5.1).

**Scheme-5.1:** Illustrating the single step, seedless/templateless room temperature tuning procedure for Au nanostars using NaOH. Different concentration of NaOH is added to DMF-PVP mixture followed by metal ions keeping PVP to metal ions ratio  $\sim 3250$ .



### 5.3 RESULTS AND DISCUSSION

Detailed characteristic optical properties of our parent gold nanostars were extensively discussed in chapter 4 (pp: 87-96), which contains LSPR modes corresponding to electric field localization at the central core around 550 nm as well as at the tips around at 900 nm along with anti-bonding plasmon band arising due to hybridization of tips and the virtual core. For the last two decades, efforts have been focused on coinage metal substrates due to localization of their SPR bands in the visible and near IR regions and the common use of lasers in these regions in typical Raman spectrometers. Tuning their optical properties through precise change in morphology seems elusive, nevertheless, could as well be utilized in better way for specific applications such as SERS [247, 260, 263, 280, 282, 284]. Thus, by tuning the wavelength of the LSPR, SERS enhancements can be maximized utilizing different available excitation wavelengths.

#### 5.3.1 Optical and Structural Effects

DMF-PVP complex brought about significant changes in the peak position of tip mode plasmons (initially occurring around 910 nm, when no NaOH is added), which concurrently blue shifts to 600 nm as shown in figure 5.1a, illustrating the simple fact that changing the ‘apparent solution’ pH with NaOH gradually and significantly affect the size/shape and number of sharp tips/edges of the parent gold nanostars with controlled precision (can be seen from TEM images as shown in figure 5.2).

With low NaOH concentration, the tips are sharper (lesser the aperture angle, higher number density; see figures 5.2 and 5.3) leading to complex hyper-branched gold nanostructures, while the tips become broader (higher the aperture angle, lesser their number density; see figures 5.2 and 5.3) at higher NaOH concentration, resulting in multipod like gold nanostructures. With further increase in NaOH concentration (15 mM), both localized SPR bands seem to merge together resembling the optical spectra as well as the corresponding morphology of Au quasi-spheroids (figures 5.1 and 5.2).

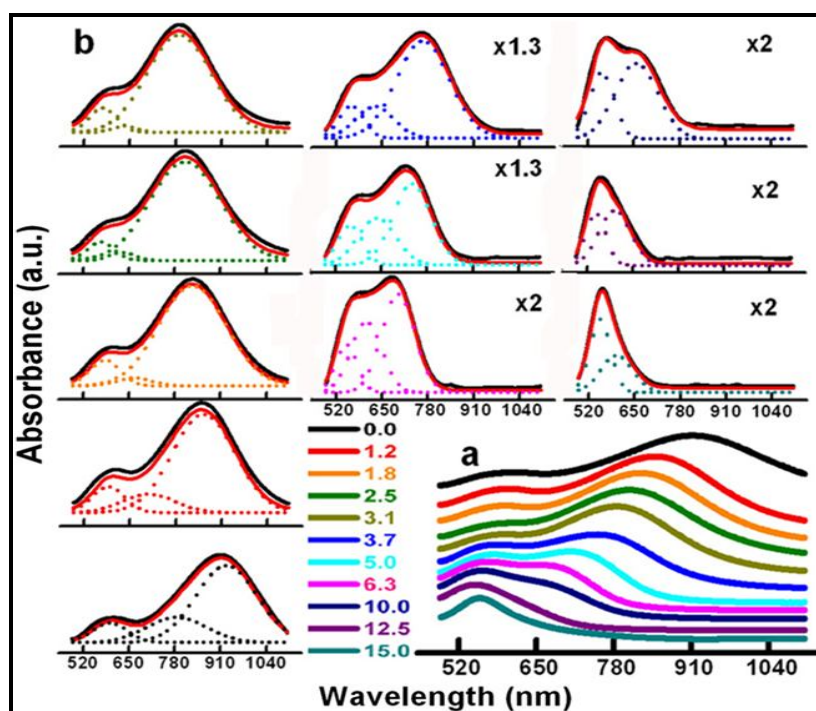


Figure-5.1: (a) Optical absorption spectra showing the effect of different NaOH concentration (in mM) to the precursor DMF-PVP complex. (b) Multiple Gaussian peaks (dashed lines) fitted for the individual optical absorption spectra for different NaOH concentration as mentioned (legend in different color). For better clarity, the optical spectra for higher NaOH concentration were suitably enhanced as shown by the given multiples.

The transition from 3D complex to planar tip-like NPs could well be correlated with the presence of distorted to regular SAED patterns respectively (inset, figure 5.2) with sequential increase in NaOH concentration. Moreover, all the SAED patterns show a spot pattern, feature of a single crystalline lattice, delineating the fact that chronological step-wise smooth changes occur in the morphology of the tips, thereby allowing the tips to preserve their mono-crystalline nature throughout the entire tuning process.

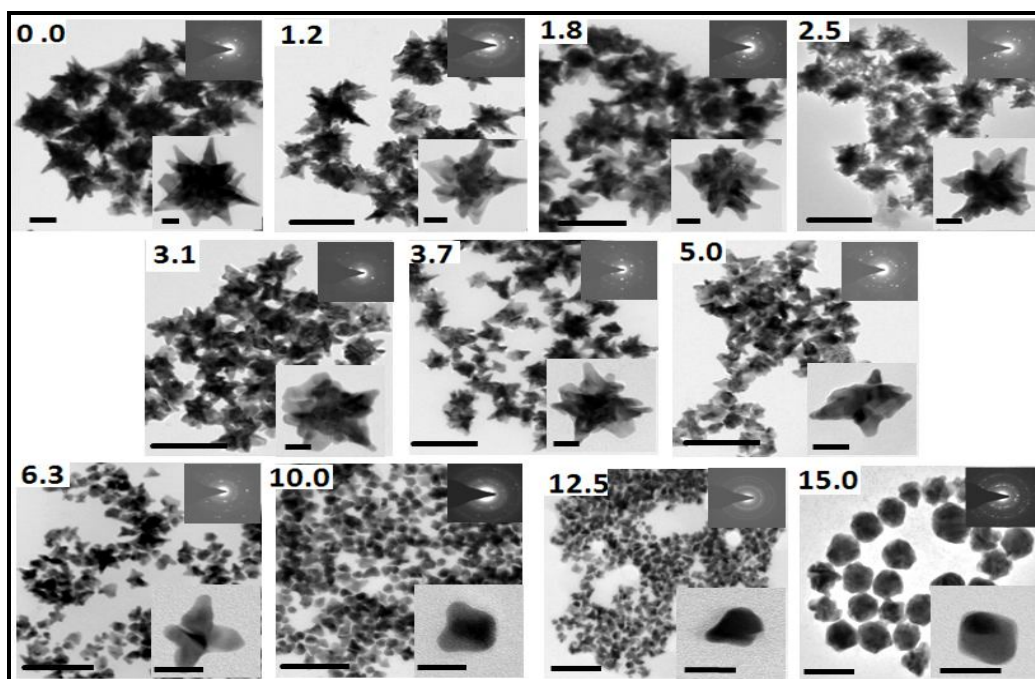


Figure-5.2: TEM (scale bar 100 nm) and HMTM images (inset, scale bar 20 nm) showing clearly the effect of NaOH concentration (in mM) on the morphology. Inset (right up) shows the related SAED patterns.

Such precise nanoengineering controlled tuning of LSPR (from near-IR to visible region) simply with NaOH concentration and their corresponding TEM characterization immediately reveals the broadening of tip like features at the expense of number of tips with decrease in the overall size of the as-formed Au nanoparticles.

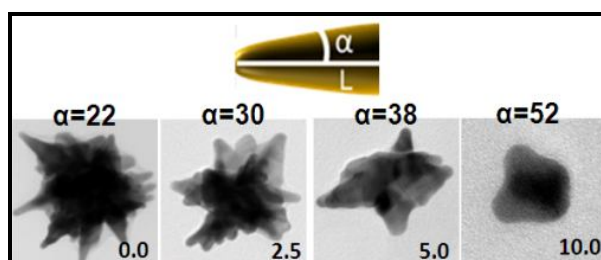


Figure-5.3: The mean aperture angle  $\alpha$  of tip like Au NPs at different NaOH concentration (in mM) signifies that with increase in NaOH volume, the angle ( $\alpha$ ) increases and hence the broadness of tips.

Plasmonic signatures of gold nanostars stems from the selective attachment of several anisotropic/elongated tiny seed particles with simultaneous ripening as well as smoothing. Hence, in terms of assimilating the extinction spectra for different NaOH concentration, each representative spectrum was analyzed utilizing Gaussian multi-peak fitting as shown in figure 5.1b with dashed line. The main observation inferred from here is that the high energy mode (transverse LSPR corresponding to the central core) is engulfed by the steadily growing peak intensity at the expense of blue shifted low energy mode (longitudinal LSPR mode related to the tips), which is in direct correlation with the observed TEM images (figure 5.2). Whereas the anti-bonding plasmon mode (occurring at 800 nm in the deconvoluted optical spectra of as prepared gold nanostars) starts blue shifting with reduction in peak intensity up to NaOH concentration of 3.1 mM in a precisely reproducible manner (see figure 5.2, where the defect free single nanoparticle morphology is shown), emphasizing the diluted coupling strength between core and tip plasmon, which strongly corroborate the fact that the tip/spike like structures cease to grow in length, rather expands in width, habitually reducing their size/number. Above this concentration and upto 6.5 mM NaOH, significant anti-bonding mode appears again indicating visually the inheritance of crystal lattice defects in the nanoparticle morphology, evidenced through the change in optical spectra as well.

Above this NaOH concentration, anti-bonding plasmonic band disappears and the transverse LSPR starts dominating the proceedings with respect to the diminishingly blue shifted longitudinal LSPR and finally

(above 10 mM NaOH), the two LSPR peaks collude together to stabilize themselves with almost constant/steady prominently broad single intense peak (deconvoluted further), indicating visually the formation of planar elongated anisotropic gold nanostructures (see figures 5.1 and 5.2). This process can be well understood from the fact that with increase in basicity of the reaction medium, the reducing action of PVP in DMF increases abundantly, resulting in faster nucleation of metal seed particles, which invariably tend to grow in a flat 2D manner (increasing width) rather than coalesce in a 1D rod/wire like manner, thereby resulting in NPs with decreasing spike/tip lengths along with extensive decrease in their number density, causing the blue shift of their respective LSPR peak positions as systematically seen from figures 5.1 and 5.2. Although various research groups worldwide have examined through complicated multi-step synthetic procedures the morphology tuning [167, 254, 291-294], our present synthetic protocol stands apart among others for its inherent simplicity and ease for its reproducible quality as well as quantity.

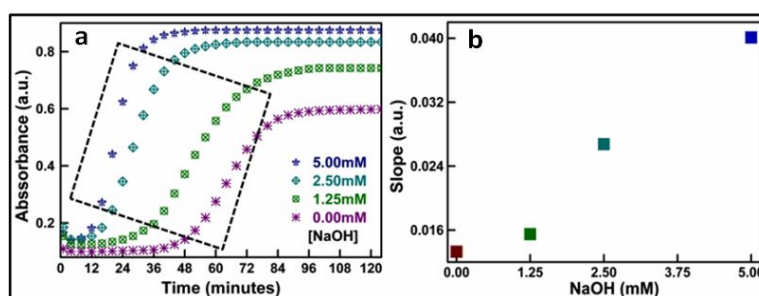


Figure-5.4: (a) Nucleation and growth curve for the as-prepared anisotropic Au Nps as shown in figure 5.2. (b) represents the slope variation (as derived from the linear growth region indicated by dashed square in (a)), which increases linearly with increase in NaOH concentration.

In this regard, temporal evolution of the particle size/shape presents a deeper insight into the contribution of nucleation and growth reactions on the particle formation, when plotted (figure 5.4a) for the isosbestic point at 400 nm (see chapter 2, pp: 37) explicitly shows that the reaction follows an autocatalytic course due to dynamic nucleation of metal seed particles followed diligently by their controlled growth and stabilization.

With gradual/sequential addition of NaOH, nucleation of seed particles happens at a faster rate compared to the pristine conditions (without NaOH, discussed on pp: 90), (figure 5.4a), hence their growth/stabilization also happens rapidly as vividly shown by the sheer increase in the slope of their growth curve with increase in alkaline nature of the surrounding medium (figure 5.4b). For higher NaOH concentration, seed particles are nucleated within 10 minutes, thereby enhancing their growth/stabilization within 30-35 minutes, as clearly reported by the exponential increase in the slope of the linear growth region (figure 5.4b). Also, the effect of different NaOH volume with different chain length of PVP (Mw = 8000 and 25000) is shown on the optical spectra and structure correlated morphology in figure 5.5.

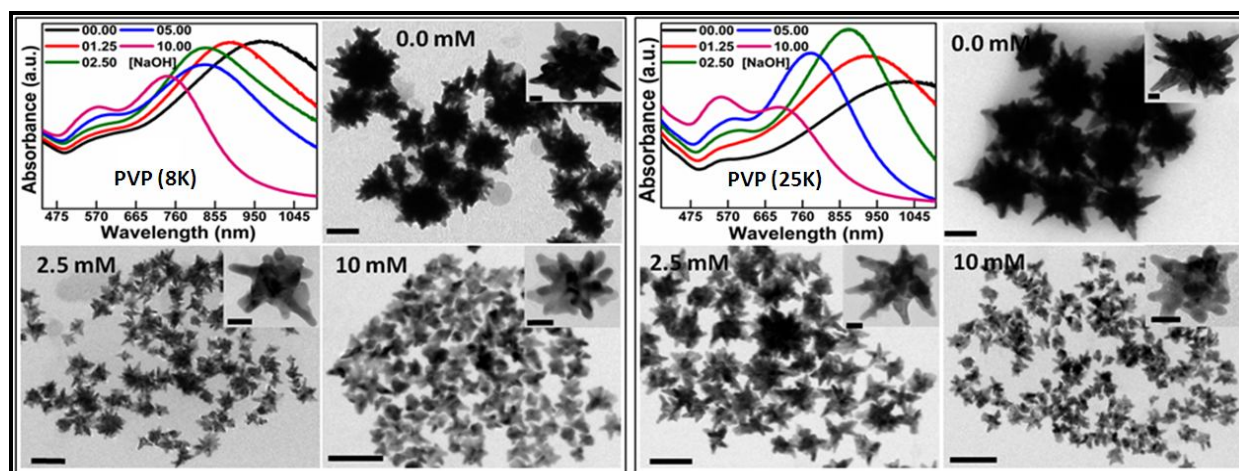


Figure-5.5: UV-Vis spectra and TEM images (scale bar=100 nm) with high magnification images in inset (scale bar 20 nm) using PVP molecular weight 8k and 25k respectively, clearly showing the similar effect on gold nanostructures as observed with PVP 10 K.

In our present synthesis procedure, addition of NaOH in PVP-DMF solution is known to have a large impact on the reaction kinetics of nanoparticle formation as well as the key factor in regulating the optical properties (in terms of morphology control), which can be very well understood utilizing the systematic FTIR and NMR measurements and their careful analysis.

### 5.3.2 NMR and FTIR Analysis

Our present  $^{13}\text{C}$  NMR data demonstrate clearly the interaction between carbonyl group of PVP monomer unit with DMF with(out) the presence of NaOH and also the polymer chain conformational variations (figure 5.6).

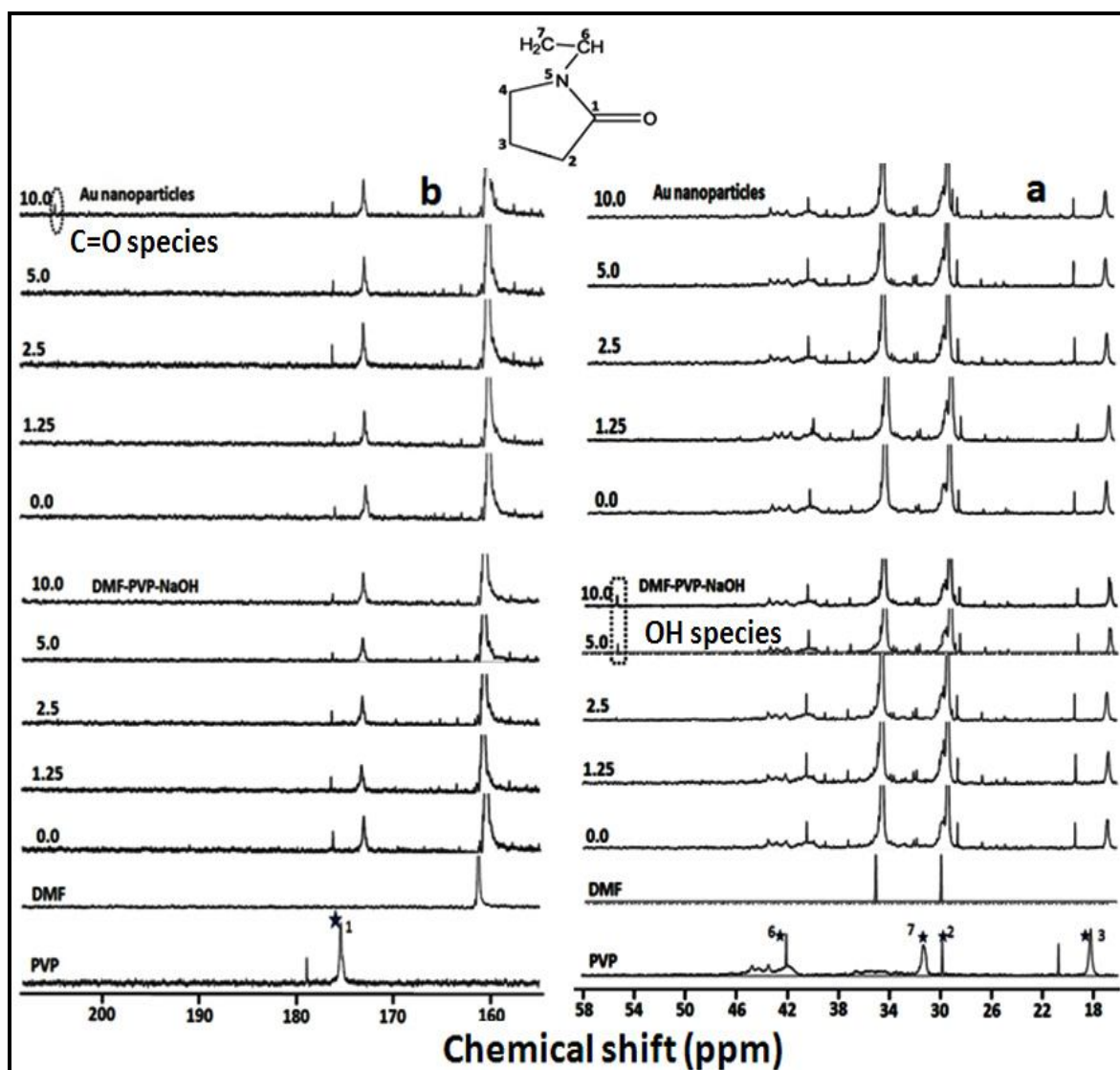
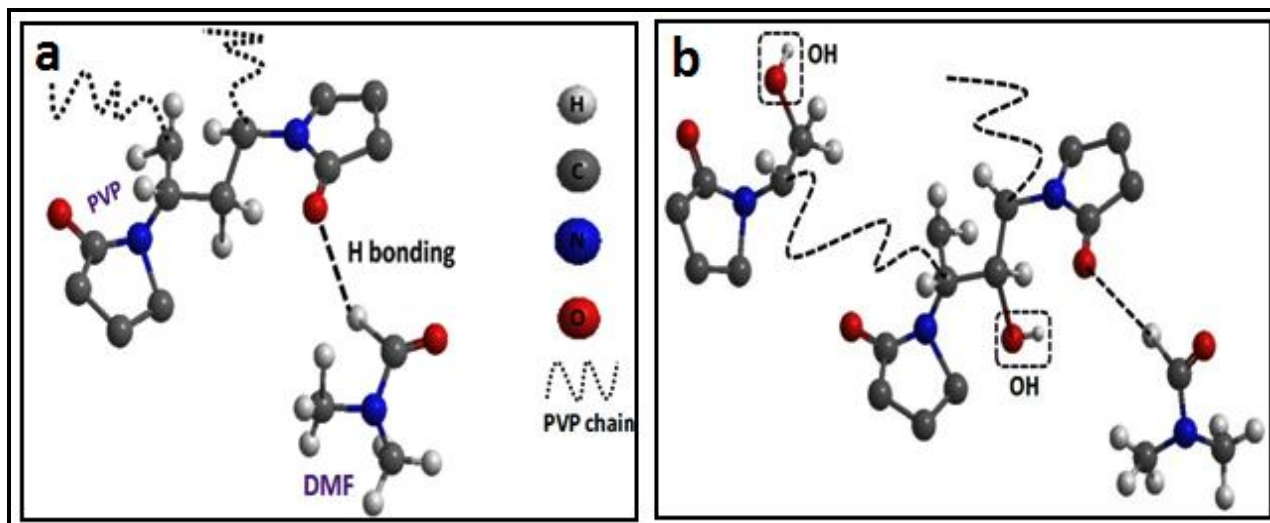


Figure-5.6: (a, b) Extended  $^{13}\text{C}$  NMR spectra depicting clearly the carbon chemical shifts/changes in different NaOH concentration samples. The emergence of new peak around 57 ppm in DMF-PVP-NaOH (in a) complex is attributed to insertion of hydroxyl (OH groups) in-between/end of the polymer chain in presence of NaOH while it get disappeared in the final nanoparticles spectrum. The emergence of new peak around 204 ppm in nanoparticles spectrum (in b) corresponds to the carbonyl group arising at the cost of peak at 57 ppm for 10 mM NaOH (in a) arising from the oxidation of OH group (present in-between of polymer chain) in addition to PVP ring carbonyl peak (175 ppm).

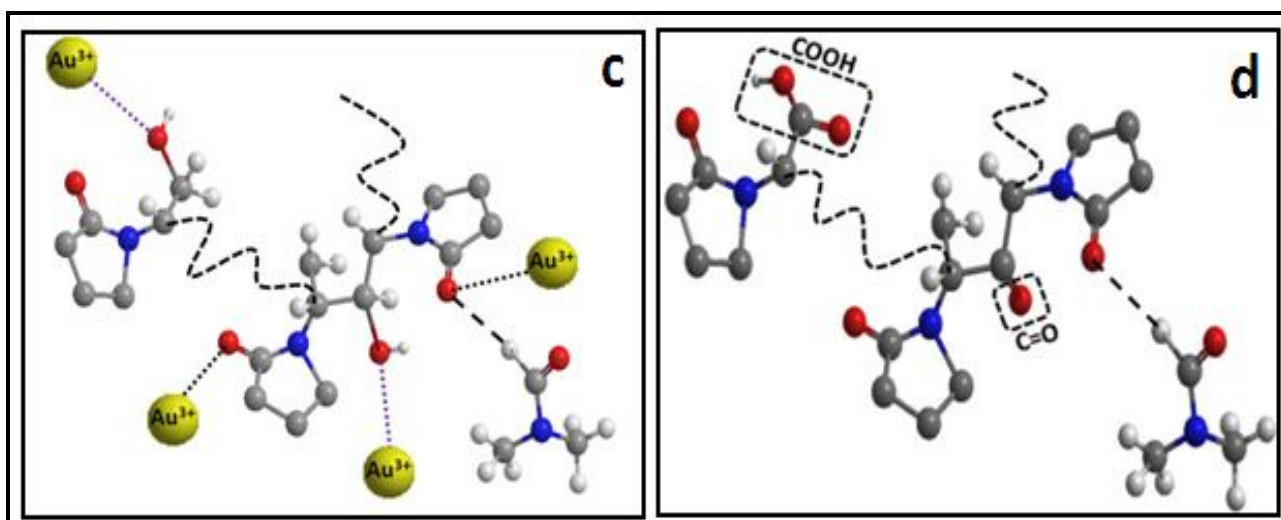
Peaks observed in the range of 180-170 ppm (figure 5.6) are related to C resonance of carbonyl group in the PVP units [172]. The interaction between DMF and PVP (as discussed in chapter 4 as well) asserts significantly the fact that along with PVP-DMF hydrogen bonding, dipole-dipole interaction is also predominant (see scheme 5.2a) [235].

**Scheme-5.2:** (a) H-bonding interaction between DMF and PVP. (b) NaOH effect by way of –OH group introduction in between or at the end of polymer chain



With the addition of NaOH, no appreciable shift is observed in the  $^{13}\text{C}$  NMR spectra of DMF-PVP-NaOH complex (when compared to pristine DMF-PVP complex) indicating the fact that pyrrolidone ring of PVP is not affected in the presence of NaOH (figure 5.6). With sequential increase in the NaOH volume in DMF-PVP complex, the emergence of new peak at 57 ppm for 5 mM addition of NaOH (figure 5.6a), which become clearly visible at 10 mM of NaOH, might be due to insertion of –OH groups in-between or at the end of the polymer chain as pictorially represented in scheme 5.2b.

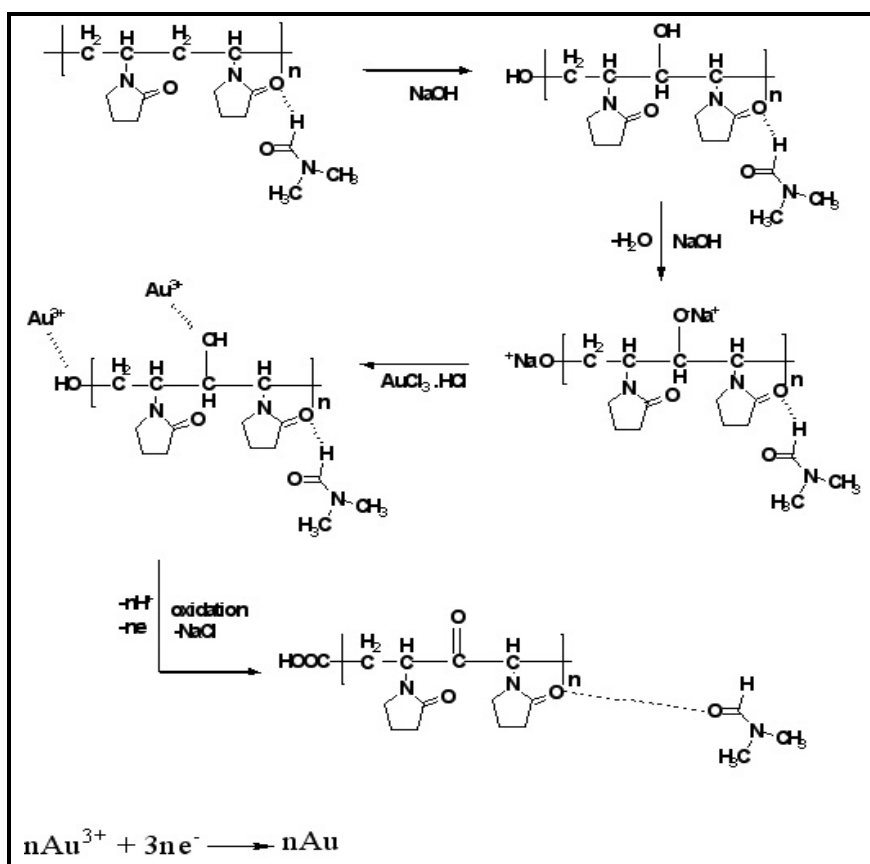
**Scheme-5.3:** (a) Interaction of the metal ion in DMF-PVP-NaOH system. (b) Formation of new carbonyl group and a carboxylic group in between and at the end of the polymer chain respectively, upon oxidation of chemically introduced OH group.



Upon addition of the gold salt, these chemically introduced hydroxyl groups at the end or in between of the PVP polymer chain further coordinates with  $\text{Au}^{3+}$  through their oxygen atom, in addition to the  $\text{C}=\text{O}$  coordination (as in the pristine case, discussed in chapter 4, pp: 103-104) as represented in scheme 5.3a.

The NMR spectra of as-prepared Au NPs signifies the presence of a new peak at 204 ppm, corresponding to the carbonyl group formation in between of polymer chain, which starts arising at the cost of peak at 57 ppm for higher NaOH concentration (say, above 5 mM; figure 5.6) due to the concurrent oxidation of -OH group (present in-between of polymer chain; scheme 5.2b) in addition to pyrrolidone ring carbonyl peak (175 ppm) as shown in the scheme 5.3b (the step-wise scheme is illustrated in scheme 5.4).

**Scheme-5.4:** Systematic formation mechanism of Au nanoparticles in the presence of NaOH.



The major difference between these two carbonyl peaks can be easily understood from their respective structural/chemical environment, as the pyrrolidone ring carbonyl peak is in conjugation with N atom; hence shielded, ensuing the NMR peak at lower ppm (say, 180 ppm); whereas the deformation at the polymer chain gives rise to 204 ppm peak. The foremost reason for the non-differentiation of these two carbonyl peaks in the FTIR spectra (figure 5.7), as they lie exactly in the same wavenumber region i.e., in-between  $1600$  to  $1700 \text{ cm}^{-1}$ [185], but clearly set apart in  $^{13}\text{C}$  NMR.

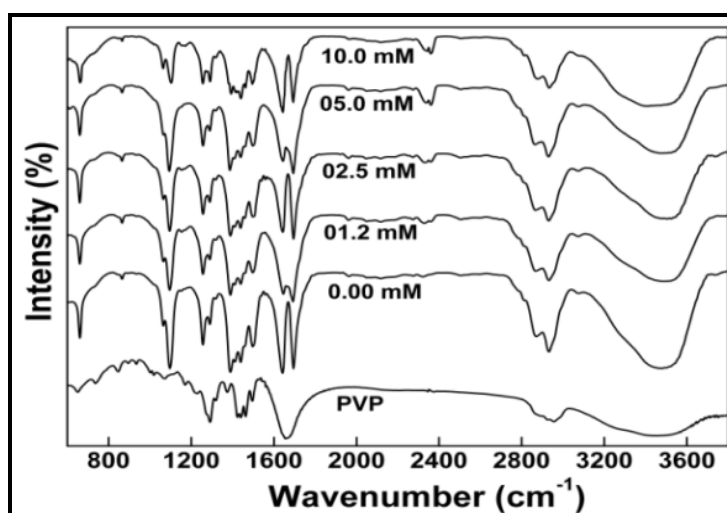


Figure-5.7: Kinetic FTIR spectra (Baseline corrected with respect to DMF) over the full energy range of Au nanostars in the presence of different NaOH volume/concentration.

Moreover a slight broadening of band in the region of O-H stretch in the FTIR spectra of final Au NPs obtained at 10 mM NaOH (figure 5.7) also showed the possibility of oxidation of  $-\text{OH}$  group (end group of

PVP) into carboxylic group which is not at all observed in  $^{13}\text{C}$  NMR indicating that insertion of  $-\text{OH}$  as end group is less favorable.

Thus, an optimal concentration (10 mM) of NaOH provides higher active chemical sites for the reduction of metal ions. At this point, there is a drastic transition from 3-D to planar elongated NPs as seen in TEM images which coherently correlates the morphological changes with the corresponding molecular changes occurred in  $^{13}\text{C}$  NMR spectra.

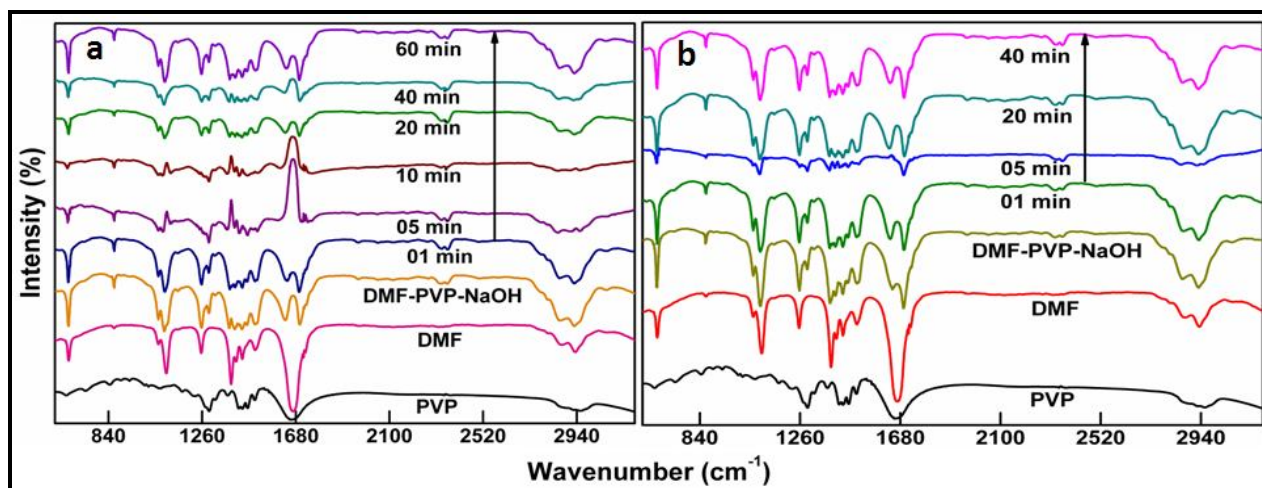


Figure-5.8: Kinetic FTIR spectra over the full energy range (baseline corrected wrt DMF) for (a) with NaOH = 2.5 mM and (b) with NaOH = 5 mM.

It is interesting to observe that when the reaction kinetics is monitored via FTIR for different NaOH concentration (see figure 5.8), the ligand exchange mechanism evolves beautifully as discussed elaborately in our chapter for as prepared gold nanostars. But, as the NaOH concentration reaches 10 mM, the  $-\text{OH}$  peak (arising at 57 ppm) in DMF-PVP-NaOH complex disappears in the final Au nanoparticles  $^{13}\text{C}$  NMR spectra along with the formation of a new polymer chain carbonyl peak at 204 ppm, indicating the dominance of reduction governed by the monomer chain of PVP having OH moieties, as quantitatively corroborated further by XPS measurements as discussed in the next section.

Essentially,  $^{13}\text{C}$  NMR as well as the FTIR spectra of final formed gold nanoparticles indicate the increasing monomer chain contribution with increase in NaOH volume/concentration in conjunction with our TEM studies, unequivocally suggesting the fact that when nanoparticle growth kinetics is governed by the pyrrolidone ring carbonyl group of PVP, anisotropic sharp tip/spike like gold nanostructures were dominant, whereas the oxidation of  $-\text{OH}$  mid/end chain functionalities in PVP (as in case of higher NaOH concentration) effectively leads to planar spheroidal gold nanostructures.

### 5.3.3 XPS Studies

On the contrary, our previous collective XPS analysis (chapter 3, pp: 76-80) duly emphasize the fact that PVP bridges the Au surface through its nitrogen as well as oxygen components in the pyrrolidone ring which further tells how precisely and systematically the PVP molecules bound on the surface of various size/shaped Au nanoparticles, evidently based on the synthesis protocol. In the present case also, we have utilized the methodical XPS study for synergistically viewing the influence of NaOH concentration on the growth and evolution of metal nanoparticle morphology.

Figure 5.9 shows the typical C 1s, O 1s and N 1s and Au 4f core level BE spectrum of the purified Au nanoparticle samples, which strongly authenticates the presence of PVP molecules on the metal surface indicating the diverse interaction of PVP with various gold crystalline facets as reported earlier [175, 241].

O 1s core level BE peak arising from the carbonyl ( $\text{C}=\text{O}$ ) oxygen (table 5.1) in comparison with pure PVP (531.3 eV) [241, 295, 296] deviates the maximum peak position to 532.52 eV (without NaOH) but starts blue shifting to 532.13, 532.04 and 531.90 eV respectively (table 5.1 and figure 5.9), for the gold nanostructures formed in the presence of different NaOH concentrations, illustrating the fact that the electron density distribution around the carbonyl oxygen decreases to the maximum extent in the pristine entangled DMF-PVP

complex, while it tends to retain/regain itself due to the increased hydroxyl bonding with increasing NaOH concentration, highlighting the dynamic shift in the equilibrium interaction between the PVP molecule and the Au nanoparticle core even under normal reaction conditions.

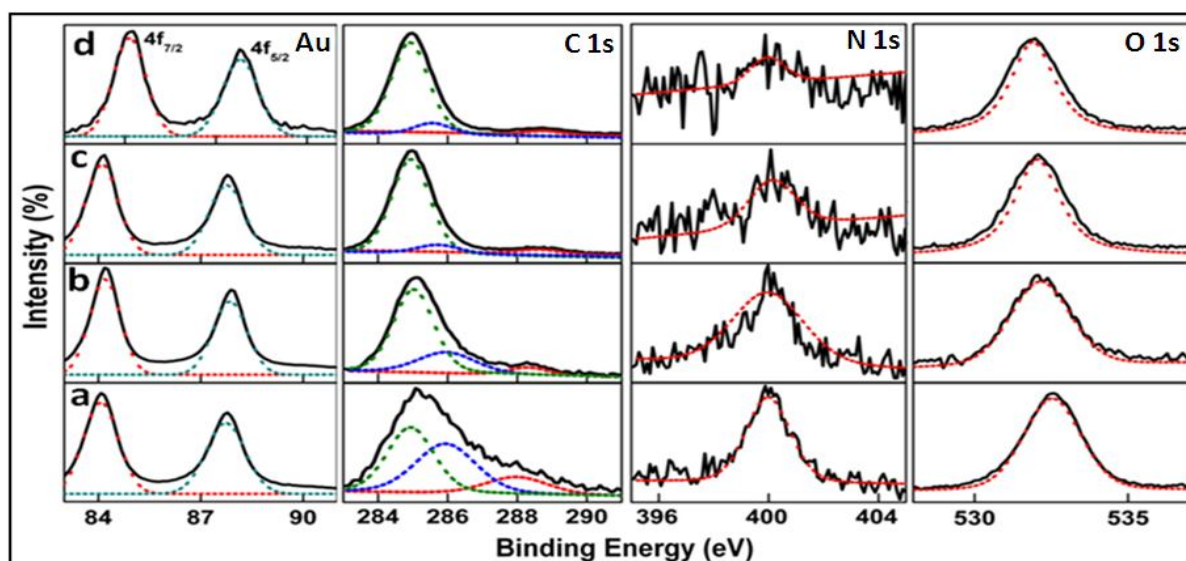


Figure-5.9: XPS spectra of (a) without NaOH and for (b) 1.2, (c) 5 and (d) 10 mM NaOH tuned PVP-capped Au nanostructures illustrating clearly the metal as well as PVP local structure modification through Au 4f, C 1s, N 1s and O 1s core level spectra. Solid black lines correspond to the experimental data and colored dashed lines represents the deconvoluted data.

Likewise, the N 1s core level BE peak of pure PVP (399.6 eV) [241, 295, 296] not only shifts to slightly higher binding energies (400.17, 400.21 and 400.02 eV) for the different Au nanostructures as shown in table 5.1 and figure 5.9, but also depict higher asymmetric peaks (strongly associated with the increased basicity in the surrounding environment, concurrently affecting the monomer chain to a large extent), directly illustrating the categorically selective but significant increase in the participation of the nitrogen component in sequentially inducing the formation of conventional planar spheroidal gold nanostructures with increasing NaOH concentration.

**Table-5.1: XPS binding energy peak positions obtained from figure 5.9**

Peak	No NaOH	1.25 mM	05 mM	10 mM	PVP
<i>Au4f<sub>7/2</sub></i>	84.10	84.19	84.10	84.15	-----
<i>Au4f<sub>5/2</sub></i>	87.70	87.86	87.76	87.80	-----
<i>CI<sub>s</sub> (C-C)</i>	284.94 (42)*	285.02 (68)*	284.94 (80)*	284.91 (85)*	285.12
<i>CI<sub>s</sub> (C-N)</i>	285.94	285.96	285.75	285.7	286.00
<i>CI<sub>s</sub> (N-C=O)</i>	287.98	288.31	288.63	288.76	287.80
<i>NI<sub>s</sub></i>	399.95	400.05	400.13	399.90	399.7
<i>OI<sub>s</sub></i>	532.53	532.14	532.04	531.90	531.35

\* Percentage contribution as extracted from the area of the C-C peak.

To get further insight into the extent of O/N binding on the regularly irregular morphology of the gold nanostructures; the subtle BE changes in the various components of the core level carbon peaks upon deconvolution (table 5.1 and figure 5.9) in comparison with pure PVP (chapter 3, see pp: 76-78) corresponds to the fact that the Au nanoparticle surface experiences a balanced electron density distribution exercised via both nitrogen and oxygen in the N-C=O component of the pyrrolidone ring of PVP, as explicitly illustrated from not only the intricate changes in the N 1s and O 1s core level BE spectra but also through the delicate changes observed in FTIR data (figures 5.7 and 5.8).

With increase in NaOH concentration, the C-C percentage contribution increases; while C-N and carbonyl carbon (N-C=O) decreases along with increase in BE of N-C=O (shown in table 5.1) in comparison with that of the pristine Au nanostars case, intuitively suggesting the indirect but significant contribution from the monomeric chain of PVP in micro-engineering the complex architecture of the multi/hyper-branched Au nanostructures.

Thus, the present comprehensive XPS analysis shows that the electron cloud density unequivocally hovers around the N-C=O region of the pyrrolidone ring of PVP through the so-called conjugation effect, confirming the impartial charge transfer from both the oxygen and nitrogen atom in the pyrrolidone ring (when the system is pure and free from NaOH addition), which sequentially gets biased through the chelating effect arising from the nitrogen component suitably supported by the monomer chain component with increase in the NaOH concentration.

Moreover, in comparison with bulk Au atoms [175, 241], the BE of Au 4f<sub>7/2</sub> and Au 4f<sub>5/2</sub> core level BE peaks shift by 0.1-0.16 eV (see table 5.1 and figure 5.9), envisaging clearly the sensitive chemical environment around the Au core corresponding to the real-time strength of interaction between Au and PVP even under normal conditions.

In summary the concomitant fluctuation (increase-decrease-increase) in the BE peak position of the Au core level components effectively corroborates the *in situ* micro-engineered size/shape tuning (see TEM images shown in figure 5.2), but drastically differs both qualitatively as well as quantitatively from the XPS results on other molecular capped Au clusters/nanoparticles, retrospectively implying the present synthesis protocol as a rational paradigm for enabling enhanced complex charge transfer process involving the dynamic active participation by each individual chemical components of PVP even under normal reaction conditions, leading to comprehensive nucleation/selective aggregation.

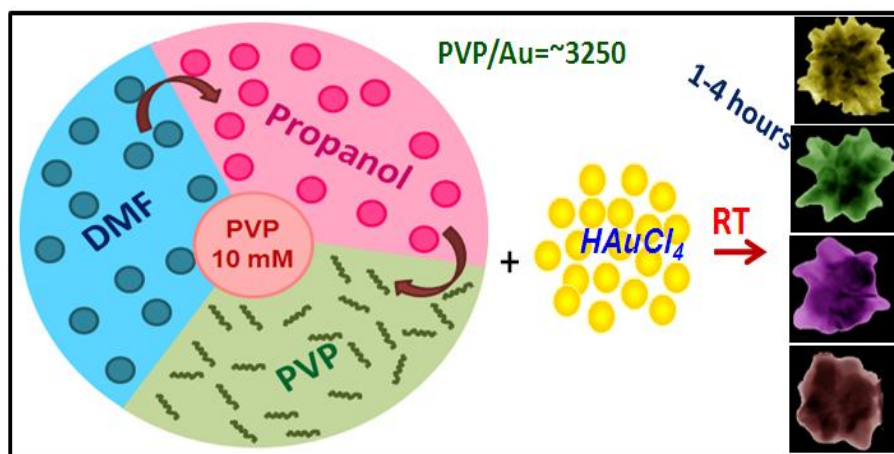
## SECTION B

This section of present chapter, provide a simple yet versatile approach for fine tuning the plasmonic signatures of 3-D complex Au nanostars by uncommon usage of the polar/non-polar binary solvent mixture (2-Propanol as a co-solvent with DMF) for precisely engineering their plasmonic response over the entire visible/NIR spectral range based on the fine tuning/reshaping strategy of metal nanocrystals. Use of binary solvent for tuning the nanoparticles morphology is no where reported till now and is first time to best of our knowledge.

### 5.4 SYNTHESIS PROTOCOL

The influence of 2-Propanol in gold nanostars growth solution (synthesis procedure for gold nanostars is mentioned in section A of this chapter) is studied by adding it into DMF in different molar ration (MF, as mentioned in text) before the addition of PVP and metal precursor (see scheme 5.5).

**Scheme-5.5:** Illustrating the facile/versatile room temperature single step tuning procedure for Au nanostars using careful selection of the binary solvent mixture (DMF and 2-propanol) at different MF of DMF followed by PVP and metal ions keeping PVP to metal ions ratio ~3250 for all cases.



## 5.5 RESULTS AND DISCUSSION

As detailed in previous chapters that the solvent-solute interaction dominates the nucleation regime in precise and further plays a significant role in the polymer chemisorption onto the surface of the metal nanoparticles directing/shaping them to anisotropically grow with different intriguing size/shapes. DMF interaction with PVP has been reiterated as a crucial factor to the formation of 3-D complex gold nanostars.

### 5.5.1 Optical Investigations

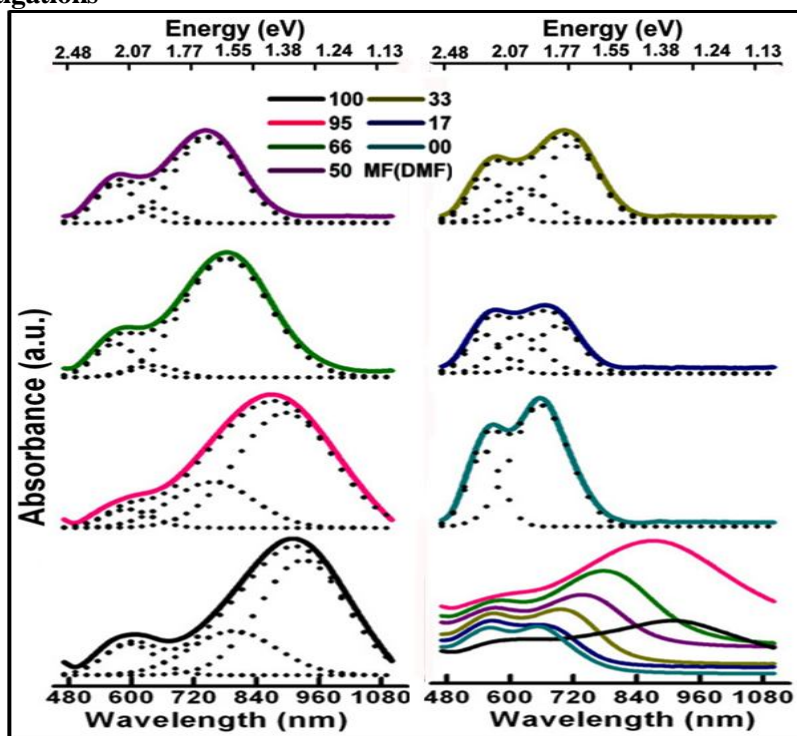


Figure-5.10: UV-Visible spectra illustrating the fine tuning of the plasmonic signatures of the as-formed Au NPs at different MF (DMF) as mentioned. Deconvolution of the individual plasmonic peaks (spectra with dotted line) correlates very well with the size/shape of the respective Au NPs, as discussed in detail in the text.

The good donor/acceptor properties of DMF [297-300] enable it to dissolve a wide range of polar and non-polar solvents and convinced by the fact that the conformational changes of PVP in different solvents lead to different size/shaped Au nanostructures. We effectively utilizes a simple binary solvent mixture, such as DMF:2-Propanol for the controlled tuning of the plasmonic response of gold nanostars in a sequential manner from visible to the near IR region. Thus, simple addition of an external alcohol like propanol into DMF (at different mole fraction (MF) of DMF) of DMF itself sequentially tunes the longitudinal LSPR peaks from 910 nm (1.35 eV, for pristine Au nanostars) to 650 nm (1.87 eV) in a precisely reproducible manner, as shown in figure 5.10.

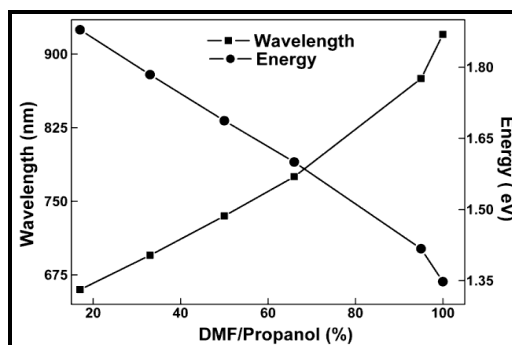


Figure-5.11: Shift in the longitudinal plasmonic wavelength/energy of gold nanostructures with respect to change in DMF-propanol ratio.

For higher propanol concentration, gold seed particles are nucleated at a faster rate resulting in the blue shifting of LSPR. Figure 5.11 clearly depicts the blue shifting in the LSPR position with respect to decrease in DMF to

Propanol ratio and curve is almost straight line with negative slop indicates LSPR shifts towards blue linearly with increase in propanol concentration.

Although the gold nanoparticle optical/morphology tuning have been successfully carried out by various research groups worldwide through complicated multi-step synthetic process [167, 254, 291, 292, 294], our present colloidal solution synthesis stands apart among others for its inherent simplicity and ease for its reproducible quality as well as quantity.

### 5.5.2 Morphological Investigations

Such visible spectral changes in the optical spectra of the nanoparticles can be easily justified in terms of the chronological changes in the morphology as seen through TEM. In comparison with the gold nanostars synthesized in DMF, where the tips/spikes are longer and sharper, the sequential addition of propanol to DMF (decrease in MF (DMF)) brought sequential changes in the sharpness, length and size of the tips/spikes as demonstrated clearly in figure 5.12 (the aperture angle alpha increases sequentially).

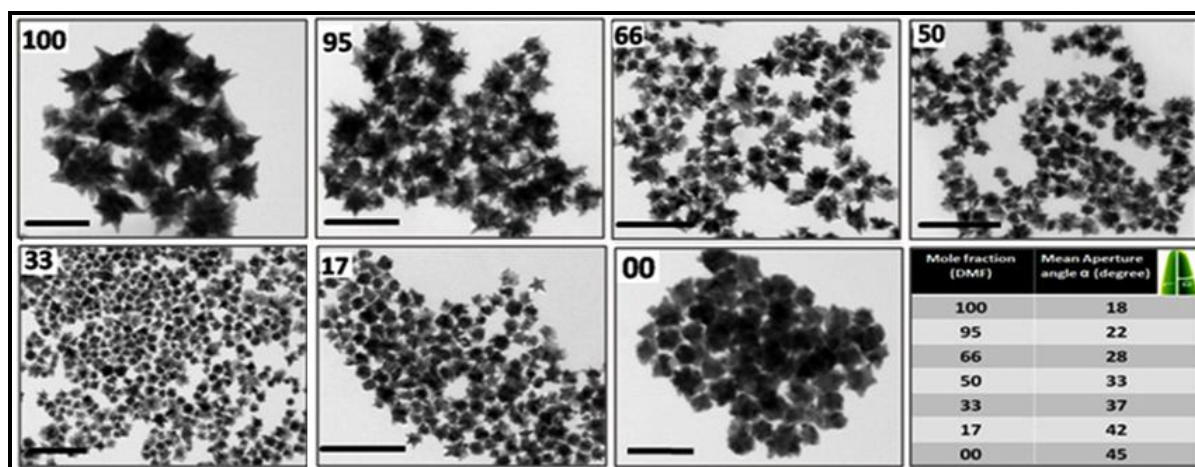


Figure-5.12: Morphology assessment with reference to the mean aperture angle of the as-formed anisotropic gold nanostructures with respect to increasing propanol addition in DMF (at different MF (DMF)) via TEM images (scale bar = 100 nm).

The pristine Au nanostars were dominated by the non-planar tip/spike like features, whereas the planar ones, whose distribution increases with decrease in MF of DMF that is with increasing propanol volume, reveal explicitly the broadening of tip/spike like features at the expense of their number density along with decrease in the overall size of the as-formed Au nanostructure, as clearly seen from the HMTEM images (figure 5.13).

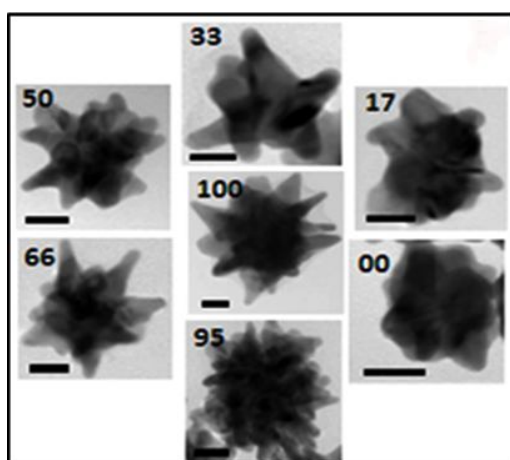


Figure-5.13: HMTEM images (scale bar = 20 nm) of the as-formed anisotropic gold nanostructures with different MF (DMF).

It is well known that the plasmon resonance of gold nanostars result from the hybridization of core and tip mode plasmons or from the near base region of the tip also [229]. Based upon this fact, we analyzed the

extinction spectra of the different gold nanostructures obtained by using various DMF-propanol ratio, utilizing the standard Gaussian multi-peak fitting procedure as illustrated in figure 5.10 with dashed lines.

The main assessment inferred from here is that the intensity of the transverse LSPR mode steadily grows at the cost of blue shifted longitudinal LSPR mode (related to the tips), in direct correlation with the observed HMTEM images (figure 5.13), strongly corroborating the fact that with increasing propanol concentration, the tip/spike like Au NPs cease to grow in length, rather expands in width, customarily reducing their overall size/number. Besides, the anti-bonding plasmon mode (see pp: 92-95) starts blue shifting with reduction in peak intensity (see figures 5.10/5.13, where the defect free single NP morphology is shown), until the MF of DMF reaches to 50, emphasizing the weakened coupling strength between the core and the tip mode plasmons, which further correlates well with the broadening as well as decrease in the overall number of tips in a single NP. But, as the MF of DMF decreases below 50, the significant anti-bonding plasmon mode appears again, depicting visually the change in the shape of the absorption spectra itself, preferably due to the inheritance of the crystal lattice defects in the nanoparticle morphology with reference to the dynamical changes in the applied synthetic procedure (see figures 5.10/5.13).

### 5.5.3 Molecular Interaction

Thus, the relevant stabilization and tuning of the as-prepared gold NPs morphology can be coherently discussed in the light of distinct molecular interaction existing between DMF-propanol-PVP mixtures [297-301].

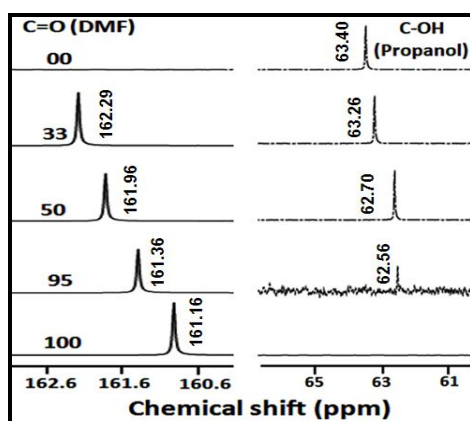
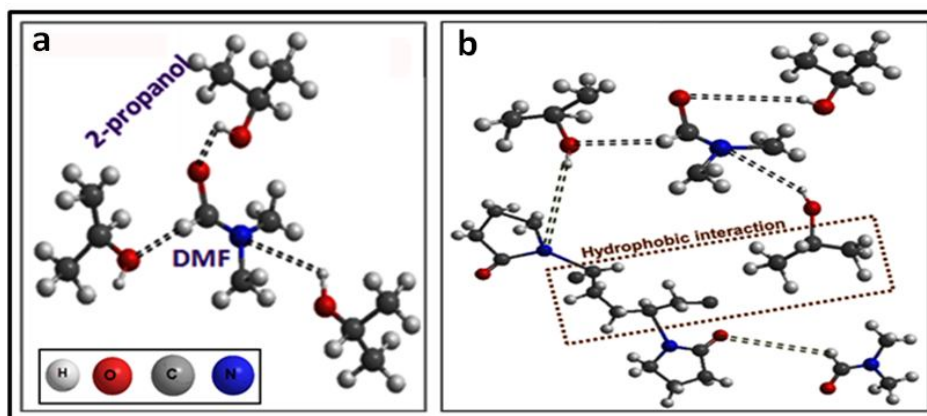


Figure-5.14: Extended  $^{13}\text{C}$  NMR spectra of DMF-propanol mixture at different MF of DMF.

Figure 5.14 shows the  $^{13}\text{C}$  NMR spectra of DMF and propanol at different MF (DMF) with respect to propanol concentration. At high MF of DMF i.e., at low concentration of propanol in DMF, the  $^{13}\text{C}$  carbonyl chemical shift of DMF increases slightly (see figure 5.14 for peak position values). Such shifts in NMR peaks signifying the changes occurring in the self-association equilibria of DMF, which are evidently due to the change in dipole-dipole interaction along with the formation of hydrogen bonds, O-H (of propanol)... O-H ...N(CH<sub>3</sub>)<sub>2</sub> or O=CN of DMF along with H-bonding between O-H of propanol and the formyl proton of DMF as schematically shown in the scheme 5.6a.

**Scheme-5.6:** H-bonding interaction between DMF and propanol



With further decrease in the MF of DMF, the  $^{13}\text{C}$  carbonyl chemical shift of DMF increases more rapidly (see figure 5.14 for peak values), demonstrating the fact that not only the DMF-propanol hydrogen bonding becomes stronger with increasing alcohol content, but also DMF prefers to be surrounded by more propanol molecules than by other DMF molecules, similar to the case of DMF in methanol [301], thereby visualizing propanol to behave more like a watermelon in which the DMF molecules act as seeds. The observed results indicate the existence of an intermolecular association between O-H group of alcohol and C=O group of amide. It is also interesting to note that DMF-alcohol interaction is weaker than the DMF-DMF or alcohol-alcohol interactions [297].

Moreover, the interaction between PVP-DMF and PVP-propanol systems were individually discussed in detail in our previous chapter 3, which talks about the dominant dipole-dipole interaction in PVP-DMF system as well as the hydrophobic interaction between PVP and propanol along with hydrophilic (H-bonding) interaction. In the present case, PVP addition to the DMF/propanol composition (for different MF) results in the slow but steady re-organization of the polymer network, as systematically depicted in the scheme 5.6b in accordance with the  $^{13}\text{C}$  NMR studies (figure 5.15).

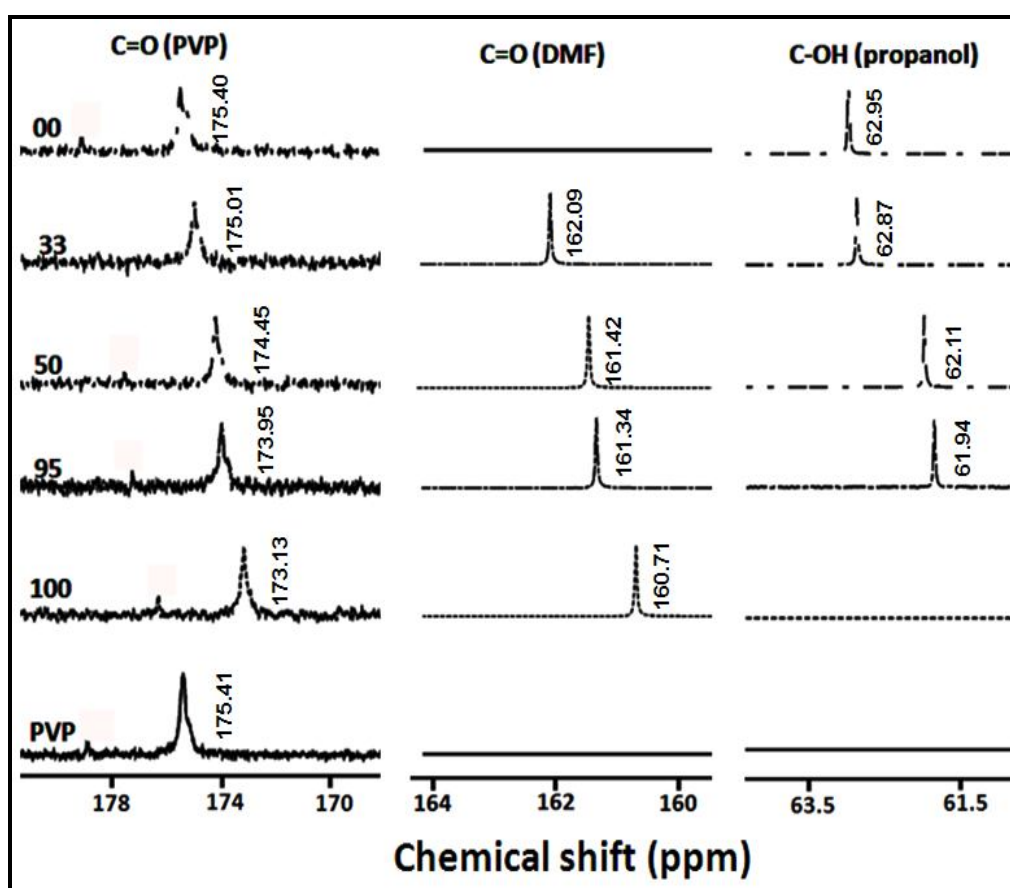


Figure-5.15: Extended range of  $^{13}\text{C}$  NMR spectra of PVP and PVP-DMF-propanol mixture at different MF of DMF.

A slight but sure downfield of the carbonyl peak (C=O peak around 175 ppm) of PVP with decrease in MF of DMF (see figure 5.15) signifies the weakening of H-bonding between DMF and propanol along with the appraisal of hydrophobic interaction between propanol and long chain of PVP molecules through hydrogen bond formation between nitrogen of PVP and HO-C of propanol as portrayed in scheme 5.6b.

The slight up-field chemical shift in the DMF carbonyl peak and the subsequent downfield shift in the C-OH bond of propanol (with increase in propanol volume) in the DMF-propanol-PVP system in comparison to DMF-propanol, exemplifies the loosening of DMF-PVP bonding in conjunction with increasing PVP-propanol H-bonding interaction with ostensibly augmenting the incremental increase in the hydrophobic interaction assimilated through the long polymer chain and the relatively smaller alcohol group and is maximum for pure PVP-propanol system.

Thus the use of binary solvent DMF and 2-propanol result in simultaneous existence of dipole-dipole, hydrophilic as well as hydrophobic interaction, the impact of which can be clearly seen with addition of metal ions.

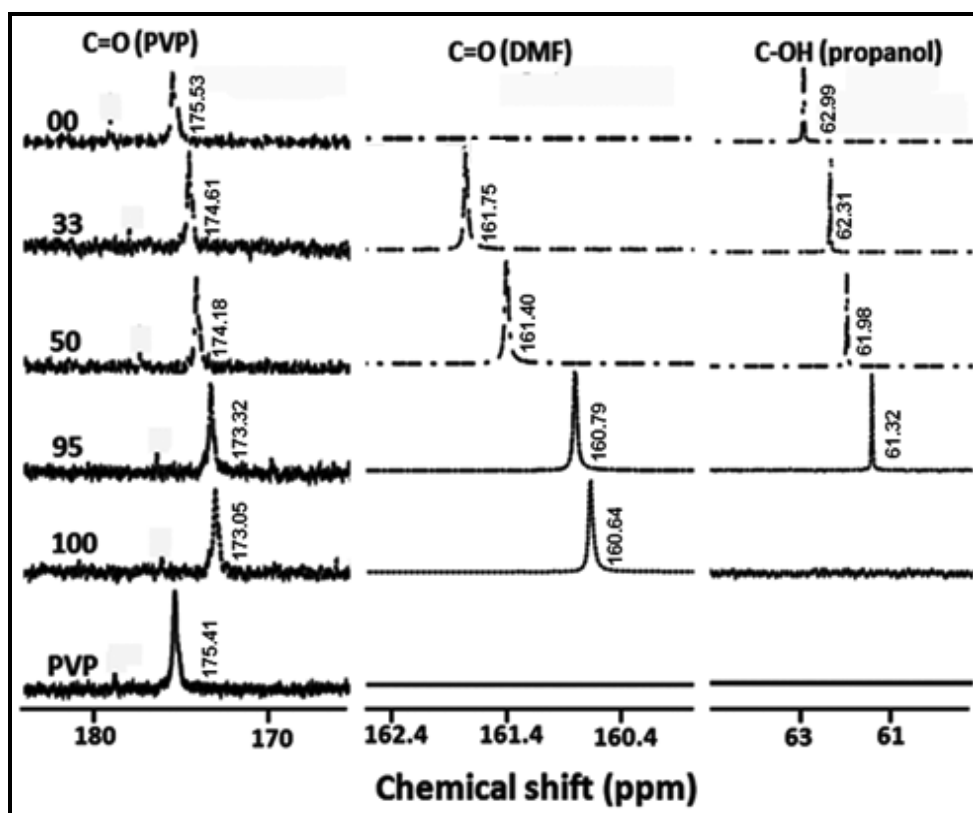


Figure-5.16: Extended range  $^{13}\text{C}$  NMR spectra of PVP and Au nanoparticles obtained at different MF of DMF.

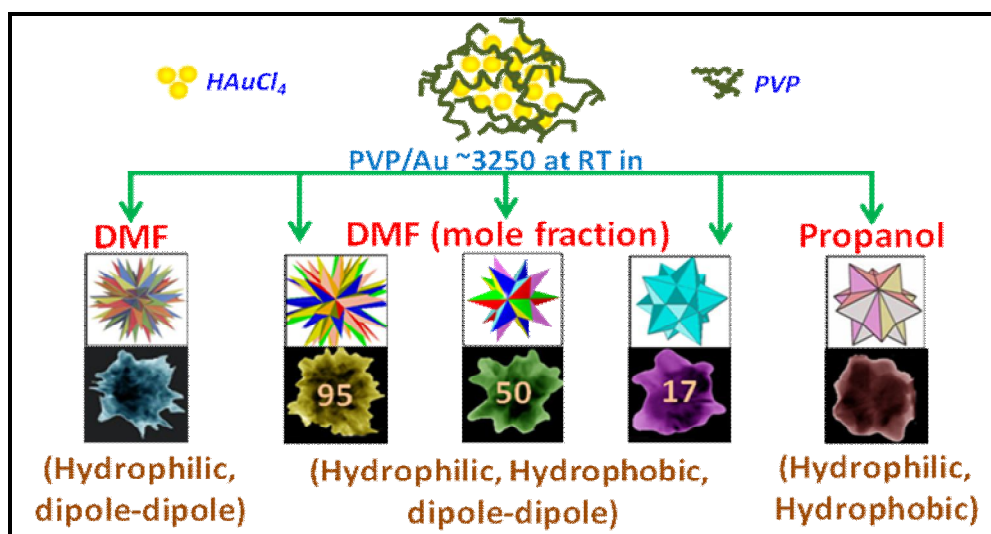
The up-field of PVP, DMF and propanol carbonyl peak in final nanoparticles spectrum (figure 5.16) in comparison to PVP-binary solvent suggesting that upon addition of  $\text{HAuCl}_4$  to this PVP-binary solvent mixture,  $\text{Au}^{3+}$  contend with PVP over the respective dielectric surroundings strongly, allowing further weakening of propanol-PVP hydrogen bonding with simultaneous desolvation of DMF molecules and finally dynamically unstable PVP- $\text{AuCl}_4$  complex disproportionating itself to yield PVP stabilized  $\text{Au}^0$  species.

On the contrary, upon addition of gold precursor to the PVP-propanol system, the observed slight downfield chemical shift of the PVP carbonyl peak (with respect to PVP-propanol, see values in figures 5.15 and 5.16) has been attributed to the fact that the hydrogen bonding between PVP and propanol remains almost intact and further dominated by strong hydrophobic interactions. This kind of composite reduction along with steric stabilization of PVP on the gold seed particles in the binary solvent system exclusively result in the steady/stable anisotropic nanoparticle growth, which has not been possible with any other conventional colloidal growth techniques.

Thus, DMF interacts with propanol by virtue of its better hydrogen bond acceptor ability resulting in both structural as well as packing effects. Mixing of DMF with an alcohol not only induces changes in the dipolar interactions within DMF, but also disrupts either partially or completely the self association of propanol, thereby allowing the essential formation of newer H-bonds between the alcohol and the DMF, which further interacts intuitively with PVP (conformational changes in PVP are inevitable in the DMF-propanol binary system), resulting in the precise size/shape tuning of the gold nanostars, as collectively summarized in the scheme 5.7.

As shown in scheme 5.7, the morphology at different mole fraction of DMF resembles to stellated polyhedra (extended polyhedra in different dimension) of different faces, edges and vertices. This difference in the geometry is result of distinct interaction of PVP in respective solvent mixture.

**Scheme-5.7:** Sequential size/shape tuning/reshaping of the gold nanostars with reference to systematic changes in the molecular interactions of PVP with the reaction mixture (2-propanol as a co-solvent with DMF at different MF).



In case of pure DMF hydrophilic/dipole-dipole interaction dominates where as with increase in propanol to reaction mixture hydrophobic interaction dominates along with hydrophilic interaction with dipole-dipole interaction freeze out and completely vanishes in pure propanol case (signifying that complex network of PVP decreases starting from DMF to propanol in the whole composition range used in the present case). Hence, in case of Pure DMF we get maximum number of faceted stellated polyhedra (PVP inter/intra chain interaction is maximum) there after it decreases with decrease in mole fraction and minimum in pure propanol case.

This is for the first time to the best of our knowledge that a well correlated molecular mechanism of the components in the reaction mixture automatically invokes the nucleation and anisotropic growth of gold nanostructures with reference to the tuning/reshaping of the pristine gold nanostars, the representative samples of which are successfully utilized as novel plasmonic substrates allowing us to study the robust enhancement of SERS signals of various analytes with ease (discussed in chapter 7).

Thus we have utilized a facile/versatile room temperature colloidal synthesis protocol for precisely engineering the morphology correlated plasmonic response of gold nanostructures over the entire visible/NIR spectral range by changing apparent pH of DMF-PVP mixture or by effectively utilizes a simple binary solvent mixture, such as DMF:2-propanol in a much more controlled and simple manner. Yet, both protocols result in tuning of plasmonic response (blue shifting of LSPR) which is in good correlation with their morphology but the driving force for tuning is poles apart.

The presence of NaOH is known to have a large impact on the reaction kinetics of nanoparticle formation due to oxidation of chemically inserted OH species in between or end of polymer chain (nucleation become faster or formation of seed particles), the key factor in regulating the optical properties as well as formation of planar elongated/spheroidal gold nanostructures.

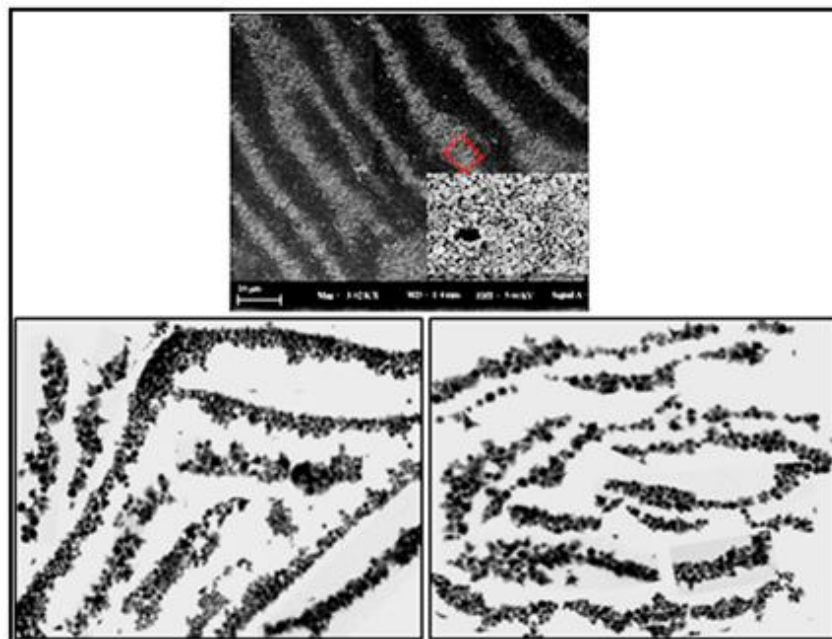
But in the case of co-solvent, foreseeable changes in the conformational changes in the PVP with introduction of 2-propanol to DMF is the major factor to control tuning of gold nanostars in later case, a DMF molecule interacts with propanol by virtue of its better hydrogen bond acceptor ability resulting in both structural as well as packing effects. Introduction of alcohol to DMF not only induces changes in the dipolar interactions within DMF, but also disrupts either partially or completely the self association of propanol, thereby allowing the essential formation of newer H-bonds between the alcohol and the DMF, which further interacts intuitively with PVP (conformational changes in PVP are inevitable in the DMF-propanol binary system), resulting in the precise tuning of gold nanostars. Since in this case reaction is not dominated by kinetic parameter hence the planar elongated/spheroidal gold nanostructures are not feasible while it is possible using NaOH at higher concentration (as governed by kinetic parameter).

We have utilized a facile/versatile room temperature colloidal synthesis protocol for not only the size/shape controlled anisotropic gold nanostructures, but also for precisely engineering their plasmonic response over the entire visible/NIR spectral range based on the fine tuning/reshaping strategy of metal nanocrystals, which has not been possible with conventional nanocrystal growth methods or realized using existing patterning/lithographic techniques. This unprecedented level of wavelength agility is achieved independently by varying the NaOH concentration or using the co-solvent.

The addition of a simple base (like NaOH) to the precursor reaction mixture or careful selection of the binary solvent mixture enhances the reproducible tuning/reshaping of the 3D star/flower-like gold nanostars with controlled precision as consistently revealed through optical absorption and TEM respectively. The modified molecular characteristics of PVP establishes a rational paradigm in better understanding the size/shape transition/evolution of reproducible Au nanostructure morphology studied in detail via NMR and FTIR spectroscopy. Further the ability to produce nanoparticles with wavelength tunable LSPRs opens up new applications in both linear and nonlinear spectroscopy. By tuning the excitation laser to the surface plasmon resonance, it should be possible to maximize the local EM field enhancement.

## Chapter-6

# Self-Organization/Reshaping of Gold Nanostars



Self-organization of reshaped gold nanostars accomplished in a precise manner with reference to the sequence of bromine ion addition into the precursor reaction mixture, the systematic plasmonic and kinetic aspects of which were studied by various correlated spectroscopic and microscopic techniques.

## 6.1 THEME OF THE CHAPTER

Owing to the strong tendency of halide ions to adsorb on the metallic surfaces with ease, they are likely to be useful in the controlled etching of the metal nanoparticle surfaces (by way of their respective surface energies) [302-308]. Quaternary ammonium surfactants having halide counter-ions at their tail end have already been utilized extensively in the synthesis and stabilization of various anisotropic metal nanoparticles [119, 302, 303, 305, 307-309]. Most of these reports employ the seed mediated approach, wherein the chloride ion tailed surfactant complexes were mostly used to obtain a wide range of crystallographic habitats [119, 302, 303, 305, 308-310] while the bromide ion tailed surfactant complexes often asserted to be vital for obtaining well defined gold nanorods (NRs) [116, 119, 303, 307, 309] and the iodide ion based complexes reportedly induces the formation of nanoplates as well as various other platonic shapes [307, 310-313].

Recently, the renowned research groups of Mirkin [119] and Murphy [118] reveal that intermediate CTA-Au-X (X=Cl, Br) complex plays an important role in determining the morphology of Au nanoparticles (in the presence or absence of Ag ions). They further demonstrate that halide counter-ions can modulate the redox potentials of the metal ions, acting as facet-specific capping agents, and/or controlling the extent of Ag under-potential deposition at the nanocrystal surface.

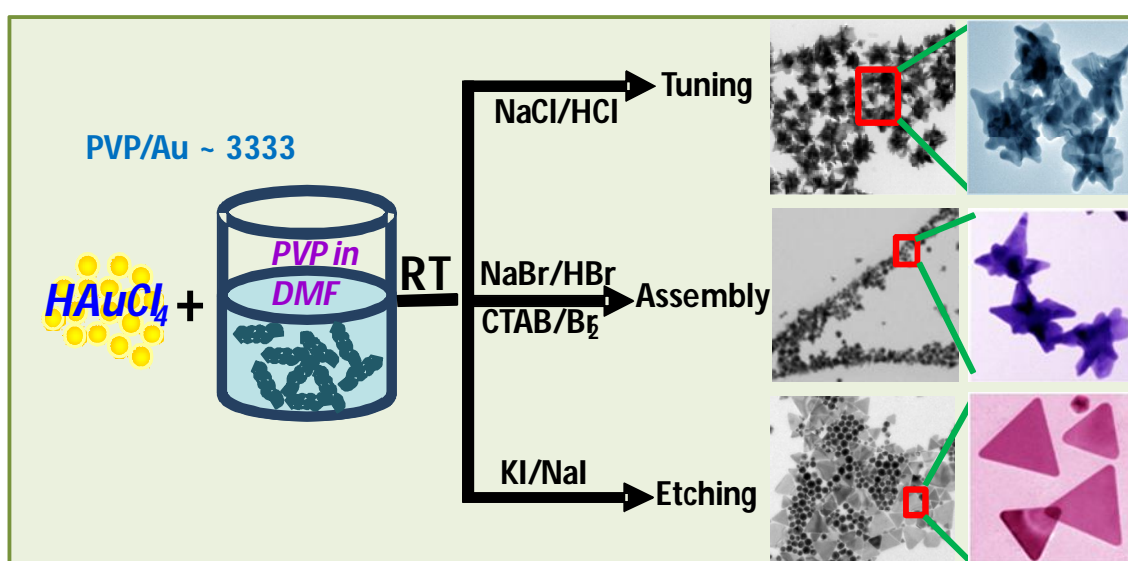
Interestingly very few reports [306, 314, 315] explicitly mentioned the effect of halide ions in the absence of quaternary ammonium surfactants, which clearly leaves a lacuna surrounding the general overall understanding of the nucleation/growth of anisotropic metal nanostructures. In this regard, we present a systematic investigation on the influence of different halide ions, especially the bromide ion (when added *in situ*), envisaging the PVP-Br-Au interaction at the early stages of the colloidal synthesis, which further exemplifies the random/self-organization of anisotropic nanostructures for the first time to best of our knowledge, vital in development and designing the substrates for sophisticated application potentials; whereas the *ex situ* addition of bromide results in reshaping of gold nanostars forms the major theme of our present chapter.

## 6.2 SYNTHESIS PROTOCOL

For *in situ* addition of *halide ions*, a freshly prepared solution of 10 mM PVP in DMF is homogeneously mixed with adequate amount of different halide ions (NaCl, NaBr, HBr, KI, CTAB, Br<sub>2</sub>) of different concentration (as mentioned in text) followed by 0.27 mM tetrachloroauric acid (HAuCl<sub>4</sub>.3H<sub>2</sub>O).

For *ex situ* experiments, NaBr at different concentration is added in preformed Au nanostars centrifuged once cycle in water.

**Scheme-6.1:** Tuning and self-organization procedure of Au nanostructures in the presence of different halide ions.



### 6.3 IN SITU ADDITION OF HALIDE IONS

We have carefully analyzed the effective role of each of the individual inorganic halide ( $\text{Cl}^-$ ,  $\text{Br}^-$  and  $\text{I}^-$ ) ions on introduction into the DMF-PVP system and their exciting results and revelations are appropriately discussed in tune with the literature reports in the following sections.

#### 6.3.1 Effect of Chloride Ions

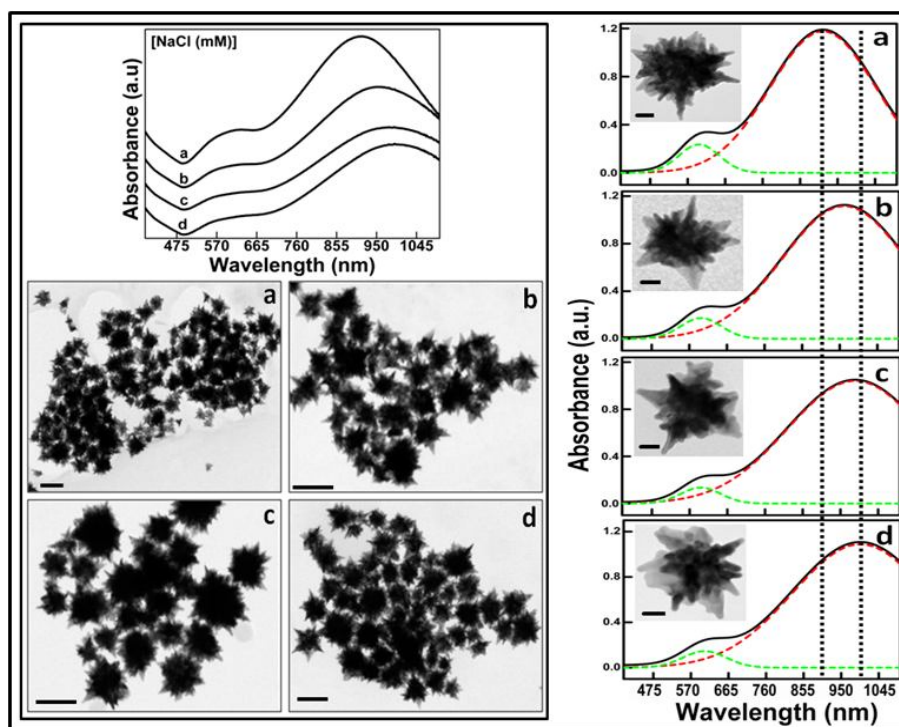


Figure-6.1: Optical spectra (a–d) and their corresponding TEM images (scale bar 200 nm) show the effect of NaCl concentrations on morphology along with its plasmonics. (a) 0.10, (b) 0.25, (c) 0.50 and (d) 1.00 mM NaCl added to the precursor reaction mixture. Multiple Gaussian peak fittings of the modified gold nanostars (the HMTM images of which are shown in the inset with a scale bar of 20 nm) are shown on right hand side. Black (solid) curves are the experimental ones and dotted lines are their respective Gaussian fits. The bandwidth (as shown by the two vertical dotted lines) illustrates the gradual red-shifting of the longitudinal peak position from (a) to (d), analytically signifying the variation in the size/shape and arrangement of the tip/spike like structures in the as-formed gold nanostars with respect to increasing NaCl concentration.

Controlled effect of HCl on the normalization of size/shape control of gold nanostars is studied in detail in chapter 4 and compared with NaCl in the following section. We have observed significant red shifting in the LSPR peaks with sequential addition of mM quantities of NaCl in the precursor DMF-PVP system. The red shift in the longitudinal SPR peak increases drastically with increasing NaCl concentration and finally stabilizing around 1000 nm as shown in figure 6.1.

Gaussian multi-peak fitting (shown by dashed lines in figure 6.1) of the individual optical absorption spectra for different NaCl concentration clearly reveals the broadening of the longitudinal plasmon peak (related to the tips) as well as the flattening of the transverse plasmon peak (corresponding to the central core), in tune with the corresponding TEM images (shown in figure 6.1a-d), illustrating visually the complex rearrangement of broadened tip/spike like structures with a continuum multi-layered core, maintaining its overall structural stability through their cohesive single crystalline nature, albeit with different sizes for increasing basicity of the medium. Whereas with increasing acidity of the surrounding medium i.e., for higher HCl addition in the precursor reaction mixture, as has already been discussed in chapter 4 sequential dissociation of the tip/spike like structures from the complex 3-D gold nanostars begins, finally condensing towards the common space conserved spheroidal morphology.

Moreover, it is interesting to note that with NaCl addition, uneven nucleation of seed particles take place as clearly depicted by the bimodal distribution in the TEM images (see figure 6.1(a-d), average diameter 90 and

60 nm respectively). Preferential solvation of the  $\text{Na}^+$  ions by DMF takes place [270] and chloride ions maintain the equilibrium concentration of  $\text{AuCl}_4^-$  in the solution (Le Chatelier principle), thereby drastically decreasing the nucleation/growth rate. It is necessary to mention here that either with HCl or NaCl addition, the inter-particle distance between the as-formed Au nanostructures invariably decreases, signaling the fact that inter-particle coupling enabled plasmon resonances predominate in these gold nanostructures.

### 6.3.2 Addition of Bromine/Bromide Ions

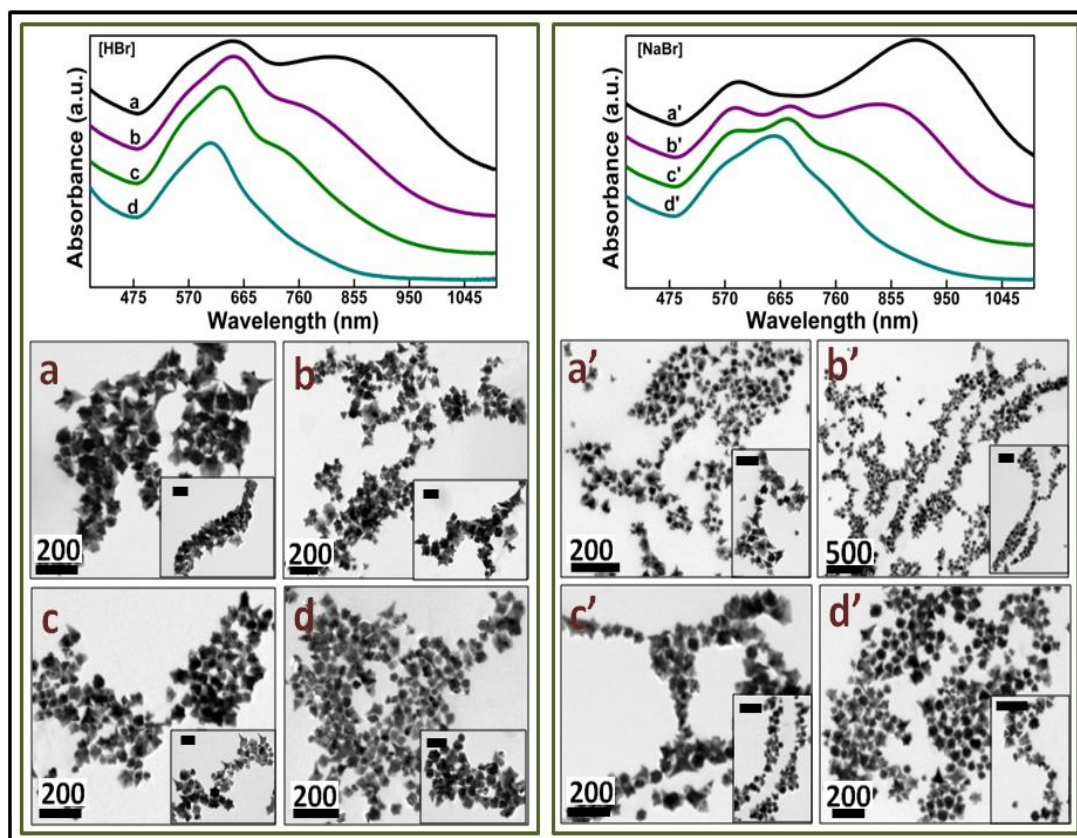


Figure-6.2: The increasing addition of (a, a') 0.20, (b, b') 0.40, (c, c') 0.60 and (d, d') 0.80 mM HBr and NaBr respectively to the precursor reaction mixture clearly influences the formation as well as the self-organization of anisotropic Au nanostructures, as prominently revealed by the optical spectra and their corresponding TEM images (scale bar 200 nm with inset scale bar 100 nm).

Significant differences in the optical absorption spectra were observed, when ample amount of NaBr or HBr (brominated halide ions) were added to the DMF-PVP complex, as distinctly enumerated in figure 6.2, as compared with that pristine Au nanostars, indicating the uncommon behavioral pattern imparted by the stern action of the bromine ions into the as-formed anisotropic gold nanostructures. The near-field interactions between nanoparticles assembled in 1/2-D arrays lead to large change in their interactive plasmon resonances depending on their existing configuration in comparison with those of discrete nanoparticles.

Both the so-called longitudinal LSPR mode (related to the tips) and transverse LSPR mode (corresponding to the central core) were blue shifted along with gradual decrease in the intensity of longitudinal LSPR mode (both in HBr and NaBr), strongly suggesting the effect of decreasing tip/spike length, their size and number, thus restructuring the overall morphology of the individual nanoparticles itself. The anisotropic broadness in the plasmonic peaks essentially (more in case of NaBr as compared to HBr) depict their highly coupled nature, associated with the collective participation of gold nanoparticles in an ordered manner (mostly through tip-to-tip rather than length-by-length, as seen from their TEM images in figure 6.2), as envisaged through *in situ* and impromptu PVP-bromine interaction in the surrounding medium (which decreases at higher NaBr/HBr concentration), the only variable parameter available within the system that warrants detailed justification, validating the formation of such stable nanostructure organization even in the solution under ambient conditions.

Hence, in terms of assimilating the extinction spectra for different HBr/NaBr concentration, each representative spectrum were deconvoluted utilizing Gaussian multi-peak fitting procedure as shown in figure 6.3 with dashed lines. The main observation inferred here is systematically explained as follows.

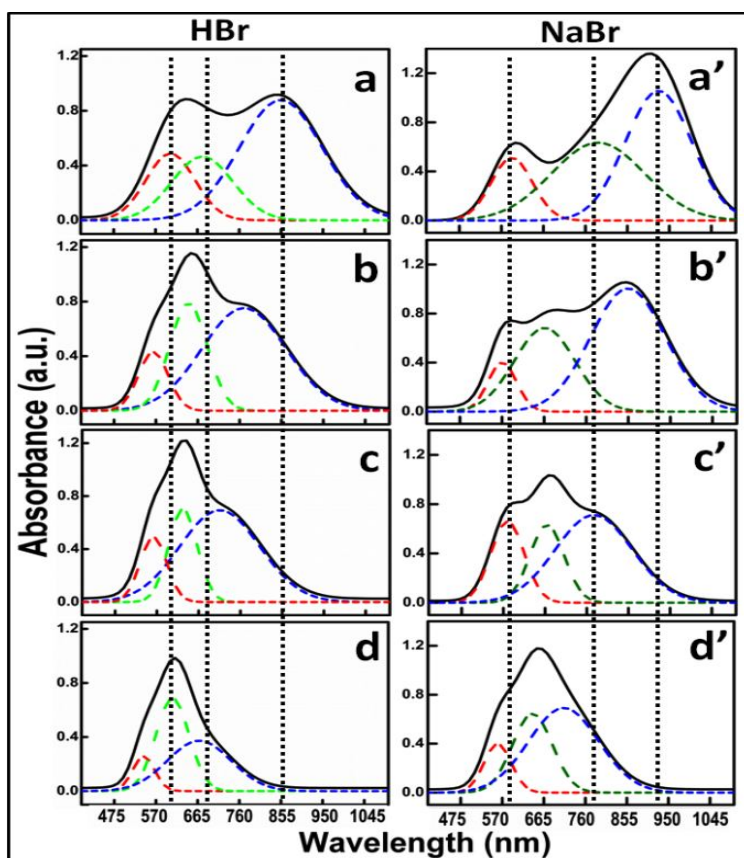


Figure-6.3: Multiple Gaussian peaks fitted optical absorption spectra of the self-organized anisotropic gold nanostructures as shown in figure 6.2 respectively. Black (solid) curves represent the experimental spectra and the dotted lines are their Gaussian fits. The anisotropic damping and formation of new plasmon peaks from (a) to (d) demonstrate clearly the convoluted change in morphology along with a sophisticated 2D self-organization with increasing HBr concentrations.

Deconvolution of these individual asymmetrical plasmon peaks with different HBr/NaBr concentration (figure 6.3) qualitatively estimates their extent of deviation from spherical symmetry with their random self-organized configuration in an intriguing fashion, in complete collusion with the observed TEM images (figure 6.2). To our surprise, we identified that 2-D organization is preferred with HBr, while tip-to-tip or 1-D assembly is favored with NaBr addition, further accounting for the dynamic strength of the solvent (DMF) interaction with the cationic counterpart of the bromine ion in precisely engineering the unconventional anisotropic assembled configuration, even in the absence of any other external energy resources.

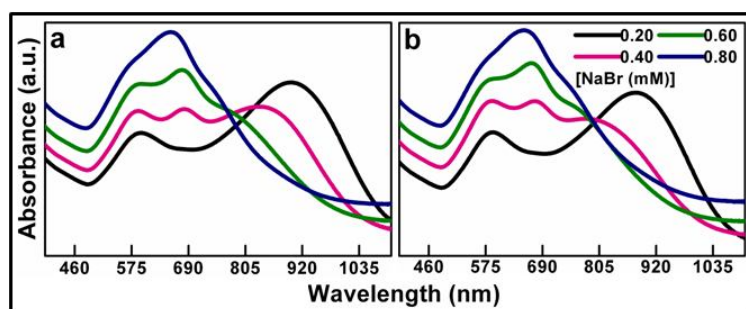


Figure-6.4: The inherent stability and the strength of self-organized anisotropic gold nanostructures formed in the presence of different NaBr concentrations, as clearly revealed by the reproducible absorption spectra (a) after 1 day and (b) after 8 months of formation.

The exclusive comparison of the optical absorption spectra of gold nanostructures formed with different NaBr concentration (after 1 day and 8 months of preparation, see figure 6.4) illustrates conveniently the stability of these novel assembled gold nanostructures, which can be directly utilized for practical application purposes.

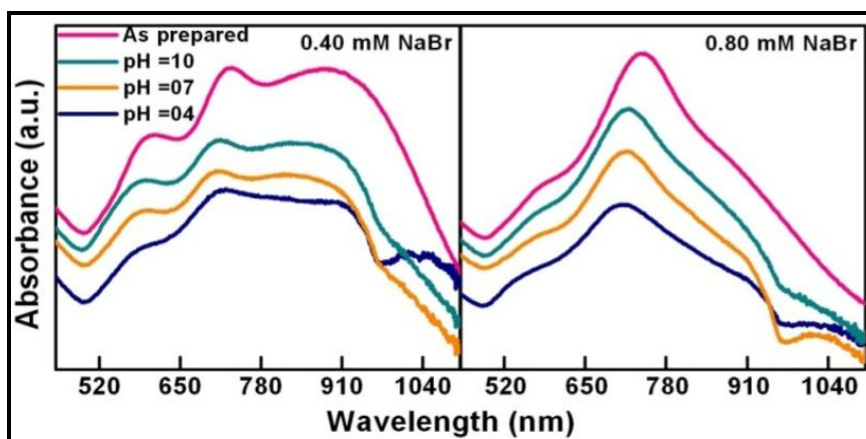


Figure-6.5: Optical spectra of Au nanostructures prepared at different reaction condition under various pH conditions. The unchanged SPR peaks at different pH indicate the stability of nanostructures. The centrifuged samples are re-dispersed in different buffer solution and then their optical spectra are recorded. A small dip around 960 nm is due to water-DMF complex.

The pH stability of these as-formed assembled gold nanostructures was conveniently demonstrated as shown in figure 6.5, where the unchanged surface plasmon peaks at different pH establishes their inherent stability and robustness.

Also, the optical spectra of gold NPs obtained at different NaBr concentration (see figure 6.6) shows elusive linear response in LSPR peak position shifts with respect to different refractive indices, which demonstrate that the as-formed Au NPs are highly stable in different dielectric environments.

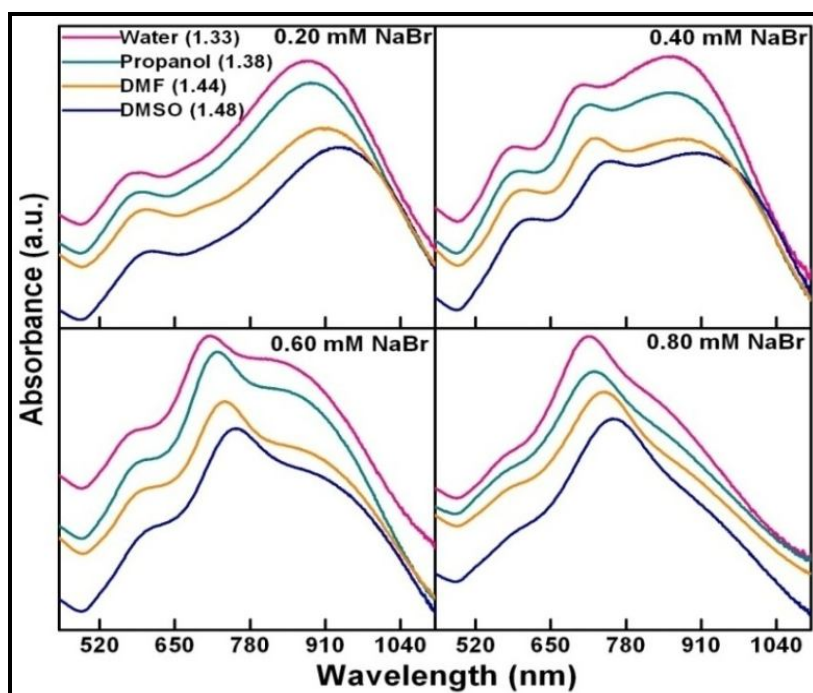


Figure-6.6: Optical spectra of Au NPs at different NaBr concentration in different solvents showing the linear shifts in LSPR peak position with respect to different refractive indices, which demonstrate that the as-formed Au NPs are highly stable in different dielectric environments. (The optical spectra were recorded by dispersing the thrice centrifuged pellets of the as-prepared Au NPs in different solvents).

Since self-organization predominates with the addition of bromine ions, as confirmed from the variation in hydrodynamic diameter obtained through dynamic light scattering (DLS) measurements shown in figure 6.7, effectively matches with our TEM images (figure 6.2), asserting the simple fact that the organized nanoparticle chain length is maximum at an optimal concentration of 0.4 mM NaBr, which randomizes for lower/higher concentration of NaBr under the present experimental conditions, thereby encouraging us to investigate the suggestive/irreversible role of bromine ions in the formation/assembly of metal nanostructures.

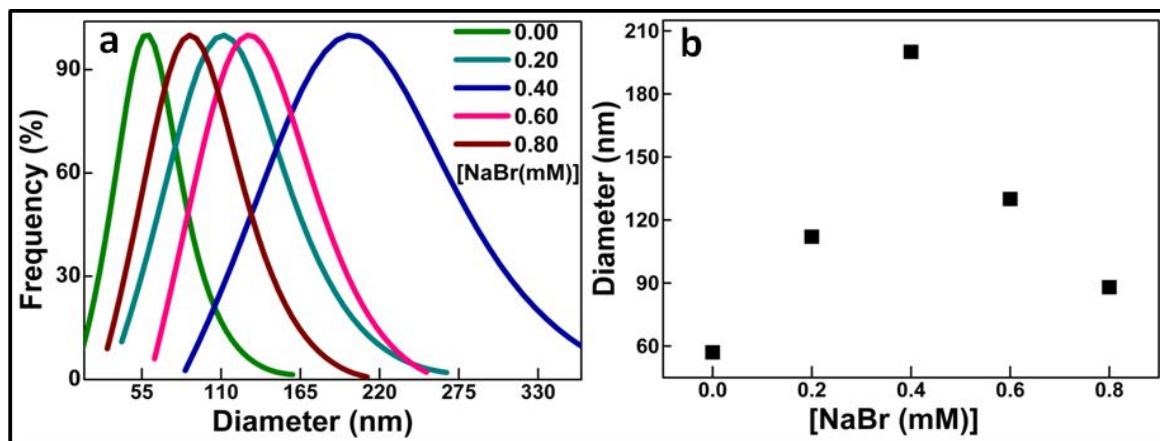


Figure-6.7: (a) Normalized hydrodynamic diameter of the as-formed Au nanostructures measured by dynamic light scattering (DLS) as shown. (b) The variation of the hydrodynamic diameter illustrates the coupling strength between adjacent Au nanoparticles resulting in stronger/longer chain length (the maximum of which appears for an optimal concentration of 0.4 mM NaBr as shown), further in direct confirmation with our TEM images given in figure 6.2.

Furthermore, UV-Vis spectra of solution and nanoparticulate thin film (drop-casted or spin-coated from the same solution, see appendix A6.1) shows similar spectra well in agreement with the standard argument that infinite dilution of the solution results in a film.

To further ascertain the character of specific charge-transfer interaction of the polymeric stabilizer with the Au metal ions in the presence of NaBr with high clarity, we intuitively utilized  $K_2AuBr_4$  (0.27 mM of which contains 1.08 mM of  $Br^-$  ions) as the metal precursor and as expected, the results were very much similar to that of 1 mM NaBr case with  $HAuCl_4$  as metal precursor (figures 6.8 and 6.2).

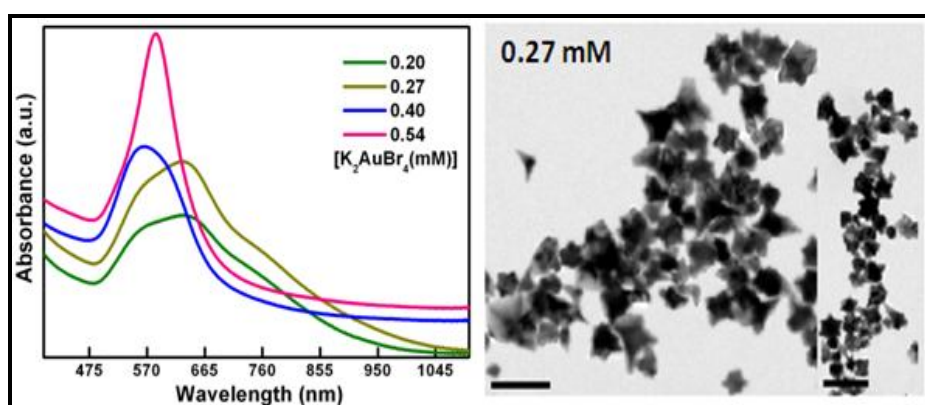
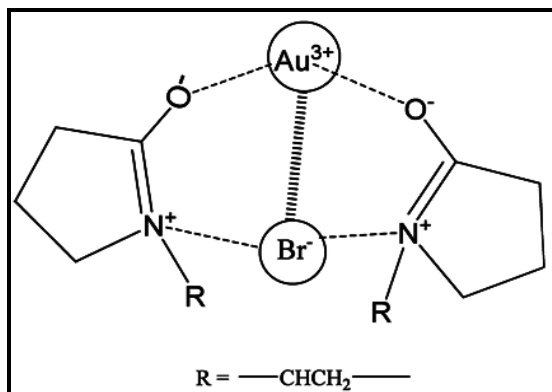


Figure-6.8: Effect of  $K_2AuBr_4$  as the gold precursor at different Au ion concentration in the pristine DMF-PVP (PVP 10 mM) complex, is shown in the optical absorption spectra with respective TEM images for 0.27 mM Au concentration (Scale bar 200 nm). Note the closely spaced anisotropic gold nanostructures signify the PVP-Br-Au interaction.

Thus, we observe the persistence of the assembled gold nanostructures in a simple but efficient manner, further establishing the formation of some PVP-Au-bromo complexes (see scheme 6.1) in conjunction with the DMF-PVP complex, thereby leading to the formation of self-assembled gold nanostructures.

**Scheme-6.1:** Plausible PVP-Au-bromo complex interaction, leading to the formation of organized nanostructured networks.



Hence, to assert the individual role of cations and bromine ions, control experiments were carried out by adding separately the well known surfactant CTAB of 0.50 mM, a well known surfactant with long chain cationic part terminated with bromine ions) and molecular Br<sub>2</sub> of 0.50 mM to the DMF-PVP complex as shown in figure 6.9 and the results are compared with NaBr.

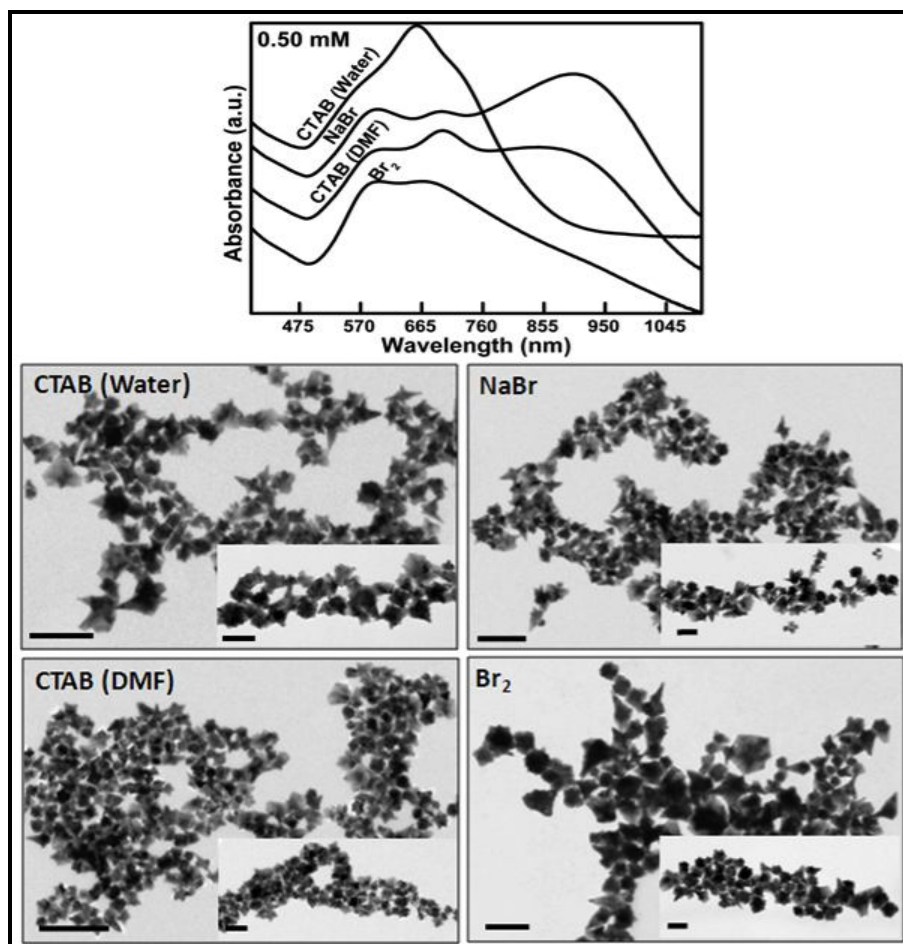


Figure-6.9: Addition of 0.50 mM CTAB in water/DMF, NaBr and Br<sub>2</sub> into the DMF-PVP complex resulting in the formation of self-organized anisotropic Au NPs as revealed by the optical absorption spectra and their corresponding TEM images ((Scale bar 200 nm, inset 100 nm).

As expected, we observe the self-organization of modified gold nanostars in all the cases, but with varied strength, emphasizing the importance of bromine ions in intuitively assembling the gold nanostructures with necessary support from the amphiphilic PVP polymer network during the nucleation/growth stage itself.

Effect of different molecular weights of PVP (shown in appendix figure A6.2) is also investigated on the optical spectra with their correlated morphology in the presence of NaBr emphasizing the extensive role of PVP in self-organized gold nanostructures.

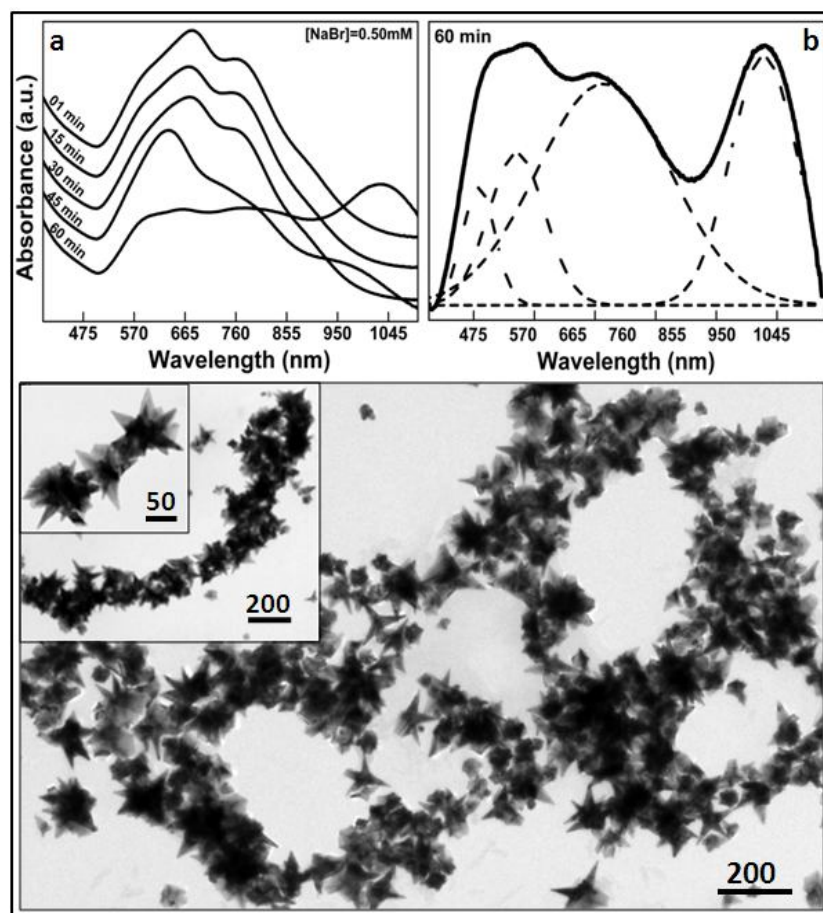


Figure-6.10: Kinetic optical spectra with addition of NaBr at different interval of time in reaction mixture along with respective TEM image at 60 min interval time.

Since self-organization in the presence of bromine ion happens with deviation in morphology of gold nanostars although it is random organization of anisotropic nanoparticles. Next, our focus is on the synthesis of organization of these gold nanostars without much divergence in their morphology so as to use them for better potential application. In our chapter 4, we have defined nucleation and growth region through kinetics of UV-Vis spectra of gold nanostars. Keeping in mind; Br effect and the nucleation and growth regime we add 0.50 mM NaBr in reaction solution after different intervals of time and their effect can be seen from figure 6.10. Addition of NaBr in the nucleation region does not have much deviation from the case, where NaBr is added in DMF-PVP complex. Surprisingly with addition of NaBr in growth region (around 60 min), optical spectra shows astonishing behavior as seen from figure 6.10, keeping the gold nanostars morphology almost intact (some polydispersity in size is observed). Upon deconvolution, this peak can be fitted into four well defined peaks positioned at 583, 660, 780 and at 1030 nm respectively arising due to hybridization/multi-polar resonance of inter-particle coupling, seen clearly from TEM images. The extension of plasmonic eigen mode to near IR can be utilized many practical application.

Furthermore, controlled inter-particle spacing in self-assembled metal nanostructures is achieved by encapsulating with organic shells of varying thicknesses or by using stimuli-responsive polymer ligands or by varying the type and location of ligands on the surface of nanoparticles [316-318]. This is also well correlated with the appearance of a new hump like feature in the near infra-red region (700-1100 nm) of the extinction spectra along with the existing transverse and longitudinal SPR peaks, indicating strong near-field plasmon coupling among the assembled anisotropic metal nanoparticles, that collectively behave as a continuous elongated quasi-1D nanostructure supporting multi-polar mode resonances in analogy with longer

metal nanowire structures. Importantly, the perseverance of these spectral features emphasize the robustness of the plasmon coupling and its ability to tolerate defects within the sub-nm spaced assembly of nanoparticles, thereby providing an unique strategy for promoting complex sub-wavelength optical using bottom up design strategies [318-323].

### 6.3.3 Effect of Iodide Ions

It is interesting to note that with addition of KI to the precursor reaction mixture; large numbers of flat triangular nanoparticles were formed along with spherical nanoparticles as clearly seen from the TEM images (figure 6.11) which are well correlated with the optical spectrum having plasmon resonance extending towards near IR region along with other plasmon band centered at 550 nm. The formation of flat gold nanotriangles happens due to the introduction of iodide ions, which inherently inhibits the formation of complex 3-D gold nanostars by sequentially etching the as-formed nanoparticle surface resulting in flat elongated gold nanostructures.

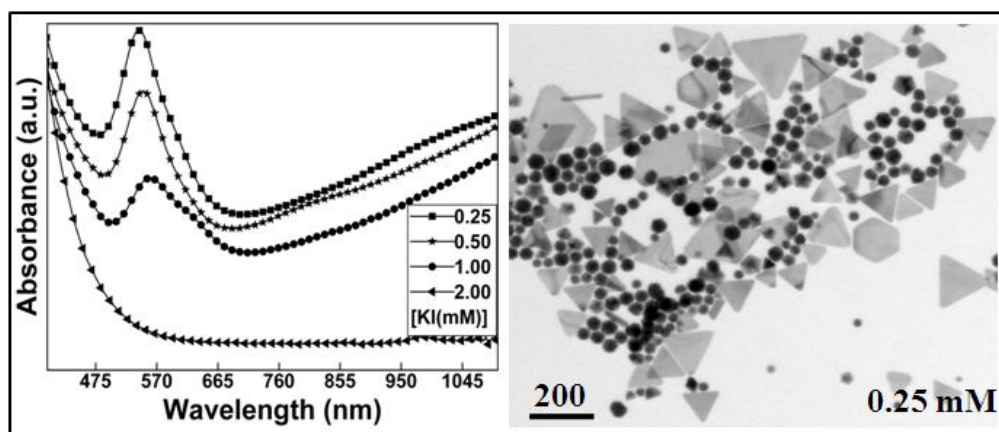


Figure-6.11: The effect of addition of KI on the formation of anisotropic gold nanostructures are illustrated using optical spectra and their representative TEM image (scale bar is in nm). The increased absorbance (extended into the near IR region) strongly reveals the increased etching effect of iodide ion with increasing concentration. Note that for iodide ion concentration higher than 1 mM, no gold nanoparticles were obtained, as shown by the flat absorbance curve.

Higher concentration of iodide ions restrains the growth of Au nanoparticles as no SPR is observed even after several months of addition of KI ([KI] = 2 mM).

Thus, in overall perspective, the halide ions present in the solution forms the Au-X (X = halide) complex, thereby strongly affecting its reduction potential (in the decreasing order Au-Cl > Au-Br > Au-I) and binding strength (increasing as Cl<sup>-</sup> < Br<sup>-</sup> < I<sup>-</sup>), subsequently inhibiting the nucleation as well as growth of gold nanoparticles by way of halide ion adsorption on the metal surface. From our present experimental results, it can be easily inferred that along with the polymer-halide ion interaction, the gold chloro complex facilitates the formation of 3-D anisotropic nanostructures and the gold bromo complex initiates the nanoparticle network formation, while the gold iodo complex extends the formation of planar Au nanostructures.

In our present work, we firmly believe that the surface chemisorbed PVP molecules not only dictates the individual size/shape of the as-formed anisotropic gold nanostructures but also effectively co-ordinates their *in-situ* as well as intuitive programmed/directed organization in the presence of sufficient amount of NaBr/HBr, the mechanistic/topological aspects of which hasn't been verified or overlooked upon till now. PVP ability in giving rise to the non-equilibrium coupled integrative self-assembly to produce extended and multiple length scale nanostructured networks has been carefully identified and understood for the first time to the best of our knowledge. It is further proposed that our as-prepared self-organized metal nanostructures can be directly utilized as plasmonic waveguides, particularly in view of the fact that the adjacent gold nanoparticles were mostly attached through their sharp tips, allowing them to transport EM energy over reasonably long distances far below the diffraction limit and hence minimizing the propagation loss to a large extent, highlighting the significance of our present bottom-up approach utilizing colloidal chemical synthesis procedures.

## 6.4 EX-SITU ADDITION OF HALIDE ION

### 6.4.1 Effect of NaBr

Most of available literature reports till now deals with the effect of bromine/halide salt on post synthesis [324-326] yet with CTAB there are plenty of reports are available where it act as a shape directing agent [117, 119, 302, 303, 305, 307, 308, 310].

As a major limitation, different shapes cube, octahedron, tetrahedron, icosahedron, bipyramid, plate, disk, bar and rods are encased by convex surfaces as detailed in review by Younan Xia [327, 328]. Our Au nanostars are multi-branched nanoparticles with sharp tips (having high convex area) having undefined periphery (High concave area) due to irregular crisscross attachment of tips which display extremely increasing plasmonic application but require optimization.

Previously Luis and his group reported that in these Au nanostars reshaping is not feasible in the presence of small inorganic molecules such as NaBr but undergo reshaping using CTAB and shows gradual transition from 3D nanostar morphology (formed by seed mediated process) into quasi-spherical gold nanoparticles, which has been ascribed to the presence of both Br and the integrated chain length of CTAB [292].

To make sure this nascent concept since *in-situ* NaBr has large impact, we have added small amount of NaBr to the preformed colloidal Au nanostars (prepared by seed mediated synthesis and one time washed with water after centrifugation) and found that reshaping takes place for sure revealing a continuous blue-shift of the LSPR tip-mode over time, which finally (after 16 hrs) seems to merge with the core mode, resembling the spectrum of Au spheroids, but slower as compared with that of CTAB as shown in figure 6.12. With their highest CTAB concentration (0.5 mM, 2 washing cycle) reshaping is negligible.

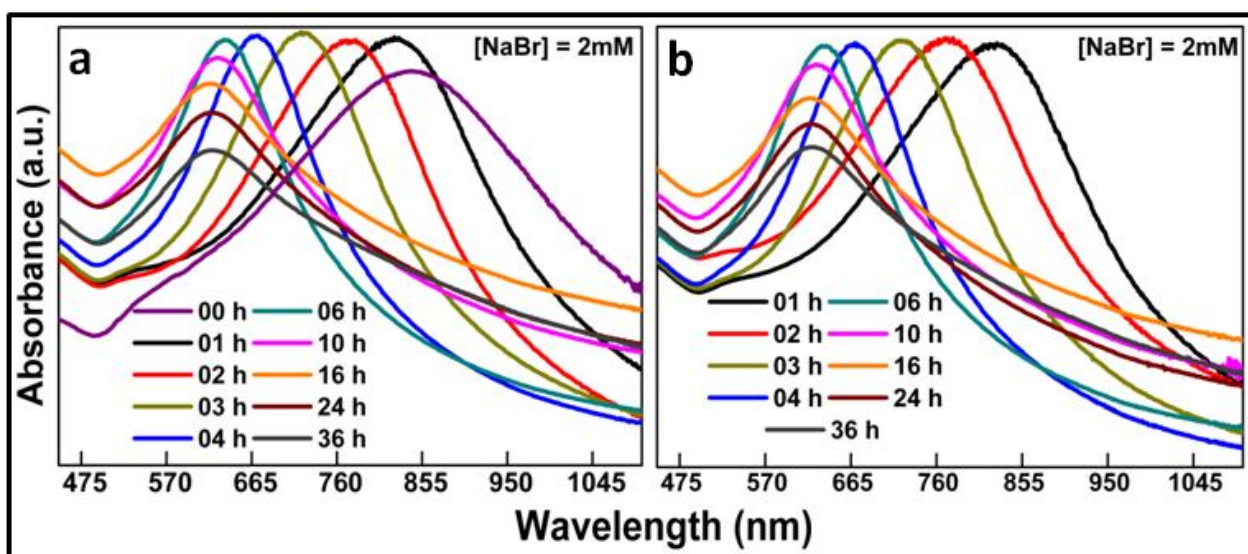


Figure-6.12: Spectral time evolution of an Au NPs colloid (centrifuged once) in the presence of NaBr 2 mM at different interval of time taken (a) immediately (b) after 2 months.

Further the reaction kinetics can be quenched at any point of time by simple addition of  $\text{AgNO}_3$  to reaction mixture (see figure 6.12), effectively neutralizes the effect of bromine ions thus provide tight control over Localized SPR. The process is slow enough from previous reports, so that reshaping can be blocked at any stage, thus allowing a better tight control over the morphology and fine tuning of the LSPR tip mode in the colloid. TEM characterization at different intermediate stages (see figure 6.13) immediately reveals the reshaping process until the almost complete loss of initially sharp tips.

It is observed from the TEM sequence that morphology degradation of the tips occur to be smooth thereby, allowing the tips to preserve their mono-crystalline nature while no twin boundaries are observed for any reshaped samples. Furthermore with NaBr addition tips become shorter and broader over time, whereas the core volume progressively increases.

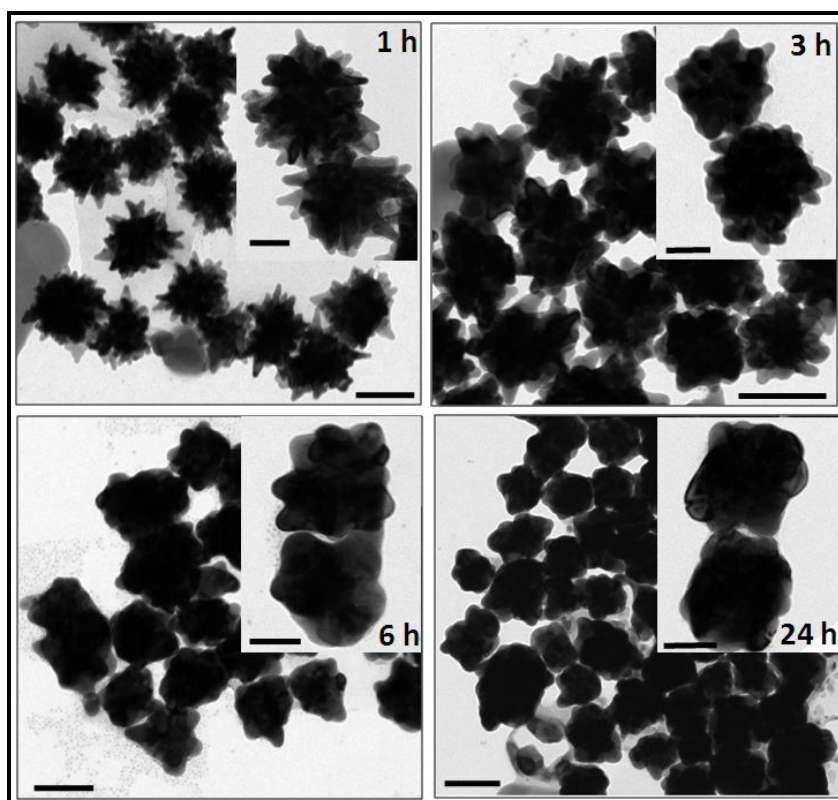


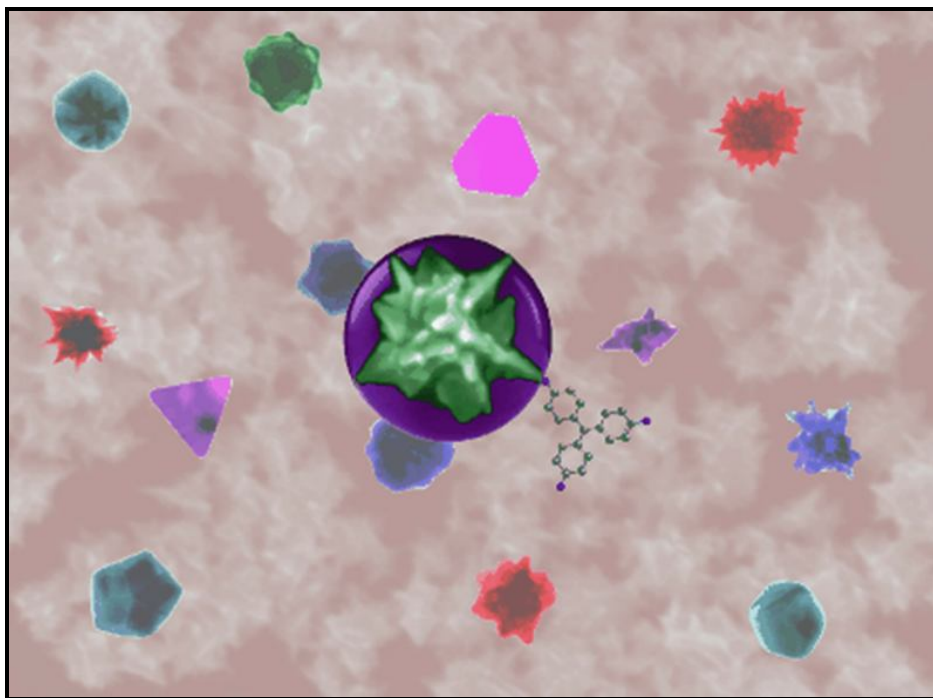
Figure-6.13: TEM images (scale bar 100, inset 50 nm) of Au Nps in the presence of NaBr 2 mM on the preformed Au nanostars (centrifuged once in water) at distinct interval of time illustrating the reshaping process from tip like structures to quasi spherical NPs.

Essentially bromine ion so as sequentially trim the anisotropic morphology which can be very well understood as the dissolution of weakly bound gold atoms at high convex curvature (at edges) and their simultaneous re-deposition at concave areas. It is well known that certain anisotropic shapes have higher Gibbs energy and can reshape into more stable ones [328]. Since, the Gibbs free energy of a concave region is always lower than that of a flat or convex region [328]. When dissolution occurs on the surface of a nanocrystal in an inhomogeneous pattern, the region experiencing faster dissolution (in present case is the tips) will deposit into a concave structure to help in minimizing the total surface energy and hence happening in our case too.

It is worth pursuing to ensure that the colossal breaking of the entangled nature of this universally soluble homogeneous polymer PVP in the presence of halide ions, especially the bromine ions, should essentially be the major factor in delineating the spatio-temporal organization of highly anisotropic metal nanostructures into long chain or any other patterned/templated shapes with ease even under normal conditions. And also when used on the preformed nanoparticles, smooth reshaping takes place depending on their reactive strength further facilitates the fine tuning of frequency related to tip mode.

## Chapter-7

# Shape Selective Surface Enhanced Raman Measurements



SERS is a powerful vibrational spectroscopy technique that allows for highly sensitive structural detection of low concentration analytes. Here in the present chapter shape effects of gold nanoparticles on SERS properties are investigated and found that different-shaped gold nanoparticles possess different SERS properties. Further results are compared for different dye molecules further extended to different SERS substrates (silicon and ITO).

### 7.1 SHAPE SELECTIVE SERS ENHANCEMENT

In chapter 3, HMTEM images (figure 3.2) demonstrates clearly the deviation from sphericity in the following order; *methanol* < *chloroform* < *ethanol* < *propanol* < *DMF*. These as-prepared anisotropic size/shaped Au NPs of different plasmonic properties are successfully utilized to investigate the role of surface roughness/sharpness on the SERS efficiency; so as to expedite them as promising SERS substrates with ease.

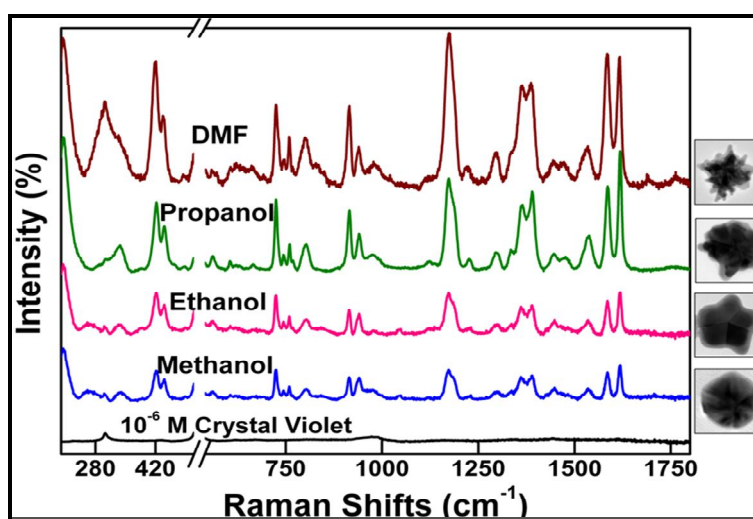


Figure-7.1: SERS signals obtained for pure CV having fixed concentration  $10^{-6}$  M adsorbed onto the as-prepared gold nanoparticles obtained in Methanol, Ethanol, 2-propanol and DMF solvent. The observed vibrational modes of CV show large enhancement for anisotropic nanoparticles obtained in DMF and propanol in comparison to quasi-spherical or decahedra nanoparticles attained in methanol or ethanol respectively.

As a case study, we present SERS data (figure 7.1) performed using the analyte CV, at a concentration of  $10^{-6}$  M coated on the monolayer surface of our as-prepared Au NPs. The different enhanced Raman peaks of the dye molecule, CV, are tabulated with reference to their molecular origin as shown in table 7.1 [280, 329].

**Table-7.1: Raman band assignments corresponding to various modes of CV**

Mode (cm <sup>-1</sup> )	Band assignments
201	breathing vibration of the central bonds
420	Central C <sup>+</sup> -phenyl and ring skeletal out-of-plane vibrations
724	C-H out-of-plane ring bending vibrations
911	ring skeletal vibration of radical orientation
1170	ring C-H bending and
1362, 1387	N-phenyl stretching vibrations
1584, 1615	ring C-C stretching

Crystal Violet

Assuming that all the CV molecules contribute equally, it is enthralling to observe that the SERS signal intensity of adsorbed CV dye molecule is typically weak for quasi spherical particles in methanol and

ethanol while it increases greatly in propanol and reaches maximum in case of DMF as seen from figure 7.1 and table 7.2 (enhancement factor (EF) is calculated (based on reports by Stefania Mura et. al. [330])).

**Table-7.2: Showing the SERS EF calculated for different shaped Au NPs obtained in different solvent at PVP/Au~3250**

System	Enhancement Factor (EF)
DMF	$1.90 \times 10^4$
Propanol	$1.20 \times 10^4$
Ethanol	$0.3 \times 10^4$
Methanol	$0.1 \times 10^4$

The stronger enhancement for nanostars obtained in DMF (the multi-branched nanostructures) compared with others NPs (figure 7.1) is likely due to the obvious structural differences of the NPs. Because of anisotropic shapes of gold nanostars, most of the SERS signal enhancements ascribed to their aesthetics that possesses very efficient SERS-active sites (such as the sharp edges/tips), with the dye molecules preferentially adsorbing onto such sites making the surface roughened branched NPs very attractive as SERS labels for biological imaging, as well as for chemical/bio-analytical sensing. The higher surface roughness enables photons give rise to complex multiple scattering and hence large increase in Raman signals.

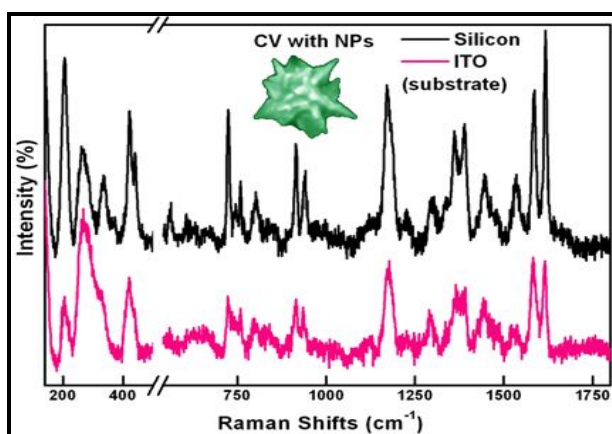


Figure-7.2: SERS signals obtained for pure CV for  $10^{-6}$ M concentration, adsorbed onto the monolayer of as-prepared Au nanostars at different substrate showing clearly the substrate effect on Raman enhancement.

Moreover it is interesting to note that SERS signal are more for equal molar of CV molecules in case where monolayer of NPs at air-water interface is lifted at silicon compared to ITO substrate as shown in figure 7.2.

As we have obtained the maximum SERS signals for the gold nanostars. Hence we have tested it for Raman enhancement for methylene blue (MB) (see figure 7.3) also and found enhancement is there but less comparison to gold nanostars. It suggests that enhancement will be distinct for different analytes depending upon its binding ability to NPs.

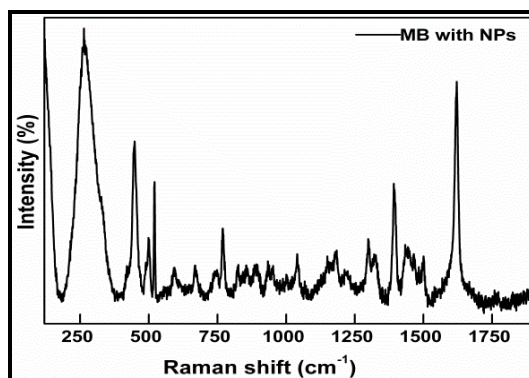


Figure-7.3: SERS signals obtained for pure Methylene Blue (MB) having fixed concentration  $10^{-6}$  M adsorbed onto the as-prepared gold nanostars obtained in DMF.

In chapter 5, we presented fine tuning of the plasmonic signatures of 3-D complex Au nanostructures using binary solvent mixture (DMF:Propanol) in the different ratio (figures 5.12/5.13). This unusual size/shape transformation strategy of gold nanostructures yields precise tuning of their respective plasmonic characteristics over the entire visible/NIR spectral range, the representative samples of which are successfully utilized as novel plasmonic substrates allowing us to study the tunable enhancement of SERS signals of analyte CV with ease, the preliminary measurements of which are systematically illustrated in the following section.

The corresponding Raman signals of CV ( $10^{-6}$  M) were greatly enhanced because with the assistance of a plasmonic substrate. Assuming that all the CV molecules contribute equally, it has been demonstrated that the maximum SERS enhanced signal is obtained for pristine gold nanostructures (see figures 7.4 and 7.5), which first decreases (until the MF (DMF) = 33) and eventually starts increasing with higher propanol volume (table 7.3).

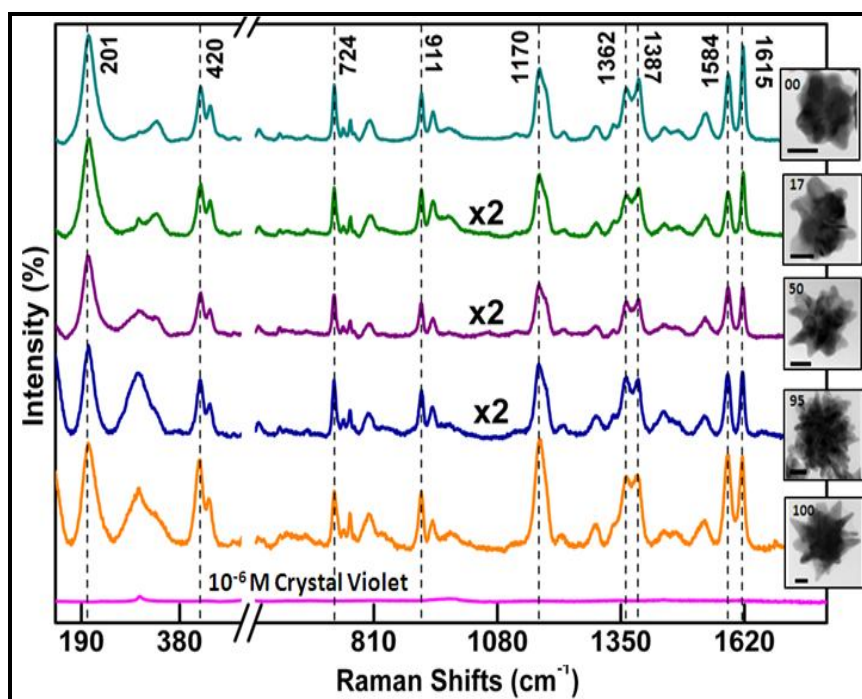


Figure-7.4: SERS Raman spectra of  $10^{-6}$  M crystal Violet without and with Au nanostructures obtained at different MF (DMF). TEM image scale bar is 20 nm.

The strong enhancements observed for the central carbon atom, nitrogen atoms and  $\pi$  electrons in the phenyl ring of the dye molecule, crystal violet (see table 7.1), suggest strong substrate-analyte interaction, which intrinsically depends upon two major factors; one is the surface roughness of the nanoparticles and the other is the inter-plasmon coupling-junction between two nanoparticles.

**Table-7.3: Showing the SERS EF calculated for different mole fraction of DMF which signifies the important of different size/shape of metal nanostructures.**

DMF (MF)	Enhancement Factor (EF)
100	$1.90 \times 10^4$
95	$0.60 \times 10^4$
66	$0.34 \times 10^4$
50	$0.43 \times 10^4$
33	$0.31 \times 10^4$
17	$0.50 \times 10^4$
00	$1.20 \times 10^4$

Hence, in the case of pristine gold nanostructures, the EM field is maximum because of its inherent surface roughness, whereas in the case pure propanol, the smaller particle size/higher surface area results in the formation of increased number of possible *hot-spots* (see figure 7.5).

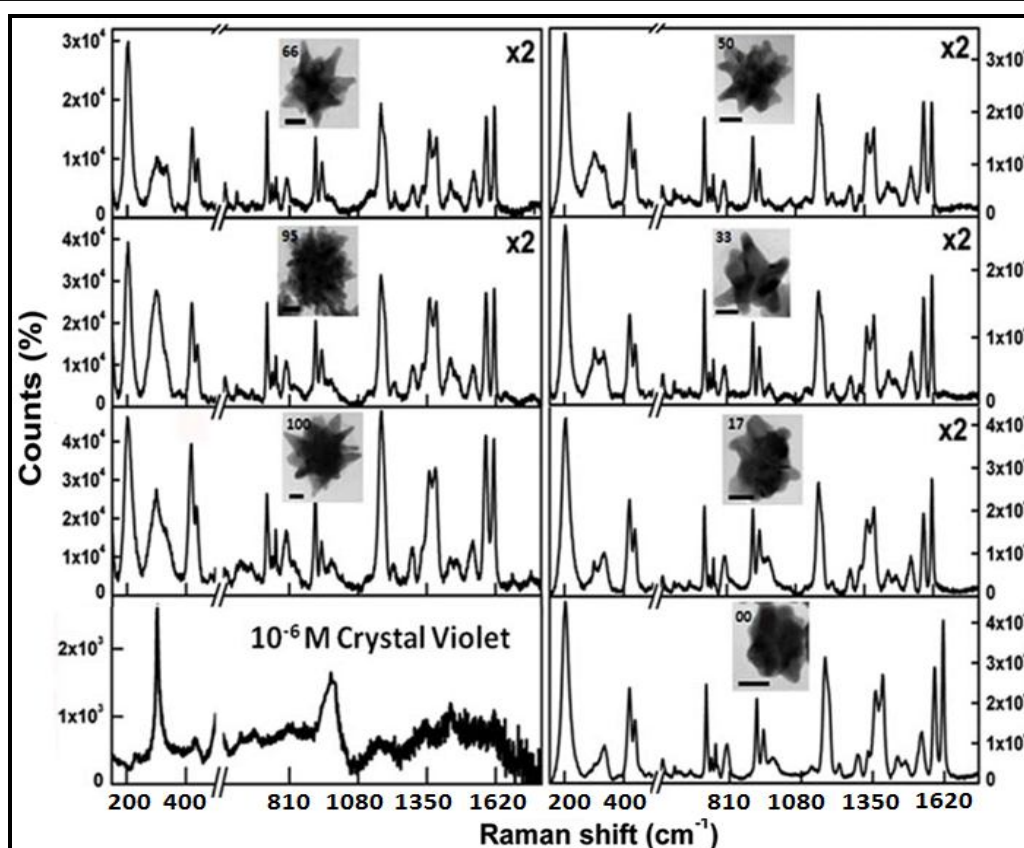


Figure-7.5: SERS Raman spectra of  $10^{-6}$  M crystal Violet without and with Au nanostructures obtained at different mole fraction (DMF) plotted separately. Some of spectra are multiplied by 2 for clarity.

Consequently, we firmly believe that the precisely controlled nanoparticle morphology along with their structurally modified rearrangement on a substrate entrusts the responsibility of maximizing the SERS signals to large possible extent. Our future plan is to quantitatively identify the specific role of the plasmonic substrate as well as the analyte in the SERS enhancement in terms of excitation wavelength, different analytes/concentration etc.

## Summary of Book

## **SUMMARY OF THE PRESENT BOOK**

The preparation of nanometer-scale metal particles in solution is a major subject in the field of nanochemistry because of their unusual optical properties (typical colors coming from gold and silver nanoparticles) and their vast potential applications. It has been shown that the oscillation of electrons at the metal dielectric interface is strongly dependent on the size and shape of metal NPs.

In this book we reviewed some facts related to gold/gold complexes. We focus on the fundamentals of plasmonics and optical properties of noble metals. A discussion on the various synthesis methods of nanomaterials and role of ligands is provided. The introduction ended with the discussion on physical/chemical/spectroscopic of PVP which was found suitable not only for stable surface stabilization but also for rendering mild reducing power towards the formation of various metal nanoparticles.

In the experimental section, PVP in different (in)organic solvents along with gold ion at the given specific monomer to metal ratio is well utilized in achieving the desired size/shape controlled synthesis of Au NPs by simultaneously considering their nucleation and kinetic growth mechanism through various spectroscopic/microscopic techniques. Furthermore, the complementary XPS data evaluates the quantitative role of coupled oxygen and nitrogen components of the pyrrolidone ring in the PVP–solvent complex in asserting seedless surface mediation as well as the morphology driven localized surface plasmon suitable for wide range of plasmonic as well as photonic applications.

Herein, we report a single step seedless/templateless organic synthesis procedure for the complex 3-D gold nanostars with a high degree of size/shape control, involving the complexation of PVP in polar solvent DMF and their reduction of  $\text{AuCl}_4^-$  ions along with HCl as an effective mediator. On the basis of the kinetic optical absorption and FTIR spectroscopy measurements, a convenient ligand exchange mechanism has been proposed for the first time to the best of our knowledge to understand the evolution of these complex shaped gold nanostructures. XPS study reveals the necessities of balance contribution from both oxygen and nitrogen component in monodisperse gold nanostars. Also CL spectroscopy was effectively utilized to locally/selectively excite and investigate the plasmonic aspects of our multi-branched gold nanostars drop-coated on silicon substrates.

Further controlled tuning of the plasmonic eigenmodes of gold nanostars in a sequential manner from visible to the near IR region with morphology correlation were accomplished with exceptional level of wavelength agility by independently introducing the NaOH or co-solvent in the precursor reaction mixture. Such pH/co-solvent induced size/shape transitions of gold nanostructures were monitored kinetically in detail through correlated molecular spectroscopic measurements NMR, FTIR and XPS and are utilized for specific applications such as the surface SERS.

Also it had been shown that different halide ions to the precursor polymer–solvent solution for the synthesis of gold nanostars drastically changes their optical properties owing to the blue/red shifting of the LSPR bands as well as the emergence of new plasmon bands, aesthetically illustrating the simultaneous size/shape tuning enhanced with intriguing self organization, as confirmed from the TEM measurements. Such a synchronized morphology tuning has been very well understood in terms of the distinct reaction kinetics imparted by the different adsorption affinities of inorganic halide ions towards metal ions/surfaces.

Finally shape effects of these gold nanoparticles on SERS properties were investigated and found that different-shaped gold nanoparticles possess different SERS properties.

## REFERENCES

**REFERENCES**

1. R. Bhattacharya and P. Mukherjee, *Biological Properties of "Naked" Metal Nanoparticles*, Adv. Drug Delivery Rev. **2008**, *60*, 1289.
2. A. S. Thakor, J. Jokerst, C. Zavaleta, T. F. Massoud and S. S. Gambhir, *Gold Nanoparticles: A Revival in Precious Metal Administration to Patients*, Nano Lett. **2011**, *11*, 4029.
3. I. Freestone, N. Meeks, M. Sax and C. Higgitt, *The Lycurgus Cup-A Roman Nanotechnology*, Gold Bulletin **2007**, *40*, 270.
4. D. J. Barber and I. C. Freestone, *An Investigation of the Origin of the Colour of the Lycurgus Cup by Analytical Transmission Electron Microscopy*, Archaeometry **1990**, *32*, 33.
5. F. E. Wagner, S. Haslbeck, L. Stievano, S. Calogero, Q. A. Pankhurst and K. P. Martinek, *Before Striking Gold in Gold-Ruby Glass*, Nature **2000**, *407*, 691.
6. M. Faraday, *Experimental Relations of gold (and other Metals) to Light*, Philos.Trans. R. Soc. **1857**, 145.
7. W. Hergert and T. Wriedt, *The Mie Theory: Basics and Applications*, Springer. 2012.
8. J. Turkevich, P. C. Stevenson and J. Hillier, *A Study of the Nucleation and Growth Processes in the Synthesis of Colloidal Gold*, Disc. Farad. Soc. **1951**, *11*, 55.
9. G. Frens, *Controlled Nucleation for the Regulation of the Particle Size in Monodisperse Gold Suspensions*, Nature Phys. Sci. **1973**, *241*, 19.
10. G. Cao, *Nanostructures & Nanomaterials; Synthesis, Properties & Applications*, Imperial College Press **2004**, pp 15-48.
11. C. N. R. Rao, G. U. Kulkarni, P. J. Thomas and P. P. Edwards, *Size-Dependent Chemistry: Properties of Nanocrystals*, Chem. Eur. J. **2002**, *8*, 29.
12. G. Schmid, *Nanoparticles: From Theory to Applications*, Wiley-VCH Weinheim **2004**.
13. G. Mie, *Beiträge zur Optik trüber Medien, speziell kolloidaler Metallösungen*, Annalen Der Physik. **1908**, *25*, 377.
14. S. K. Ghosh and T. Pal, *Interparticle Coupling Effect on the Surface Plasmon Resonance of Gold Nanoparticles: From Theory to Application*, Chem. Rev. **2007**, *107*, 4797.
15. R. J. D. Tilley, *Colour and the Optical Properties of Materials*, John Wiley & Sons Ltd. **2011**, pp 477-480.
16. A. E. Rider, K. Ostrikov and S. A. Furman, *Plasmas Meet Plasmonics-Everything Old is New Again*, Eur. Phys. J. D **2012**, *66*, 226.
17. U. Kreibig and M. Vollmer, *Optical Properties of Metal Clusters*, Springer **1995**, pp 35-36.
18. P. B. Johnson and R. W. Christy, *Optical Constants of Noble Metals*, Phys. Rev. B **1972**, *6*, 4370.
19. M. J. Weber, *Handbook of Optical Materials*, CRC: New York **2003**, section 4.
20. E. D. Palik, *Handbook of Optical Constants of Solids II*, Academic Press: Boston **1991**.
21. T. Rangel, D. Kecik, P. E. Trevisanutto, G. M. Rignanese, H. V. Swygenhoven and V. Olevano, *The Band Structure of Gold from Many-Body Perturbation Theory*, Phys. Rev. B **2012**, *86*, 125125.
22. M. F. Xiao, *Competing Intra- and Inter-Band Transitions in Quantum Dots as Manifested in Optical Absorption Spectra*, Phys. Lett. A **2001**, *288*, 37.
23. L. Novotny, *Principles of Nano-Optics*, Cambridge University Press **2012**, pp: 378-418.
24. C. Noguez, *Surface Plasmons on Metal Nanoparticles: The Influence of Shape and Physical Environment*, J. Phys. Chem. C **2007**, *111*, 3806.

25. K. L. Kelly, E. Coronado, L. L. Zhao and G. C. Schatz, *Optical Properties of Metal Nanoparticles: The Influence of Size, Shape, and Dielectric Environment*, J. Phys. Chem. B **2003**, 107, 668.
26. A. Moores and F. Goettmann, *The Plasmon Band in Noble Metal Nanoparticles: an Introduction to Theory and Applications*, New J. Chem. **2006**, 30, 1121.
27. J. Z. Zhang and C. Noguez, *Applications of Metal Nanostructures*, Plasmonics **2008**, 3, 127.
28. K. Y. Kim, *Plasmonics-Principles and Applications*, Published by InTech, **2012**, pp 256-270. [\\_<http://dx.doi.org/10.5772/2633>](http://dx.doi.org/10.5772/2633)
29. R. Schasfoort and A. Tudos, *Handbook of Surface Plasmon Resonance*, Royal Society of Chemistry **2008**, pp 15-31.
30. K. A. Willets and R. P. V. Duyne, *Localized Surface Plasmon Resonance Spectroscopy and Sensing*, Annu. Rev. of Phys. Chem. **2007**, 58, 267.
31. E. Hutter and J. H. Fendler, *Exploitation Surface Plasmon Resonance*, Adv. Mater. **2004**, 16, 19.
32. D. J. Campbell and Y. Xia, *Plasmons: Why Should We Care?*, J. Chem. Educ. **2007**, 84, 91.
33. J. Zheng, *Highly Fluorescent Noble Metal Quantum Dots*, Annu. Rev. Phys. Chem. **2007**, 58, 409.
34. N. W. Ashcroft and N. D. Mermin, *Solid State Physics*, New York: HOLT, Rinehart and Winston **1976**.
35. S. Eustis and M. A. El-Sayed, *Why Gold Nanoparticles are More Precious than Pretty Gold: Noble Metal Surface Plasmon Resonance and its Enhancement of the Radiative and Nonradiative Properties of Nanocrystals of Different Shapes*, Chem. Soc. Rev. **2006**, 209.
36. L. M. Liz-Marzan, *Nanometals: Formation and Color*, Mater. Today **2004**, 7, 26.
37. M. Bahadory, *Synthesis of Noble Metal Nanoparticles*, Ph.D Thesis, Drexel University **2009**.
38. P. Englebienne, A. V. Hoonacker and M. Verhas, *Surface Plasmon Resonance: Principles, Methods and Applications in Biomedical Sciences*, Spectroscopy **2003**, 17, 255.
39. E. Ringe, B. Sharma, A. I. Henry, L. D. Mark and R. P. V. Duyne, *Single Nanoparticle Plasmonics*, Phys. Chem. Chem. Phys. **2013**, 15, 4110.
40. H. Atwater, *The Promise of Plasmonics*, Sci. Am. **2007**, 296, 56.
41. I. H. El-Sayed, X. Huang and M. A. El-Sayed, *Selective Laser Photo-Thermal Therapy of Epithelial Carcinoma using Anti-EGFR Antibody Conjugated Gold Nanoparticles*, Cancer Lett. **2006**, 239, 129.
42. J. N. Anker, W. P. Hall, O. Lyandres, N. C. Shah, J. Zhao and R. P. V. Duyne, *Biosensing with Plasmonic Nanosensors*, Nat. Mater. **2008**, 7, 442.
43. P. Fortina, L. J. Kricka, D. J. Graves, J. Park, T. Hyslop, F. Tam, N. Halas, S. Surrey and S. A. Waldman, *Applications of Nanoparticles to Diagnostics and Therapeutics in Colorectal Silver Nanoparticles*, J. Am. Chem. Soc. **2007**, 124, 10596.
44. M. Navarro-Cia and S. A. Maier, *Broad-Band Near-Infrared Plasmonic Nanoantennas for Higher Harmonic Generation*, ACS Nano **2012**, 6, 3537.
45. X. Gu, T. Qiu, W. Zhang and P. K. Chu, *Light-Emitting Diodes Enhanced by Localized Surface Plasmon Resonance*, Nanoscale Res. Lett. **2011**, 6, 199.
46. J. B. Pendry, *Negative Refraction Makes a Perfect Lense*, Phys. Rev. Lett. **2000**, 85, 3966.
47. H. J. Lezec, J. A. Dionne and H. A. Atwater, *Negative Refraction at Visible Frequencies*, Science **2007**, 316, 5823.
48. N. I. Zheludev, *A Roadmap for Metamaterials*, Opt. Photonics News **2011**, 22, 30.

49. D. K. Gramotnev and S. I. Bozhevolnyi, *Plasmonics Beyond the Diffraction Limit*, Nature Photonics **2010**, *4*, 83.
50. S. A. Maier, *Plasmonics: Fundamentals and Applications*, Springer **2007**.
51. S. A. Maier, P. G. Kik, H. A. Atwater, S. Meltzer, E. Harel, B. E. Koel and A. A. G. Requicha, *Local Detection of Electromagnetic Energy Transport Below the Diffraction Limit in Metal Nanoparticle Plasmon Waveguides*, Nat. Mater. **2003**, *2*, 229.
52. E. Verhagen, *Subwavelength Light Confinement with Surface Plasmon Polaritons*, Ph.D Thesis, Utrecht University **2009**.
53. E. L. Ru and P. Etchegoin, *Principles of Surface Enhanced Raman Scattering and Related Plasmonic Effects*, Elsevier Sci. Inc., New York, USA **2009**, pp 123-143,.
54. A. Laguna, *Modern Supramolecular Gold Chemistry: Gold-Metal Interactions and Applications*, Wiley-Vch Verlag GmbH & Co. KGaA, Weinheim **2008**, pp 2-4.
55. R. J. Puddephatt, *The Chemistry of Gold*, Elsevier **1978**.
56. T. Mortier, *An Experimental Study on the Preparation of Gold Nanoparticles and their Properties*, Ph.D Thesis, University of Leuven. **2006**.
57. B. Lim, P. H. C. Camargo and Y. Xia, *Mechanistic Study of the Synthesis of Au Nanotadpoles, Nanokites and Microplates by Reducing Aqueous HAuCl<sub>4</sub> with Poly(Vinylpyrrolidone)*, Langmuir **2008**, *24*, 10437.
58. N. E. Motl, A. F. Smith, C. J. Desantisa and S. E. Skrabalak, *Engineering Plasmonic Metal Colloids Through Composition and Structural Design*, Chem. Soc. Rev. **2014**, Doi: 10.1039/C3CS60347D
59. E. C. Dreaden, A. M. Alkilany, X. Huang, C. J. Murphy and M. A. El-Sayed, *The Golden Age: Gold Nanoparticles for Biomedicine*, Chem. Soc. Rev. **2012**, *41*, 2740.
60. N. Li, P. Zhao and D. Astruc, *Anisotropic Gold Nanoparticles: Synthesis, Properties, Applications, and Toxicity*, Angew. Chem. Int. Ed. **2014**, *53*, 2.
61. A. P. Alivisatos, *Nanocrystals: Building Blocks for Modern Materials Design*, Endeavour **1997**, *21*, 56.
62. M. Haruta, *Size- and support-Dependency in the Catalysis of Gold*, Catal. Today **1997**, *36*, 153.
63. R. Narayanan and M. A. El-Sayed, *Shape-Dependent Catalytic Activity of Platinum Nanoparticles in Colloidal Solution*, Nano Lett. **2004**, *4*, 1343.
64. D. M. Koller, A. Hohenau, H. Ditlbacher, N. Galler, F. Reil, F. R. Aussenegg, A. Leitner, E. J. W. List and J. R. Krenn, *Organic Plasmon-Emitting Diode*, Nat. Phot. **2008**, *2*, 684.
65. A. L. Falk, F. H. L. Koppens, C. L. Yu, K. Kang, N. D. L. Snapp, A. V. Akimov, M. H. Jo, M. D. Lukin and H. Park, *Near-Field Electrical Detection of Optical Plasmons and Single-Plasmon Sources*, Nat. Phys. **2009**, *5*, 475.
66. P. Zijlstra, J. M. Chon and M. Gu, *Five-Dimensional Optical Recording Mediated by Surface Plasmons in Gold Nanorods*, Nature **2009**, *459*, 410.
67. D. Schindel, *The Study of Optoelectronics in Semiconductor and Metallic Nanoparticle Hybrid Systems*, Ph.D Thesis, University of Western Ontario **2013**.
68. V. Amendola and M. Meneghetti, *Synthesis of Gold and Silver Nanoparticles for Photonic Application*, Ph.D Thesis, University of Padova **2008**.
69. C. Sonnichsen, *Plasmons in Metal Nanostructures*, Ph.D Thesis, University of Munich **2001**.
70. C. E. Tabor, *Some Optical and Catalytic Properties of Metallic Nanoparticles*, Ph.D Dissertation, Georgia Institute of Technology **2009**.

71. M. M. Hossain, *Study of functional Metallic Nano/Microstructures for Photonics Applications*, Ph.D Thesis, Swinburne University of Technology **2012**.
72. K. J. Klabunde, *Nanoscale Materials in Chemistry*, Wiley-Interscience, New York. **2001**.
73. C. Burda, X. B. Chen, R. Narayanan and M. A. El-Sayed, *Chemistry and Property of Nanocrystal of Different Shapes*, Chem. Rev. **2005**, 105, 1025.
74. A. T. Sennuga, *Biological Synthesis of Metallic Nanoparticles and their Interactions with Various Biomedical Targets*, Ph.D Thesis, Rhodes University **2011**.
75. K. N. Thakkar, S. S. Mhatre and R. Y. Parikh, *Biological Synthesis of Metallic Nanoparticles*, Nanomed-Nanotechnol., Bio-Med. **2010**, 6, 257.
76. H. R. Ghorbani, A. A. Safekordi, H. Attar and S. M. R. Sorkhabadi, *Biological and Non-biological Methods for Silver Nanoparticles Synthesis*, Chem. Biochem. Eng. **2011**, 25, 317.
77. C. A. Mirkin, *Programming the Assembly of Two- and Three-Dimensional Architectures with DNA and Nanoscale Inorganic Building Blocks*, Inorg. Chem. **2000**, 39, 2258.
78. K. J. Klabunde, *Organic Chemistry of Metal Vapors*, Acc. Chem. Res. **1975**, 8, 393.
79. C. Xue, *Metal Nanoprisms: Synthesis, Optical Properties, and Assembly*, Ph. D Dissertation, Northwestern University **2007**.
80. K. T. Nam, D. W. Kim, P. J. Yoo, C. Y. Chiang, N. Meethong, P. T. Hammond, Y. M. Chiang and A. M. Belcher, *Virus-Enabled Synthesis and Assembly of Nanowires for Lithium Ion Battery Electrodes*, Science **2006**, 312, 885.
81. P. R. Selvakannan, S. Mandal, S. Phadtare, A. Gole, R. Pasricha, S. D. Adyanthaya and M. Sastry, *Water-Dispersible Tryptophan-Protected Gold Nanoparticles Prepared by the Spontaneous Reduction of Aqueous Chloroaurate Ions by the Amino Acid*, J. Colloid Interface Sci. **2004**, 269, 97.
82. N. Kroger, R. Deutzmann and M. Sumper, *Polycationic Peptides from Diatom Biosilica That Direct Silica Nanosphere Formation*, Science **1999**, 286, 1129.
83. Y. Xia, Y. Xiong, B. Lim and S. E. Skrabalak, *Shape-Controlled Synthesis of Metal Nanocrystals: Simple Chemistry Meets Complex Physics?*, Angew. Chem. Int. Ed. **2009**, 48, 60.
84. C. E. Hoppe, M. Lazzari, I. N. Pardinias-Blanco and M. A. Lopez-Quintela, *One-Step Synthesis Of Gold and Silver Hydrosols using Poly(N-Vinyl-2-Pyrrolidone) as a Reducing Agent*, Langmuir **2006**, 22, 7027.
85. W. H. D. Jong and P. J. A. Borm, *Drug Delivery and Nanoparticles: Applications and Hazards*, Int. J. Nanomed. **2008**, 3, 133.
86. S. Zeng, K. Yong, I. Roy, X. Dinh, X. Yu and F. Luan, *A Review on Functionalized Gold Nanoparticles for Biosensing Applications*, Plasmonics **2011**, 6, 491.
87. M. Brust, J. Fink, D. Bethell, D. J. Schiffrin and C. Kiely, *Synthesis and Reactions of Functionalised Gold Nanoparticles*, J. Chem. Soc., Chem. Commun. **1995**, 1655.
88. M. C. Daniel and D. Astruc, *Gold Nanoparticles: Assembly, Supramolecular Chemistry, Quantum-Size-Related Properties, and Applications toward Biology, Catalysis, and Nanotechnology*, Chem. Rev. **2004**, 104, 293.
89. T. Llnaert, P. Mulvaney and A. Henglein, *Surface Chemistry of Colloidal Silver: Surface Plasmon Damping by Chemisorbed  $I^-$ ,  $SH^-$ , and  $C_6H_5S^-$* , J. Phys. Chem. **1993**, 97, 679.
90. R. C. Doty, T. R. Tshikhudo, M. Brust and D. G. Fernig, *Extremely Stable Water-Soluble Ag Nanoparticles*, Chem. Mater. **2005**, 17, 4630.
91. K. V. Sarathy, G. Raina, R. T. Yadav, G. U. Kulkarni and C. N. R. Rao, *Thiol-Derivatized Nanocrystalline Arrays of Gold, Silver, and Platinum*, J. Phys. Chem. B **1997**, 101, 9876.

92. S. C. Cook, J. D. Padmos and P. Zhanga, *Surface Structural Characteristics and Tunable Electronic Properties of Wet-Chemically Prepared Pd Nanoparticles*, J. Chem. Phys. **2008**, 128, 154705.
93. M. Green and P. O'Brien, *A Simple One Phase Preparation of Organically Capped Gold Nanocrystals*, Chem. Commun. **2000**, 1831.
94. A. L. Rogach, A. Kornowski, M. Gao, A. Eychmuller and H. Weller, *Synthesis and Characterization of a Size Series of Extremely Small Thiol-Stabilized CdSe Nanocrystals*, J. Phys. Chem. B **1999**, 103, 3065.
95. A. Kumar, S. Mandal, P. R. Selvakannan, R. Pasricha, A. B. Mandale and M. Sastry, *Investigation into the Interaction between Surface-Bound Alkylamines and Gold Nanoparticles*, Langmuir **2003**, 19, 6277.
96. S. Datar, M. Chaudhari, M. Sastry and C. V. Dharmadhikari, *Scanning Tunneling Microscopy/Spectroscopy on Au Nanoparticles Assembled using lauryl Amine (LAM) and Octadecane Thiol (ODT)*, Appl. Surf. Sci. **2007**, 253, 5109.
97. A. Kumar, H. Joshi, R. Pasricha, A. B. Mandale and M. Sastry, *Phase transfer of silver nanoparticles from aqueous to organic solutions using fatty amine molecules*, J. Colloid and Interface Sci. **2003**, 264, 396.
98. A. Kumar, H. M. Joshi, A. B. Mandale, R. Srivastava, S. D. Adyanthaya, R. Pasricha and M. Sastry, *Phase Transfer of Platinum Nanoparticles from Aqueous to Organic Solutions using Fatty Amine Molecules*, J. Chem. Sci. **2004**, 116, 293.
99. E. Ramirez, S. Jansat, K. Philippot, P. Lecante, O. Gomez, A. M. Masdeu-Bulto and B. Chaudret, *Influence of Organic Ligands on the stabilization of Palladium Nanoparticles*, J. Organomet. Chem. **2004**, 689, 4601.
100. W. Wang, S. Efrima and O. Regev, *Directing Oleate Stabilized Nanosized Silver Colloids into Organic Phases*, Langmuir **1998**, 14, 602.
101. X. C. Wei Wang and S. Efrima, *Silver Nanoparticles Capped by Long-Chain Unsaturated Carboxylates*, J. Phys. Chem. B **1999**, 103, 7238.
102. T. Bala, A. Swami, B. L. V. Prasad and M. Sastry, *Phase Transfer of Oleic Acid Capped Ni Core Ag Shell Nanoparticles Assisted by the Flexibility of Oleic Acid on the Surface of Silver*, J. Colloid and Interface Sci. **2005**, 283, 422.
103. N. Wu, L. Fu, M. Su, M. Aslam, K. C. Wong and V. P. Dravid, *Interaction of Fatty Acid Monolayers with Cobalt Nanoparticles*, Nano Lett. **2004**, 4, 383.
104. P. M. Shem, R. Sardar and J. S. Shumaker-Parry, *One-Step Synthesis of Phosphine-Stabilized Gold Nanoparticles using the Mild Reducing Agent 9-BBN*, Langmuir **2009**, 25, 13279.
105. C. B. Murray, S. Sun, W. Gaschler, H. Doyle, T. A. Betley and C. R. Kagan, *Colloidal Synthesis of Nanocrystals and Nanocrystal Superlattices*, IBM J. R & D **2001**, 45, 47.
106. T. Hyeon, *Chemical Synthesis of Magnetic Nanoparticles*, Chem. Commun. **2003**, 9, 927.
107. T. M. Owens, K. T. Nicholson, M. M. B. Holl and S. Suzer, *Formation of Alkylsilane-Based Monolayers on Gold*, J. Am. Chem. Soc. **2002**, 124, 6800.
108. T. M. Owens, K. T. Nicholson, D. R. Fossnacht, B. G. Orr and M. M. B. Holl, *Formation of Mixed Monolayers of Silsesquioxanes and Alkylsilanes on Gold*, Langmuir **2006**, 22, 9619.
109. A. Y. Fadeev and T. J. McCarthy, *A New Route to Covalently Attached Monolayers: Reaction of Hydrosilanes with Titanium and Other Metal Surfaces*, J. Am. Chem. Soc. **1999**, 121, 12184.
110. Y. Chen, X. Gu, C.-G. Nie, Z.-Y. Jiang, Z.-X. Xie and C.-J. Lin, *Shape Controlled Growth of Gold Nanoparticles by a Solution Synthesis*, Chem. Commun. **2005**, 4181.

111. I. Pastoriza-Santos and L. M. Liz-Marzan, *N,N-Dimethylformamide as a Reaction Medium for Metal Nanoparticle Synthesis*, *Adv. Funct. Mater.* **2009**, *19*, 679.
112. Y. Sun and Y. Xia, *Shape-Controlled Synthesis of Gold and Silver Nanoparticles*, *Science* **2002**, *298*, 2176.
113. X. Xia, J. Zeng, L. K. Oetjen, Q. Li and Y. Xia, *Quantitative Analysis of the Role Played by Poly(Vinylpyrrolidone) in Seed-Mediated Growth of Ag Nanocrystals*, *J. Am. Chem. Soc.* **2012**, *134*, 1793.
114. Y. Borodko, H. S. Lee, S. H. Joo, Y. Zhang and G. Somorjai, *Spectroscopic Study of the Thermal Degradation of PVP-Capped Rh and Pt Nanoparticles in H<sub>2</sub> and O<sub>2</sub> Environments*, *J. Phys. Chem. C* **2010**, *114*, 1117.
115. C. Wang, H. Daimon, Y. Lee, J. Kim and S. Sun, *Synthesis of Monodisperse Pt Nanocubes and Their Enhanced Catalysis for Oxygen Reduction*, *J. Am. Chem. Soc.* **2007**, *129*, 6974.
116. B. Lim, M. Jiang, J. Tao, P. H. C. Camargo, Y. Zhu and Y. Xia, *Shape-Controlled Synthesis of Pd Nanocrystals in Aqueous Solutions*, *Adv. Funct. Mater.* **2009**, *19*, 189.
117. N. Garg, C. Scholl, A. Mohanty and R. Jin, *The Role of Bromide Ions in Seeding Growth of Au Nanorods*, *Langmuir* **2010**, *26*, 10271.
118. S. E. Lohse, N. D. Burrows, L. Scarabelli, L. M. Liz-Marzan and C. J. Murphy, *Anisotropic Noble Metal Nanocrystal Growth: The Role of Halides*, *Chem. Mater.* **2014**, *26*, 34.
119. M. R. Langille, M. L. Personick, J. Zhang and C. A. Mirkin, *Defining Rules for the Shape Evolution of Gold Nanoparticles*, *J. Am. Chem. Soc.* **2012**, *134*, 14542.
120. H. Xiaoge, W. Tie and D. Shaojun, *Rapid Synthesis of Cubic Pt Nanoparticles and Their Use for the Preparation of Pt Nanoagglomerates*, *J. Nanosci. Nanotechnol.* **2006**, *6*, 2056.
121. M.-P. Pileni, *The Role of Soft Colloidal Templates in Controlling the Size and Shape of Inorganic Nanocrystals*, *Nat. Mater.* **2003**, *2*, 145.
122. T. K. Sau and C. J. Murphy, *Room Temperature, High-Yield Synthesis of Multiple Shapes of Gold Nanoparticles in Aqueous Solution*, *J. Am. Chem. Soc.* **2004**, *126*, 8648.
123. W. Niu, Z.-Y. Li, L. Shi, X. Liu, H. Li, S. Han, J. Chen and G. Xu, *Seed-Mediated Growth of Nearly Monodisperse Palladium Nanocubes with Controllable Sizes*, *Cryst. Growth Des.* **2008**, *8*, 4440.
124. D. Seo, C. I. Yoo, J. C. Park, S. M. Park, S. Ryu and H. Song, *Directed Surface Overgrowth and Morphology Control of Polyhedral Gold Nanocrystals*, *Angew. Chem. Int. Ed.* **2008**, *47*, 763.
125. X. Liu, R. Huang and J. Zhu, *Functional Faceted Silver Nano-Hexapods: Synthesis, Structure Characterizations, and Optical Properties*, *Chem. Mater.* **2007**, *20*, 192.
126. D. O. Yener, J. Sindel, C. A. Randall and J. H. Adair, *Synthesis of Nanosized Silver Platelets in Octylamine-Water Bilayer Systems*, *Langmuir* **2002**, *18*, 8692.
127. L. Huang, H. Wang, Z. Wang, A. Mitra, K. N. Bozhilov and Y. Yan, *Nanowire Arrays Electrodeposited from Liquid Crystalline Phases*, *Adv. Mater.* **2002**, *14*, 61.
128. L. Wang, X. Chen, J. Zhan, Y. Chai, C. Yang, L. Xu, W. Zhuang and B. Jing, *Synthesis of Gold Nano- and Microplates in Hexagonal Liquid Crystals*, *J. Phys. Chem. B* **2005**, *109*, 3189.
129. M. Wirtz and C. R. Martin, *Template-Fabricated Gold Nanowires and Nanotubes*, *Adv. Mater.* **2003**, *15*, 455.
130. C. K. Preston and M. Moskovits, *New Technique for the Determination of Metal Particle Size in Supported Metal Catalysts*, *J. Phys. Chem. B* **1988**, *92*, 2957.

131. S. Yang, R. Zhang, Q. Wang, B. Ding and Y. Wang, *Coral-Shaped 3D Assemblies of Gold Nuclei Induced by UV Irradiation and its Disintegration*, Colloids Surf. A: Physicochem. Eng. Aspects **2007**, 311, 174.
132. S. S. Shankar, A. Rai, B. Ankamwar, A. Singh, A. Ahmad and M. Sastry, *Biological Synthesis of Triangular Gold Nanoprisms*, Nat. Mater. **2004**, 3, 482.
133. T. K. Sau and A. L. Rogach, *Nonspherical Noble Metal Nanoparticles: Colloid-Chemical Synthesis and Morphology Control*, Adv. Mater. 22, 1781.
134. T. Ming, W. Feng, Q. Tang, F. Wang, L. Sun, J. Wang and C. Yan, *Growth of Tetrahedral Gold Nanocrystals with High-Index Facets*, J. Am. Chem. Soc. **2009**, 131, 16350.
135. D. V. Leff, P. C. Ohara, J. R. Heath and W. M. Gelbart, *Thermodynamic Control of Gold Nanocrystal Size: Experiment and Theory*, J. Phys. Chem. **1995**, 99, 7036.
136. N. R. Jana, L. Gearheart and C. J. Murphy, *Wet Chemical Synthesis of Silver Nanorods and Nanowires of Controllable Aspect Ratio*, Chem. Commun. **2001**, 617.
137. C. H. Kuo and M. H. Huang, *Synthesis of Branched Gold Nanocrystals by a Seeding Growth Approach*, Langmuir **2005**, 21, 2012.
138. S. E. Skrabalak, L. Au, X. D. Li and Y. Xia, *Facile Synthesis of Ag Nanocubes and Au Nanocages*, Nat. Protocols **2007**, 2, 2182.
139. J. H. Fendler, *Chemical Self-assembly for Electronic Applications*, Chem. Mater. **2001**, 13, 3196.
140. R. G. Nuzzo and D. L. Allara, *Adsorption of Bifunctional Organic Disulfides on Gold Surfaces*, J. Am. Chem. Soc. **1983**, 105, 4481.
141. B. Ak, I. F. D. Je, T.-A. T, R. Tp and R. Vm, *Self-assembly of Nanoparticles into Structured Spherical And Network Aggregates*, Nat. Commun. **2000**, 404, 746.
142. S. Sotiropoulou, Y. Sierra-Sastre, S. S. Mark and C. A. Batt, *Biotemplated Nanostructured Materials*, Chem. Mater. **2008**, 20, 821.
143. Z. Li, S.-W. C. Dr., J.-M. Nam, D. S. G. Dr. and C. A. M. Prof., *Living Templates for the Hierarchical Assembly of Gold Nanoparticles*, Angew. Chem. Int. Ed. **2003**, 42, 2306.
144. Y. Xia, J. A. Rogers, K. E. Paul and G. M. Whitesides, *Unconventional Methods for Fabricating and Patterning Nanostructures*, Chem. Rev. **1999**, 99, 1823.
145. C. A. Mirkin, *The Power of the Pen: Development of Massively Parallel Dip-Pen Nanolithography*, ACS Nano **2007**, 1, 79.
146. G. Schmid and L. F. Chi, *Metal Clusters and Colloids*, Adv. Mater. **1998**, 10, 515.
147. M. Burghard, G. Philipp, S. Roth, K. V. Klitzing, R. Pugin and G. Schmid, *Multilayered Langmuir-Blodgett Films of Thiol-Substituted Ultrasmall Gold Clusters*, Adv. Mater. **1998**, 10, 842.
148. C. N. R. Rao, G. U. Kulkarni, P. J. Thomas and P. P. Edwards, *Metal Nanoparticles and Their Assemblies*, Chem. Soc. Rev. **2000**, 29, 27.
149. M. Brust, M. Walker, D. Bethell, D. J. Schiffrin and R. Whyman, *Synthesis of Thiol-Derivatized Gold Nanoparticles in a Two-Phase Liquid-Liquid System*, J. Chem. Soc., Chem. Commun. **1994**, 801.
150. B. L. V. Prasad, S. I. Stoeva, C. M. Sorensen and K. J. Klabunde, *Digestive-Ripening Agents for Gold Nanoparticles: Alternatives to Thiols*, Chem. Mater. **2003**, 15, 935.
151. S. T. S. Joseph, B. I. Ipe, P. Pramod and K. G. Thomas, *Gold Nanorods to Nanochains: Mechanistic Investigations on Their Longitudinal Assembly Using  $\alpha$ ,  $\omega$ -Alkanedithiols and Interplasmon Coupling*, J. Phys. Chem. B **2006**, 110, 150.

152. C. A. Mirkin, R. L. Letsinger, R. C. Mucic and J. J. Storhoff, *A DNA-Based Method for Rationally Assembling Nanoparticles into Macroscopic Materials*, *Nature* **1996**, 382, 6592.
153. V. Bühler, *Polyvinylpyrrolidone-Excipients for Pharmaceuticals*, Springer Verlag **2005**.
154. <http://www.basf.com>.
155. G. Oster and E. H. Immergut, *Ultraviolet and Infrared Spectral Studies of Polyvinylpyrrolidone*, Polytechnic institute of Brooklyn **1954**, 1393.
156. G. Oster, *Spectral Studies of Polyvinylpyrrolidone (PVP)*, *J. Polym. Sci.* **1952**, 6, 553.
157. G. Oster, *Dye Binding To High Polymers*, *J. Polym. Sci.* **1955**, XVI, 235.
158. C. Peniche, D. Zaldivar, M. Pazos, S. Paz, A. Bulay and J. S. Romans, *Study of the Thermal Degradation of Poly (N-Vinyl-2-Pyrrolidone) by Thermogravimetry-FTIR*, *J. Appl. Polym. Sci.* **1993**, 50, 485.
159. G. Bianco, M. S. Soldi, E. A. Pinheiro, A. T. N. Pires, M. H. Gehlen and V. Soldi, *Thermal Stability of Poly(N-Vinyl-2-Pyrrolidone-Co-Methacrylic Acid) Copolymers in Inert Atmosphere*, *Poly. Degradation and Stability* **2003**, 80, 567.
160. M. V. Bogatyrev, N. V. Borisenko and V. A. Pokrovskii, *Thermal Degradation of Polyvinyl Pyrrolidone on the Surface of Pyrogenic Silica*, *Russ. J. Appl. Chem.* **2001**, 74, 839.
161. M. I. Loria-Bastarrachea, W. Herrera-Kao, J. V. Cauich-Rodriguez, J. M. Cervantes-Uc, H. Vazquez-Torres and A. Avila-Ortega, *A TG/FTIR Study on the Thermal Degradation of Poly(Vinyl Pyrrolidone)*, *J. Therm. Anal. Calorim.* **2011**, 104, 737.
162. F. Kim, S. Connor, H. Song, T. Kuykendall and P. Yang, *Platonic Gold Nanocrystals*, *Angew. Chem. Int. Ed.* **2004**, 43, 3673.
163. J. Zhang, H. Liu, Z. Wang and N. Ming, *Shape-Selective Synthesis of Gold Nanoparticles with Controlled Sizes, Shapes, and Plasmon Resonances*, *Adv. Funct. Mater.* **2007**, 17, 3295.
164. E. Ringe, *Building the Nanoplasmonics Toolbox Through Shape Modeling and Single Particle Optical Studies*, Ph.D Thesis, Northwestern University **2012**.
165. J. Xian, Q. Hua, Z. Jiang, Y. Ma and W. Huang, *Size-Dependent Interaction of the Poly(N-Vinyl-2-Pyrrolidone) Capping Ligand with Pd Nanocrystals*, *Langmuir* **2012**, 28, 6736.
166. Z. Zhang, B. Zhao and L. Hu, *PVP Protective Mechanism Of Ultrafine Silver Powder Synthesized by Chemical Reduction Processes*, *J. Solid State Chem.* **1996**, 121, 105.
167. A. R. Tao, S. Habas and P. Yang, *Shape Control of Colloidal Metal Nanocrystals*, *Small* **2008**, 4, 310.
168. D. Chen and L. Gao, *Large-Scale Growth and End-To-End Assembly of Silver Nanorods by PVP-Directed Polyol Process*, *J. Cryst. Growth* **2004**, 264, 216.
169. M. Rycenga, C. M. Cobley, J. Zeng, W. Li, C. H. Moran, Q. Zhang, D. Qin and Y. Xia, *Controlling the Synthesis and Assembly of Silver Nanostructures for Plasmonic Applications*, *Chem. Rev.* **2011**, 111, 3669.
170. X. Lu, M. Rycenga, S. E. Skrabalak, B. Wiley and Y. Xia, *Chemical Synthesis of Novel Plasmonic Nanoparticles*, *Annu. Rev. Phys. Chem.* **2009**, 60, 167.
171. Y. Sun and Y. Xia, *Large scale synthesis of Uniform Silver Nanowires Through a Soft, Self Seeding, Polyol Process*, *Adv. Mater.* **2002**, 14, 833.
172. I. Washio, Y. Xiong, Y. Yin and Y. Xia, *Reduction by the End Groups of Poly(Vinyl Pyrrolidone): A New and Versatile Route to the Kinetically Controlled Synthesis of Ag Triangular Nanoplates*, *Adv. Mater.* **2006**, 18, 1745.

173. J. Wu, F. Qin, Z. Lu, H.-J. Yang and R. Chen, *Solvothermal Synthesis of Uniform Bismuth Nanospheres using Poly(N-Vinyl-2-Pyrrolidone) as a Reducing Agent*, *Nanoscale Res. Lett.* **2011**, 6, 1.
174. C. Kan, W. Cai, C. Li and A. L. Zhang, *Optical Studies of Polyvinylpyrrolidone Reduction Effect on Free and Complex Metal Ions*, *J. Mater. Res.* **2005**, 20, 320.
175. M. Zhou, B. Wang, Z. Rozynek, Z. Xie, J. O. Fossum, X. Yu and S. Raaen, *Minute Synthesis Of Extremely Stable Gold Nanoparticles*, *Nanotech.* **2009**, 20, 505606.
176. D. F. Swinehart, *The Beer-Lambert Law*, *J. Chem. Educ.* **1962**, 39, 333.
177. T. Owen, *Fundamentals of UV-Visible Spectroscopy*, Hewlett-Packard Company **1996**.
178. M. Hu, J. Chen, Z.-Y. Li, L. Au, G. V. Hartland, X. Li, M. Marquez and Y. Xia, *Gold Nanostructures: Engineering their Plasmonic Properties for Biomedical Applications*, *Chem. Soc. Rev.* **2006**, 35, 1084.
179. S. Link and M. A. El-Sayed, *Size and Temperature Dependence of the Plasmon Absorption of Colloidal Gold Nanoparticles*, *J. Phys. Chem. B* **1999**, 103, 4212.
180. C. F. Bohren and D. R. Huffman, *Absorption and Scattering of Light by Small Particles*, John Wiley and Sons: New York **1983**, pp: 530.
181. J. A. Edgar, A. M. Mcdonagh and M. B. Cortie, *Formation of Gold Nanorods by a Stochastic "Popcorn" Mechanism*, *ACS Nano* **2012**, 6, 1116.
182. T. K. Sau and C. J. Murphy, *Seeded High Yield Synthesis of Short Au Nanorods in Aqueous Solution*, *Langmuir* **2004**, 20, 6414.
183. J. Rodriguez-Fernandez, J. Perez-Juste, P. Mulvaney and L. M. Liz-Marzan, *Spatially-Directed Oxidation of Gold Nanoparticles by Au(III)-CTAB Complexes*, *J. Phys. Chem. B* **2005**, 109, 14257.
184. M. Quinten, *Optical Effects Associated with Aggregates of Clusters*, *J. Cluster Sci.* **1999**, 10, 321.
185. D. L. Pavia, G. M. Lampman and G. L. Kriz, *Introduction to Spectroscopy*, Harcourt Brace College, New York **2008**.
186. C. N. Banwell and E. M. Mccash, *Fundamentals of Molecular Spectroscopy*, McGrawHill, United Kingdom **1996**, Ch. 3, pp: 55.
187. J.L. Koenig, *Spectroscopy of Polymers*, Elsevier Sci. Inc., New York, USA **1999**, 2<sup>nd</sup> Ed.
188. H.-S. Wang, F. Lu and H. Zhai, *A Method to Collect an Infrared Spectrum in Solution*, *Analytical Sciences* **2007**, 23, 869.
189. I. Szaraz and W. Forsling, *A Spectroscopic Study Of The Solvation of 1-Vinyl-2-Pyrrolidone and Poly(1-Vinyl-2-Pyrrolidone) in Different Solvents*, *Polymer* **2000**, 41, 4831.
190. J. L. Koenig, *Infrared and Raman Spectroscopy of Polymer*, Rapra Review Report No.134, Rapra Technology Ltd. Shawbury **2001**.
191. E. Smith and G. Dent, *Modern Raman Spectroscopy-A Practical Approach*, John Wiley and Sons, England **2005**.
192. J. P. Sibilía, *A Guide to Material Characterization and Chemical Analysis*, Wiley-VCH, Weinheim **1988**.
193. M. Rycenga, *Engineering Noble-Metal Nanoparticles for Sensing and Imaging with Surface-Enhanced Raman Scattering*, Ph. D Dissertation, Washington University **2011**.
194. P. L. Stiles, J. A. Dieringer, N. C. Shah and R. P. V. Duyne, *Surface-Enhanced Raman Spectroscopy*, *Annu. Rev. Anal. Chem.* **2008**, 1, 601.

195. I. Geiman, M. Leona and J. R. Lombardi, *Application of Raman Spectroscopy and Surface-Enhanced Raman Scattering to the Analysis of Synthetic Dyes Found in Ballpoint Pen Inks*, J. Forensic Science **2009**, *54*, 947.
196. K. Kim, H. S. Han, I. Choi, C. Lee, S. Hong, S.-H. Suh, L. P. Lee and T. Kang, *Interfacial Liquid-State Surface-Enhanced Raman Spectroscopy*, Nat. Commun. **2012**, *4*, 2182.
197. K. M. Kosuda, J. M. Bingham, K. L. Wustholz and R. P. V. Duyne, *Nanostructures and Surface-Enhanced Raman Spectroscopy*, Comprehensive Nanosci. Technol **2011**, *3*, 263.
198. S. Nie and S. R. Emory, *Probing Single Molecules and Single Nanoparticles by Surface-Enhanced Raman Scattering*, Science **1997**, *275*, 1102.
199. M. Fleischmann, P. J. Hendra and A. J. Mcquillan, *Raman Spectra of Pyridine Adsorbed at a Silver Electrode*, Chem. Phys. Lett. **1974**, *26*, 163.
200. D. L. Jeanmaire and R. P. V. Duyne, *Surface Raman Spectroelectrochemistry: Part I. Heterocyclic, Aromatic, and Aliphatic Amines Adsorbed on the Anodized Silver Electrode*, J. Electroanal. Chem. Interfacial Electrochem. **1977**, *84*, 1.
201. M. G. Albrecht and J. A. Creighton, *Anomalously Intense Raman Spectra of Pyridine at a Silver Electrode*, J. Am. Chem. Soc. **1977**, *99*, 5215.
202. J. M. McLellan, A. Siekkinen, J. Chen and Y. Xia, *Comparison of the Surface-Enhanced Raman Scattering on Sharp and Truncated Silver Nanocubes*, Chem. Phys. Lett. **2006**, *427*, 122.
203. M. J. Mulvihill, X. Y. Ling, J. Henzie and P. Yang, *Anisotropic Etching of Silver Nanoparticles for Plasmonic Structures Capable of Single-Particle SERS*, J. Am. Chem. Soc. **2010**, *132*, 268.
204. N. R. Jana and T. Pal, *Anisotropic Metal Nanoparticles for Use as Surface-Enhanced Raman Substrates*, Adv. Mater. **2007**, *19*, 1761.
205. O. Siiman and W. P. Hsu, *Surface-Enhanced Raman Scattering (SERS) Enhancements and Excitation Profiles for 3,5-pyridinedicarboxylate and Dabsyl Aspartate on Colloidal Gold*, J. Chem. Soc. Faraday Trans. 1 **1986**, *82*, 851.
206. F. Bloch, *Nuclear Induction*, Phys. Rev. **1946**, *70*, 460.
207. E. M. Purcell, H. C. Torrey and R. V. Pound, *Resonance Absorption by Nuclear Magnetic Moments in a Solid*, Phys. Rev. B **1946**, *69*, 37.
208. S. Hufner, *Photoelectron Spectroscopy: Principles and Applications*, Springer Verlag **1995**.
209. B. C. Carter and D.B. Williams, *Basics I, in Transmission Electron Microscopy.*, Plenum Press, New York **1996**.
210. X. Gao, *Characterization of Nanomaterials by Transmission Electron Microscopy and Related Techniques*, Ph. D Dissertation, The University of Texas **2005**.
211. D. E. Newbury, D. C. Joy, P. Echlin, C. E. Fiori and J. Goldstein, *Advanced Scanning Electron Microscopy and X-ray Microanalysis*, Plenum Press, New York **1986**.
212. M. Kuttge, *Cathodoluminescence Plasmon Microscopy*, Ph.D Thesis, Utrecht University **2009**.
213. Y. Borodko, S. E. Habas, M. Koebel, P. Yang, H. Frei and G. A. Somorjai, *Probing the Interaction of Poly(Vinylpyrrolidone) with Platinum Nanocrystals by Uv-Raman and FTIR*, J. Phys. Chem. B **2006**, *110*, 23052.
214. M. M. Chili, *The Synthesis and Characterization of Gold Nanoparticles in Water-Soluble Polymers*, Ph.D Thesis, University Of Zululand **2010**.
215. P. S. Mdluli, *Synthesis and Growth Dynamics Study of Silver Nanoparticles*, Ph.D Thesis, University of Zululand **2009**.

216. A. J. Biacchi and R. E. Schaak, *The Solvent Matters: Kinetic Versus Thermodynamic Shape Control in the Polyol Synthesis of Rhodium Nanoparticles*, ACS Nano **2011**, 5, 8089.
217. C. Hao, Y. Zhao, X. Dong, Y. Zhou, Y. Xu, Dujinwang, G. Laia and J. Jianga, *Anomalous Rheological Behavior of Poly(1-Vinyl-2-Pyrrolidone) and CuCl<sub>2</sub> in Solution and their Interactions in Solid Composites*, Polym. Int. **2009**, 58, 906.
218. R. Sathiyarayanan, M. Alimohammadi, Y. Zhou and K. A. Fichthorn, *Role of Solvent in the Shape-Controlled Synthesis of Anisotropic Colloidal Nanostructures*, J. Phys. Chem. C **2011**, 115, 18983.
219. O. Gven and E. Yigit, *Hydrophilic and Hydrophobic Interactions in Alcohol Solutions of High Molecular Weight Poly(N-Vinyl-2-Pyrrolidone)*, Colloid Polym. Sci. **1984**, 262, 892.
220. Y. E. Kirsh, *Water-Soluble Poly(N-Vinylamides)" Microstructure, Solvation, Conformational State and Complex Formation in Aqueous Solutions*, Prog. Polym. Sci. **1993**, 18, 519.
221. R. J. Sengwa, Abhilasha, N. M. More and S. C. Mehrotra, *Dynamic Structure of Poly(Vinyl Pyrrolidone)/Ethyl Alcohol Mixtures Studied by Time Domain Reflectometry*, J. Polym. Sci. B Polym. Phys. **2005**, 43, 1134.
222. L. Turker, A. Guner, E. Yigit and O. Guven, *Spectrophotometric Behavior of Polyvinylpyrrolidone in Aqueous and Nonaqueous Media (I)*, Coll. Polym. Sci. **1990**, 268, 337.
223. W. A. Al-Saidi, H. Feng and K. A. Fichthorn, *Adsorption of Polyvinylpyrrolidone on Ag Surfaces: Insight into a Structure-Directing Agent*, Nano Lett. **2012**, 12, 997.
224. J. Zhang, H. Liu, Z. Wang and N. Ming, *Synthesis of High Purity Au Nanobelts Via the One-Dimensional Self-Assembly of Triangular Au Nanoplates*, Appl. Phys. Lett. **2007**, 91, 133112.
225. B. L. Sanchez-Gaytan, Z. Qian, S. P. Hastings, M. L. Reza, Z. Fakhraai and S.-J. Park, *Controlling the Topography and Surface Plasmon Resonance of Gold Nanoshells by a Templated Surfactant-Assisted Seed Growth Method*, J. Phys. Chem. C **2013**, 117, 8916.
226. T. K. Sau, A. L. Rogach, M. Döblinger and J. Feldmann, *One-Step High-Yield Aqueous Synthesis of Size-Tunable Multispiked Gold Nanoparticles*, Small **2011**, 7, 2188.
227. S. Trigari, A. Rindi, G. Margheri, S. Sottini, G. Dellepiane and E. Giorgetti, *Synthesis and Modelling of Gold Nanostars with Tunable Morphology and Extinction Spectrum*, J. Mater. Chem. **2011**, 21, 6531.
228. S. K. Dondapati, T. K. Sau, C. Hrelescu, T. A. Klar, F. D. Stefani and J. Feldmann, *Label-Free Biosensing Based on Single Gold Nanostars as Plasmonic Transducers*, ACS Nano **2010**, 4, 6318.
229. F. Hao, C. L. Nehl, J. H. Hafner and P. Nordlander, *Plasmon Resonances of a Gold Nanostar*, Nano Lett. **2007**, 7, 729.
230. T. Schumacher, K. Kratzer, D. Molnar, M. Hentschel, H. Giessen and M. Lippitz, *Nanoantenna-Enhanced Ultrafast Nonlinear Spectroscopy of a Single Gold Nanoparticle*, Nat. Commun. **2011**, 1334.
231. G. H. Jeong, Y. W. Lee, M. Kim and S. W. Han, *High-Yield Synthesis Of Multi-Branched Gold Nanoparticles and their Surface-Enhanced Raman Scattering Properties*, J. Colloid and Interface Sci. **2009**, 329, 97.
232. Y. Zhang, F. Xu, Y. Sun, C. Guo, K. Cui, Y. Shi, Z. Wen and Z. Li, *Seed-Mediated Synthesis of Au Nanocages and their Electrocatalytic Activity Towards Glucose Oxidation*, Chem. Eur. J. **2010**, 16, 9248.
233. M. Distaso, R. N. K. Taylor, N. Taccardi, P. Wasserscheid and W. Peukert, *Influence of the Counterion on the Synthesis of ZnO Mesocrystals Under Solvothermal Conditions*, Chem. Eur. J. **2011**, 17, 2923.

234. V. I. Dubrovin and V. P. Panov, *Carbon-13 NMR Investigation of Microtactic Structure of Polyvinylpyrrolidone*, *J. Appl. Spec.* **1980**, *33*, 754.
235. C. Hao, Y. Zhao, Y. Zhou, L. Zhou, Y. Xu, D. Wang and D. Xu, *Interactions Between Metal Chlorides and Poly(Vinyl Pyrrolidone) in Concentrated Solutions and Solid-State Films*, *J. Polym. Sci. B: Polym. Phys.* **2007**, *45*, 1589.
236. N. Shinyashiki, A. Spanoudaki, W. Yamamoto, E. Nambu, K. Yoneda, A. Kyritsis, P. Pissis, R. Kita and S. Yagihara, *Segmental Relaxation of Hydrophilic Poly(vinylpyrrolidone) in Chloroform Studied by Broadband Dielectric Spectroscopy*, *Macromolecules* **2011**, *44*, 2140.
237. R. Paynter, *XPS Theory*, <[http://csacs.mcgill.ca/francais/docs/CHEM634/XPS\\_Paynter\\_t.pdf](http://csacs.mcgill.ca/francais/docs/CHEM634/XPS_Paynter_t.pdf)>.
238. E. Jagst, *Surface Functional Group Characterization Using Chemical Derivatization X-ray Photoelectron Spectroscopy (CD-XPS)*, Ph.D Dissertation, Free University of Berlin **2010**.
239. H.-D. Wu, I.-D. Wu and F.-C. Chang, *The Interaction Behavior of Polymer Electrolytes Composed of Poly(Vinyl Pyrrolidone) and Lithium Perchlorate (LiClO<sub>4</sub>)*, *Polymer* **2001**, *42* 555.
240. Y. Borodko, S. M. Humphrey, T. D. Tilley, H. Frei and G. A. Somorjai, *Charge-Transfer Interaction of Poly(Vinylpyrrolidone) with Platinum and Rhodium Nanoparticles*, *J. Phys. Chem. C* **2007**, *111*, 6288.
241. P. Jiang, J. J. Zhou, R. Li, Z. L. Wang and S. S. Xie, *Poly(Vinyl Pyrrolidone)-Capped Five-Fold Twinned Gold Particles with Sizes from Nanometres to Micrometres*, *Nanotech.* **2006**, *17*, 3533.
242. Y. Gao, P. Jiang, D. F. Liu, H. J. Yuan, X. Q. Yan, Z. P. Zhou, J. X. Wang, L. Song, L. F. Liu, W. Y. Zhou, G. Wang, C. Y. Wang and S. S. Xie, *Evidence for the Monolayer Assembly of Poly(Vinylpyrrolidone) on the Surfaces of Silver Nanowires*, *J. Phys. Chem. B* **2004**, *108*, 12877.
243. W. L. Jolly, *Modern Inorganic Chemistry*, McGraw-Hill Inc. New York **1991**, pp 489-94.
244. P. S. Mdluli, N. M. Sosibo, N. Revaprasadu, P. Karamanis and J. Leszczynski, *Surface Enhanced Raman Spectroscopy (Sers) and Density Functional Theory (DFT) Study for Understanding the Regioselective Adsorption of Pyrrolidinone on the Surface of Silver and Gold Colloids*, *J. Mol. Struct.* **2009**, *935*, 32.
245. C. G. Khoury and T. Vo-Dinh, *Gold Nanostars for Surface Enhanced Raman Scattering: Synthesis, Characterization and Optimization*, *J. Phys. Chem. C* **2008**, *112*, 18849.
246. P. S. Kumar, I. P. Santos, B. R.-. Gonzalez, F. J. G. Abajo and L. M. Liz-Marzan, *High Yield Synthesis and Optical Response of Gold Nanostars*, *Nanotech.* **2008**, *19*, 015606.
247. L. Rodriguez-Lorenzo, R. A. Alvarez-Puebla, I. Pastoriza-Santos, S. Mazzucco, O. Stephan, M. Kociak, L. M. Liz-Marzan and F. J. G. Abajo, *Zeptomol Detection Through Controlled Ultrasensitive Surface-Enhanced Raman Scattering*, *J. Am. Chem. Soc.* **2009**, *131*, 4616.
248. L. Rodriguez-Lorenzo, R. A. Alvarez-Puebla, F. J. G. Abajo and L. M. Liz-Marzan, *Surface Enhanced Raman Scattering Using Star-Shaped Gold Colloidal Nanoparticles*, *J. Phys. Chem. C* **2010**, *114*, 7336.
249. P. Das, A. Kedia, P. S. Kumar, N. Large and T. K. Chini, *Local Electron Beam Excitation and Substrate Effect on the Plasmonic Response of Single Gold Nanostars*, *Nanotech.* **2013**, *24*, 405704.
250. S. H. Im, Y. T. Lee, B. Wiley and Y. Xia, *Large-Scale Synthesis of Silver Nanocubes: The Role of HCl in Promoting Cube Perfection and Monodispersity*, *Angew. Chem. Int. Ed.* **2005**, *44*, 2154.
251. E. S. Allgeyer, A. Pongan, M. Browne and M. D. Mason, *Optical Signal Comparison of Single Fluorescent Molecules and Raman Active Gold Nanostars*, *Nano lett.* **2009**, *9*, 3816.
252. D. H. M. Dam, J. H. Lee, P. N. Sisco, D. T. Co, M. Zhang, M. R. Wasielewski and T. W. Odom, *Direct Observation of Nanoparticle-Cancer Cell Nucleus Interactions*, *ACS Nano* **2012**, *6*, 3318.

253. A. Guerrero-Martínez, S. Barbosa, I. Pastoriza-Santos and L. M. Liz-Marzán, *Nanostars Shine Bright for You. Colloidal Synthesis, Properties and Applications of Branched Metallic Nanoparticles*, *Curr. Opin. Coll. Inter. Sci.* **2011**, *16*, 118.
254. S. Barbosa, A. Agrawal, L. R. Guez-Lorenzo, I. Pastoriza-Santos, R. A. Alvarez-Puebla, A. Kornowski, H. Weller and L. M. Liz-Marzan, *Tuning Size and Sensing Properties in Colloidal Gold Nanostars*, *Langmuir* **2010**, *26*, 14943.
255. N. Tian, Z.-Y. Zhou, S.-G. Sun, L. Cui, B. Ren and Z.-Q. Tian, *Electrochemical Preparation of Platinum Nanothorn Assemblies with High Surface Enhanced Raman Scattering Activity*, *Chem. Commun.* **2006**, 4090.
256. C. Hrelescu, T. K. Sau, A. L. Rogach, F. Jäckel and J. Feldmann, *Single Gold Nanostars Enhance Raman Scattering*, *Appl. Phys. Lett.* **2009**, *94*, 153113.
257. C. Hrelescu, T. K. Sau, A. L. Rogach, F. Jackel, G. Laurent, L. Douillard and F. Charra, *Selective Excitation of Individual Plasmonic Hotspots at the Tips of Single Gold Nanostars*, *Nano Lett.* **2011**, *11*, 402.
258. G. Maiorano, L. Rizzello, M. A. Malvindi, S. S. Shankara, L. Martiradonna, A. Falqui, R. Cingolani and P. P. Pompa, *Monodispersed and Size-Controlled Multibranching Gold Nanoparticles with Nanoscale Tuning of Surface Morphology*, *Nanoscale Res. Lett.* **2011**, *3*, 2227.
259. H. Wang and N. J. Halas, *Mesoscopic Au “Meatball” Particles*, *Adv. Mater.* **2008**, *20*, 820.
260. J. Xie, Q. Zhang, J. Y. Lee and D. I. C. Wang, *The Synthesis of SERS-Active Gold Nanoflower Tags for in Vivo Applications*, *ACS Nano* **2008**, *2*, 2473.
261. E. Giorgetti, S. Trigari, A. Rindi, G. Margheri, S. Sottini, G. Dellepiane, G. Brusatin, L. Brigo, M. Muniz-Miranda and I. Timtcheva, *Tunable Gold Nanostars for Surface Enhanced Raman Scattering*, *Phys. Status Solidi B* **2012**, *249*, 118.
262. M. Pradhan, J. Chowdhury, S. Sarkar, A. K. Sinha and T. Pal, *Hierarchical Gold Flower with Sharp Tips from Controlled Galvanic Replacement Reaction for High Surface Enhanced Raman Scattering Activity*, *J. Phys. Chem. C* **2012**, *116*, 24301.
263. P. R. Sajanlal and T. Pradeep, *Mesoflowers: A New Class of Highly Efficient Surface-Enhanced Raman Active and Infrared-Absorbing Materials*, *Nano Res.* **2009**, *2*, 306320.
264. E. Prodan, C. Radloff, N. J. Halas and P. Nordlander, *A Hybridization Model for the Plasmon Response of Complex Nanostructures*, *Science* **2003**, *302*, 419.
265. H. Wang, D. W. Brandl, F. Le, P. Nordlander and N. J. Halas, *Nanorice: A Hybrid Plasmonic Nanostructure*, *Nano Lett.* **2006**, *6*, 827
266. S. Mazzucco, O. Stephan, C. Colliex, I. Pastoriza-Santos, L. M. Liz-Marzan, F. J. G. D. Abajo and M. Kociak, *Spatially Resolved Measurements of Plasmonic Eigenstates in Complex-Shaped, Asymmetric Nanoparticles: Gold Nanostars*, *Eur. Phys. J. Appl. Phys.* **2011**, *54*, 1.
267. J. Perez-Juste, I. Pastoriza-Santos, L. M. Liz-Marzan and P. Mulvaney, *Gold nanorods: Synthesis, Characterization and Applications*, *Coord. Chem. Rev.* **2005**, *249*, 1870.
268. Q. Su, X. Ma, J. Dong, C. Jiang and W. Qian, *A Reproducible SERS Substrate Based on Electrostatically Assisted APTES-Functionalized Surface-Assembly of Gold Nanostars*, *ACS Appl. Mater. Interfaces.* **2011**, *3*, 1873.
269. W. A. Alves, C. A. T. E. Soto, E. Hollauer and R. B. Faria, *Vibrational Studies on the Selective Solvation of Na<sup>+</sup> and ClO<sub>3</sub><sup>-</sup> ions in Dimethylformamide- Formamide Mixture*, *Spectrochim. Acta. A* **2005**, *62*, 755.
270. H. Kobara, A. Wakisaka, K. Takeuchi and T. Ibusuki, *Preferential Solvation of Na<sup>+</sup> in N,N,-Dimethylformamide- Water Binary Mixture*, *J. Phys. Chem. B* **2003**, *107*, 11827.

271. M. Selvakumar, D. K. Bhat and N. G. Renganathan, *Molecular interactions of Polyvinylpyrrolidone and Cellulose Acetate Butyrate Solutions in Dimethylformamide*, Ind. J. Chem. **2008**, 47A, 1014.
272. A. V. Gaikwad, *Nanocatalysts: Properties and Applications*, Ph.D Thesis, University of Amsterdam. **2009**.
273. H. Kawasaki, H. Yamamoto, H. Fujimori, R. Arakawa, Y. Iwasaki and M. Inada, *Stability of the DMF-Protected Au Nanoclusters: Photochemical, Dispersion, and Thermal Properties*, Langmuir **2010**, 26, 5926.
274. S. K. Rastogi, B. D. Denn and A. L. Branen, *Synthesis of Highly Fluorescent and Thio-Linkers Stabilize Gold Quantum Dots and Nano Clusters in DMF for Bio-Labeling*, J. Nanopart. Res. **2012**, 14, 673.
275. S. Xie, M. C. Paa, Y. Zhang, S. Shuang, W. Chan and M. M. F. Choi, *High-Performance Liquid Chromatographic Analysis of as-Synthesised N,N-Dimethylformamide-Stabilised Gold Nanoclusters Product*, Nanoscale Res. Lett. **2012**, 4, 5325.
276. W. X. Tu, *Study of Interaction between Polyvinylpyrrolidone and Platinum Metals during the Formation of Colloidal Metal Nanoparticles*, Chin. J. Poly. Sci. **2008**, 26, 23.
277. T. C. Jao and I. Scott, *The Vibrational Spectra of Amides-Dimethyl Formamide*, J. Mol. Spect. **1982**, 92, 1.
278. C. M. V. St-Lhandske, J. Mink, M. Sandström, I. Pfiipai and P. Johansson, *Vibrational Spectroscopic and Force Field Studies of N,N-Dimethylthioformamide, N,N-dimethylformamide, their Deuterated Analogues and Bis (N, N-dimethylthioformamide) Mercury(II) perchlorate*, Vib. Spect. **1997**, 14, 207.
279. M. Liu, X. Yan, H. Liu and Weiyong, *An Investigation of the Interaction between Polyvinylpyrrolidone and Metal Cations*, React. Funct. Polym. **2000**, 44, 55.
280. E. N. Esenturk and A. R. H. Walker, *Surface-Enhanced Raman Scattering Spectroscopy via Gold Nanostars*, J. Raman Spectrosc. **2009**, 40, 86.
281. J. D. Lee, *Concise Inorganic Chemistry*, Oxford University Press **2005**.
282. G. Duan, W. Cai, Y. Luo, Z. Li and Y. Li, *Electrochemically Induced Flowerlike Gold Nanoarchitectures and their Strong Surface Enhanced Raman Scattering Effect*, Appl. Phys. Lett. **2006**, 89, 211905
283. A. M. Fales, H. Yuan and T. Vo-Dinh, *Silica-Coated Gold Nanostars for Combined Surface-Enhanced Raman Scattering (SERS) Detection and Singlet-Oxygen Generation: A Potential Nanoplatforrm for Theranostics*, Langmuir **2011**, 27, 12186.
284. H. Liang, Z. Li, W. Wang, Y. Wu and H. Xu, *Highly Surface-roughened "Flower-like" Silver Nanoparticles for Extremely Sensitive Substrates of Surface-enhanced Raman Scattering*, Adv. Mater. **2009**, 21, 4614.
285. C. Nehl, *Single Nanoparticle Spectroscopy: Plasmonic Properties and Biosensing Applications*, Ph.D Thesis, Rice University **2008**.
286. I. Baginskiy, T.-C. Lai, L.-C. Cheng, Y.-C. Chan, K.-Y. Yang, R.-S. Liu, M. Hsiao, C.-H. Chen, S.-F. Hu, L.-J. Her and D. P. Tsai, *Chitosan-Modified Stable Colloidal Gold Nanostars for the Photothermolysis of Cancer Cells*, J. Phys. Chem. C **2013**, 117, 2396.
287. J. R. G. Navarro, A. Liotta, A.-C. Faure, F. Lerouge, F. Chaput, G. Micouin, P. L. Baldeck and S. Parola, *Tuning Dye-to-Particle Interactions toward Luminescent Gold Nanostars*, Langmuir **2013**, 29, 10915.
288. H. Yuan, C. G. Khoury, H. Hwang, C. M. Wilson, G. A. Grant and T. Vo-Dinh, *Gold Nanostars: Surfactant-free Synthesis, 3D Modelling and Two-Photon Photoluminescence Imaging*, Nanotech. **2012**, 23, 075102.

289. M. Käll, *Plasmonic Nanosensors: Inverse Sensitivity*, Nat. Mater. **2012**, *11*, 570.
290. R. A. Puebla, L. M. Liz-Marzan and F. J. G. Abajo, *Light Concentration at the Nanometer Scale*, J. Phys. Chem. Lett. **2010**, *1*, 2428.
291. E. C. Argibay, B. R. Gonzalez, J. Pacifico, I. P. Santos, J. P. Juste and L. M. Liz-Marzan, *Chemical Sharpening of Gold Nanorods: The Rod-to-Octahedron Transition*, Angew. Chem. Int. Ed. **2007**, *119*, 9141.
292. L. Rodríguez-Lorenzo, J. M. Romo-Herrera, J. Pérez-Juste, R. A. Alvarez-Puebla and L. M. Liz-Marzán, *Reshaping and LSPR Tuning of Au Nanostars in the Presence of CTAB*, J. Mater. Chem. **2011**, *21*, 11544.
293. D. Seo, J. C. Park and H. Song, *Polyhedral Gold Nanocrystals with  $O_h$  Symmetry: From Octahedra to Cubes*, J. Am. Chem. Soc. **2006**, *128*, 14863.
294. X. Xia, J. Zeng, B. Mcdearmon, Y. Zheng, Q. Li and Y. Xia, *Silver Nanocrystals with Concave Surfaces and Their Optical and Surface-Enhanced Raman Scattering Properties*, Angew. Chem. Int. Ed. **2011**, *50*, 12542.
295. H. H. Huang, X. P. Ni, G. L. Loy, C. H. Chew, K. L. Tan, F. C. Loh, J. F. Deng and G. Q. Xu, *Photochemical Formation of Silver Nanoparticles in Poly(N-vinylpyrrolidone)*, Langmuir **1996**, *12*, 909.
296. T. Zhao, R. Sun, S. Yu, Z. Zhang, L. Zhou, H. Huang and R. Du, *Size-controlled Preparation of Silver Nanoparticles by a Modified Polyol Method*, Colloid and Surf. A: Physicochem. Eng. Aspects **2010**, *366*, 197.
297. A. N. Kannappan, S. Thirumaran and R. Palani, *Volumetric and Thermodynamic Studies of Molecular Interactions in Ternary Liquid Mixtures At 303, 308 and 313K*, J. Phys. Sci. **2009**, *20*, 97.
298. Y. Lei, H. Li, H. Pan and S. Han, *Structures and Hydrogen Bonding Analysis of N,N-Dimethylformamide and N,N-Dimethylformamide-Water Mixtures by Molecular Dynamics Simulations*, J. Phys. Chem. A **2003**, *107*, 1574.
299. K. Ramachandran, P. Sivagurunathan, K. Dharmalingam and S. C. Mehrotra, *Dielectric Relaxation Study of Amide-Alcohol Mixtures by using Time Domain Reflectometry*, Acta Phys. Chim. Sin. **2007**, *23*, 1508.
300. R. J. Sengwa, V. Khatri and S. Sankhla, *Structure and H Bonding in Binary Mixtures of N,N-Dimethylformamide with Some Dipolar Aprotic and Aprotic Solvents by Dielectric Characterization*, Indian J. Chem. **2009**, *48*, 512.
301. C. Wang, L. Z. H. Li and S. Han, *NMR and Excess Volumes Studies in DMF-Alcohol Mixtures*, J. of Solution Chem. **2002**, *31*, 109.
302. P.-J. Chung, L.-M. Lyu and M. H. Huang, *Seed-Mediated and Iodide-Assisted Synthesis of Gold Nanocrystals with Systematic Shape Evolution from Rhombic Dodecahedral to Octahedral Structures*, Chem. Eur. J. **2011**, *17*, 9746.
303. J. S. Duchene, W. Niu, J. M. Abendroth, Q. Sun, W. Zhao and F. Huo, *Halide Anions as Shape-Directing Agents for Obtaining High-Quality Anisotropic Gold Nanostructures*, Chem. Mater. **2013**, *25*, 1392.
304. S. Gomez-Grana, B. Goris, T. Altantzis, C. Fernandez-Lopez, E. Carbo-Argibay, A. S. Guerrero-Martínez, N. Almora-Barrios, N. Lopez, I. Pastoriza-Santos, J. Perez-Juste, S. Bals, G. V. Tendeloo and L. M. Liz-Marzan, *Au@Ag Nanoparticles: Halides Stabilize {100} Facets*, J. Phys. Chem. Lett. **2013**, *4*, 2209.
305. T. H. Ha, H.-J. Koo and B. H. Chung, *Shape-Controlled Syntheses of Gold Nanoprisms and Nanorods Influenced by Specific Adsorption of Halide Ions*, J. Phys. Chem. C **2007**, *111*, 1123.

306. A. Rai, A. Singh, A. Ahmad and M. Sastry, *Role of Halide Ions and Temperature on the Morphology of Biologically Synthesized Gold Nanotriangles*, *Langmuir* **2006**, *22*, 736.
307. P. J. Straney, C. M. Andolina and J. E. Millstone, *Seedless Initiation as an Efficient, Sustainable Route to Anisotropic Gold Nanoparticles*, *Langmuir* **2013**, *29*, 4396.
308. J. Zhang, M. R. Langille, M. L. Personick, K. Zhang, S. Li and C. A. Mirkin, *Concave Cubic Gold Nanocrystals with High-Index Facets*, *J. Am. Chem. Soc.* **2010**, *132*, 14012.
309. Q. Zhang, C. H. Moran, X. Xia, M. Rycenga, N. Li and Y. Xia, *Synthesis of Ag Nanobars in the Presence of Single-Crystal Seeds and a Bromide Ions, and Their Surface-Enhanced Raman Scattering (SERS) Properties*, *Langmuir* **2012**, *28*, 9047.
310. X. Ye, Y. Gao, J. Chen, D. C. Reifsnnyder, C. Zheng and C. B. Murray, *Seeded Growth of Monodisperse Gold Nanorods using Bromide-Free Surfactant Mixtures*, *Nano Lett.* **2013**, *13*, 2163.
311. A. K. Das and C. R. Raj, *Iodide-Mediated Reduction of AuCl<sub>4</sub><sup>-</sup> and a New Green Route for the Synthesis of Single Crystalline Au Nanostructures with Pronounced Electrocatalytic Activity*, *J. Phys. Chem. C* **2011**, *115*, 21041.
312. X. Fan, Z. R. Guo, J. M. Hong, Y. Zhang, J. N. Zhang and N. Gu, *Size-Controlled Growth of Colloidal Gold Nanoplates and their High-Purity Acquisition*, *Nanotech.* **2010**, *21*, 10560.
313. J. E. Millstone, W. Wei, M. R. Jones, H. Yoo and C. A. Mirkin, *Iodide Ions Control Seed-Mediated Growth of Anisotropic Gold Nanoparticles*, *Nano Lett.* **2008**, *8*, 2526.
314. A. Filankembo and M. P. Pileni, *Is the Template of Self-Colloidal Assemblies the Only Factor That Controls Nanocrystal Shapes?*, *J. Phys. Chem. B* **2000**, *104*, 5865.
315. S. Singh, R. Pasricha, U. M. Bhatta, P. V. Satyam, M. Sastry and B. L. V. Prasad, *Effect of Halogen Addition to Monolayer Protected Gold Nanoparticles*, *J. Mater. Chem.* **2007**, *17*, 1614.
316. K. K. Caswell, J. N. Wilson, U. H. F. Bunz and C. J. Murphy, *Preferential End-to-End Assembly of Gold Nanorods by Biotin-Streptavidin Connectors*, *J. Am. Chem. Soc.* **2003**, *125*, 13914.
317. Y. Wang, Y. F. Li, J. Wang, Y. Sang and C. Z. Huang, *End-to-End Assembly of Gold Nanorods by Means of Oligonucleotide-Mercury(II) Molecular Recognition*, *Chem. Commun.* **2010**, *46*, 1332.
318. A. Wei, *Calixarene-Encapsulated Nanoparticles: Self-Assembly into Functional Nanomaterials*, *Chem. Commun.* **2006**, 1581.
319. P. K. Jain, *Plasmons in Assembled Metal Nanostructures: Radiative and Nonradiative Properties, Near-Field Coupling and its Universal Scaling Behavior*, Ph.D Thesis, Georgia Institute of Technology **2008**.
320. W. K. Jung and K. M. Byun, *Fabrication of Nanoscale Plasmonic Structures and their Applications to Photonic Devices and Biosensors*, *Biomed. Eng. Lett.* **2011**, *1*, 153.
321. S. A. Maier, P. G. Kik and H. A. Atwater, *Optical Pulse Propagation in Metal Nanoparticle Chain Waveguides*, *Phys. Rev. B* **2003**, *67*, 205402.
322. H. Staleva, S. E. Skrabalak, C. R. Carey, T. Kosel, Y. Xia and G. V. Hartland, *Coupling to Light, and Transport and Dissipation of Energy in Silver Nanowires*, *Phys. Chem. Chem. Phys.* **2009**, *11*, 5889.
323. F. Zaato, *Processes for Forming Plasmonic Waveguides from Self-assembled Gold Nanoparticle Thin Films*, Ph.D Thesis, Virginia Polytechnic Institute and State University **2006**.
324. M. G. Espinoza, M. L. Hinks, A. M. Mendoza, D. P. Pullman and K. I. Peterson, *Kinetics of Halide-Induced Decomposition and Aggregation of Silver Nanoparticles*, *J. Phys. Chem. C* **2012**, *116*, 8305.
325. X. Han, J. Goebel, Z. Lu and Y. Yin, *Role of Salt in the Spontaneous Assembly of Charged Gold Nanoparticles in Ethanol*, *Langmuir* **2011**, *27*, 5282.

326. B. Tang, S. Xu, J. An, B. Zhao, W. Xu and J. R. Lombardi, *Kinetic effects of Halide Ions on the Morphological Evolution of Silver Nanoplates*, Phys. Chem. Chem. Phys. **2009**, *11*, 10286.
327. B. Lim and Y. Xia, *Metal Nanocrystals with Highly Branched Morphologies*, Angew. Chem. Int. Ed. **2011**, *50*, 76.
328. H. Zhang, M. Jin and Y. Xia, *Noble-Metal Nanocrystals with Concave Surfaces: Synthesis and Applications*, Angew. Chem. Int. Ed. **2012**, *51*, 7656 .
329. S. Yao, C. Zhou and D. Chen, *Highly Porous PVA Dried Gel with Gold Nanoparticles Embedded in the Network as A Stable and Ultrasensitive SERS Substrate*, Chem. Commun. **2013**, *49*, 6409.
330. S. Mura, G. Greppi, P. Innocenzi, M. Piccinini, C. Figus, M. L. Marongiu, C. Guob and J. Irudayaraj, *Nanostructured Thin Films as Surface-Enhanced Raman Scattering Substrates*, J. Raman Spectrosc. **2013**, *44*, 35.

## **Appendix: Chapter-1: Introduction**

**Table-A1.1: showing physical/chemical properties of bulk gold and silver**

<b>Bulk properties</b>	<b>Silver</b>	<b>Gold</b>
Electronic configuration	[Kr]4d <sup>10</sup> 5s <sup>1</sup>	[Xe] 5d <sup>10</sup> 6s <sup>1</sup>
Atomic Number- Weight	47-107.87 a.u.	79-196.97 a.u.
Lattice	f.c.c.	f.c.c.
Lattice Parameter	0.409 nm	0.408 nm
Density	10.50 g cm <sup>-3</sup>	19.28 g cm <sup>-3</sup>
Atomic Density	5.86x10 <sup>28</sup> m <sup>-3</sup> -58.6 nm <sup>-3</sup>	5.90x10 <sup>28</sup> m <sup>-3</sup> -59 nm <sup>-3</sup>
Volume for Atom	0.017 nm <sup>3</sup>	0.017 nm <sup>3</sup>
Wigner- Seitz Radius	0.160 nm	0.159 nm
Electronic Density	5.86x10 <sup>28</sup> m <sup>-3</sup>	5.90x10 <sup>28</sup> m <sup>-3</sup>
Fermi Speed	1.39x10 <sup>8</sup> cm s <sup>-1</sup>	1.40x10 <sup>8</sup> cm s <sup>-1</sup>
Fermi Energy	5.48 eV	5.51 eV
Plasma frequency	1.30x 10 <sup>16</sup> rad s <sup>-1</sup>	1.31x 10 <sup>16</sup> rad s <sup>-1</sup>
Relaxation time	4.01x 10 <sup>-14</sup> s	2.94x 10 <sup>-14</sup> s
Ionization Energy	7.57 eV	9.22 eV
Electric Resistivity	1.61x 10 <sup>-6</sup> Ωcm	2.20x 10 <sup>-6</sup> Ωcm
Melting Temperature	1235 K	1338 K
Boiling Temperature	2435 K	3243 K
Thermal Conductivity	4.29 W cm <sup>-1</sup> K <sup>-1</sup>	3.17 W cm <sup>-1</sup> K <sup>-1</sup>
Heat Capacity	(25 °C) 25.350 J mol <sup>-1</sup> K <sup>-1</sup>	(25 °C) 25.418 J mol <sup>-1</sup> K <sup>-1</sup>
Standard Potential	0.80 V	1.69 V
Electronegativity	1.9	2.4

**Table-A1.2: solubility of PVP both hydrophobic and in extremely hydrophilic solvents.**

<b>Soluble in</b>	<b>Insoluble in</b>
Acetic acid, Chloroform	Acetone, Butane, Xylene
Methanol, Ethanol, Propanol ,Butanol	Carbon tetrachloride
Dimethyl sulfoxide	Chlorobenzene, Cyclohexane
Diethylene glycol, Formic acid	Cyclohexanone
Ethylene glycol, Ethylene diamine	Diethyl ether, Dimethyl ether
Dimethyl acetamide, Glycerin	Dioxane, Methyl acetate
Butylamine, Water	Ethyl acetate, Propane
Cyclohexanol, Isopropanol	Hexane, Mineral oil
Methylene chloride	Methyl ethyl ketone
Methylcyclohexanone	Petroleum ether
Propylene glycol, Triethanolamine	Tetrahydrofuran
Pyrrolidone ,Vinylpyrrolidone N-Methylpyrrolidone	Toluene

## **Appendix: Chapter-3: Poly (Vinyl Pyrrolidone) Induced.....**

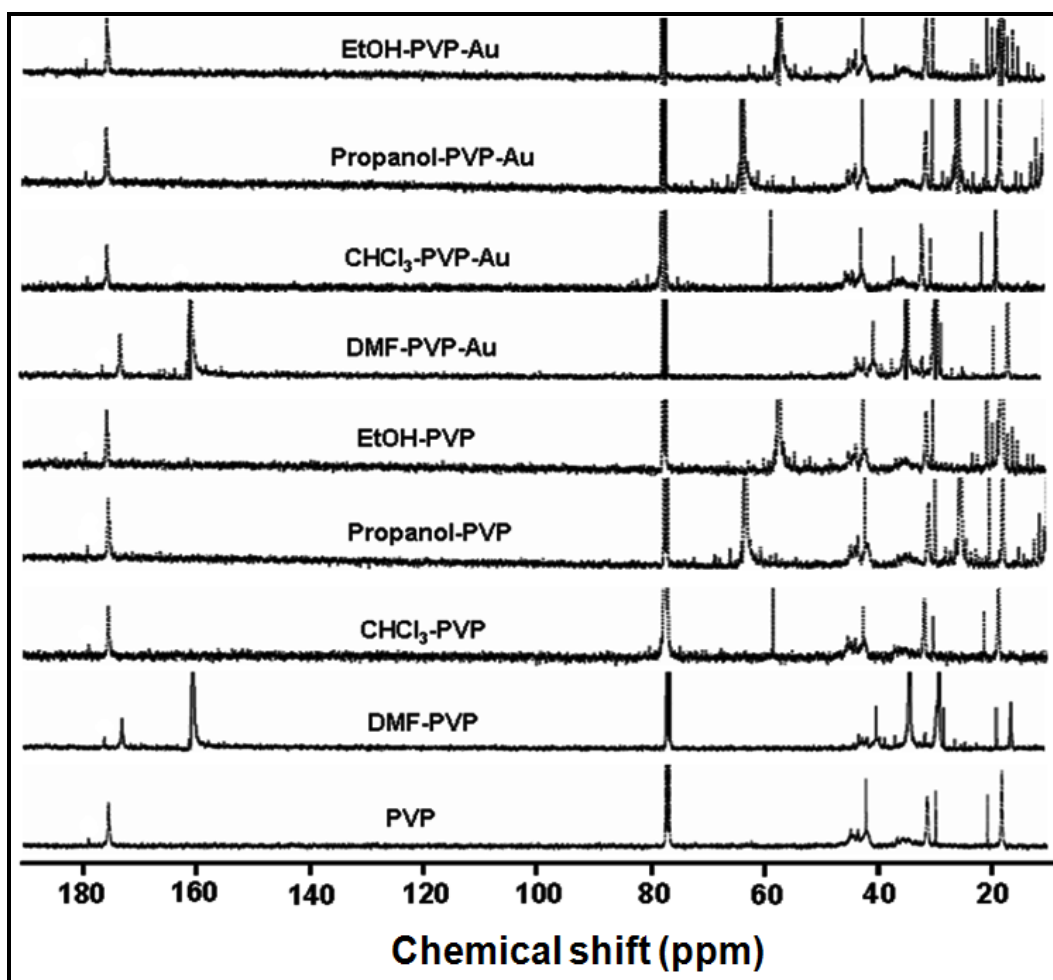


Figure-A3.1: Full range  $^{13}\text{C}$  NMR spectra of PVP, PVP-solvent/Au nanoparticles formed in respective solvents. The spectra show no appreciable changes in the as formed nanoparticle peaks line when compared to that of respective PVP-solvent complex.

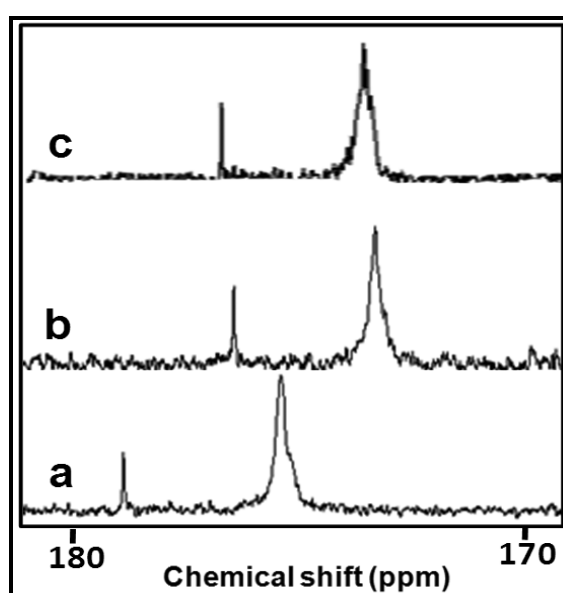


Figure-A3.2: Extended  $^{13}\text{C}$  NMR spectra of (a) PVP (b) DMF-PVP (c) DMSO-PVP depicting clearly the strong carbonyl (C-6) up-field chemical shift attributed to strong interaction of DMF and DMSO with PVP.

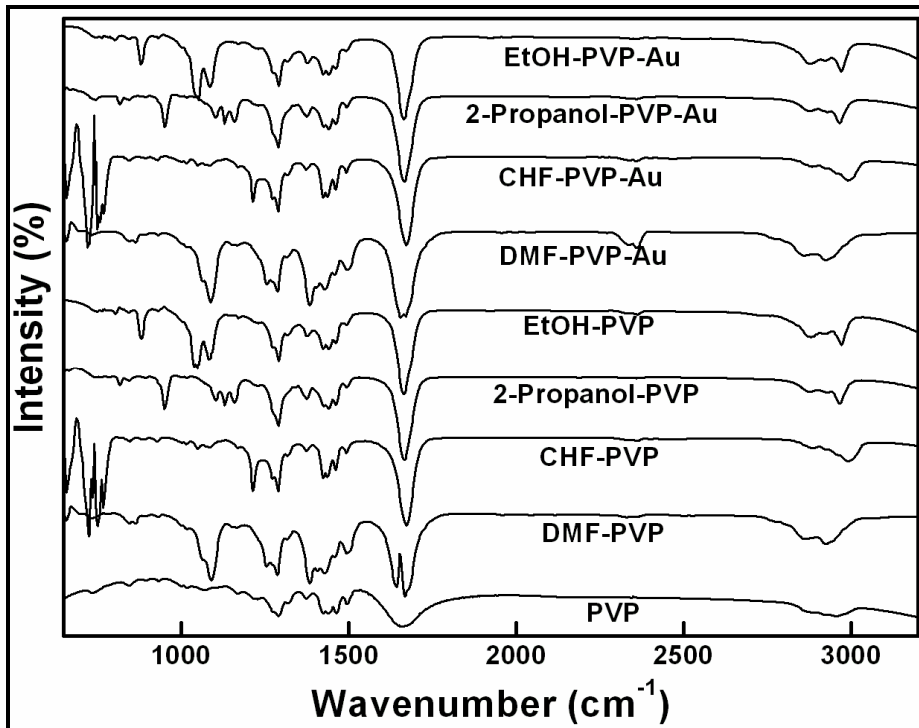


Figure-A3.3: Baseline corrected FTIR spectra over the full wavenumber range for the different samples clearly showing the varied carbonyl and nitrogen interaction of PVP in different solvents.

## **Appendix: Chapter-4: One Step Synthesis of Gold Nanostars.....**

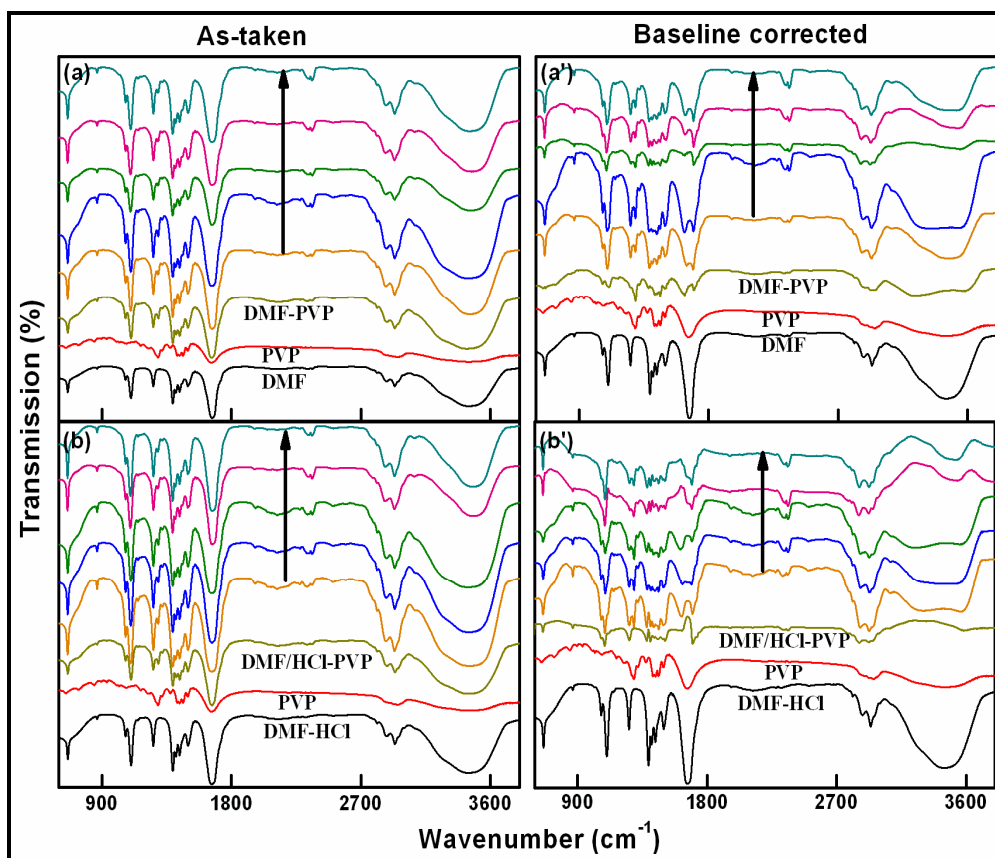


Figure A4.1: Kinetic FTIR spectra of as-taken and Baseline corrected with respect to DMF of Au nanostars over the full energy range (a, a') without HCl (b, b') with 0.6mM HCl. For comparison, individual spectra for DMF/HCl, PVP and DMF/HCl-PVP are also given. The arrow mark indicates the increasing reaction time, starting from 1, 20, 50, 80 and 100minutes in all the figures.

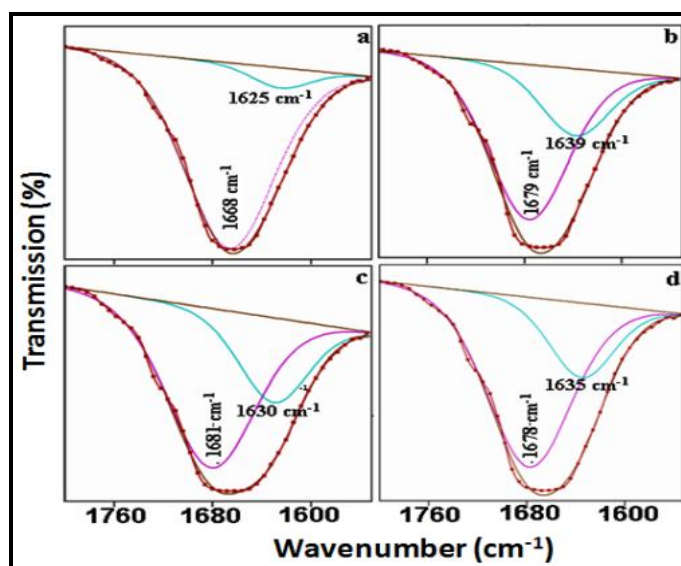


Figure-A4.2: Deconvoluted C=O peak in FTIR spectra of DMF-PVP complex (a) and DMF-PVP-HAuCl<sub>4</sub> reaction at 1min. (b), 20min. (c) and 100min.(d), which are in clear agreement with respect to DMF baseline corrected spectra.

## **Appendix: Chapter-6: Self-Organization/Reshaping of Gold Nanostars**

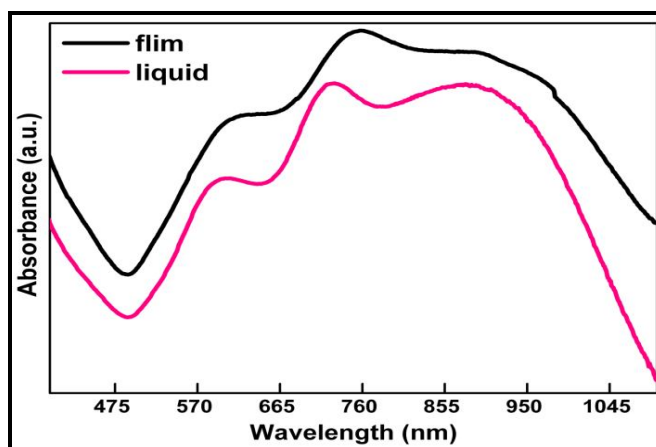


Figure-A6.1: UV-Vis spectra of solution and nanoparticulate thin film (drop-casted or spin-coated from the same solution shows similar spectra in agreement with the standard argument that infinite dilution of the solution results in a film.

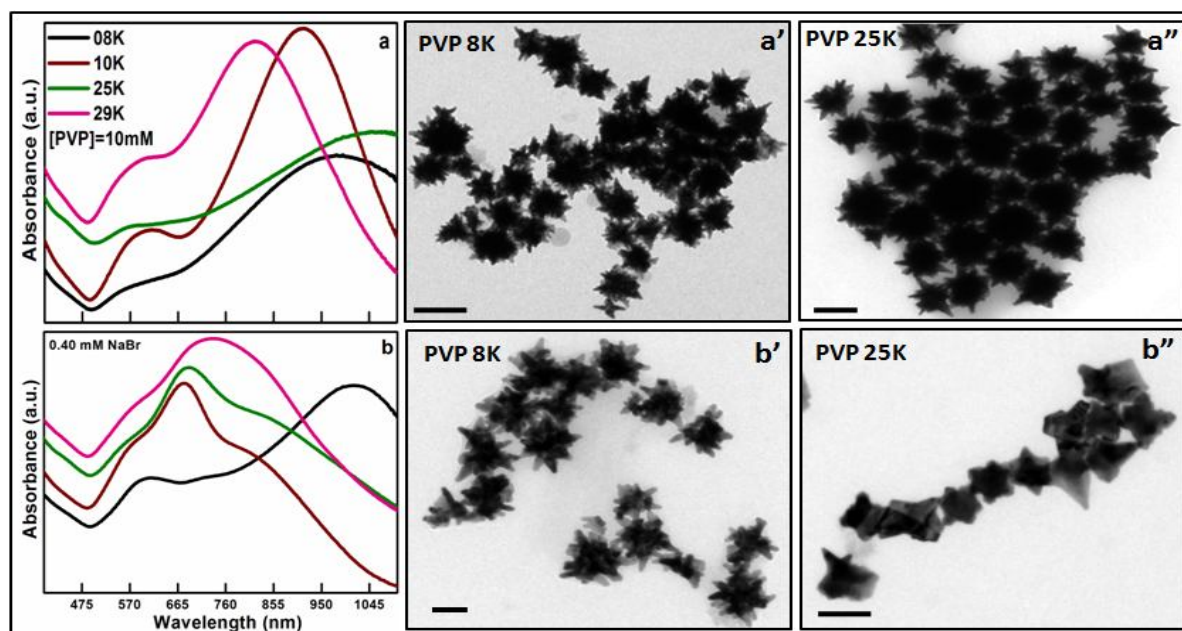


Figure-A6.2: Effect of different molecular weights of PVP is investigated on the optical spectra with their correlated morphology in the presence of NaBr emphasizing the extensive role of PVP in self-organized gold nanostructures.

## ABOUT AUTHORS



Dr. Abhitosh Kedia, is currently working as an assistant professor in Department of physics in UKA Tarsadia University, Bardoli, Gujarat since March, 2016. He completed his Masters and Ph.D from Department of Physics (University of Delhi). He has many credentials under his name such as being district topper in CBSE class 12 physics, qualifying JAM-IIT (Mathematics), CSIR-NET-Physical Sciences (JRF), first prize in state level quiz competition. He has more than twelve international publications in reputed journals with an average impact factor of 4. He has more than 130 citations to his credit. He has represented his work in several national and international conferences and has also bagged the best poster presentation award in ICYRAM, Singapore, 2012.

His major research interest has been in the synthesis of metal nanoparticles of different shapes and sizes. He has also shown his curiosity in understanding the plasmonic aspects and applications of nanoparticles. His major subject of interest covers quantum mechanics and condensed matter physics. With this book the author wants to share his findings on nanoparticles which can act as a reference material for all the aspirants of bachelors, masters and research levels.



Dr. Pandian Senthil Kumar, the experimental condensed matter physicist, is currently an assistant professor at the the department of physics @ Astrophysics, University of Delhi, INDIA. His major research interests include nanoplasmonics and nanophotonics, utilizing a wide range of spectroscopic/microscopic techniques.

## ABOUT THE BOOK

Plasmonics is an emerging research field for studying the interactions between electromagnetic waves and matter at the nanoscale. This book Gold nanoparticles: “Plasmonic Aspects and Applications” presents an appealing overview of the topic to both UG & PG students and researchers in describing the interaction of light with metal nanoparticles and nanoantennas for light radiation from concepts to recent discoveries in synthesis as well as applications.

Further this book gives detailed information on the systematic tuning/reshaping procedures for the synthesis of unusual new asymmetrical shape of the metal nanoparticles in high yield and purity, having plasmonic resonances spanning the entire visible region of the electromagnetic spectrum, that has not been envisaged before with much ease.



**Empyreal Publishing House**  
Guwahati, Assam  
Email: [info@editedbook.in](mailto:info@editedbook.in)

ISBN 978-81-939070-0-9



9 788193 907009